

GRAVITY GRADIENT STABILIZATION SYSTEM for the

DOCUMENT NO. 645D4361

16 OCTOBER, 1964

ADVANCED
TECHNOLOGICAL
SATELLITE

FACILITY FORM 602

N66 24502

(ACCESSION NUMBER)

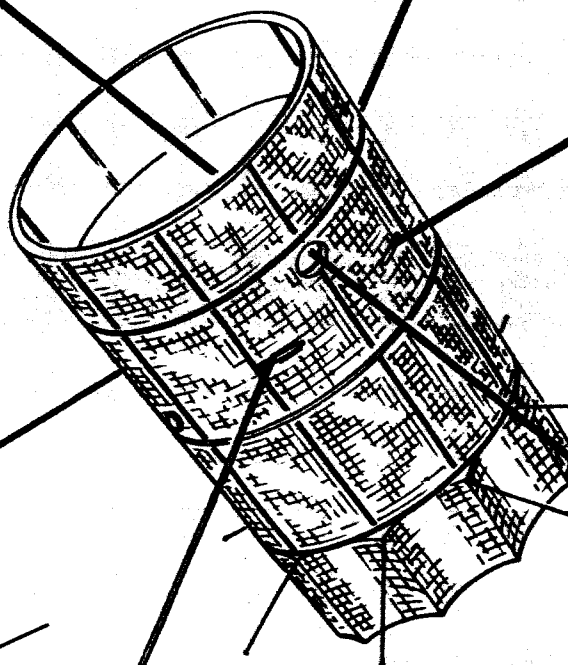
(THRU)

(PAGES)

(CODE)

(NASA CR OR TMX OR AD NUMBER)

(CATEGORY)



GPO PRICE \$ _____

CFSTI PRICE(S) \$ _____

Hard copy (HC) 6.00

Microfiche (MF) 1.25

653 July 65

FIRST QUARTERLY REPORT

NASA CONTRACT NAS 5-9042

GENERAL ELECTRIC
SPACECRAFT DEPARTMENT

DOCUMENT NO. 64SD4361
16 OCTOBER 1964

GRAVITY GRADIENT SYSTEM
FOR THE
ADVANCED TECHNOLOGICAL SATELLITE

FIRST QUARTERLY REPORT
29 JUNE 1964 THROUGH 30 SEPTEMBER 1964

CONTRACT NO. NAS 5-9042

FOR

NATIONAL AERONAUTICS AND SPACE ADMINISTRATION
GODDARD SPACE FLIGHT CENTER

APPROVED BY


R. J. KATUCKI, MANAGER
PASSIVE ATTITUDE CONTROL PROGRAMS

GENERAL  ELECTRIC

SPACECRAFT DEPARTMENT

A Department of the Missile and Space Division

Valley Forge Space Technology Center

P. O. Box 8555 • Philadelphia, Penna. 19101

TABLE OF CONTENTS

Section	Page
1. INTRODUCTION	1-1
1.1 Scope	1-1
1.2 Program Objectives	1-1
2. TECHNICAL DISCUSSION	2-1
2.1 Systems Analysis and Integration	2-1
2.1.1 Orbit Test Plan	2-1
2.1.1.1 Philosophy and Objectives	2-1
2.1.1.2 Preliminary Definition of Tests	2-2
2.1.1.3 "Crab" Angles Versus "Sensors Angles"	2-2
2.1.1.4 Eclipse Season Studies	2-4
2.1.2 Orbit Test Simulation Exercise	2-5
2.1.3 Definition of Coordinate System	2-10
2.1.4 Systems Analysis	2-10
2.1.4.1 Capture Studies	2-10
2.1.4.2 Transient Performance Studies	2-24
2.1.4.3 Magnetic Torque Studies of 6000-Mile Orbit	2-30
2.1.4.4 Magnetic Torque Studies of 24-Hour Orbit	2-41
2.1.4.5 Crab Angle of the 6000-Mile Orbit Configuration	2-52
2.1.4.6 Bottoming of the Damper Due To Thermal Bending	2-54
2.1.5 ATS Mathematical Model Coordinate Frames	2-57
2.1.5.1 Inertial Reference Frame	2-57
2.1.5.2 Geographic Reference Frame	2-60
2.1.5.3 Orbital Reference Frame	2-61
2.1.5.4 Satellite Body Reference Frame	2-62
2.1.5.5 Secondary Boom Reference Frame	2-65
2.1.5.6 Gravity Gradient Rod Reference Frames (Rods Attached to Main Body)	2-66
2.1.5.7 Gravity Gradient Rod Reference Frames (Rods Attached to Secondary Body)	2-67
2.1.6 Boom Studies	2-69
2.1.6.1 Gravity Bending	2-69
2.1.6.2 Thermal Bending	2-75
2.1.6.3 Boom Dynamic Response	2-78
2.1.7 Mass Properties Data	2-87
2.2 Boom Subsystem	2-89
2.2.1 Design and Analysis	2-89
2.2.1.1 Design Concept Selection	2-89
2.2.1.2 Major Subcontractor	2-90
2.2.1.3 Boom Subsystem Specification	2-92
2.2.1.4 Delineation of Design	2-92
2.2.1.5 Interface Consideration	2-107
2.2.1.6 Current Weight Status	2-113
2.2.2 Test (Development)	2-113
2.2.3 Expected Activity Next Quarter	2-113
2.3 Combination Passive Damper	2-120
2.3.1 Introduction	2-120
2.3.2 Design and Analysis	2-120
2.3.2.1 General	2-120
2.3.2.2 Development Testing	2-137
2.3.2.3 Expected Activity Next Quarter	2-147
2.3.3 Conclusions and Recommendations	2-150
2.4 Attitude Sensor Subsystem	2-151
2.4.1 Subsystem Description	2-151
2.4.2 Power Control and Distribution	2-151
2.4.3 Solar Aspect Sensor	2-152
2.4.4 RF Attitude Sensor Subsystem Requirements	2-153

TABLE OF CONTENTS (cont.)

Section	Page
2.4.4.1	Proposed Evaluation 2-153
2.4.4.2	Vehicle Attitude Determination 2-158
2.4.4.3	Development Tests 2-158
2.4.5	TV Camera Subsystem 2-160
2.4.5.1	Design and Analysis 2-170
2.4.5.2	Resolution and Accuracy 2-170
2.4.5.3	Limitation of the TVCS Due to Orbital Illumination 2-174
2.4.5.4	Development Tests 2-177
2.5	Reliability 2-180
2.5.1	Apportionment Factors 2-180
2.5.2	Apportionment 2-181
2.5.2.1	TV Camera 2-181
2.5.2.2	Sensor Components 2-181
2.5.2.3	Power Distribution 2-181
2.5.2.4	Gravity Gradient Rods 2-182
2.5.2.5	Combination Passive Damper 2-182
2.5.3	Parts 2-182
2.5.4	Standards 2-183
2.6	Quality Control Activity 2-184
2.7	Manufacturing 2-185
3.	NEW TECHNOLOGIES 3-1
4.	BIBLIOGRAPHY 4-1
5.	GLOSSARY 5-1
APPENDIX	A. Determination of Gravity Gradient Stabilization Advanced Technological Satellite Pitch, Roll and Yaw Angles from Solar Aspect Information A-1

LIST OF ILLUSTRATIONS

Figure No.		Page
2.1-1	First Shadow Encounter as a Function of Local Injection Hour . . .	2-6
2.1-2	Shadow History of a 6000 Nautical Mile, Circular Orbit . . .	2-7
2.1-3	Functional Schematic of Orbit Test Simulation Exercise . . .	2-8
2.1-4	ATS Coordinate System	2-11
2.1-5	ATS Capture Phase Normal Agena Position	2-13
2.1-6	ATS Capture Phase Normal Agena Position	2-14
2.1-7	ATS Capture Phase Normal Agena Position	2-15
2.1-8	ATS Capture Phase 90-Degree Agena Yaw	2-16
2.1-9	ATS Capture Phase 90-Degree Agena Yaw	2-17
2.1-10	ATS Capture Phase 90-Degree Agena Yaw	2-18
2.1-11	ATS Capture Phase 90-Degree Agena Yaw	2-19
2.1-12	ATS Capture Phase 1-Degree/Second Pitch Rate Bias.	2-20
2.1-13	ATS Capture Phase 1 Degree/Second Pitch Rate Bias.	2-21
2.1-14	ATS Capture Phase 1 Degree/Second Pitch Rate Bias.	2-22
2.1-15	ATS Capture Phase 1 Degree/Second Pitch Rate Bias.	2-23
2.1-16	Transient Performance, 31-Degree Half Angle Between X-Rods . . .	2-25
2.1-17	Transient Performance, 25-Degree Half Angle Between X-Rods . . .	2-26
2.1-18	Transient Performance, 19-Degree Half Angle Between X-Rods . . .	2-27
2.1-19	Transient Performance, 15-Degree Half Angle Between X-Rods . . .	2-28
2.1-20	Transient Performance, 11-Degree Half Angle Between X-Rods . . .	2-29
2.1-21	ATS Medium Altitude Gravity Gradient Experiment	2-32
2.1-22	ATS Medium Altitude Gravity Gradient Experiment	2-33
2.1-23	ATS Medium Altitude Gravity Gradient Experiment	2-34
2.1-24	ATS Medium Altitude Gravity Gradient Experiment	2-35
2.1-25	ATS Medium Altitude Gravity Gradient Experiment	2-36
2.1-26	ATS Medium Altitude Gravity Gradient Experiment	2-37
2.1-27	ATS Medium Altitude Gravity Gradient Experiment	2-38
2.1-28	ATS Medium Altitude Gravity Gradient Experiment	2-39
2.1-29	ATS Medium Altitude Gravity Gradient Experiment	2-40
2.1-30	ATS Synchronous Altitude Gravity Gradient Experiment	2-43
2.1-31	ATS Synchronous Altitude Gravity Gradient Experiment	2-44
2.1-32	ATS Synchronous Altitude Gravity Gradient Experiment	2-45
2.1-33	ATS Synchronous Altitude Gravity Gradient Experiment	2-46
2.1-34	ATS Synchronous Altitude Gravity Gradient Experiment	2-47
2.1-35	ATS Synchronous Altitude Gravity Gradient Experiment	2-48
2.1-36	ATS Medium Altitude Gravity Gradient Experiment	2-49
2.1-37	ATS Synchronous Altitude Gravity Gradient Experiment	2-50
2.1-38	ATS Synchronous Altitude Gravity Gradient Experiment	2-51
2.1-39	Effect of Rod Half Angle on Yaw Bias Angle (Crab Angle)	2-53
2.1-40	X_2 as a Function of Time	2-54
2.1-41	X_2 Versus t	2-55
2.1-42	X_1 Versus t	2-56
2.1-43	X_1 Versus t	2-58
2.1-44	Inertial Reference Frame	2-59
2.1-45	Geographic Reference Frame	2-60
2.1-46	Orbital Reference Frame	2-62
2.1-47	Satellite Body Reference Frame	2-63
2.1-48	Satellite Main Body, Rod and Secondary Boom Reference Frames. . .	2-64
2.1-49	Rod Reference Frame (Secondary Body)	2-68
2.1-50	Reference Frames	2-70
2.1-51	Gravity Acting on a Straight Rod With a Tip Weight	2-71
2.1-52	Nodes of Gravity Gradient Rod	2-76
2.1-53	Damping Analysis Results	2-79
2.1-54	Bending Moment Diagrams	2-80
2.1-55	Motion of Tip Mass Relative to Vehicle Body.	2-86

LIST OF ILLUSTRATIONS (cont'd)

Figure No.		Page
2.2-1	Extendable Boom Storage Methods: (a) End Storage, (b) Side Storage	2-91
2.2-2	ATS Gravity Gradient Rods, Play Shape and Guidance Sections.	2-93
2.2-3	Outline of Primary Boom	2-95
2.2-4	Primary Erection Unit Schematic	2-98
2.2-5	Scissoring and Drive Train Schematics	2-99
2.2-6	Primary Boom Subsystem Outline and Installation	2-101
2.2-7	Outline and Installation-Data-Damper Boom	2-105
2.2-8	Pertinent Interface Dimensions - MAGGE.	2-109
2.2-9	Gravity Gradient Boom/TV Camera View Pattern Supplement	2-111
2.2-10	Gravity Gradient Boom/R-F Sensor Field of View Intercepts	2-115
2.2-11	Envelope of Boom Positions in R. E. S. Field of View.	2-117
2.3-1	Combination Passive Damper Envelope History.	2-121
2.3-2	Preliminary Design Load Requirements	2-122
2.3-3	Combination Passive Damper for ATS	2-125
2.3-4	Combination Passive Damper Details	2-127
2.3-5	Force on Diamagnetic Specimen in Non-Uniform Field	2-132
2.3-6	Diamagnetic Suspension Schematic	2-134
2.3-7	Diamagnetic Suspension Characteristic	2-135
2.3-8	Simplified Hysteresis Damper.	2-139
2.3-9	Flux Density Measurements	2-142
2.3-10	Flux Density Measurements Effect of Pole Pieces	2-142
2.3-11	Magnetic Arrangement for Single and Double Penetration	2-143
2.3-12	Diamagnetic Suspension Test Set-Up Using Bismuth Samples	2-145
2.3-13	Low Order Force Fixture for Evaluating Pyrolytic Graphite	2-147
2.3-14	Overall View of Low Order Force Fixture Test Set-Up	2-147
2.3-15	Torque Angle Characteristics Bismuth and Various Thicknesses of Pyrolytic Graphite	2-148
2.3-16	Torque Angle Characteristics Bismuth and Various Thicknesses of Pyrolytic Graphite	2-149
2.4-1	Solar Aspect Sensor Detector Alignment	2-154
2.4-2	Ground Plane Antenna Model for Boom Interference Evaluation	2-159
2.4-3	Antenna Model Without Ground Plane	2-161
2.4-4	RF Altitude Sensor Antenna Pattern No. 1	2-162
2.4-5	RF Altitude Sensor Antenna Pattern No. 2	2-163
2.4-6	RF Altitude Sensor Antenna Pattern No. 3	2-164
2.4-7	RF Altitude Sensor Antenna Pattern No. 4	2-165
2.4-8	RF Altitude Sensor Antenna Pattern No. 5	2-166
2.4-9	RF Altitude Sensor Antenna Pattern No. 6	2-167
2.4-10	RF Altitude Sensor Antenna Pattern No. 7	2-168
2.4-11	RF Altitude Sensor Antenna Pattern No. 8	2-169
2.4-12	Target Illumination Effects	2-175
2.4-13	Resolution of Black Spot in Center of Illuminated Disc by Oscilloscope Trace of the Video Sweep Line	2-179
2.4-14	Relative Signal Strength for Other Than Normal Sunlight and Target.	2-179
A-1	Schematic Top View of Solar Detector	A-1
A-2	Unit Vector R to the Sun	A-2
A-3	Position of Detectors D ₁ through D ₅ with Respect to the Vehicle Axes	A-4
A-4	Detector Axes with Respect to the Vehicle Axes (Top View).	A-5
A-5	Detector Axes with Respect to the Vehicle Axes (Side View).	A-6

ABSTRACT

~~SECRET~~

The "First Quarterly Report" (GE Document No. 64SD4361) issued by the Spacecraft Department of the General Electric Company describes the technical progress made in the development of the Gravity Gradient Stabilization System for use on the Advanced Technological Satellite (ATS). The report, prepared under NASA Contract NAS 5-9042, describes the systems analysis and system development undertaken from the inception of the program, covering the period from June 29 to September 30, 1964.

The report contains a preliminary definition of the Orbit Test Plan and the first documentation of the Orbit Test Simulation Exercise. Coordinate frames required to derive the mathematical model are described. Results of the system analysis to date are also detailed.

A discussion of the factors that influence the design concept selection of the Boom Subsystem are presented and status of boom specifications and subcontractor work statements are discussed. A delineation of all design details thus far definitized is presented. Progress to date on the three critical interface areas (spacecraft, power and sensors) is included, and testing activities conducted on the Boom Subsystem are detailed

Activities in the design of the Combination Passive Damper have been concerned with establishing compatibility between an eddy current damper and a hysteresis damper. Twelve different concepts have been considered and studies are continuing to develop the final approach.

The Attitude Sensor Subsystem has been selected to meet the NASA requirement for monitoring vehicle attitude.

~~SECRET~~

SECTION 1. INTRODUCTION

1.1 Scope

This document is the first quarterly report issued since the inception of NASA Contract 5-9042 between the National Aeronautics and Space Administration and the Spacecraft Department of the General Electric Company leading to the design of those components and subsystems that make up the Advanced Technological Satellite Gravity Gradient Stabilization System. As required by the contract, this is a Type II report intended to inform scientific and technical personnel of the technical progress made toward the design of the ATS Gravity Gradient Stabilization System during the reporting period from 29 June to 30 September 1964.

1.2 Program Objectives

The Gravity Gradient Stabilization System is applied to three vehicles: on a 6000-nautical miles, inclined orbit and two at synchronous-equatorial.

The objective of the experiment at 6000 nm is to verify a previously developed mathematical model so that model can be employed for the design, and dynamic performance predictions of gravity gradient stabilized vehicles at other altitudes and conditions. It is also an objective to demonstrate compatibility between gravity gradient stabilization systems and other equipments, such as communication, meteorological, etc.

The mathematical model will then be employed to predict performance of the two synchronous experiments which will demonstrate compatibility of long life experiments with gravity gradient stabilization at synchronous altitudes.

SECTION 2. TECHNICAL DISCUSSION

2.1 Systems Analysis and Integration

2.1.1 Orbit Test Plan

2.1.1.1 Philosophy and Objectives

The ATS Orbit Test Plan is, fundamentally, a detailed statement of the operational plan for accomplishing the basic objectives of the ATS Program. The total plan must provide sufficient flexibility and time for the accomplishment of the several goals of ATS, on a non-interference basis between experiments and in the order of descending priority of experiments. The gravity gradient experimenter, in planning orbit tests, must keep in mind the dual role of his responsibility: that of experimenter and that of prime spacecraft attitude control contractor for all 6000-mile orbit (MAGGE) and the 24-hour orbit (SAGGE) flights. These responsibilities are best fulfilled, it is believed, by concentrating the major portion of gravity gradient experimentation on the MAGGE flight and reserving the SAGGE flights for demonstrations of compatibility with mission requirements of long-life applications-type satellites. Gravity gradient experimentation, per se, will therefore be minimized on SAGGE; only those experiments which require the unique environment and parameters of a synchronous orbit will be planned.

The primary gravity gradient objective on MAGGE is the verification of the ATS Mathematical Model. This is also considered to have the highest priority of all MAGGE experiments. The MAGGE Orbit Test Plan must, therefore, contain those tests deemed necessary and sufficient for the accomplishment of model verification. The tests described in the next section are tentative but reflect preliminary thinking in terms of verification requirements. The basic concept is to provide a series of tests which:

1. Isolate the major perturbative effects on the dynamic stability of gravity gradient satellites
2. Provide parametric data for use in design of future gravity gradient satellites
3. Demonstrate operational feasibility of gravity gradient satellites with sophisticated missions.

In the first category are tests designed to amplify (and thereby isolate) the effects of torques due to solar pressure and magnetic field interactions, the effect of thermal, and dynamic stress transients in the erecting torque and damping torque booms, and the effect of orbit eccentricity. In the second category are tests design to vary the satellite inertia ratios and magnitudes and compare alternative damper designs. In the third category are inversion and capture tests and compatibility tests with meteorological and communications satellite mission objectives. The ATS Mathematical Model will be used to predict satellite performance throughout the entire range of orbit tests. Flight data will then be used to verify and/or modify the Model. Flight Data will be reduced by the GE-developed Attitude Determination Program; this program will also provide "missing link" data between ground stations by interpolation of data obtained when the satellite is in view of ground stations. Verification and/or modification of the ATS Mathematical Model will be implemented through the GE-developed Data Correlation Program. The Data Correlation program will be designed to compare predictions with observations and identify the source of basic discrepancies.

2.1.1.2 Preliminary Definition of Tests

Table 2.1-1 summarizes preliminary thinking as to the nature, sequence and duration of gravity gradient orbital tests. The inclusion of tests which require the use of a "Center of Pressure Relocation (CPR) Boom" and a "Three-Axis Magnetic Torquing Coil" are especially tentative in nature since neither item of hardware has, as yet, received approval for procurement. This does not lessen their importance to the Orbit Test Plan, however, since they are fundamentally essential to current philosophies on ATS Mathematical Model verification. Time indicated for execution of the orbit eccentricity change is also tentative. Current studies on damper bottoming and boom dynamics, under the influence of various excitation modes from the eccentricity thruster, must be completed before the optimum maneuver time is established. Time for execution of the eccentricity change is also dependent upon the initial value of eccentricity; if initial eccentricity is excessive, the capabilities of the thruster may be used to circularize the orbit rather than increase the eccentricity. The requirement for an initial period of continuous sunlight imposes "launch-on-time" problems as discussed in paragraph 2.1.1.4.

2.1.1.3 "Crab" Angles Versus "Scissor" Angles

One of the earliest and most basic of the planned gravity gradient orbit test experiments is the scissoring of the "X-booms." The nominal half-angle, measured in a plane containing the local vertical and the tip masses of the primary stabilization booms, is 19 degrees. The "crab" angle (measured between the plane of the X-boom tip masses and the orbital plane) is, nominally, 20.5 degrees for the 19 degree X-boom half-angle. It is this nominal crab angle which dictates the angular alignment of the plane of the X-boom tip masses to the longitudinal axis of the basic cylindrical configuration of the spacecraft and ensures a nominal, normal orientation of the spacecraft's cylindrical axis relative to the plane of the orbit. Since the crab angle is a function of the spacecraft's inertia ratios, and since the spacecraft's inertia ratios are a function of the X-boom half-angles, the scissoring experiment will change the nominal crab angle of the spacecraft relative to the plane of the orbit. It should be pointed out, however, that the nominal crab angle is defined in terms of steady-state behavior. The scissoring experiment constitutes a series of large angle displacements, at various X-boom half-angles, over the entire range of scissor angles. The cross-coupling effects, during settling from the large displacements to steady state, will induce yaw oscillations about the steady state crab angle value as discussed and illustrated in paragraph 2.1.4.2. Electrical power computations during scissor angle experiments should, therefore, consider the transient case rather than the static case since current plans call for continuous disturbances from steady state throughout the range of scissors experiments. Unless the scissors experiment indicates an optimum X-boom half-angle other than 19 degrees, 19 degrees will be the nominal angle maintained throughout orbital life when scissor angle tests are not being conducted. Table 2.1-2 presents the nominal, steady-state crab angles versus X-boom half-angles and provides estimates of the total time, based

TABLE 2.1-1. ORBIT TEST PLAN, MAGGE (PRELIMINARY)

(MAGGE)				
TEST NO.	TEST OBJECTIVE	TEST MECHANICS	ALLOWED TEST TIME	COMMENTS
0	Capture in "upright position without deployment of damper rod or uncaging of damper. (Required as "set up" for Test No. 1)	Deploy X-boom (at 19° half-angle) and damper booms at sufficient rate to prevent tumble; both dampers caged.	2 days	If capture is inverted, a contingency test plan is required. Tentatively, the contingency plan calls for inversion with the subliming rockets two days after capture. Test No. 1 is performed in the inverted orientation.
1	Establish the presence or absence of measurable structural damping.	Observe telemetered attitude data from time of capture with both dampers caged.	2 days	This test is contingent upon the success of capture without damping.
2	Determine "settling time" for No. 1 damper (X-boom half-angle = 19°)	Uncage No. 1 damper, observe behavior down to steady state.	5 days	Estimated settling time = 3 days
3	Determine "settling time" for No. 2 damper (X-boom half angle = 19°)	Cage No. 1 damper, uncage No. 2 damper, observe steady state behavior for 1 day; displace approximately 45° in pitch or roll, observe behavior down to steady state (X-boom half angle still at 19°)	6 days	(a) 1 day for observance in steady state prior to large angle displacement; 5 days settling time as in Test No. 2 (b) 45° displacements are indicated in this and subsequent tests only as order of magnitude. Displacements are tentatively assumed to be provided via on-off commands to subliming rockets.
4	Determine effect of "large" CP/CM offset (X-boom half angle = 19°) (Solar incidence angle ≈ 0)	Extend SP boom; observe change in steady state attitude data; retract boom.	8 days	(a) Estimated time for settling to new steady state conditions 3 days; 2 days observation time under new steady state conditions; 3 days to settle back to original steady state mode after retraction of SP boom. (b) A back-up device for discarding the boom will be provided in the event of a retraction failure. Retraction desirable since test should be repeated in about 4 months under new solar incidence conditions. (c) Preliminary estimate on boom length for MAGGE, assuming a $1/2$ " dia rod = 30 feet.
5	Isolate effect of eclipse disturbances due to change in thermal bending of X-booms (X-boom half angle still 19°)	Enter eclipse period in steady state condition with No. 2 damper still uncaged; observe effect on steady state behavior for 2 days; cage No. 2 damper, uncage No. 1 damper; observe effect on steady state behavior for additional 2 days.	4 days	An inexact period of time between the end of Test No. 4 and the beginning of Test No. 5 will prevail due to the uncertainties associated with the launch-on-time and design orbit achievement problems. The exact time of eclipse encounter can be established only after orbit injection and orbit determination. The time of eclipse encounter, however, should be biased "downstream" to ensure completion of the first 4 tests and steady state attitude dynamics at time of first eclipse encounter.
6	Determine the effect of X-boom half angles on settling times and steady state behavior for dampers No. 1 and No. 2 (X-boom half angles = 31° , 25° , 15° , 11°)	Change the X-boom half angle from 19° to 31° with damper No. 1 still uncaged; observe steady state behavior for 2 days; displace to 45° (see note on Test No. 3); observe settling time for 2 days; cage No. 1 damper, uncage No. 2 damper; displace to 45° , observe settling time to steady state (5 days). Repeat with opposite sequence on dampers, at X-boom half angle of 25° . Ditto at 15° and 11° .	9 days 9 days 18 days	Getting steady state data on the new X-boom angle prior to displacement eliminates the requirement for settling to steady state with that damper prior to switching to the alternate damper and displacing it to the 45° angle. At end of test sequence (after completion of test with X-boom half angle = 11°), damper No. 2 is caged and damper No. 1 is uncaged.
7	Determine the effect on steady state conditions of "large" satellite dipole moment. No. 1 damper X-boom half angle = 19°	Return the X-boom half angle to 19° ; introduce known orthogonal dipole moments (on the order of 3 times the estimated residual dipole moments) along orthogonal spacecraft axes by means of magnetic torquing coils. Observe change in steady state behavior (3 days each axis). Turn coils off, return to original steady state conditions.	9 days	Only significant design problem is elimination of coil-produced residual fields after shut-down of torquing coils.
No Gravity Gradient Tests for about 60 days (MET, and COMM, Experiments) - Preliminary evaluation of Gravity Gradient data to ensure successful completion of all prior tests. Wait for appropriate orbital conditions for desired new solar incidence angle for repeat of Test No. 4. Total elapsed time to this point approximately 72 days.				
8	Repeat Test No. 4 with new solar incidence angle and 3-4 months degradation on "painted" surfaces.	(Same as Test No. 4)	8 days	(Same as Test No. 4)
9	Isolate effect of orbit eccentricity	Change e by 0.01 (No. 1 damper uncaged) Change e by additional 0.01 (No. 2 damper) Repeat Tests No. 2 - No. 8	30 days 30 days 140 days	If initial orbit has an eccentricity on the order of 0.01 or greater, it may be desirable to attempt a decrease in e rather than an increase. 140 days for repetition of Tests No. 2 - No. 8 includes 60 days of no test between No. 7 and No. 8.
10	Demonstrate inversion capability.	Invert with subliming rockets and re-invert.	6 days	As an alternate inversion technique, boom retraction at a sufficient rate to introduce a tumbling tendency can be employed.
11	Determine effect of large inertia change and thermal rod bending change	Retract X-booms to 50 feet	14 days	Rate of retraction must be slow enough to avoid the introduction of tumbling torques.
Total elapsed time to this point approximately 360 days (240 days gravity-gradient experiment time)				

on Table 2.1-1, for which each half-angle will be maintained. Results of the scissors experiment will be used to optimize the X-boom half-angle for SAGGE; no scissors experiments are presently planned for SAGGE, however.

TABLE 2.1-2. "CRAB" ANGLE VERSUS "SCISSOR" ANGLE

NO. OF DAYS	X-BOOM HALF-ANGLE	CRAB ANGLE	TEST NO.	% OF TOTAL
27	19°	0	0-5	7-1/2
9	31°	-13.6°	6	2-1/2
9	25°	- 9.7°	6	2-1/2
9	15°	+11°	6	2-1/2
9	11°	+25.5°	6	2-1/2
164	19°	0	7-9	45-1/2
9	31°	-13.6°	9	2-1/2
9	25°	- 9.7°	9	2-1/2
9	15°	+11°	9	2-1/2
9	11°	+25.5°	9	2-1/2
97	19°	0	9-11	27
360				100

2.1.1.4 Eclipse Season Studies

As indicated in Table 2.1-1, current plans call for an initial 27 days of continuous sunlight prior to the first encounter with the earth's shadow. This is for the purpose of removing the extraneous effects of thermal "twang" from observations of settling times using alternate dampers and various values of X-boom half-angles. (Thermal "twang" is the term used to describe the sudden thermal bending which the booms will experience in passing from a region of total eclipse into a region of continuous sunlight and vice versa.) It is also desirable to observe (via the TV camera) the effect of increasing lengths of eclipse time on thermal bending, beginning with an eclipse time of near-zero. Since the accomplishment of an initial period of continuous sunlight represents a constraint on launch parameters, and since orbit injection time errors affect the feasibility of accomplishing a pre-specified length of time for continuous sunlight, the General Electric "Shadow History Program" was utilized to study the general characteristics of eclipse seasons compatible with a planned launch date of October 15, 1966. Specified orbit characteristics were as follows:

1. 6,000 nautical mile, circular orbit
2. 28-degree inclination to equator
3. Injection latitude = 26 degrees, South
4. Injection longitude = 96 degrees, East
5. Launch date = October 15, 1966 (day 288).

Injection latitude and longitude were based on data in the Hughes Aircraft Corporation (HAC) "Advanced Technological Satellite Program Presentation" brochure, dated June, 1964 (SSD 4277B). Results of these studies are presented in Figures 2.1-1 and 2.1-2. Figure 2.1-1 indicates an extreme sensitivity to injection time errors. To accomplish the desired 27 days continuous sunlight prior to first eclipse encounter, Figure 2.1-1 indicates a local time (at the coordinates of the injection point) of 7.64 hours, P.M. (time 1938). An error of only 6 minutes injection time, however, represents a shift of almost two days in the time of first eclipse encounter. This represents an extremely tight constraint on launch time and may be incompatible with other launch time constraints. (The GE "Shadow History Program," it should be pointed out, assumes a cylindrical rather than a conical earth shadow. This should not, however, significantly affect the predicted trends.) Figure 2.1-2 presents the entire eclipse season profile, for approximately two years, after the assumed injection time of 7.64 hours, P.M., local time. The maximum shadow period per orbit is approximately 46.5 minutes with time in shadow initially increasing at a rate of slightly less than one minute per orbit.

2.1.2 Orbit Test Simulation Exercise

Due to the complexities of the operational gravity gradient orbit test plan and the necessity of checking out the data processing and data correlation programs and the personnel related functions associated with efficient handling of the quantities of data anticipated, an orbit test simulation exercise has been proposed. Figure 2.1-3 illustrates, functionally, the elements necessary to a complete orbit test simulation. At least one complete test, including telemetry transmission of simulated data, is felt to be mandatory to a meaningful simulation exercise. The remainder of the tests could logically by-pass the telemetry portion of Figure 2.1-3 (as indicated by the dashed line on Figure 2.1-3) and serve mainly as a checkout of the data correlation and Mathematical Model verification procedure. The following notes refer to the individual blocks of Figure 2.1-3.

NOTE NO. 1: Initial conditions will be based on requirements of the gravity gradient orbit test plan (Table 2.1-1). Nominal steady-state conditions, prior to the application of perturbation commands, will be assumed. Inputs to the ATS Mathematical Model and the Spacecraft Dynamics Simulation Program will generally be identical. However, one test might be of the effect of slightly different initial conditions for the two programs. This would simulate the inability, in the operational sense, to exactly match initial conditions to those of the orbiting spacecraft.

NOTE NO. 2: The ATS Mathematical Model, presently under development, will be used to predict spacecraft behavior in orbit under the stimulus of planned orbital tests. Verification of this model is one of the fundamental objectives of the ATS program. Once verified, this model will be used as a design tool for future gravity oriented satellites. The output of the ATS Mathematical Model program is recorded on tape for subsequent correlation with the output of the Attitude Determination Program.

NOTE NO. 3: The Spacecraft Dynamics Simulation Program is, essentially, a "gimmicked" ATS Mathematical Model. It is used to generate an output that simulates the actual behavior of the spacecraft in orbit. In tests using the telemetry link, the "gimmicks" are omitted. The outputs of the Mathematical Model and the Spacecraft Dynamics Simulation Program are then identical. Perfect correlation should prevail except for errors introduced in the telemetry data reduction. This provides a technique for the identification and subsequent recognition of telemetry-induced errors in data correlation. Tests which omit the telemetry link (dashed

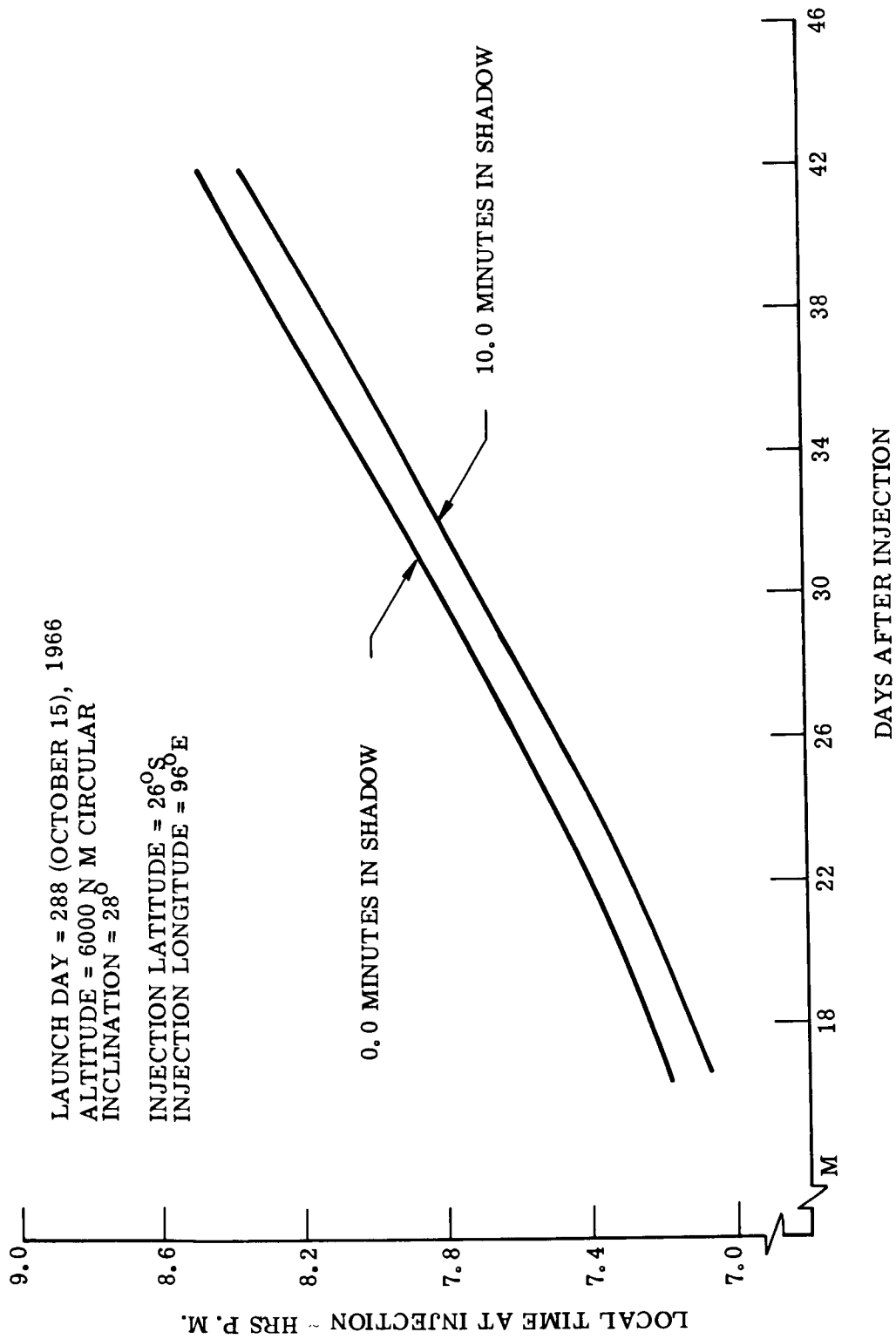


Figure 2.1-1. First Shadow Encounter as a Function of Local Injection Hour

INJECTION: DAY = 288, HOUR = 7:38 PM
LATITUDE = 26°S
LONGITUDE = 96°E
INCLINATION = 28°

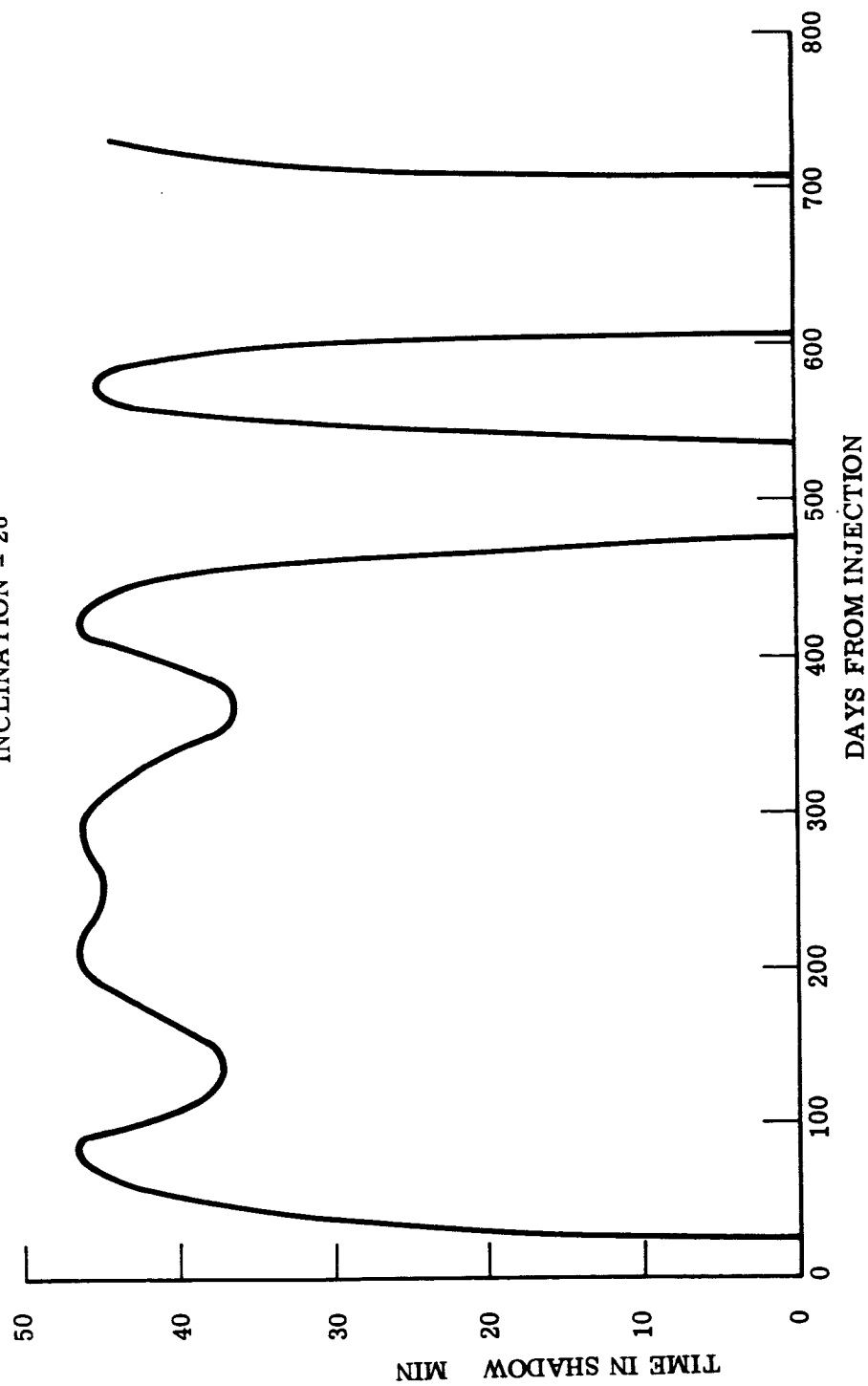


Figure 2.1-2. Shadow History of a 6000 Nautical Mile, Circular Orbit

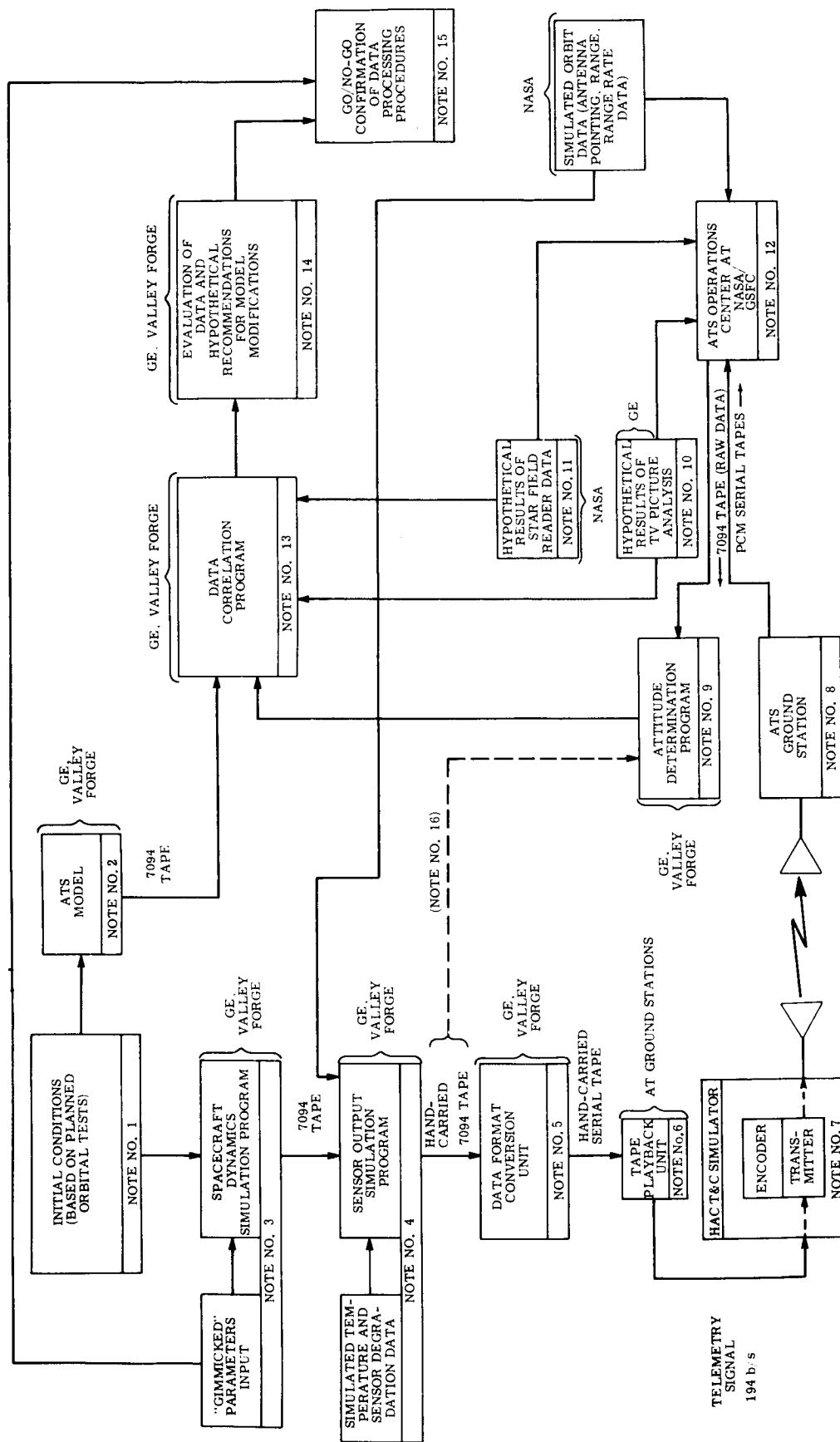


Figure 2.1-3. Functional Schematic of Orbit Test Simulation Exercise

line in Figure 2.1-3) introduce pre-selected variations in the Mathematical Model to test the ability of the Data Correlation Program (and responsible technicians) to detect those variations. As an example, the magnetic dipole in the ATS Mathematical Model will be based on system measurements prior to launch. The "gimmick" in the Spacecraft Dynamics Simulation Program, for one test, could be a re-orientation and possible change of magnitude of the magnetic dipole (to simulate a re-orientation due to launch environment vibrations). The test of the Data Correlation Program would then be the ability of the responsible technicians to recognize this "gimmick" using the Data Correlation Program as a tool. The "gimmick" used in any given test would remain unknown to the responsible technicians until after they have made their conclusions based on analysis with the Data Correlation Program.

NOTE NO. 4: The Sensor Output Simulation Program must essentially work backwards through the equations for reduction of sensor output signals to spacecraft attitude data. Since the outputs of some of the sensors (notably the earth sensor) are temperature sensitive, simulated temperature data must be provided. Degradation data can also be provided to make the simulation even more realistic and check the adequacy of the data system to recognize and utilize degraded sensor data.

NOTE NO. 5: The output of the Sensor Output Simulation Program is on tape in 7094 format; prior to use at the ground stations, it must be converted to PCM serial format.

NOTE NO. 6: Simulated sensor output signals, in PCM serial format, are generated on a tape playback unit and fed directly into a duplicate of the ATS telemetry transmitter. (NOTE NO. 7)

NOTE NO. 8: Telemetered data is received at the ATS ground stations and transmitted to the NASA/GSFC Operations Center.

NOTE NO. 9: Raw telemetry data, in 7094 format, is fed into the Attitude Determination Program to get spacecraft attitude and rate data. The Attitude Determination Program also provides data interpolation between ground stations. To check out this aspect of the Program, data from each of the ground stations (containing sufficient information to be representative of a complete ground station pass) will be supplied. "Missing link" data between stations will then be generated in a test of the sufficiency and adequacy of this subroutine.

NOTE NO. 10: Current plans do not include the simulation of TV data transmission. For use in the Data Correlation Program, hypothetical results of TV data reduction will be generated. This will include partial time histories of boom thermal bending phenomena.

NOTE NO. 11: Simulation of Star Field Reader data will be in the format to be supplied by the Star Field Reader vendor so that simulated results can be fed into the Data Correlation Program. Since the same data correlation program will be used for both MAGGE and SAGGE flights, the Star Field Reader data capability must be included even though the sensor will not fly on MAGGE.

NOTE NO. 12: The shipment of data to the ATS Operations Center at NASA/GSFC is intended, primarily, to identify personnel related duties associated with the use of that data and obtain an indication of the time-phasing requirements. As a part of the simulation exercise, "emergency" situations could be simulated requiring decisions in real time by the personnel manning the center.

NOTE NO. 13: The Data Correlation Program represents the "working tool" of the Mathematical Model verification procedure. A team of trained technicians will utilize this program to isolate and identify discrepancies between predictions of the ATS Mathematical Model and actual spacecraft attitude data as determined from the Attitude Determination Program. These technicians will, in a sense, be the detectives that track down the errors and recommend the modifications in the ATS Mathematical Model. It is the validity of this technique, and this program, that is at the heart of the requirement for a detailed and sophisticated orbit test simulation exercise. Since Mathematical Model verification is a fundamental MAGGE objective, and since the ATS Data Correlation Program is being proposed as an essential part of the verification procedure, a thorough checkout of this program, under realistic operational conditions, seems mandatory.

NOTE NO. 14: The recommendations of the Data Correlation Program technicians are documented.

NOTE NO. 15: A comparison of the recommendations of the Data Correlation Program technicians with the nature of the "gimmick" used in the Spacecraft Dynamics Simulation Program (NOTE NO. 3) reveals a "go/no-go" confirmation of the data processing procedures.

NOTE NO. 16: After establishing the nature and characteristics of errors due to telemetry data processing, the telemetry link can be by-passed as indicated by the dashed line of Figure 2.1-3.

2.1.3 Definition of Coordinate Systems

As directed by NASA/GSFC at the September 21 interface meeting with HAC, the coordinate system illustrated in Figure 2.1-4 will be used in all subsequent ATS analytical work. Section 2.1.5, this report, expands on this system and defines all coordinate frames required for a complete description of the ATS Mathematical Model. The system to be used for mass properties analysis replaces the Z axis with an L axis where L is the distance "forward," in inches, from the spacecraft separation plane. The distance L, then, designates station location. The "forward" end of the spacecraft is the end opposite the separation plane. To convert from the X, Y, Z system to the X, Y, L system.

$$L = l_{CM} - Z$$

where l_{CM} is the center of mass station location.

2.1.4 System Analysis

2.1.4.1 Capture Studies

A gravity gradient stabilized satellite is oriented by the torques produced by the gradient in the gravitational field and augmented by orbital dynamics. These torques are proportional to the differences in the moments of inertia of the satellite. Since moments of inertia have an axis, but not a direction, the gravity gradient torques merely align the axes of the satellite. As a consequence, the satellite is stable in both the "upside down" and the "rightside up" position (in addition to the "forward" and "backward" position). Once stabilized, the satellite will remain in the position it is in, and to achieve "rightside up" capture, it is only necessary to insure that the position the vehicle stabilizes to initially, is the correct one. The technique employed for 6000-mile orbit vehicle is to correctly position the satellite at separation and reduce the separation rates to a very small value by extending the gravity gradient rods.

The performance of the ATS gravity gradient system at capture can be best explained in terms of total energy (kinetic plus potential) with reference to computer runs from a three-axis rod extension computer program. For the vehicle to capture without tumbling, the total energy content of the system at the completion of rod deployment must be less than the potential energy required to tumble. The potential energy is that associated with gravity gradient and is calculated with respect to a coordinate system rotating at orbital rate. The kinetic energy must, however, be calculated with respect to inertial space and, as a consequence, the envelope of capture conditions is symmetrical with respect to

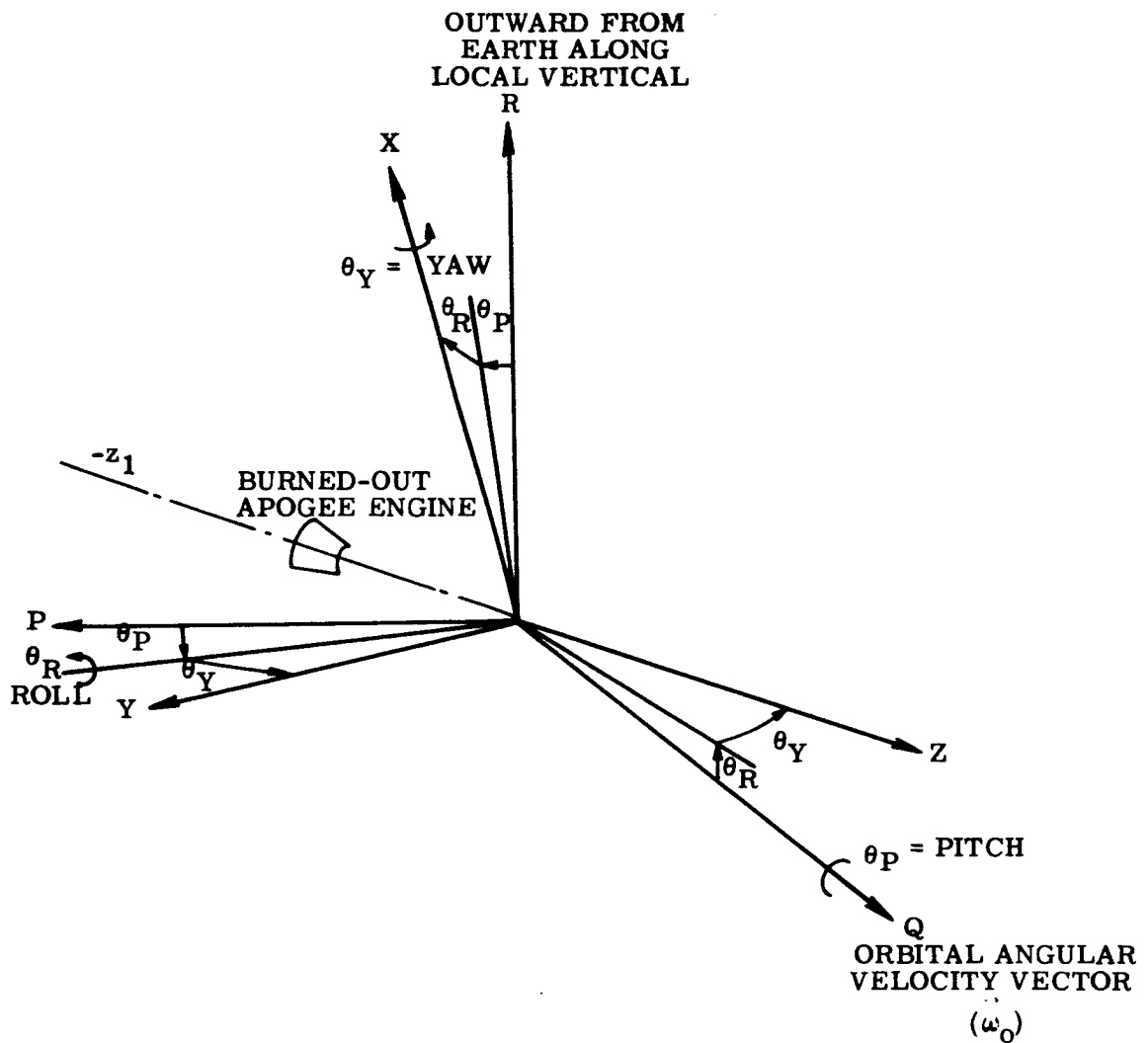


Figure 2.1-4. ATS Coordinate System

orbital rate rather than zero rate. The ability to capture will therefore depend upon the magnitude and direction of the separation rates. The condition most likely to cause tumble is a backward pitch rate (pitch up).

To relate the conditions after rod deployment to those at separation, the rod lengths, initial moments of inertia, etc., must be known. In this preliminary analysis only oscillations in the undamped mode with four rods extended to form an X will be considered. The initial moments of inertia for the satellite body are 67.5 slug-ft^2 , and the rod lengths are 100 feet, extended at 2 ft/sec. A 3σ separation tolerance of 1 deg/sec was assumed about any axis except the roll axis, which was assumed to have a $1/4 \text{ deg/sec}$ rate (the axes are the Agena axes). During the rod erection phase, the initial separation rate is reduced by the laws of conservation of momentum, and kinetic energy is lost. Preliminary calculations indicated that if the 1 deg/sec separation rate was in the negative pitch direction, the vehicle would tumble. To verify this conclusion, a computer run was made with this condition, and the vehicle did tumble in pitch (Figure 2.1-5). Yaw also "tumbled", a condition which is normal and makes the "forward" capture of yaw virtually impossible. If the rate were forward in the pitch direction, the total energy is less than that required to tumble and the vehicle captures (Figure 2.1-6). The roll rate for both these runs was $1/4 \text{ deg/sec}$. Note that the time to erect the rod is short compared to the printout interval, and the vehicle appears to "jump" to an initial position.

If the separation rate occurs on the yaw axis, the final yaw rate will be high (because of the small moment of inertia growth), and the total energy content of the vehicle is greater than that required to tumble. Figure 2.1-7, however, indicates that the vehicle did not tumble, but is precessing about an axis slightly offset from the local vertical. It is expected that the introduction of the damper boom into this situation will cause significant oscillations, and tumble may occur.

To circumvent the tumble problem indicated in Figure 2.1-5, two approaches are possible. The first approach requires the Agena to be yawed 90 degrees such that the $1/4 \text{ deg/sec}$ roll rate appears on the orbital pitch axis. This case should capture whether the rate is positive or negative, and Figures 2.1-8 and 2.1-9 indicate that capture does occur (note that the growth of the roll amplitude is accompanied by a decrease in pitch amplitude as would be expected from the conservation of energy law). To ensure that the separation rate uncertainties do not interfere with capture, a 1 deg/sec pitch rate (now an orbital roll rate) was added and the vehicle still captured (Figure 2.1-10). Placing the initial rate on yaw also produced a capture situation (Figure 2.1-11).

The alternative to yawing the Agena is to provide the vehicle with a nominal 1 deg/sec pitch separation rate and a pitch position bias. With a nominal variation in separation of approximately 1 deg/sec, the final pitch rate would be between 0 and 2 deg/sec depending upon the direction of the 1 deg/sec uncertainty.

Figures 2.1-12 and 2.1-13 indicate that capture did occur with the rate bias even without the pitch position bias. Figure 2.1-14 shows the pitch bias rate with the separation rate about yaw, and Figure 2.1-15 shows a run with the pitch rate zero and the yaw rate 1 deg/sec. Both conditions captured. With a pitch position bias on the booster, the satellite would "exactly" capture with no attitude or rate error. As a consequence the effect of

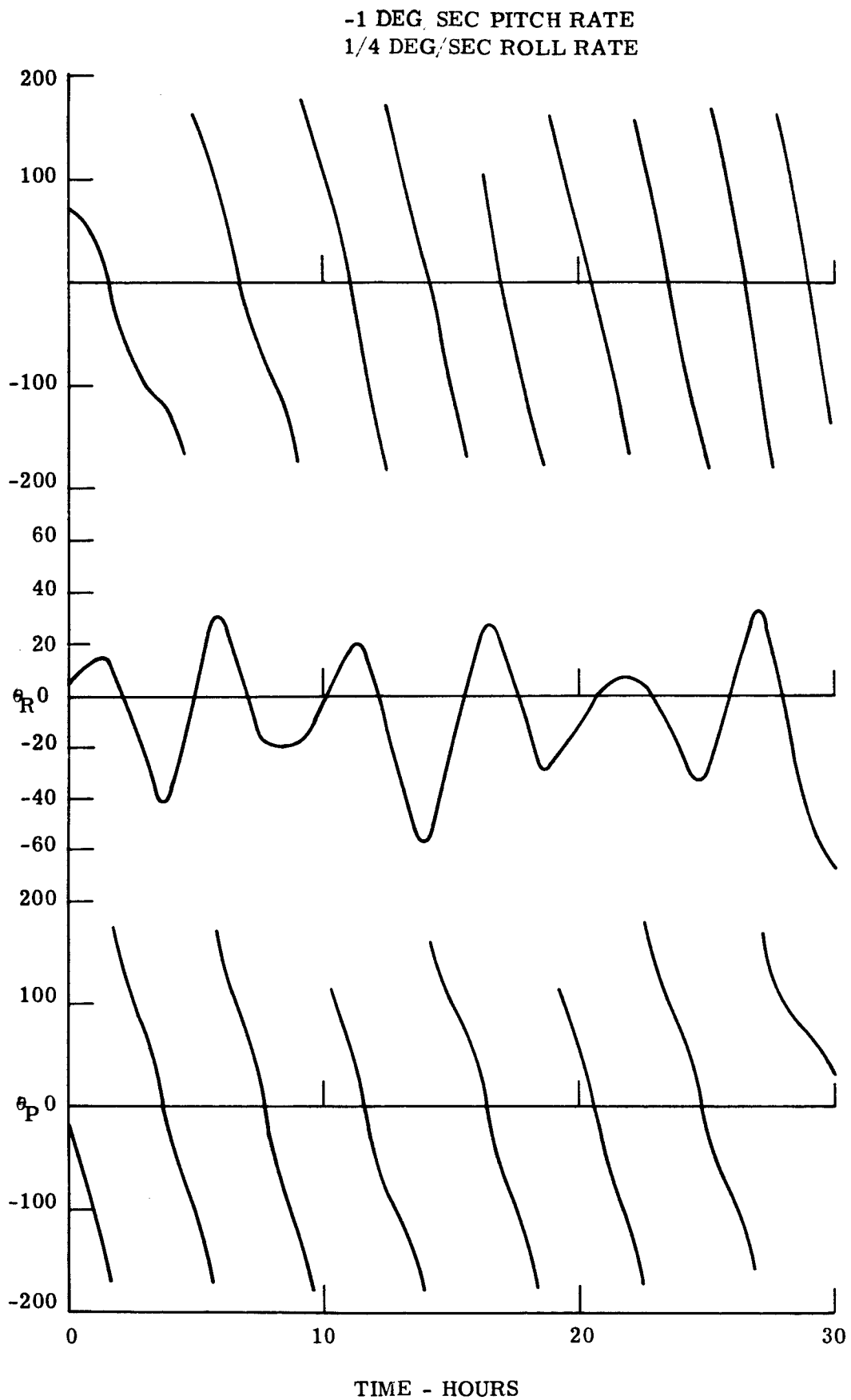


Figure 2.1-5. ATS Capture Phase Normal Agena Position

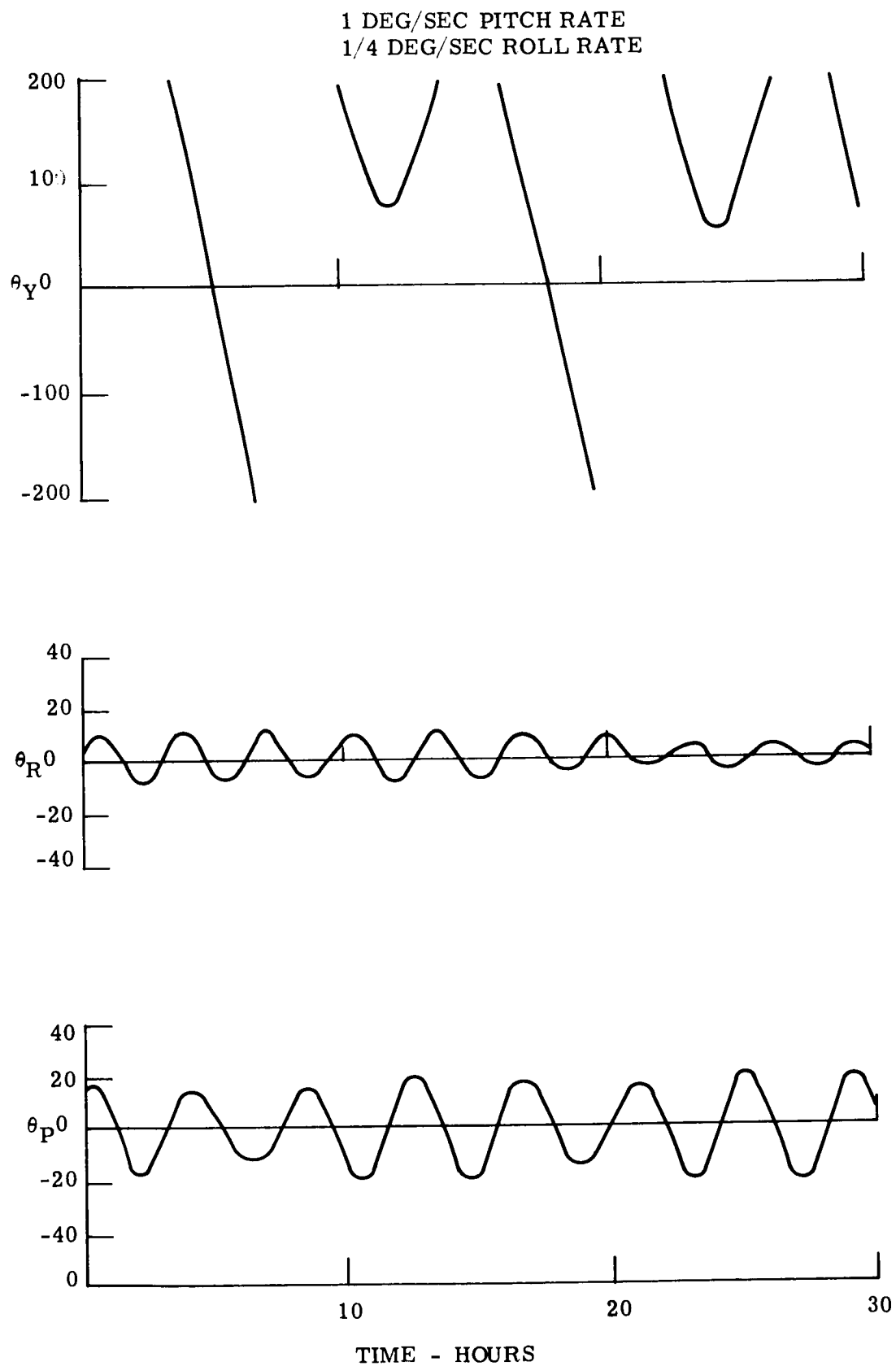


Figure 2.1-6. ATS Capture Phase Normal Agena Position

1 DEG/SEC YAW RATE
1/4 DEG/SEC ROLL RATE

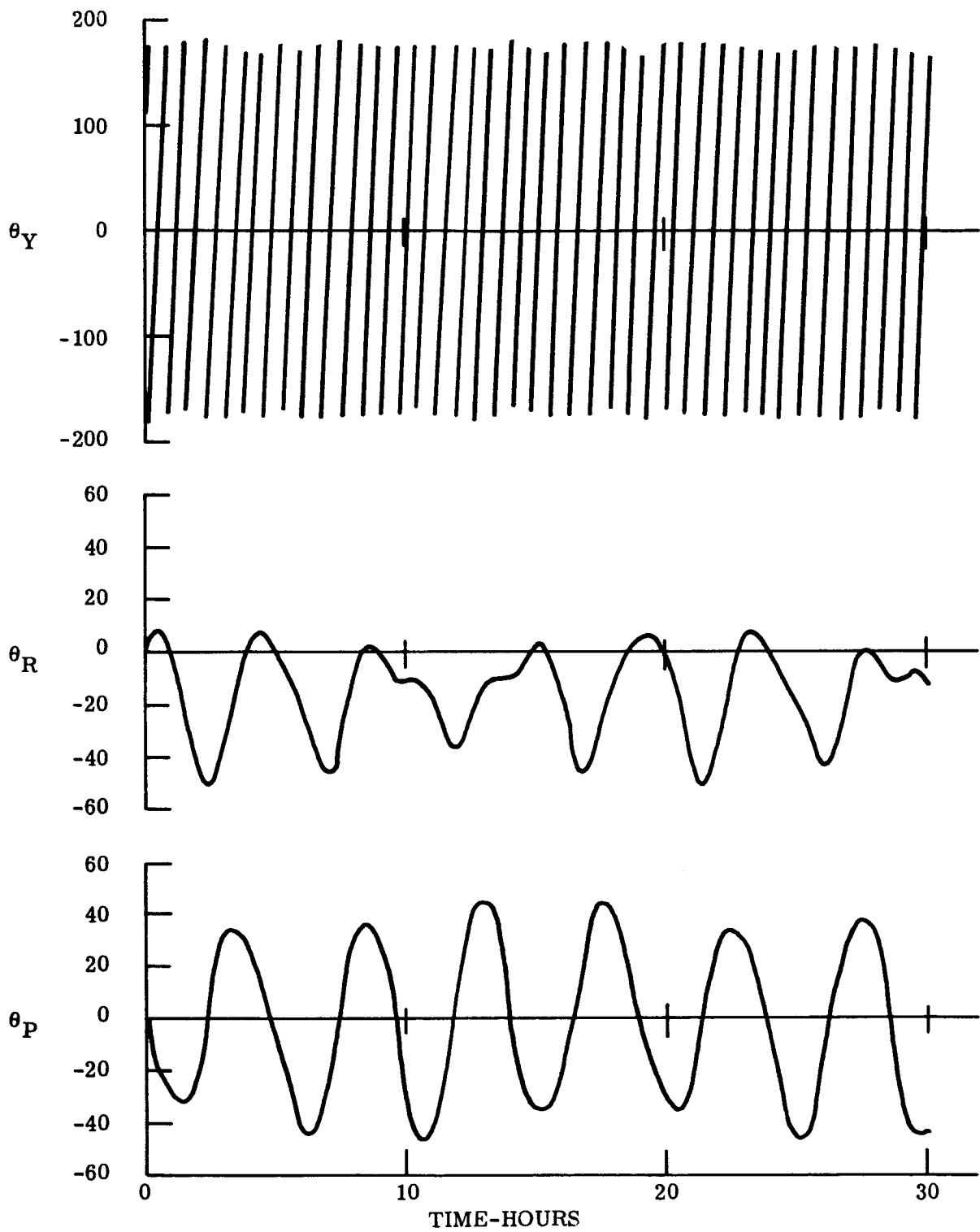


Figure 2.1-7. ATS Capture Phase Normal Agena Position

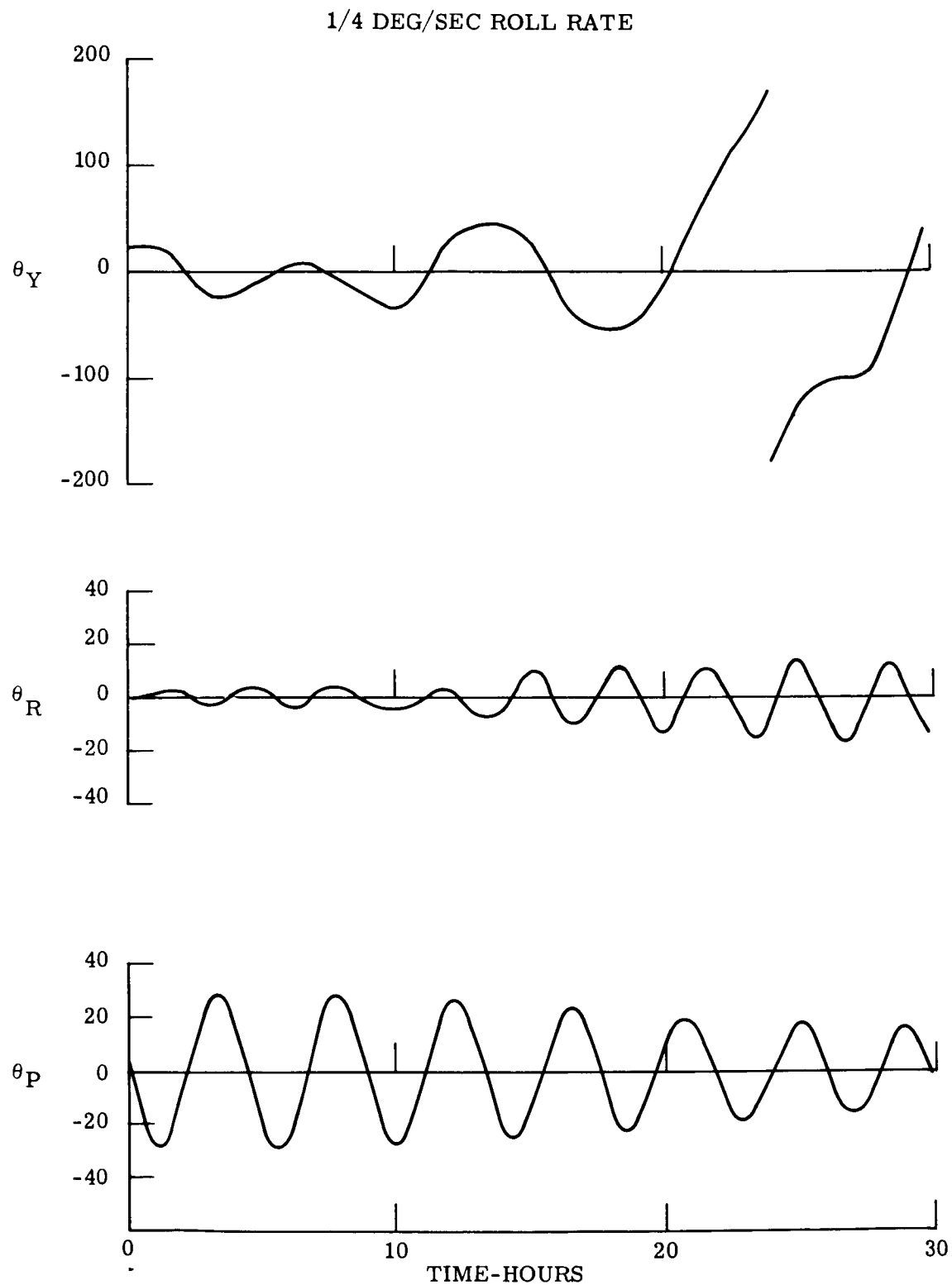


Figure 2.1-8. ATS Capture Phase 90-Degree Agena Yaw

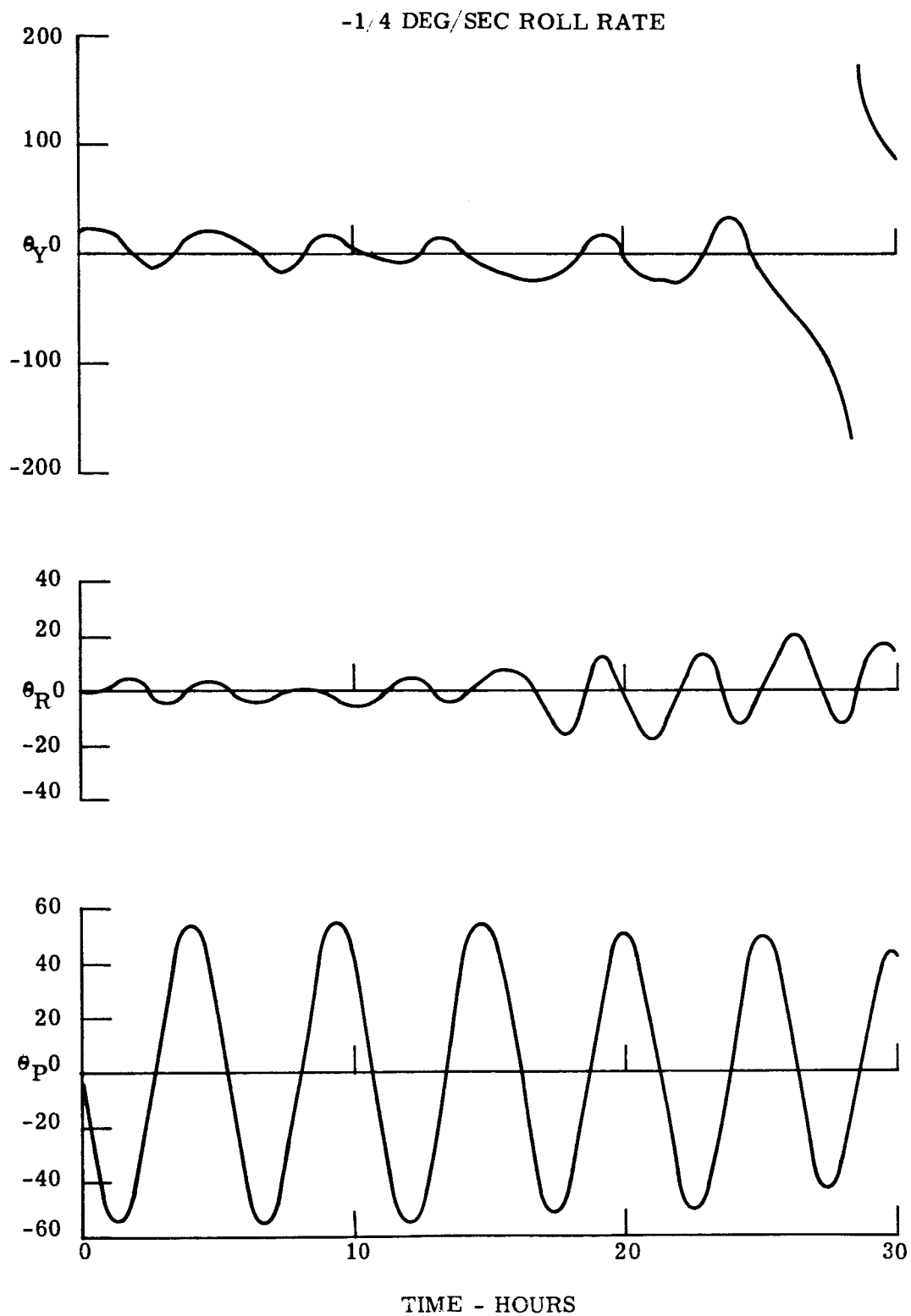


Figure 2.1-9. ATS Capture Phase 90-Degree Agena Yaw

-1/4 DEG/SEC ROLL RATE
1 DEG/SEC PITCH RATE

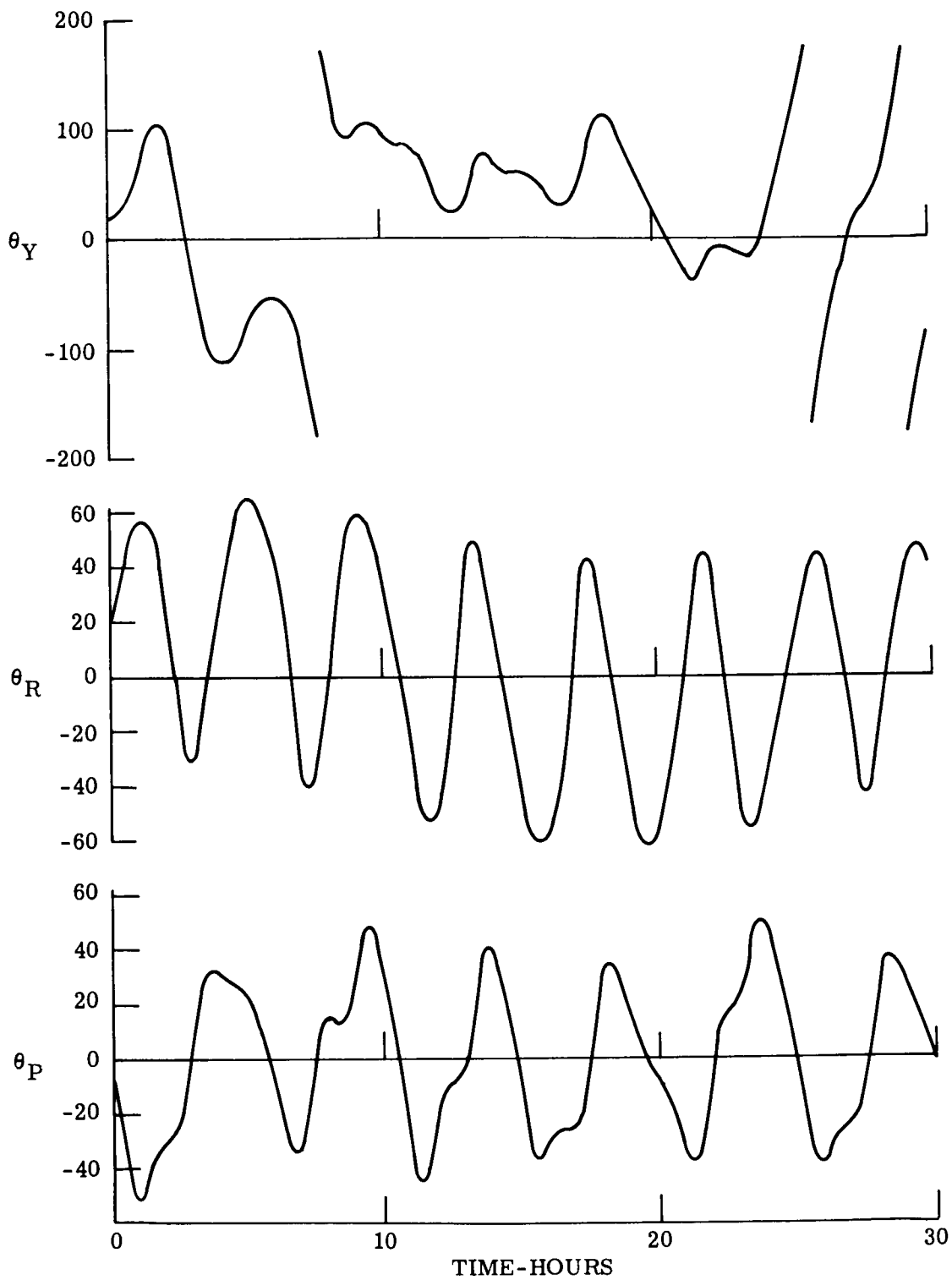


Figure 2.1-10. ATS Capture Phase 90-Degree Agena Yaw

-1/4 DEG/SEC ROLL RATE
1 DEG/SEC YAW RATE

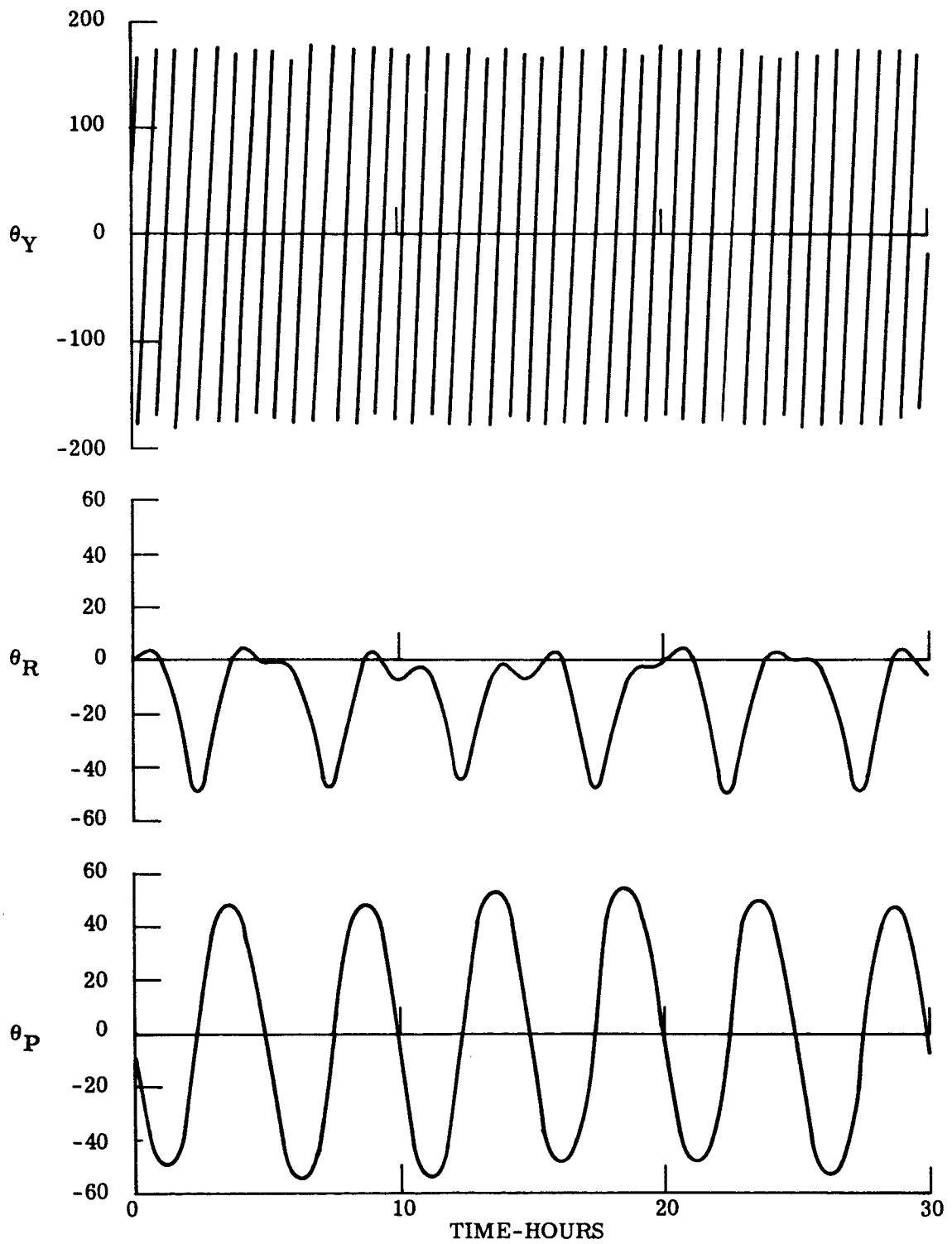


Figure 2.1-11. ATS Capture Phase 90-Degree Agena Yaw

1/4 DEG/SEC ROLL RATE
1 DEG/SEC PITCH RATE

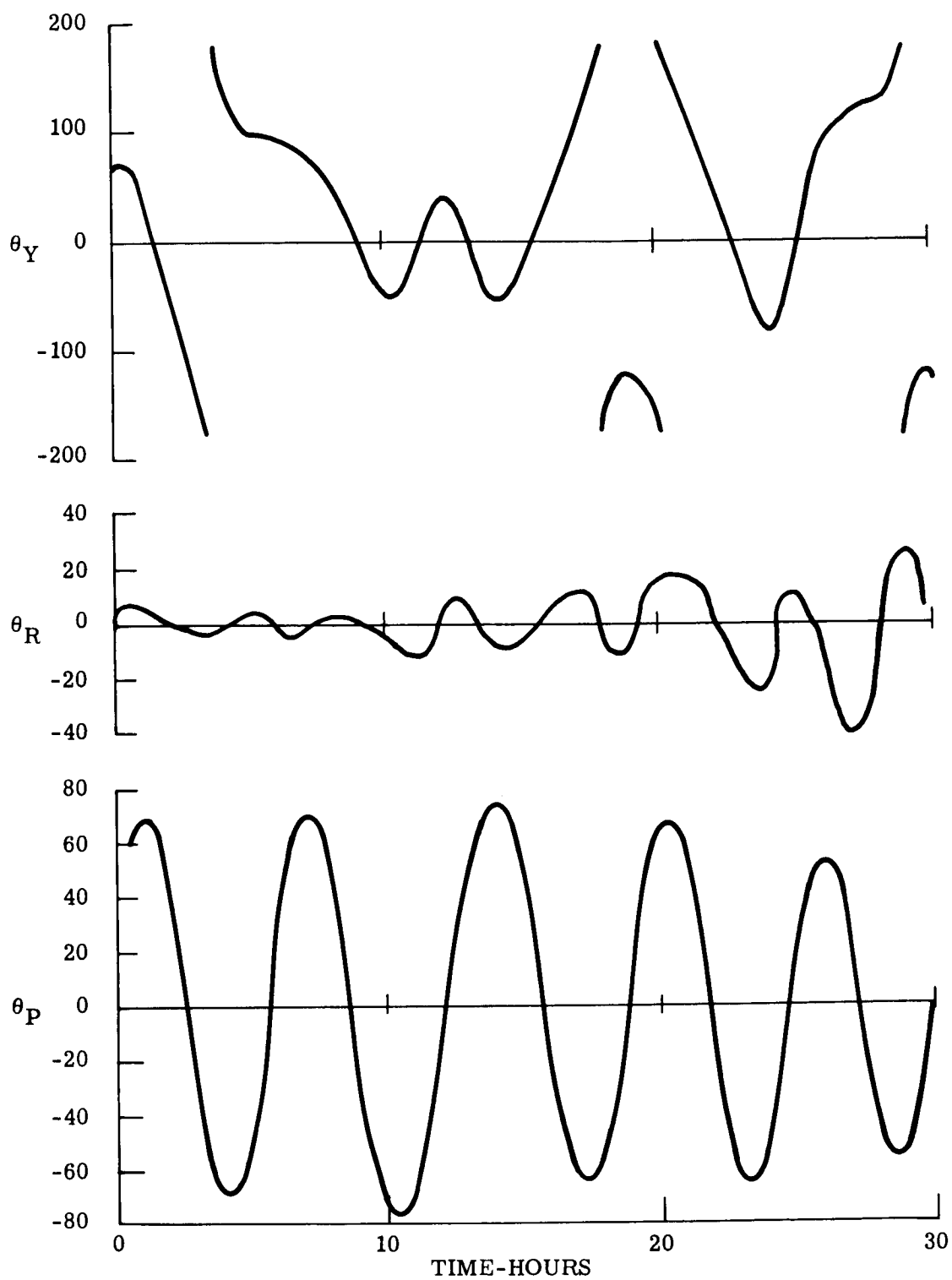


Figure 2.1-12. ATS Capture Phase 1-Degree/Second Pitch Rate Bias

1 4 DEG SEC ROLL RATE
-1 DEG SEC PITCH RATE

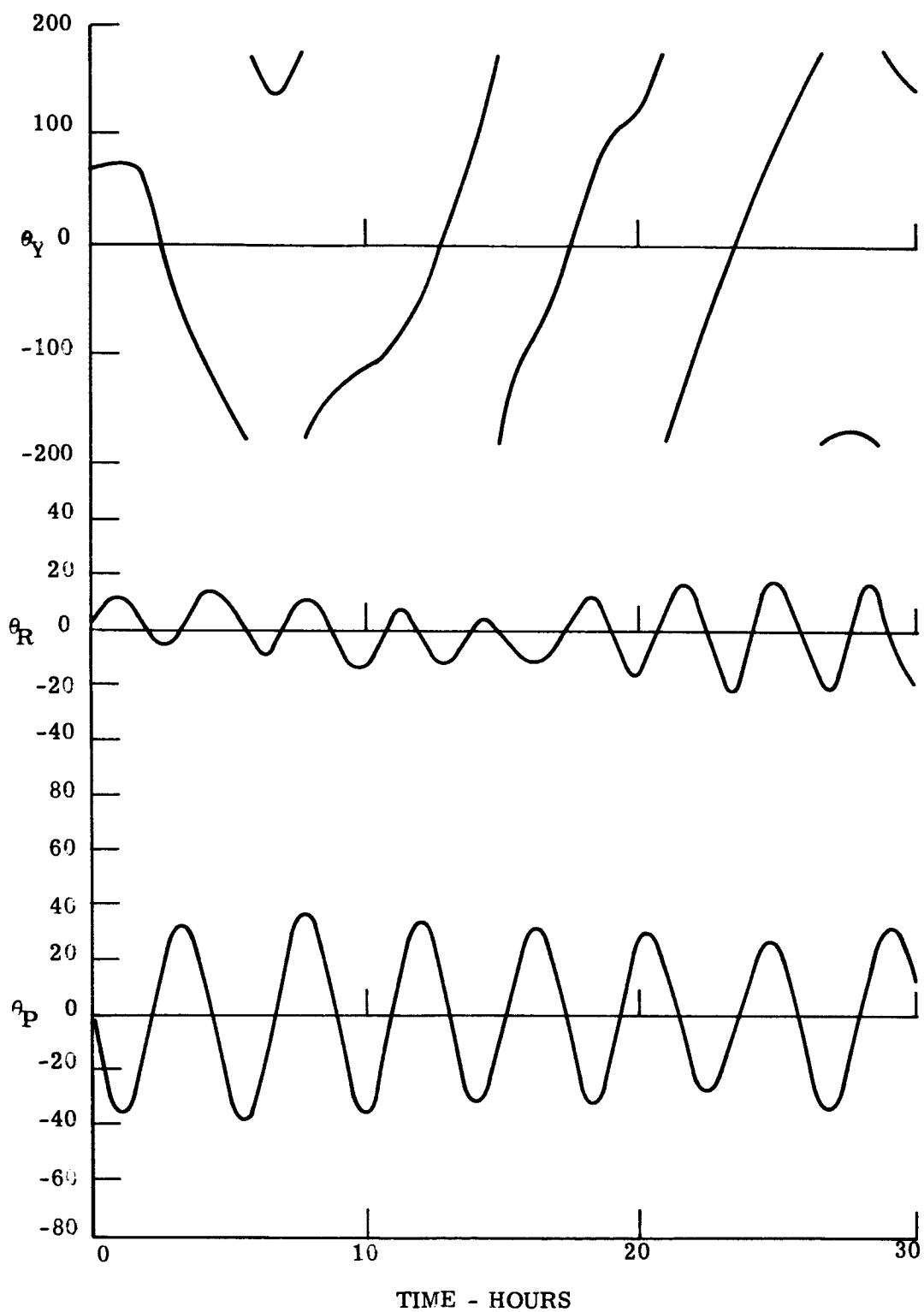


Figure 2.1-13. ATS Capture Phase 1-Degree/Second Pitch Rate Bias

1/4 DEG/SEC ROLL RATE
-1 DEG/SEC PITCH RATE
1 DEG/SEC YAW RATE

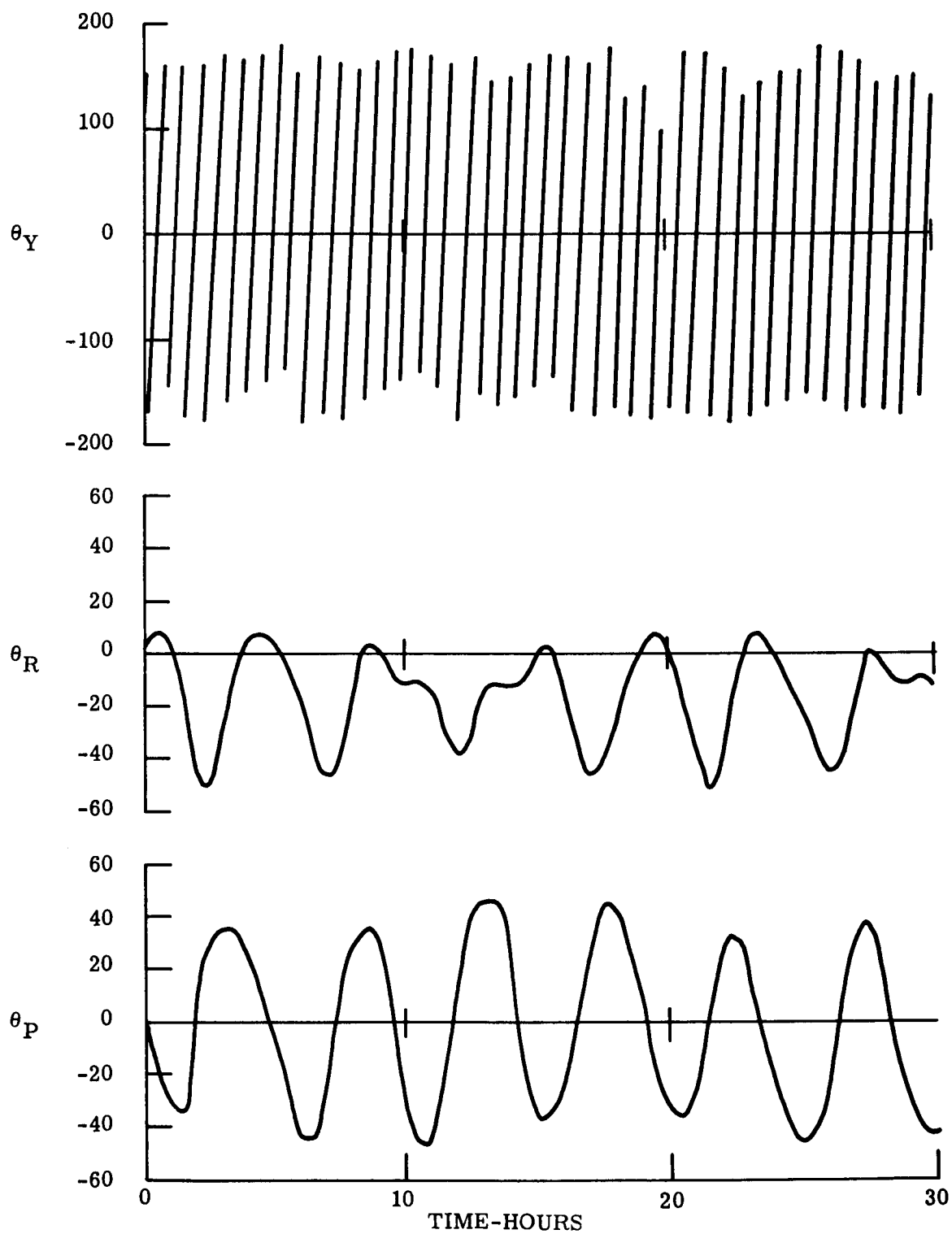


Figure 2.1-14. ATS Capture Phase 1-Degree/Second Pitch Rate Bias

1/4 DEG/SEC ROLL RATE
1 DEG/SEC YAW RATE

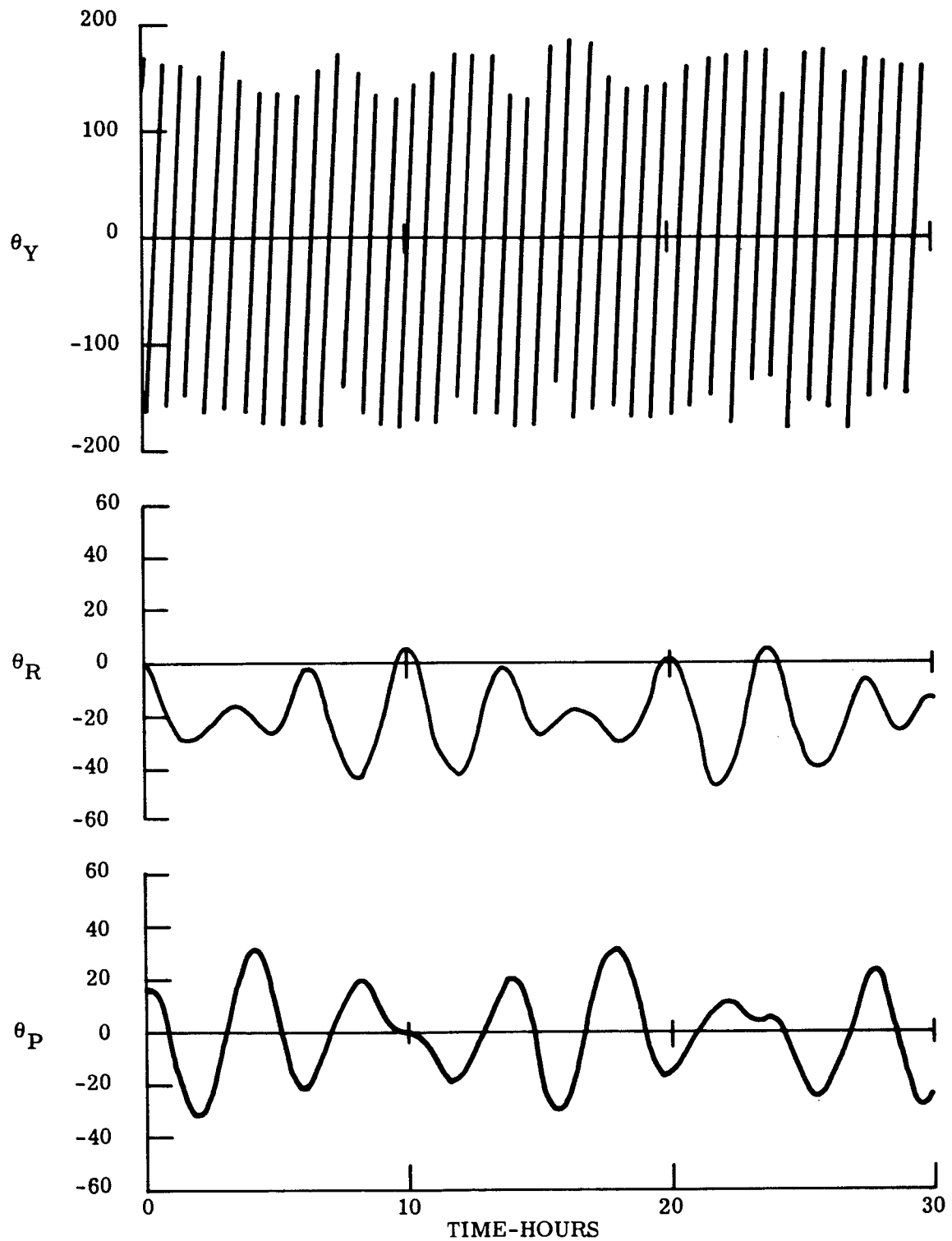


Figure 2.1-15. ATS Capture Phase 1-Degree/Second Pitch Rate Bias

rate variations is symmetrical (i. e., a -1 deg/sec rate and a +1 deg/sec rate produce the identical performance with a 180 degree phase shift). From the foregoing runs and from energy considerations, the placement of 1 deg/sec (approximately) positive pitch rate (pitch down) and a negative pitch position bias on the vehicle will ensure capture in the undamped mode. This technique appears to be the simplest to implement and is recommended for this reason. The exact value of the rate and position at separation will be specified when the initial and final moments of inertia are finalized. From Figure 2.1-12, a tentative value of -15 degrees was selected.

2.1.4.2 Transient Performance Studies

During the flight of the ATS Gravity Gradient System tests will be performed to determine the damping characteristics of the vehicle with several values of half angle between the X rods. To determine the transient characteristics, as well as estimate the time to reach steady state, a series of computer runs was made using the GAPS III, three-axis computer program. The results of these runs are discussed in the following section.

The transient performances of the ATS Gravity Gradient configurations were evaluated using the GAPS III, three-axis computer program. The five configurations selected were those with a 31, 25, 19, 15, and 11 degree angle between the main rods of the satellite. Each of the configurations has 100-foot rod lengths with 2.5 pound tip masses and a secondary boom of length 45 feet (90 feet tip to tip) with 1.91 pound tip masses. To provide a basis for performance comparison, the vehicle was assumed to be stopped in in space (inertial stop) with no external disturbance torques applied. These conditions result in a smooth transient which permits accurate calculation of the time constants.

Figures 2.1-16 thru 2.1-20 show the results of the computer runs. The initial pitch and roll angles were zero, and the initial yaw angle was 180 degrees. Experience has indicated that the vehicle will yaw around when the pitch and roll amplitudes are large. By starting at 180 degrees, the final yaw oscillations were about zero, which are more convenient to plot than oscillations about 180 degrees.

With an initial pitch rate of zero, the peak of the first oscillation will be negative, with an amplitude dependent upon the configuration. The 31-degree configuration has the largest peak (60 degrees) and the 11 degree-configuration has the smallest (38 degrees). To include the effect of the initial amplitude in the calculation of time to reach steady state, a time constant is computed for the pitch axis based upon this peak. The time constants are expressed in orbits to damp and are listed in Table 2.1-3. Time constants cannot be defined for the roll and yaw axes since the oscillations in these axes are induced by the pitch oscillations. Their characteristics can be observed from the runs, however.

A reference line has been included in the yaw axis plots to indicate where the vehicle stabilizes, since it is biased from zero except for the 19-degree configuration.

At the end of 80 hours, only the 11-degree configuration shows an appreciable oscillation amplitude. This can be attributed to the proximity of the damping axis (the axis about which the damper rotates) to the orbital pitch axis (the axis normal to the orbit plane.) If the damping axis and the pitch axis were coincident, pitch motion would decouple from roll and yaw motion, and small amplitude roll and yaw oscillations would not damp.

31 DEGREE HALF ANGLE BETWEEN X RODS

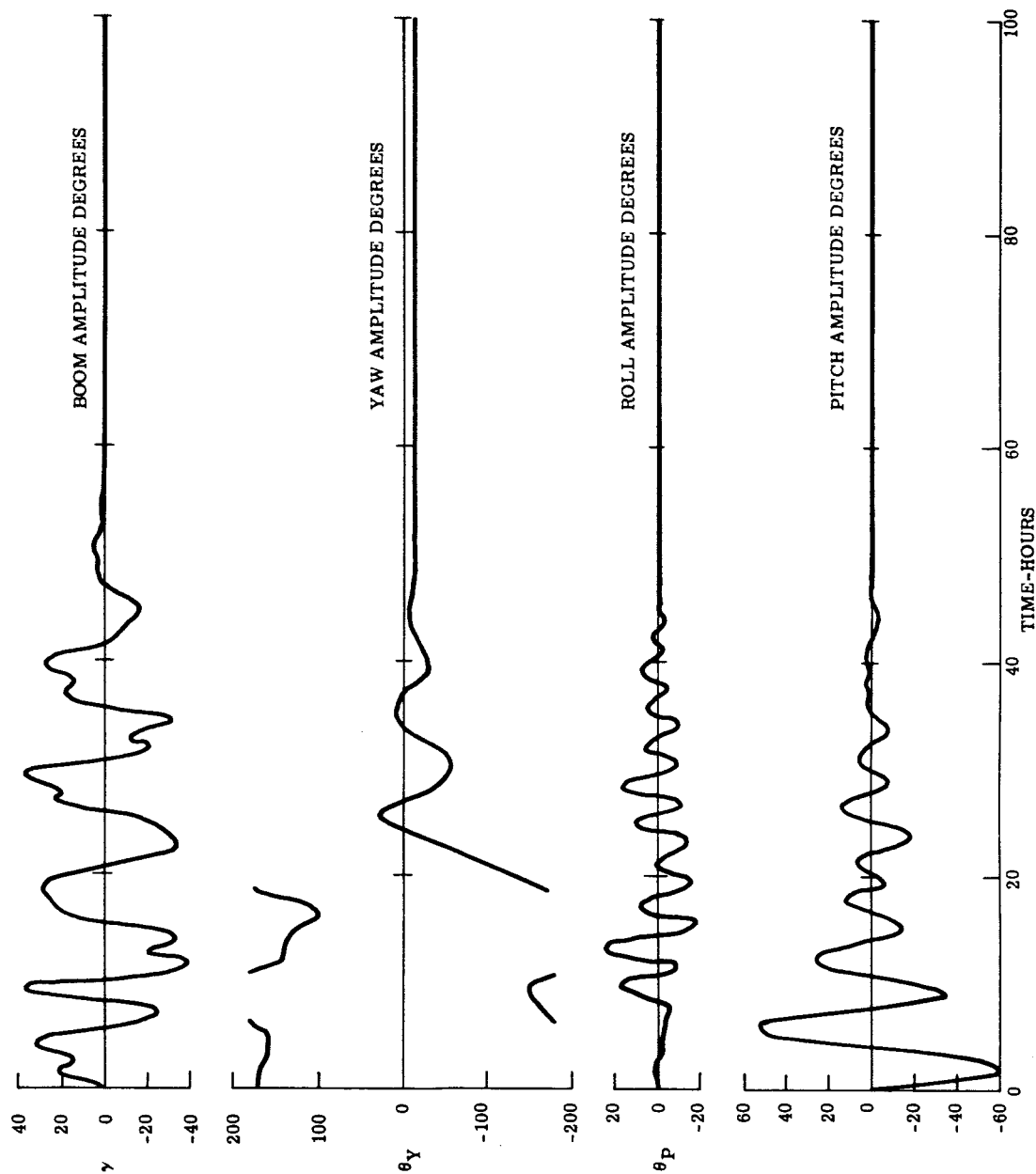


Figure 2.1-16. Transient Performance, 31-Degree Half Angle Between X-Rods

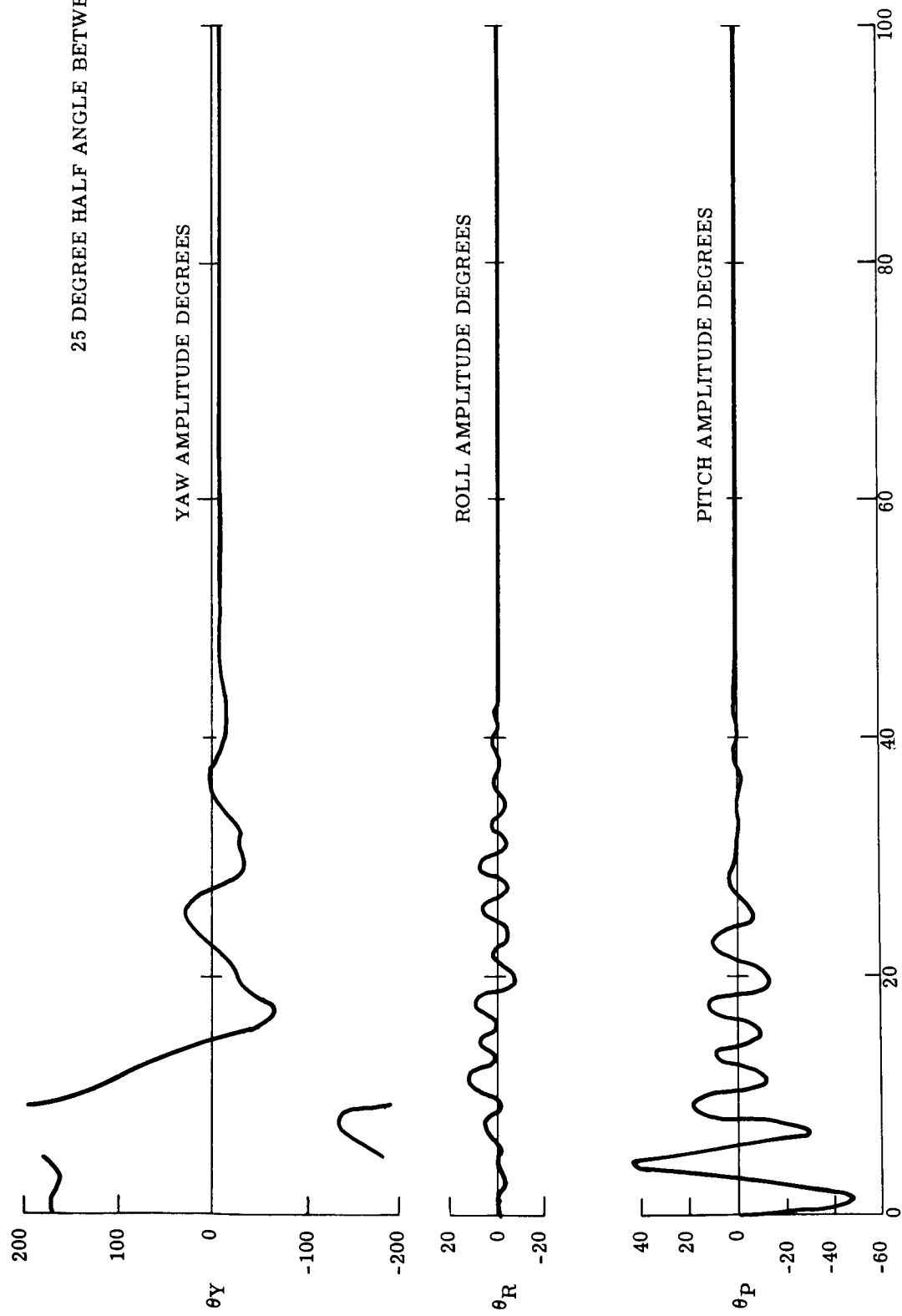


Figure 2.1-17. Transient Performance, 25-Degree Half Angle Between X-Rods

19 DEGREE HALF ANGLE BETWEEN X RODS

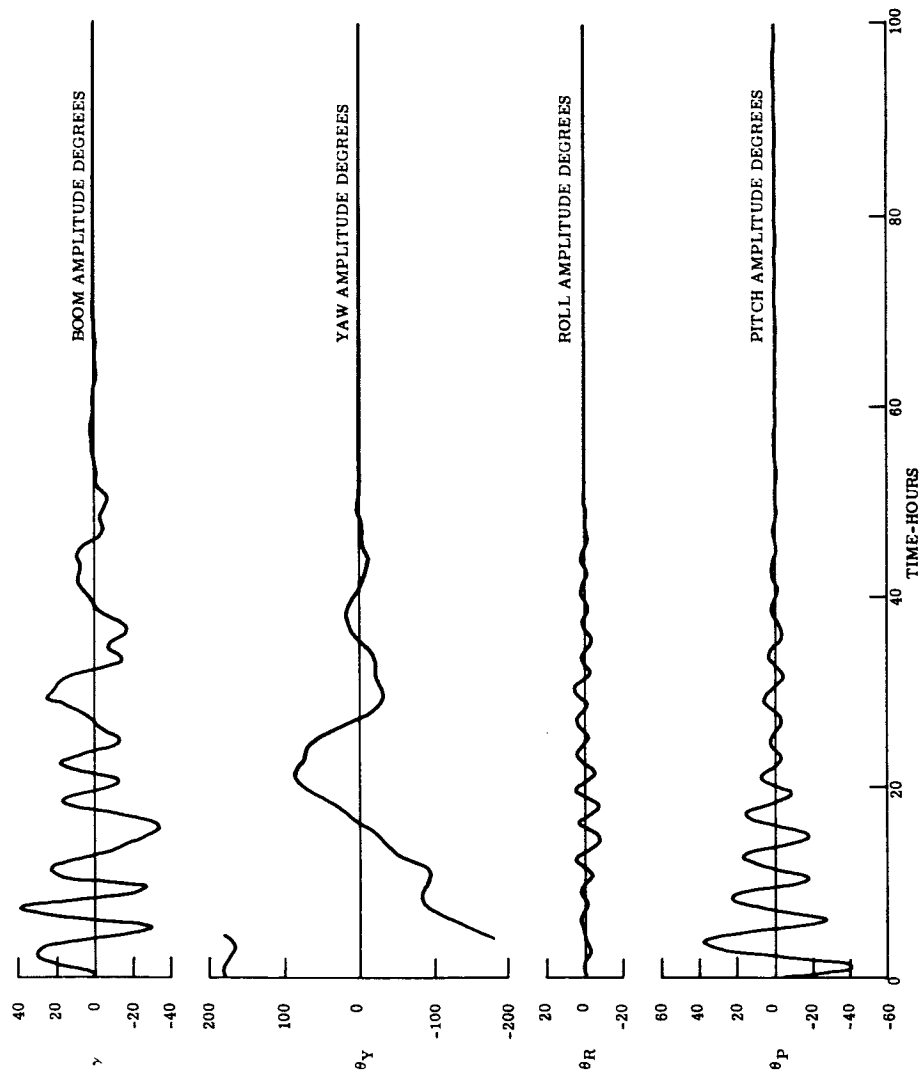


Figure 2.1-18. Transient Performance, 19-Degree Half Angle Between X-Rods

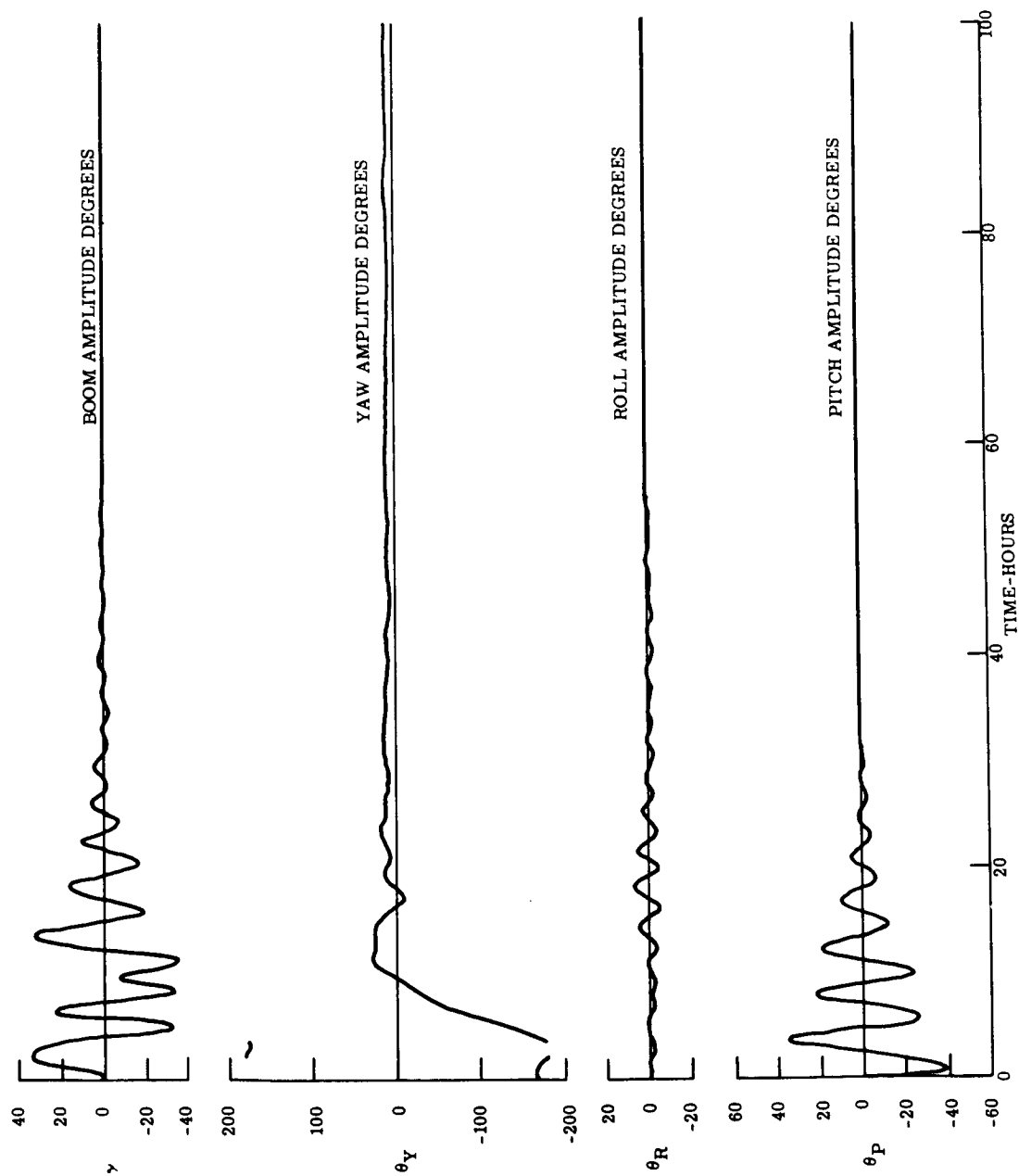


Figure 2.1-19. Transient Performance, 15-Degree Half Angle Between X-Rods

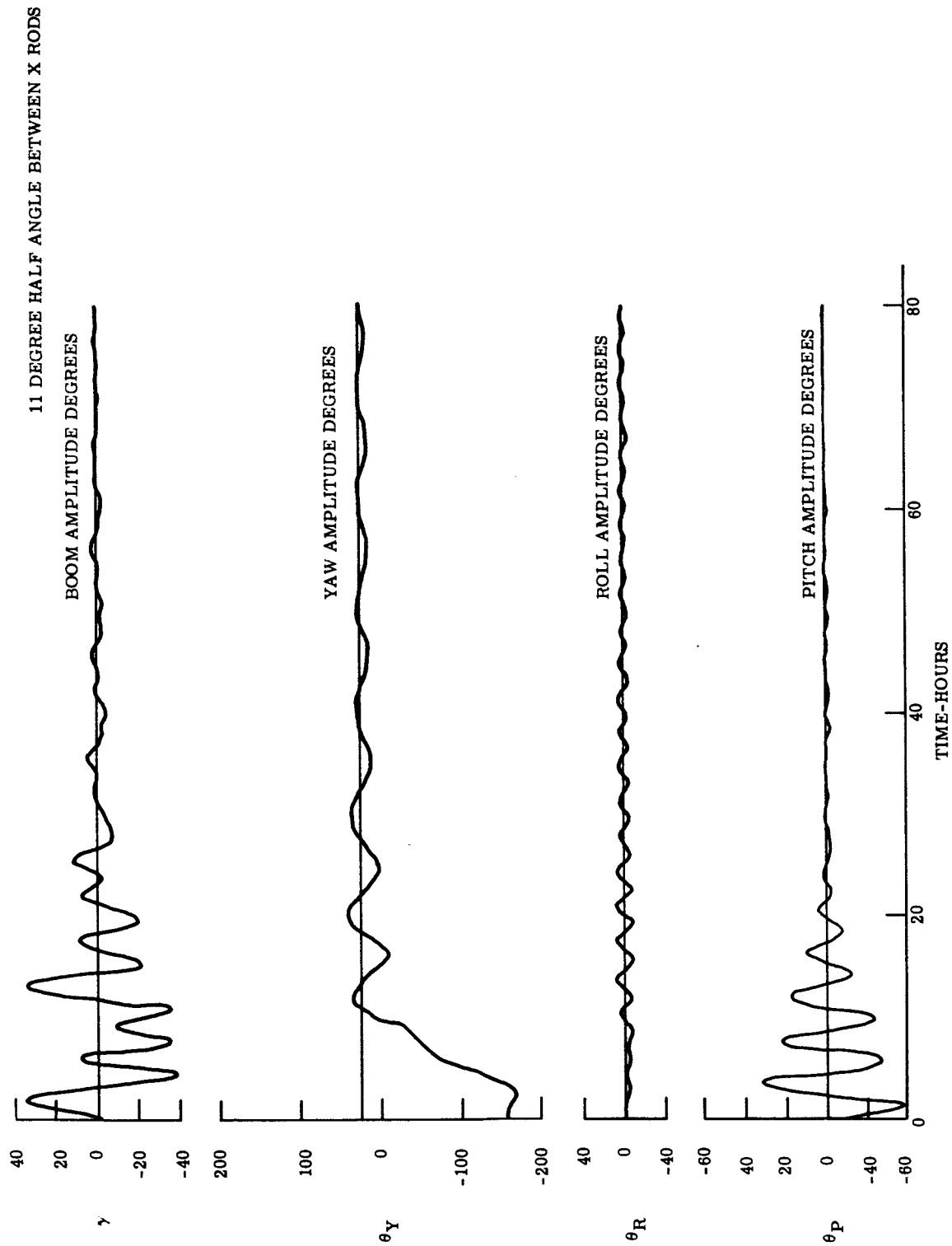


Figure 2.1-20. Transient Performance, 11-Degree Half Angle Between X-Rods

Because of the low yaw moment of inertia of the X-rods (on the 11 degree-configuration), the secondary boom causes the damping axis to be 20.6 degrees closer to the pitch axis than the 19-degree configuration. There is still cross coupling, but roll and yaw damp slowly.

Table 2.1-3 and Figures 2.1-16 thru 2.1-20 contain additional information available from the GAPS III computer program. The boom motion associated with these capture runs is plotted on the figures for all except the 25-degree configuration, and the maximum amplitudes are listed in Table 2.1-3. This table also contains the peak cocking torque the damper experiences during the transient. This is the torque normal to both the rod axis and the damping axis. During the capture phase of the flight, the cocking torque may easily exceed this value.

TABLE 2.1-3. VEHICLE DAMPING SUMMARY

<u>Configuration Half Angle</u> (degrees)	<u>Time Constant</u> (orbits)	<u>Boom Oscillation</u> (degrees)	<u>Cocking Torque</u> (dyne cm)
31	2.43	36.5	612
25	2.08	42.3	673
19	2.22	38.8	703
15	1.47	35.3	701
11	1.80	38.5	556

2.1.4.3 Magnetic Torque Studies of 6000-mile Orbit

As a part of the ATS gravity gradient experiment, it has been proposed that the vehicle be provided with a controllable magnetic dipole. This dipole will be used to determine the effect on the attitude control of the vehicle of interaction between the earth's magnetic field, and a dipole of known orientation and strength. Since the vehicle will oscillate due to orbit eccentricity (thermal bending, solar torque, etc.) the error due to the controllable dipole must induce oscillations which are large enough to be clearly distinguishable from the normal oscillations. As a consequence, a dipole moment of 20,000 pole-cm (2.51×10^{-4} weber-m) was selected.

A magnetic dipole of this size will cause a pitch error of from four to six degrees and a roll error of from two to eight degrees, depending upon vehicle configuration and magnetic dipole orientation. The dipole is, however, strong enough to orient the satellite in yaw, and the vehicle will nominally point to the magnetic field. To avoid this, without reducing the pitch and roll errors to below sensor threshold level, the dipole should be placed along the yaw axis. A measurable roll and pitch bias will be obtained with an oscillation on the pitch axis due to the rotation of the earth. Since there is some evidence that a yaw bias interferes with the damping, the above technique is recommended. If the yaw performance is to be studied, a small dipole (approximately 400 pole-cm) could be placed on either the roll or pitch axes.

The performance of the vehicle was determined using the GAPS III, three-axis computer program. This program contains a magnetic subroutine which accurately simulates the known magnetic field to within one degree in direction and one percent in magnitude. A

series of computer runs were made with the dipole component of 20,000 pole-cm located on each of the principal axes, and the response in the pitch, roll and yaw axes was determined. Since the effect of the dipole depends upon vehicle configuration, the nominal 6000-mile orbit configuration (19 degrees half angle between the X-rods), as well as the extreme configurations (11 degrees and 31 degrees half angle) were considered. The rod lengths are 100 feet with tip weights of 2.5 pounds and the secondary rod has a 45-foot rod (90 feet tip to tip) with a 1.91-pound tip weight. With these physical characteristics, the 31-degree and 11-degree configurations will have nominal yaw biases of approximately -13.6 and 26 degrees respectively. The orbit inclination is 28 degrees.

Figure 2.1-21 shows the response of the nominal configuration with the dipole located on the pitch axis. In this position, there is no direct effect on pitch (θ_p), and the oscillations on this axis are the result of cross coupling of the roll (θ_r) oscillations and the yaw (θ_y) bias. The effect on yaw is quite severe with the satellite oscillating at ten degrees half amplitude about a twenty-degree bias (all vertical scales are in degrees).

Figure 2.1-22 shows the response of the configuration when the dipole is on the roll axis. The pitch amplitude is approximately the same as in Figure 2.1.21 but the characteristics of the motion have changed. The roll error has both increased in magnitude and changed characteristics. The yaw error has significantly increased, the bias error being 50 degrees with a 20-degree dynamic oscillation error. The cross coupling between the axes is very evident when the pitch and yaw motions are compared, and it is evident to a lesser extent when pitch and roll are compared.

With the dipole located on the yaw axis (Figure 2.1-23), there is no bias on the yaw axis, and the only oscillations are those due to pitch coupling. Roll exhibits a relatively smooth bias, and the oscillations appearing on the pitch axis are probably due to the rotation of the earth (note the nearly 24-hour cycle).

Figures 2.1-24 thru 2.1-29 contain the same series of runs with the 31 degree and 11 degree rod angle configurations in that order. The horizontal axis on the yaw scale marks the position about which the vehicle would settle if undisturbed since it is not equal to zero.

Comparing all the runs, it is evident that those runs which have the dipole located on the same axis exhibit the same characteristics of motion but with different amplitudes. The largest errors occur when the dipole is on the roll axis, and the least errors occur when the dipole is on the yaw axis. The errors induced when the dipole is on the pitch axis will be the same if the dipole is along the positive or negative pitch axis, since the maximum gravity gradient restoring torque in yaw is less than the maximum magnetic torque, and the vehicle will align itself to the magnetic field. Figures 2.1-21 thru 2.1-28 illustrate that alignment to the magnetic field does occur. Figures 2.1-21, 2.1-24 and 2.1-27 all have the same yaw bias even though the configurations are different and have different undisturbed yaw positions. The same is true of Figures 2.1-22, 2.1-25 and 2.1-28.

Comparing configurations, the 31-degree configuration has the worst characteristics and the largest oscillation amplitudes. The 11 degree and 19 degree configurations are very similar with small pitch and roll oscillations. Some of the runs indicate the existence of a transient although the vehicle should be in steady state, and it is probable that the biases associated with the axes have interfered with the normal damping mode.

20,000 POLE-CENTIMETER MAGNET ON PITCH AXIS
19-DEGREE HALF ANGLE BETWEEN RODS

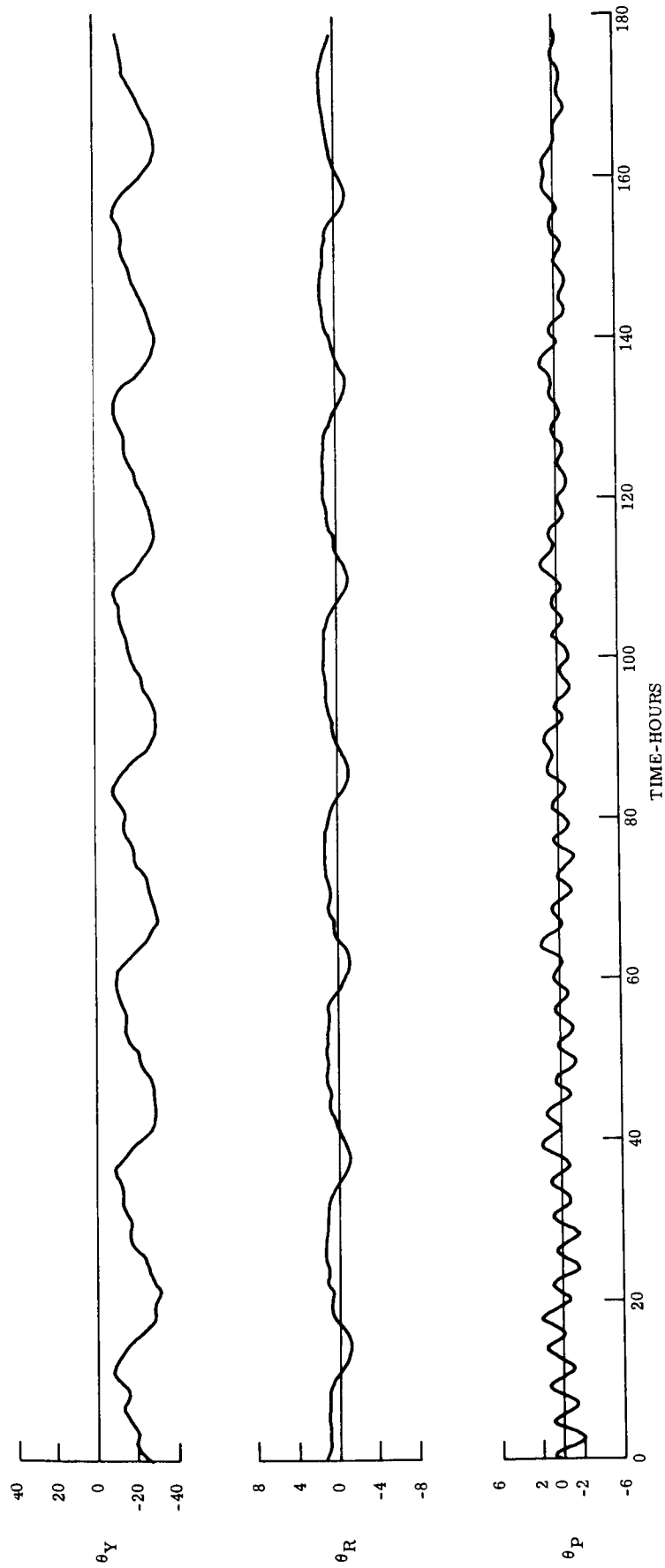


Figure 2.1-21. ATS Medium Altitude Gravity Gradient Experiment

20,000 POLE-CENTIMETER MAGNET ON ROLL AXIS
19-DEGREE HALF ANGLE BETWEEN RODS

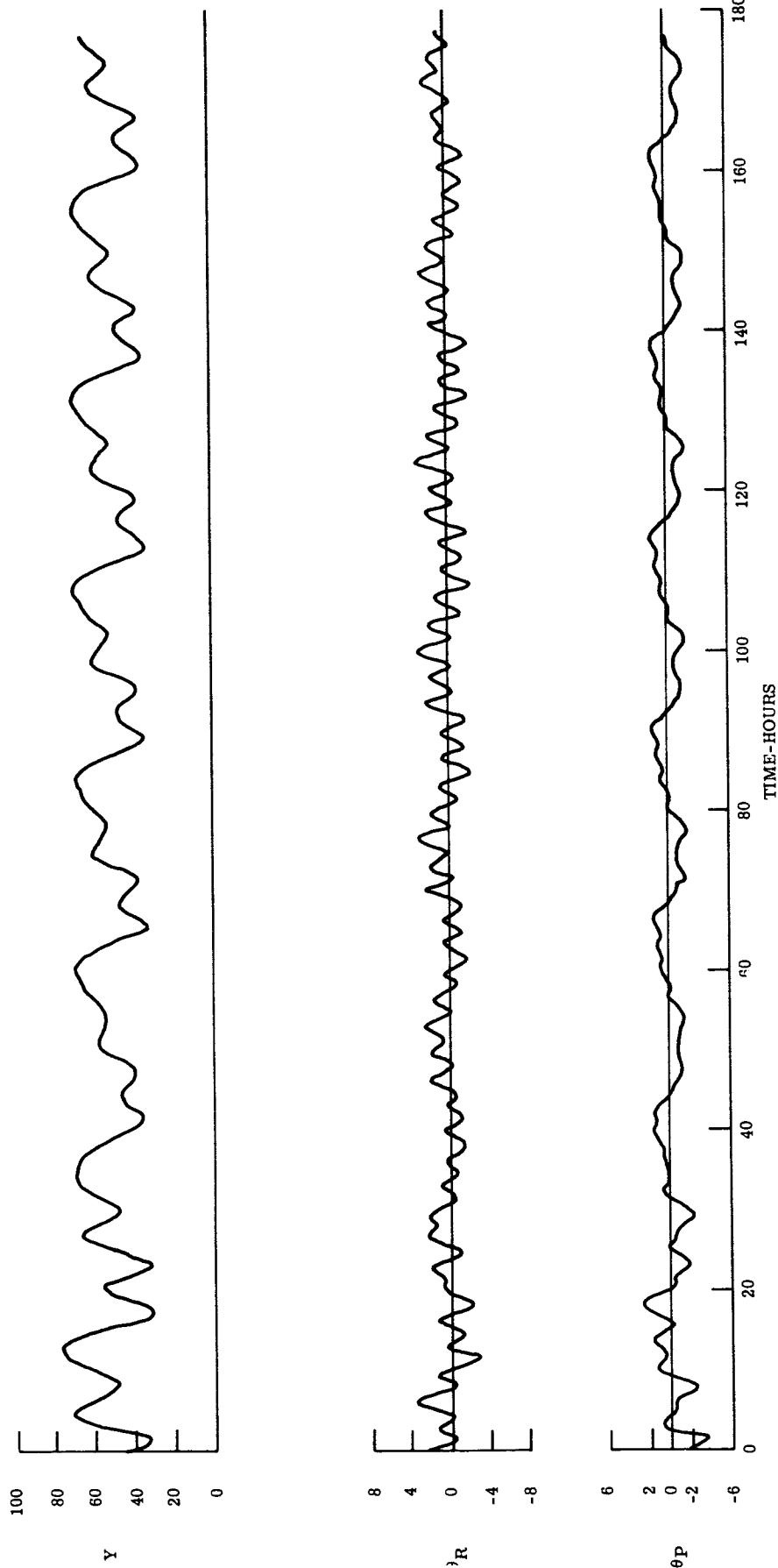


Figure 2.1-22. ATS Medium Altitude Gravity Gradient Experiment

20, 000 POLE-CENTIMETER MAGNET ON YAW AXIS
19-DEGREE HALF ANGLE BETWEEN RODS

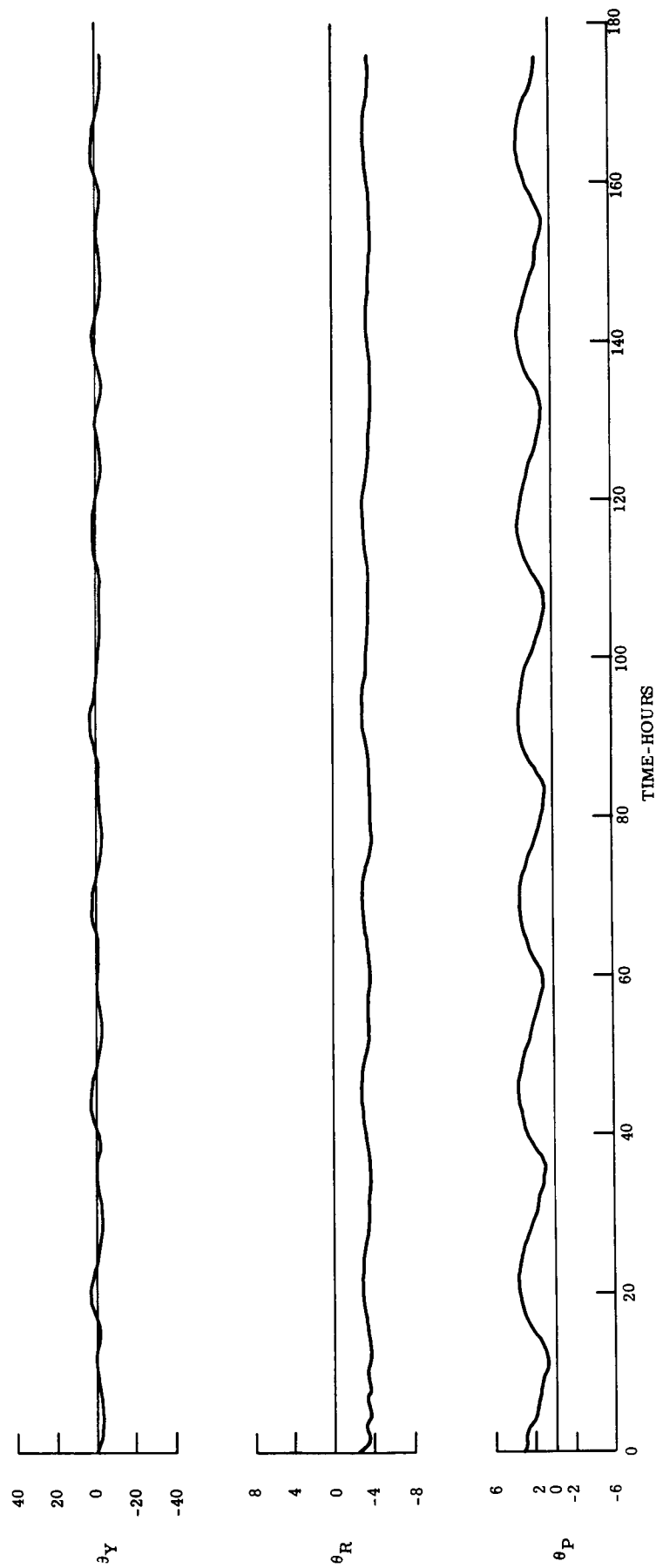


Figure 2.1-23. ATS Medium Altitude Gravity Gradient Experiment

20,000 POLE-CENTIMETER MAGNET ON PITCH AXIS
31-DEGREE HALF ANGLE BETWEEN RODS

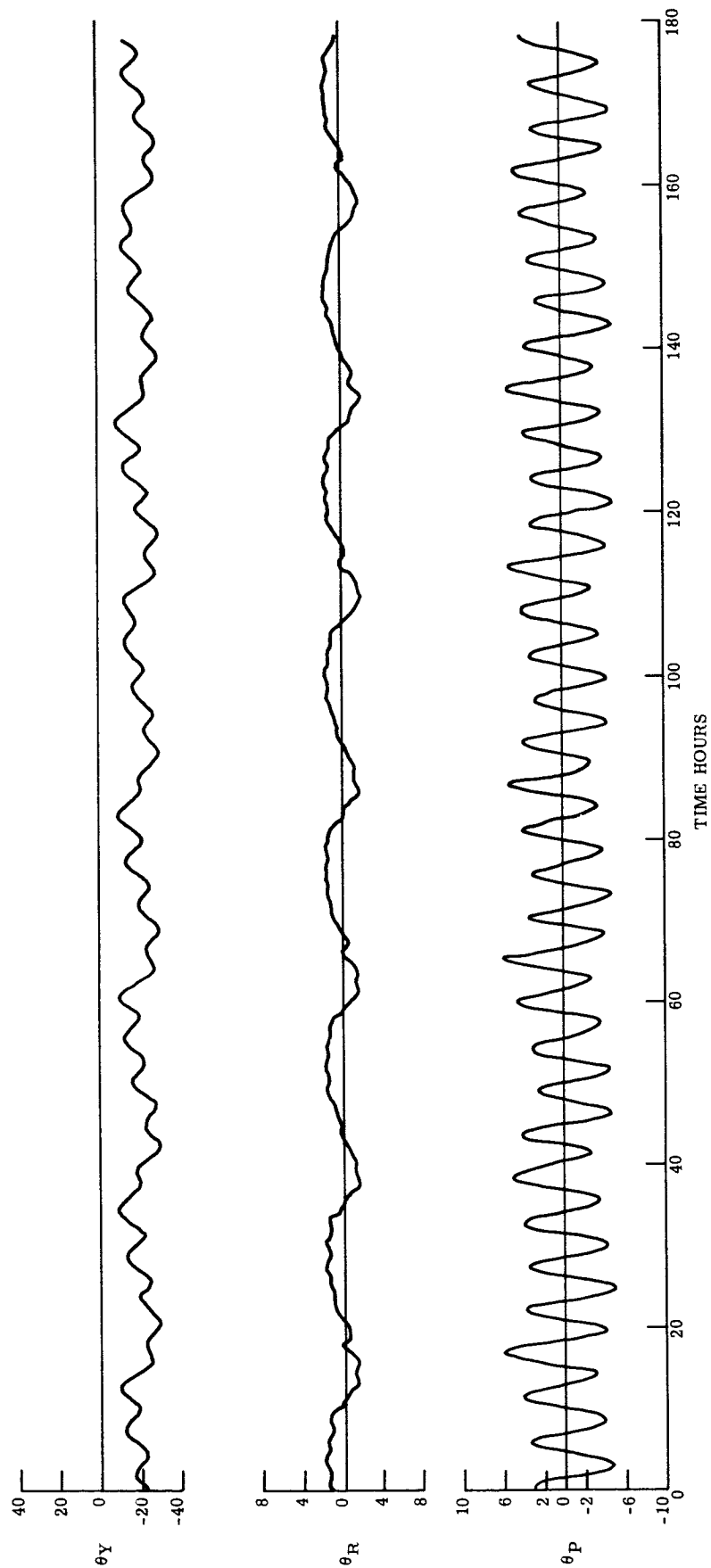


Figure 2.1-24. ATS Medium Altitude Gravity Gradient Experiment

20,000 POLE-CENTIMETER MAGNET ON ROLL AXIS
31-DEGREE HALF ANGLE BETWEEN RODS

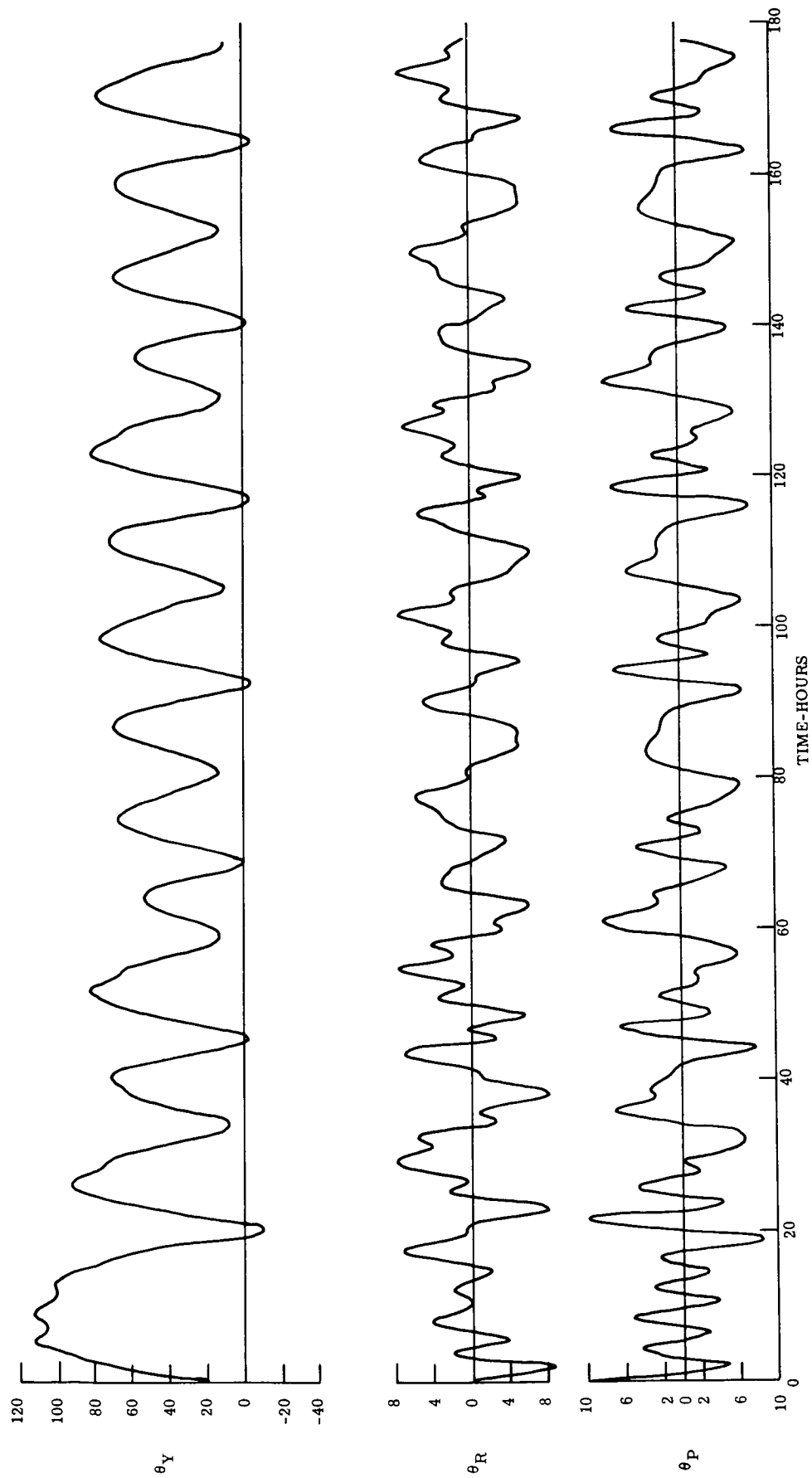


Figure 2.1-25. ATS Medium Altitude Gravity Gradient Experiment

20,000 POLE-CENTIMETER MAGNET ON YAW AXIS
31-DEGREE HALF ANGLE BETWEEN RODS

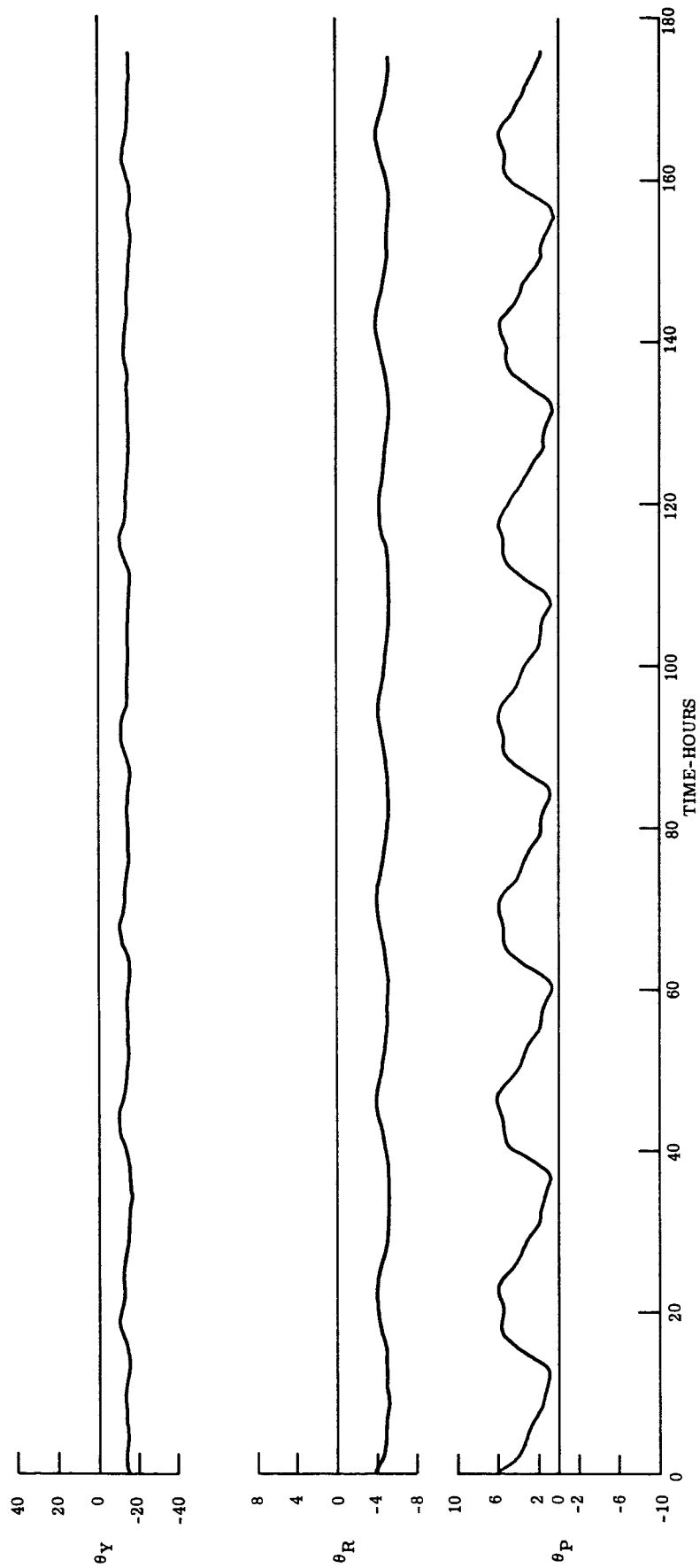


Figure 2.1-26. ATS Medium Altitude Gravity Gradient Experiment

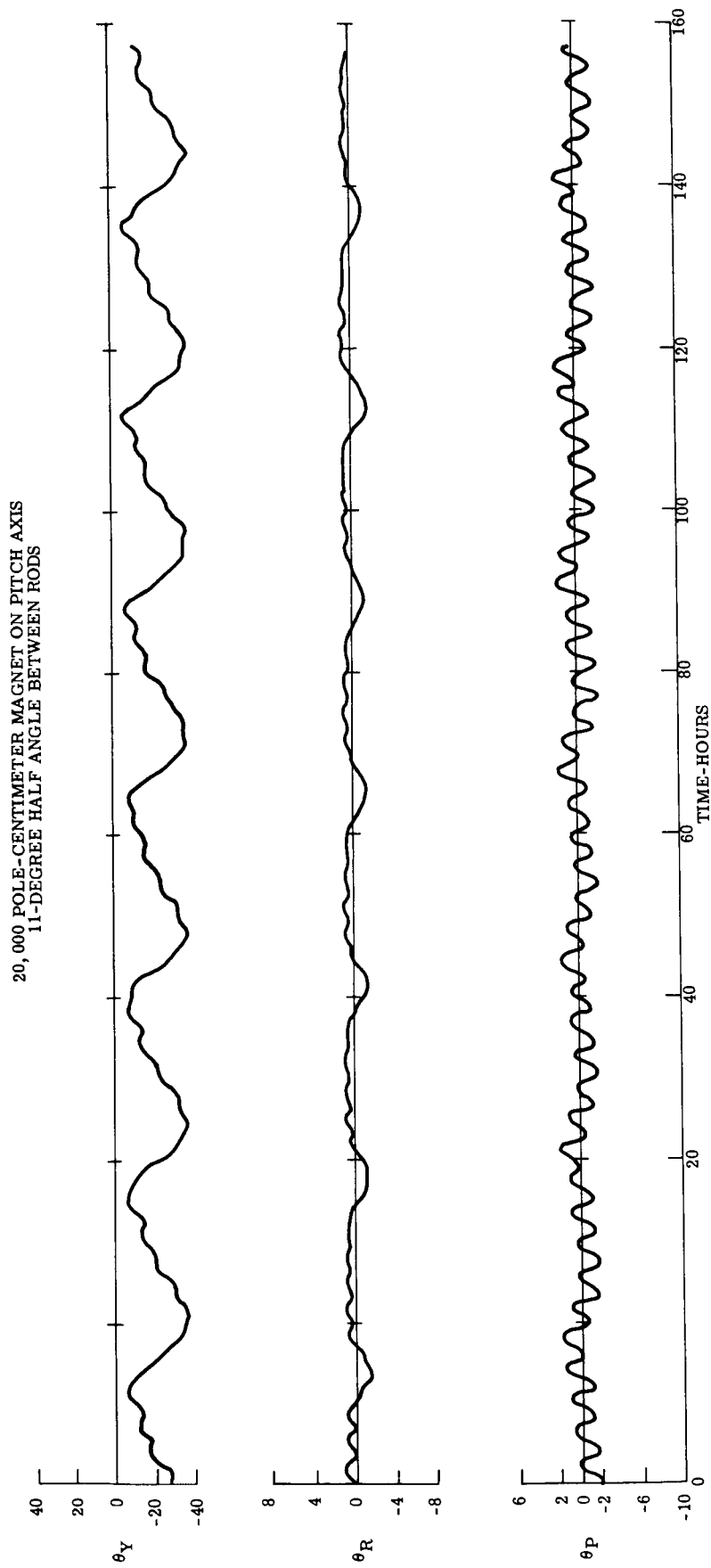


Figure 2.1-27. ATS Medium Altitude Gravity Gradient Experiment

20,000 POLE-CENTIMETER MAGNET ON ROLL AXIS
11-DEGREE HALF ANGLE BETWEEN RODS

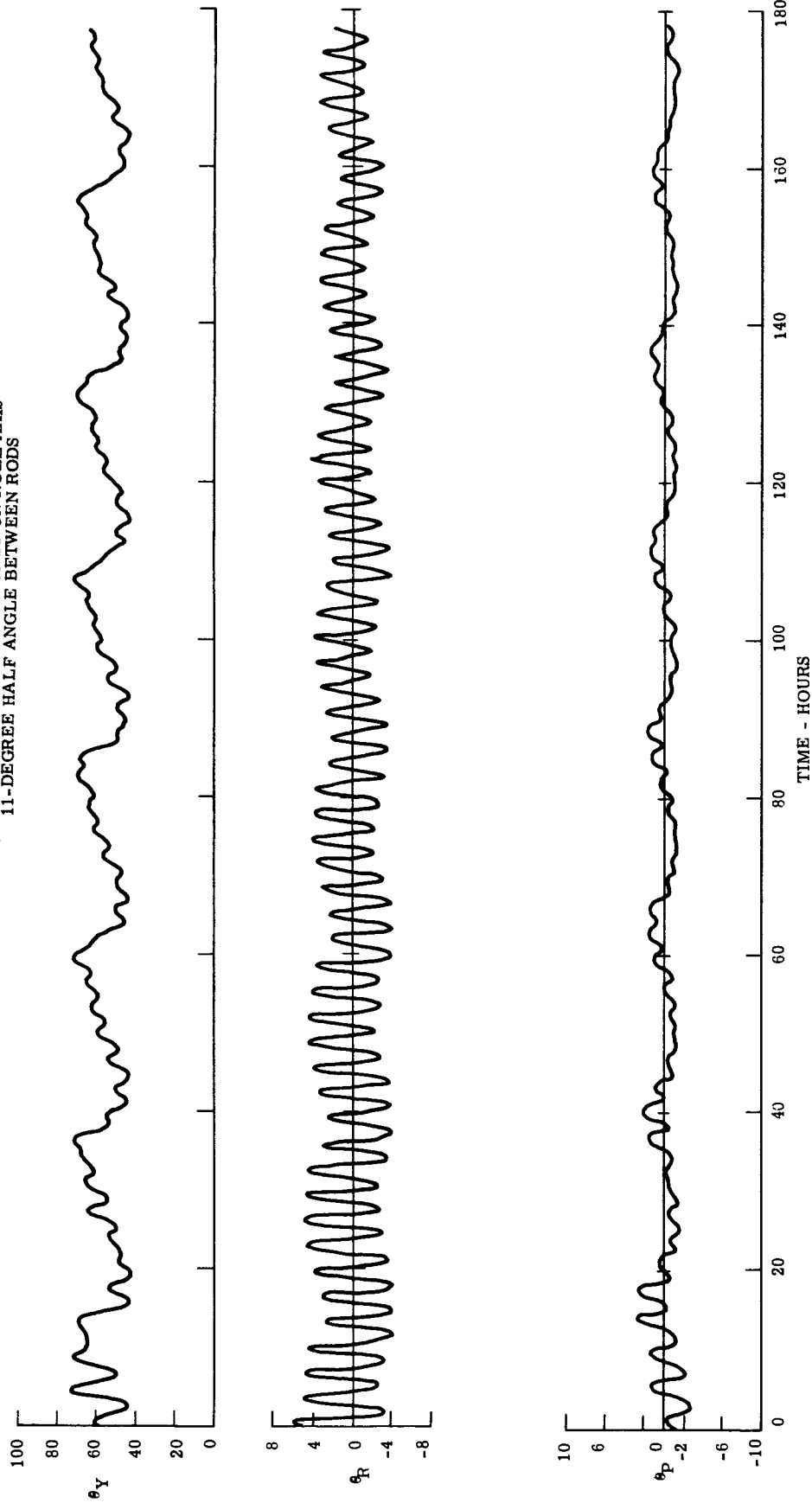


Figure 2.1-28. A TS Medium Altitude Gravity Gradient Experiment

20,000 POLE-CENTIMETER MAGNET ON YAW AXIS
11-DEGREE HALF ANGLE BETWEEN RODS

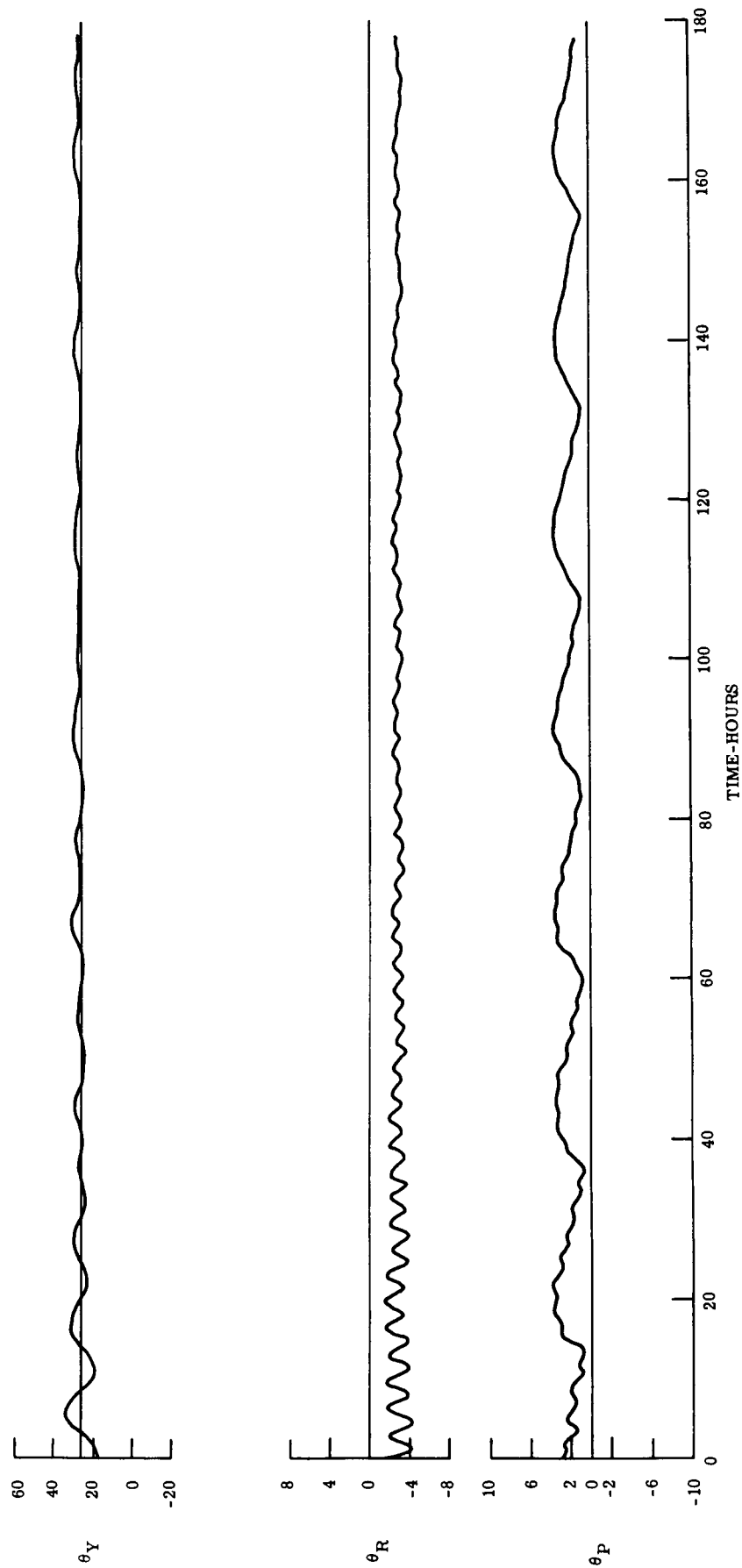


Figure 2.1-29. ATS Medium Altitude Gravity Gradient Experiment

2.1.4.4 Magnetic Torque Studies of 24-Hour Orbit

The effect of a magnetic dipole on the performance of the 6000-mile orbit configuration was discussed in paragraph 2.1.4.3. The effect of a dipole on the 24-hour orbit configuration must also be considered, particularly since the presence of the empty rocket motor case (from the orbit circularization maneuver) may cause a large dipole moment. The magnitudes of the magnetic errors for 24-hour orbit configuration should be no larger than those for 6000-mile orbit configuration (with the same magnetic moment) because the gravity gradient and magnetic torques decrease as the inverse cube of the orbit radius. However, the magnetic field is stationary with respect to the satellite, and the characteristics of the oscillations will be different at synchronous altitude than at intermediate altitudes. To determine these characteristics and pinpoint the exact attitude errors, a series of computer runs was made. The results of these runs are discussed in the following sections.

Any magnetic moment within the vehicle will produce satellite attitude errors. If these errors are small, their amplitudes are approximately linear with dipole strength. The magnitude of the magnetic moment which results in small errors is a function of the axes on which the dipole is located. With the magnet on the yaw axis, the errors are approximately linear up to a dipole strength of 40,000 pole-cm. Linearity is maintained up to a 20,000 pole-cm if the dipole is on the pitch axis, and to less than 10,000 pole-cm if

the magnet is on the roll axis. The linearity functions are given in Table 2.1-4 for the 24-hour orbit configuration.

Since the dipole orientation is arbitrary, good pointing accuracy can be achieved only if the magnetic moment of the satellite is kept small. If the yaw error is limited to 3 degrees (worst case), the dipole moment should be 1000 pole-cm or less.

The performance of the vehicle was determined using the GAPS III, three-axis computer program. A series of computer runs was made with the 24-hour orbit configuration and three different values of magnetic dipole. The 24-hour orbit configuration has four rods, each of which is 100 feet long and has a tip weight of 10 pounds. The rods form an X with a 19 degree half angle between them. In addition, there is a secondary boom composed of two rods each 45 feet long with a 7.5 pound tip weight. The three values of magnetic strength selected were 10,000, 20,000 and 40,000 pole-cm. It is expected that the rocket motor case would have a dipole moment of this magnitude. Since the satellite response is dependent on the orientation of the dipole within the satellite, as well as its magnitude, computer runs were made with the magnetic moment along the yaw, pitch and roll axes. The results of these runs are shown in Figures 2.1-3 to 2.1-39.

Figures 2.1-30, 2.1-31 and 2.1-32 show the performance of the 24-hour orbit configuration vehicle with the dipoles located on the vehicle yaw axes. The magnet is almost at right angles to the magnetic field, and produces a roll torque which is essentially constant. The primary effect of this torque is to cause a roll bias with resulting pitch and yaw oscillations. Comparing the roll biases in Figures 2.1-30, 2.1-31 and 2.1-32 it is evident that the bias is linear with magnet strength. The 40,000 pole-cm magnet yields a 4 degree roll bias, the 20,000 pole-cm magnet yields a 2 degree bias and the 10,000 pole-cm magnet yields a 1 degree bias. The small amplitude oscillations which appear on the roll axis give the same appearance of linearity.

Analysis of the pitch and roll motions from these three figures indicates that the errors on these axes are also linear with magnet strength. Table 2.1-4 summarizes the amplitude of the errors (bias and oscillation) for these three computer runs as well as the remainder of the runs.

Figures 2.1-33, 2.1-34 and 2.1-35 are the same runs but with the magnet on the pitch axis. The behavior is approximately linear for all axes for magnet strengths of 20,000 pole-cm or less, but the character of the motion is altered when the dipole is 40,000 pole-cm, and the linearity is no longer maintained. The oscillations of the pitch axes are probably due to cross coupling since there is little torque on this axis.

Figures 2.1-36, 2.1-37 and 2.1-38 are computer runs with the magnet on the roll axis. This is the worst position for the magnet since it is almost at right angles to the magnetic field and produces a large torque on the yaw axis. The yaw restoring torque (due to gravity gradient) is only three percent of the roll restoring torque and the yaw bias is very large. Figures 2.1-37 and 2.1-38 have almost the same yaw bias (90 degrees) and it appears that the dipole has completely overpowered the vehicle and aligned it with the magnetic field. As a consequence the system oscillations are completely non-linear and the damping has been significantly altered.

Analysis of the figures, and Table 2.1-4 indicates that if good pointing accuracy is to be achieved, the residual magnetic moment of the vehicle must be less than 10,000 pole-cm. The tolerable value would depend upon the orientation of the dipole, but if it is assumed to be randomly oriented, 1000 pole-cm appears to be a realistic value.

TABLE 2.1-4. ATTITUDE ERRORS

		Magnet Strength (pole-cm)			Linearity Factor Deg/pole-cm
		10, 000	20, 000	40, 000	
<u>MAGNET ON YAW AXIS</u>					
Pitch Error (Deg.)	Bias	.2	.4	.7	2.10^{-5}
	Oscillation	.5	1.0	1.9	5.10^{-5}
Roll Error (Deg.)	Bias	1.0	2.0	4.0	1.10^{-4}
	Oscillation	--	--	--	--
Yaw Error (Deg.)	Bias	.15	.3	.5	$1.5.10^{-5}$
	Oscillation	.15	.3	.5	$1.5.10^{-5}$
<u>MAGNET ON PITCH AXIS</u>					
Pitch Error (Deg.)	Bias	0	.2	.2	1.10^{-5}
	Oscillation	1	1.6	1.8	1.10^{-4}
Roll Error (Deg.)	Bias	0	.2	.9	1.10^{-5}
	Oscillation	1	2.0	3.3	1.10^{-4}
Yaw Error (Deg.)	Bias	.5	.5	1	5.10^{-5}
	Oscillation	6.5	12.5	15	$6.5.10^{-4}$

10,000 POLE-CENTIMETER MAGNET ON YAW AXIS
19-DEGREE HALF-ANGLE BETWEEN RODS

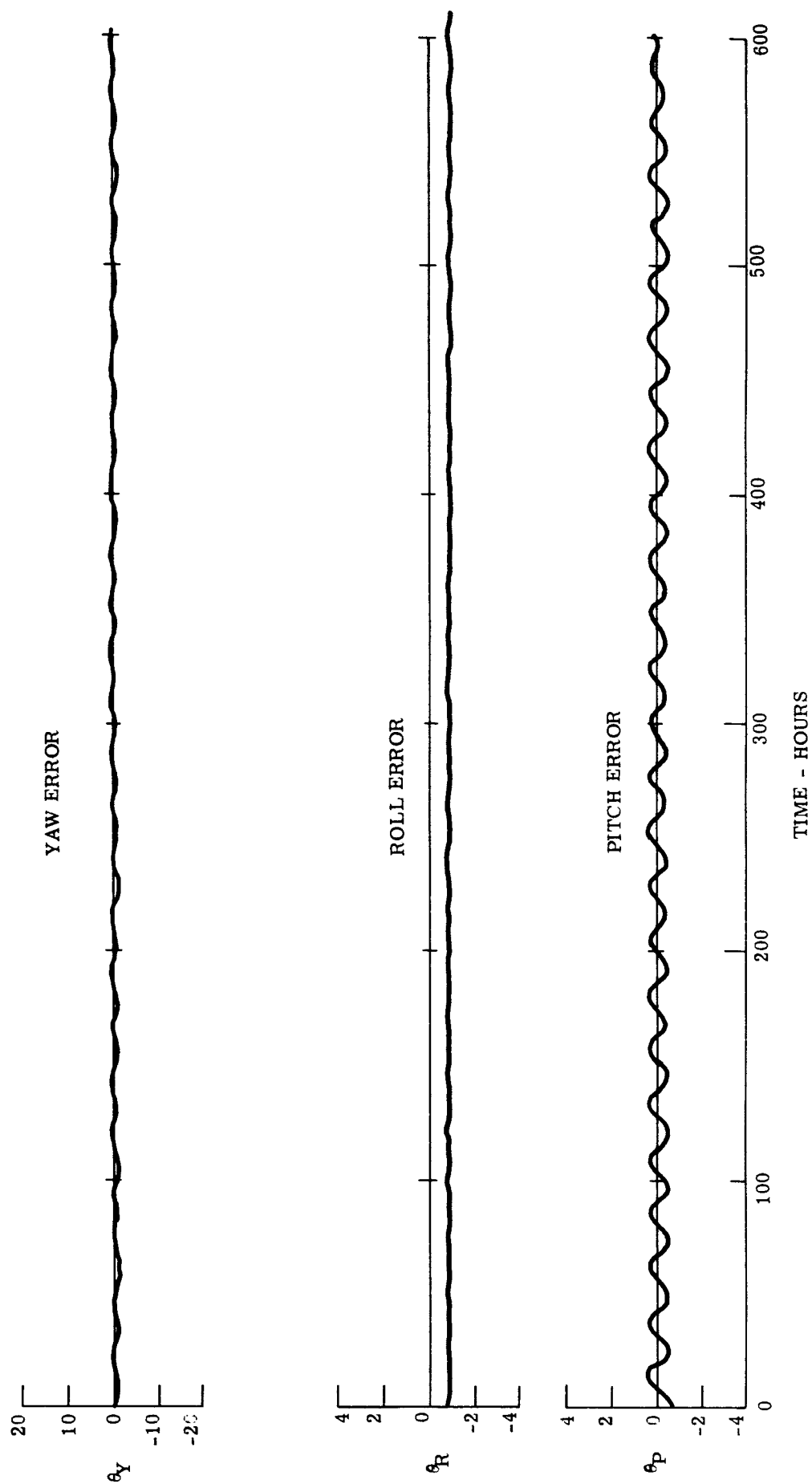


Figure 2.1-30. ATS Synchronous Altitude Gravity Gradient Experiment

20,000 POLE-CENTIMETER MAGNET ON YAW AXIS
19-DEGREE HALF-ANGLE BETWEEN RODS

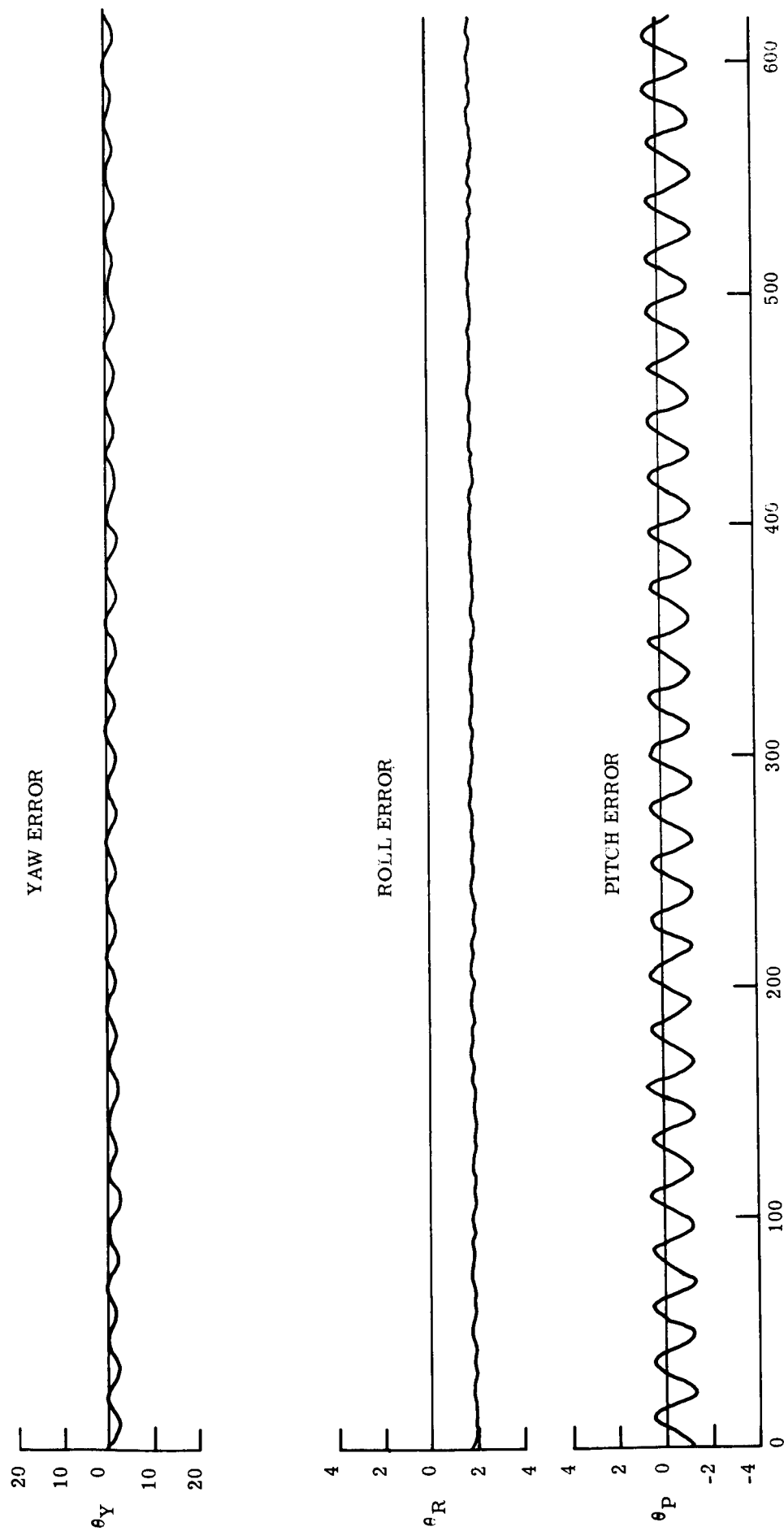


Figure 2.1-31. ATS Synchronous Altitude Gravity Gradient Experiment

40,000 POLE-CENTIMETER MAGNET ON YAW AXIS
19 DEGREE HALF-ANGLE BETWEEN RODS

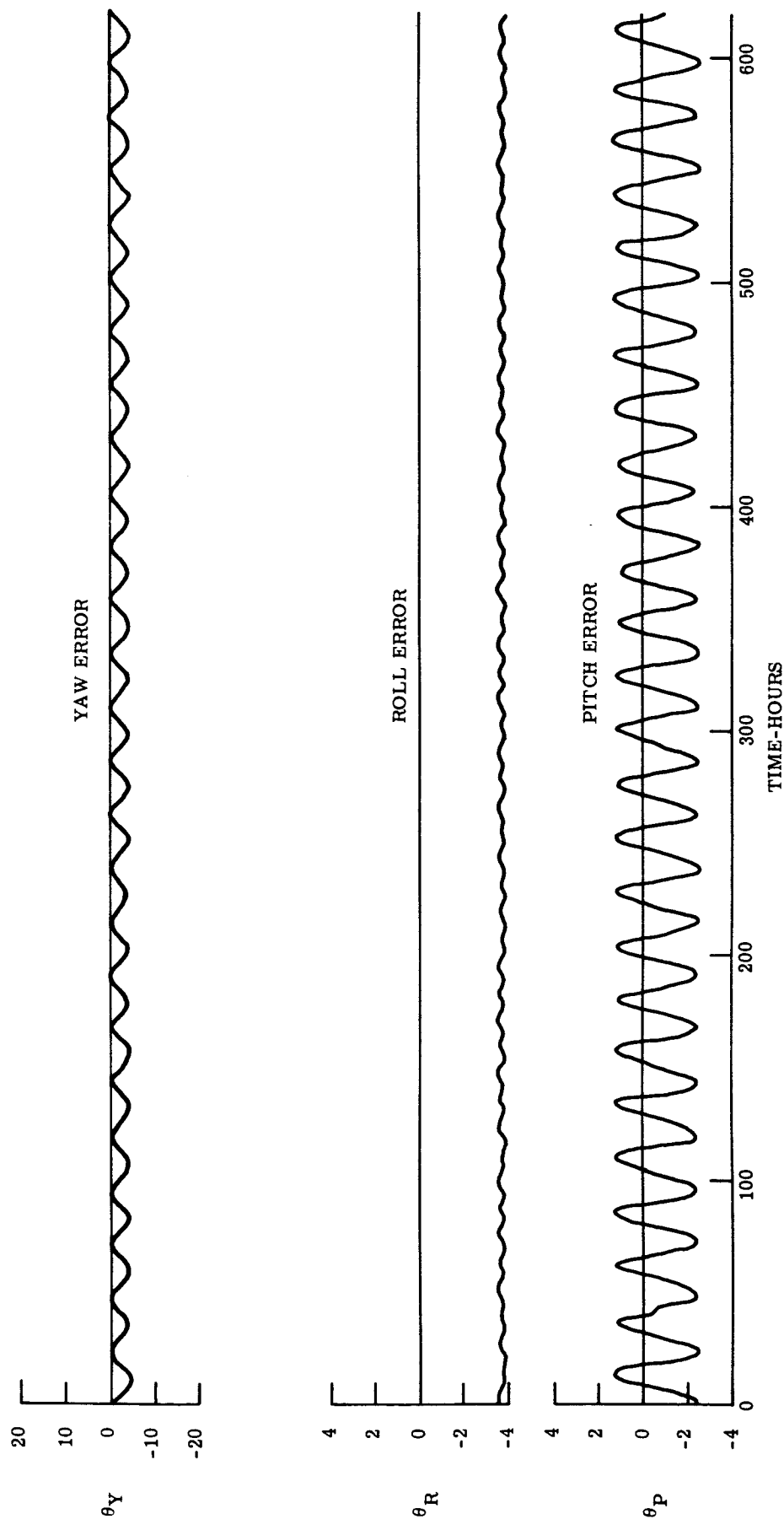


Figure 2.1-32. ATS Synchronous Altitude Gravity Gradient Experiment

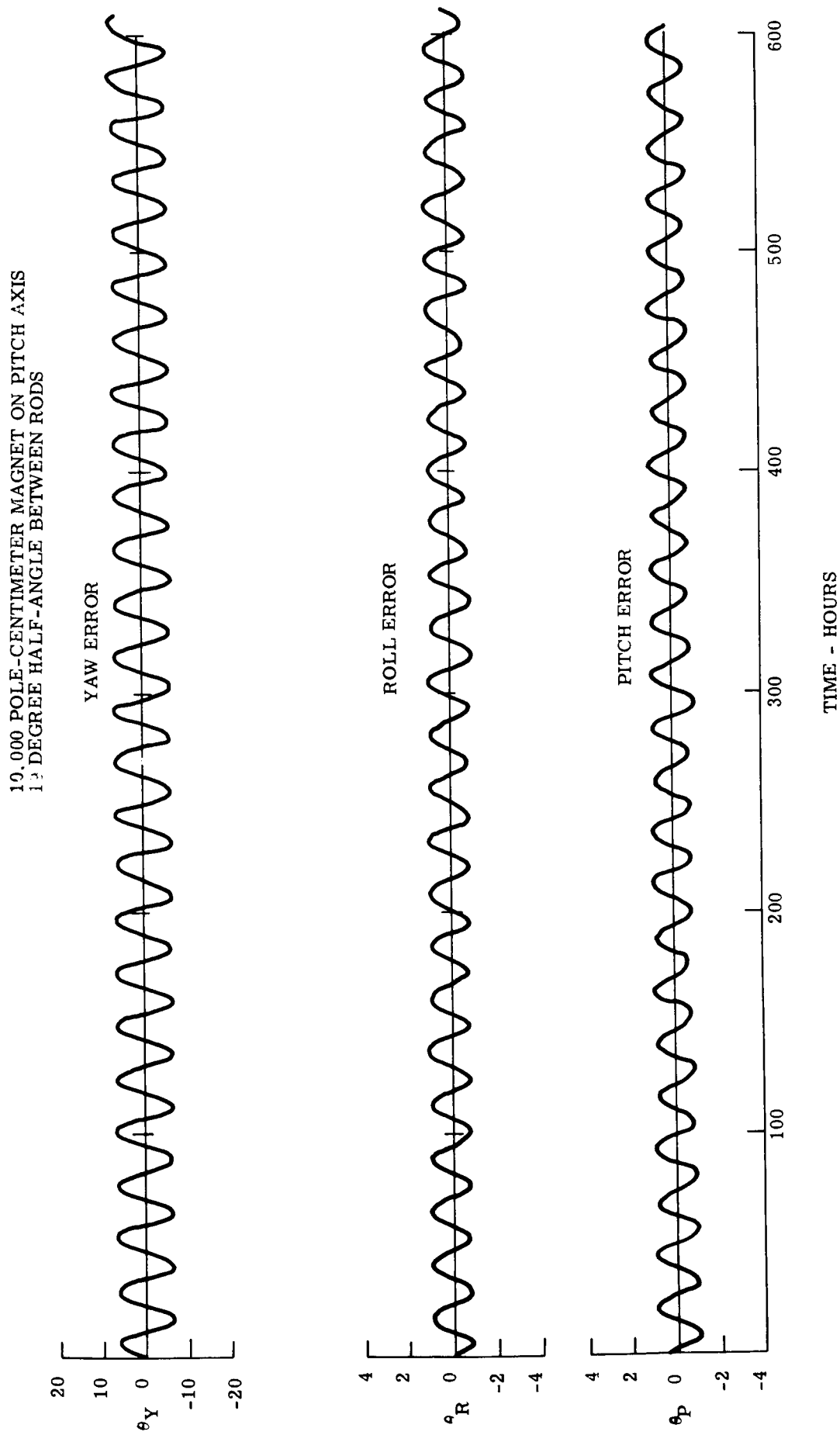


Figure 2.1-33. ATS Synchronous Altitude Gravity Gradient Experiment

20,000 POLE-CENTIMETER MAGNET ON PITCH AXIS
19 DEGREE HALF-ANGLE BETWEEN RODS

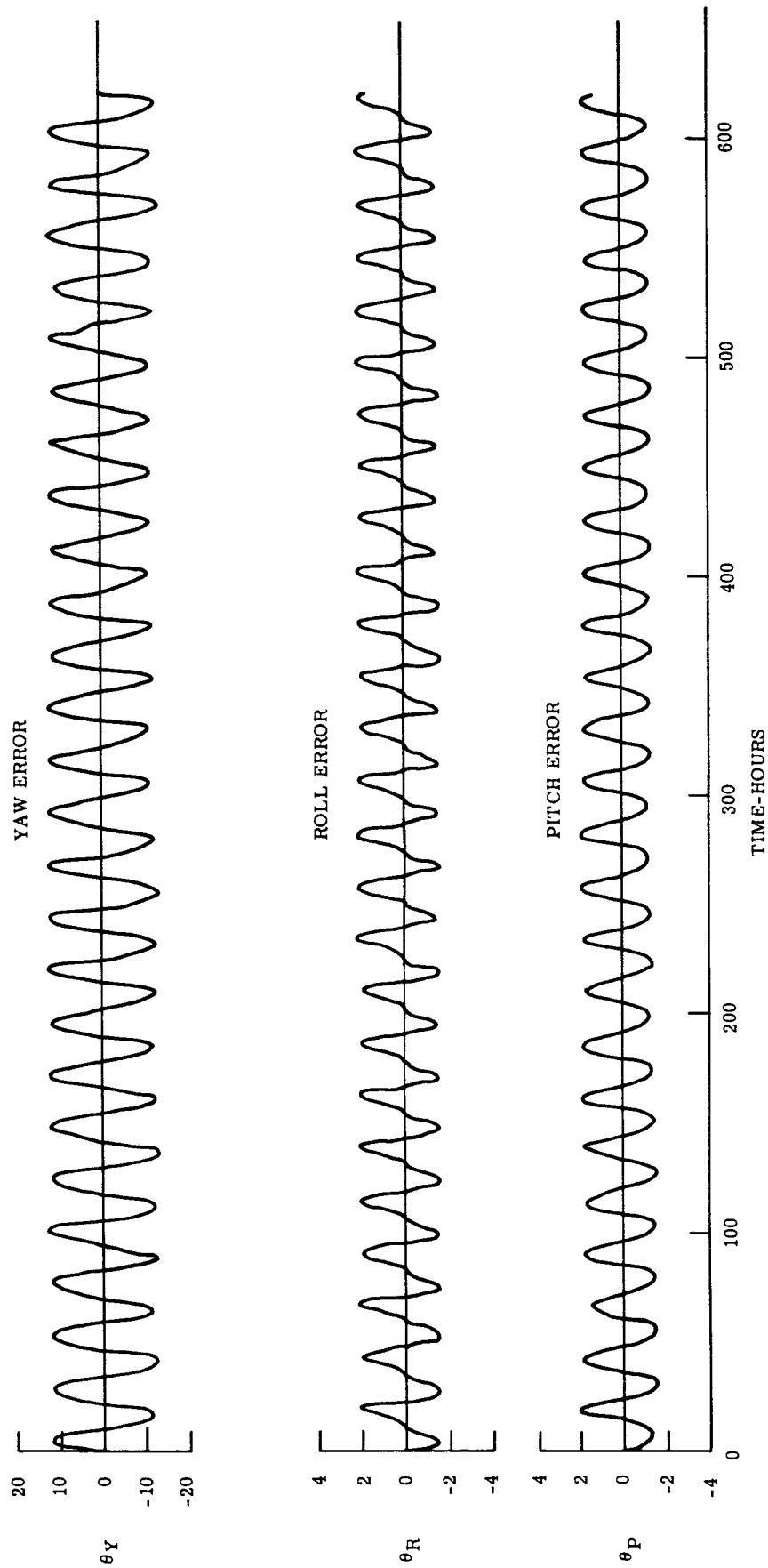


Figure 2.1-34. ATS Synchronous Altitude Gravity Gradient Experiment

40,000 POLE-CENTIMETER MAGNET ON PITCH AXIS
19 DEGREE HALF-ANGLE BETWEEN RODS

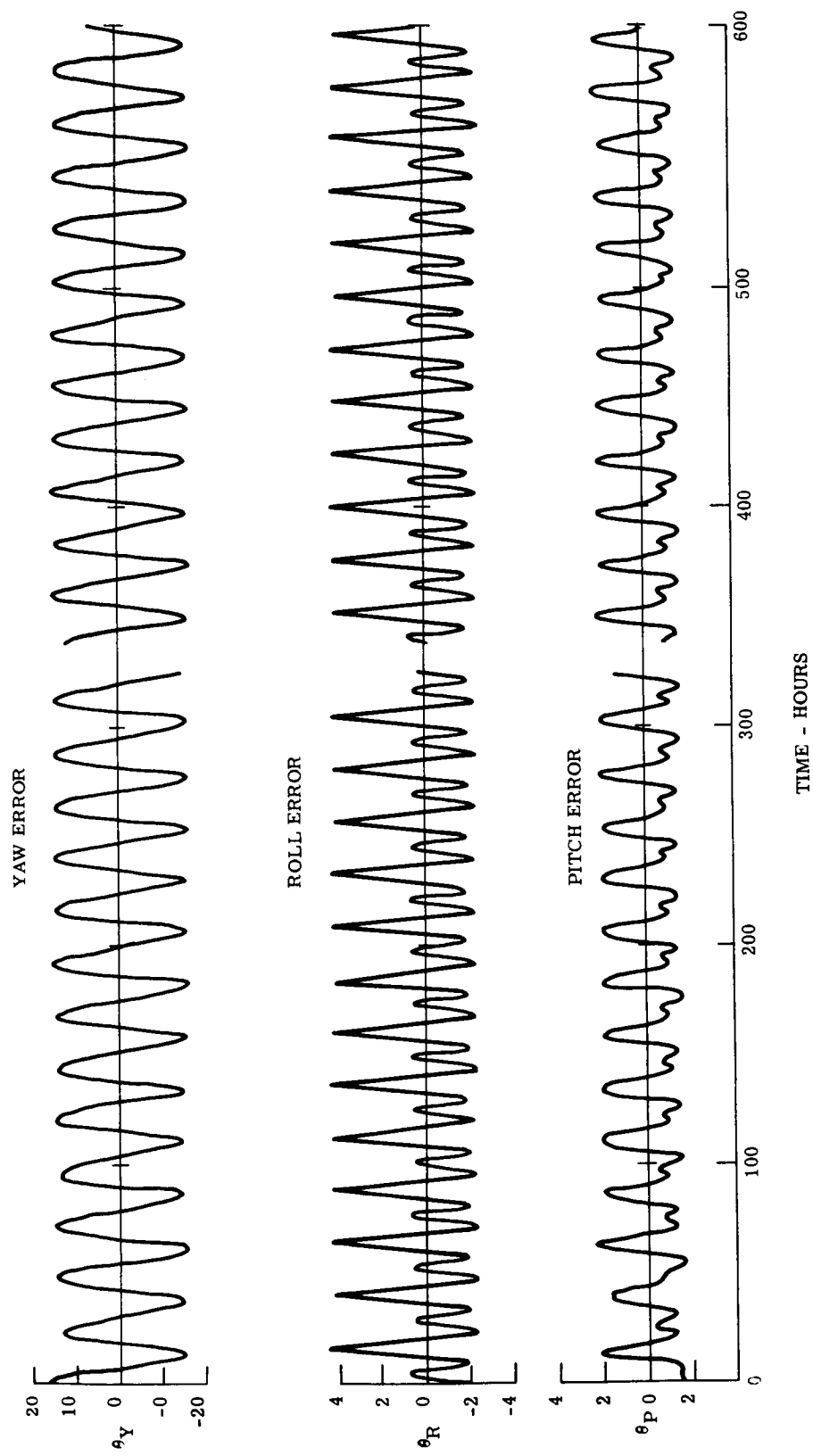


Figure 2.1-35. ATS Synchronous Altitude Gravity Gradient Experiment

10,000 POLE - CENTIMETER MAGNET ON ROLL AXIS
19 DEGREE HALF-ANGLE BETWEEN RODS

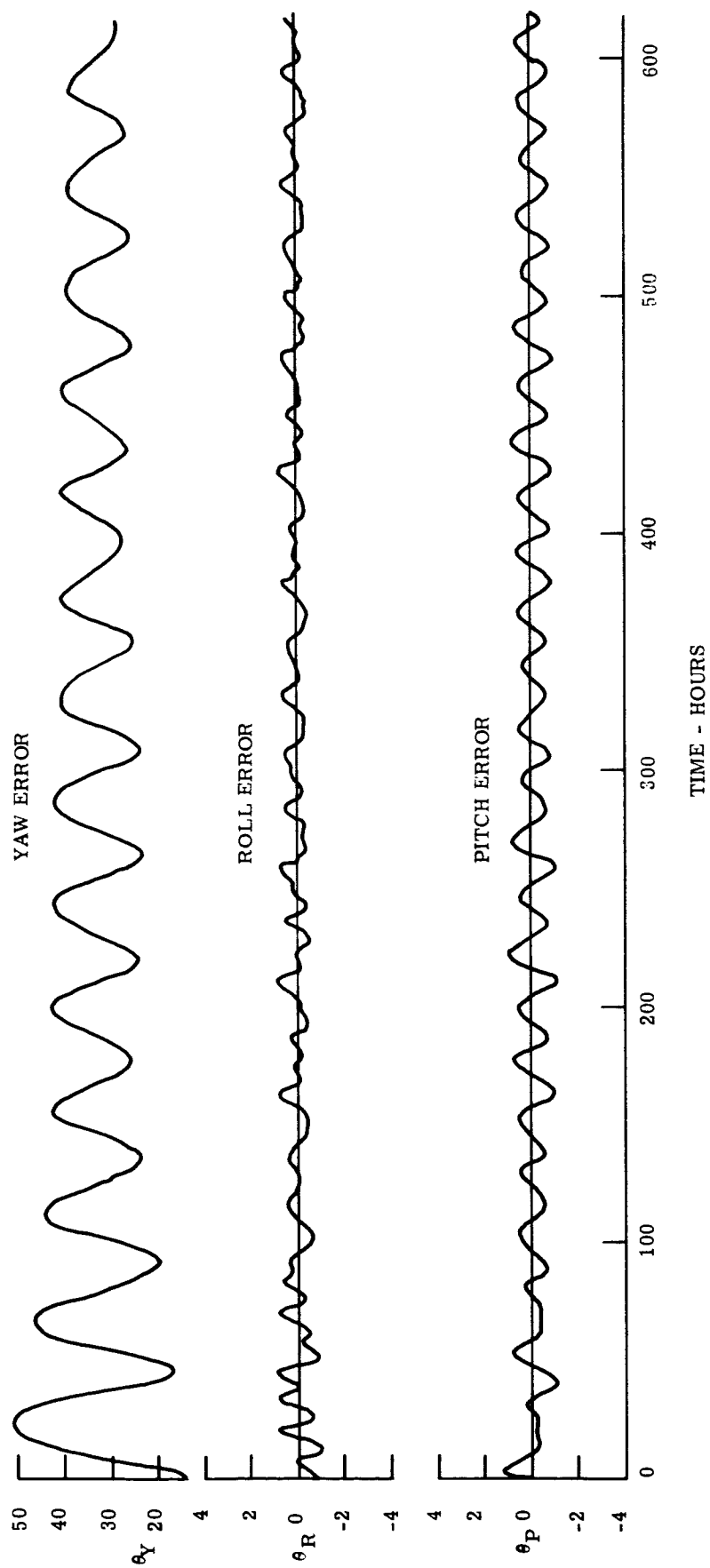


Figure 2.1-36. ATS Medium Altitude Gravity Gradient Experiment

20,000 POLE-CENTIMETER MAGNET ON ROLL AXIS
19 DEGREE HALF-ANGLE BETWEEN RODS

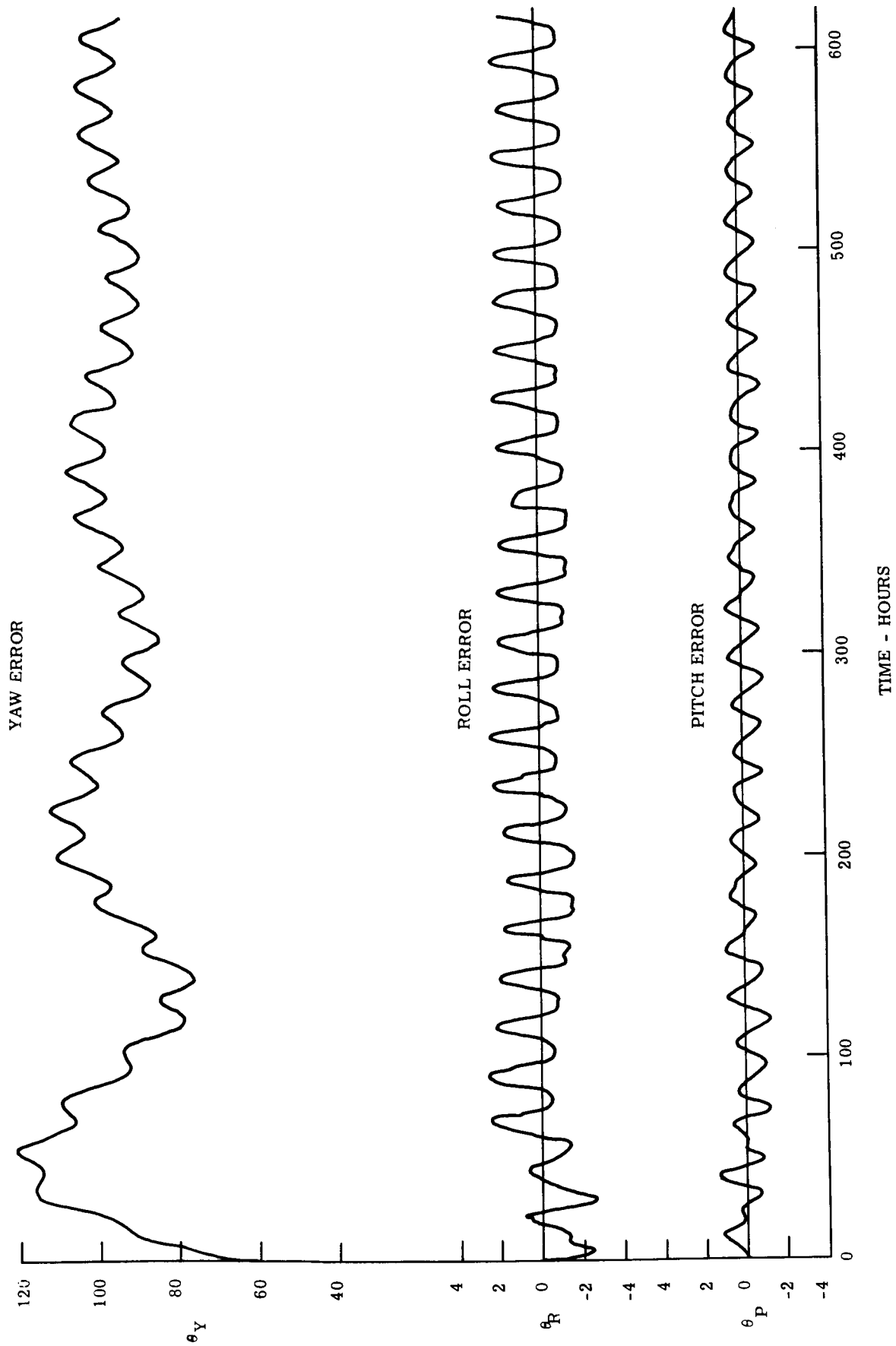


Figure 2.1-37. ATS Synchronous Altitude Gravity Gradient Experiment

40,000 POLE-CENTIMETER MAGNET ON ROLL AXIS
19 DEGREE HALF-ANGLE BETWEEN RODS

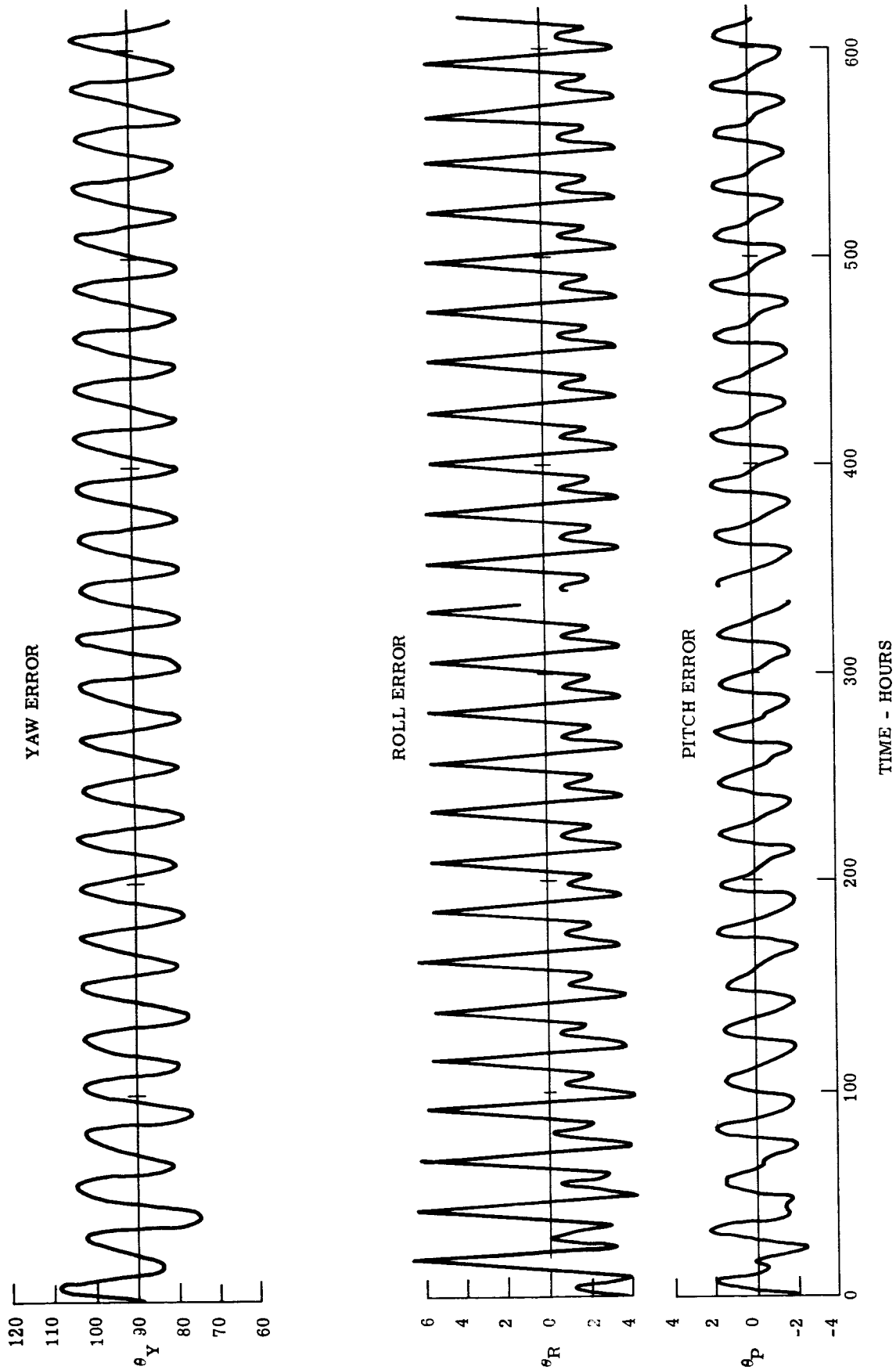


Figure 2.1-38. ATS Synchronous Altitude Gravity Gradient Experiment

TABLE 2.1-3. ATTITUDE ERRORS (cont'd)

		Magnet Strength (pole-cm)			Linearity Factor Deg/pole-cm
		10,000	20,000	40,000	
<u>MAGNET ON ROLL AXIS</u>					
Pitch Error (Deg.)	Bias	.8	.8	2.2	--
	Oscillation	.15	.20	.2	--
Roll Error (Deg.)	Bias	0	.5	2.8	--
	Oscillation	.6	1.5	4.6	--
Yaw Error (Deg.)	Bias	32	95	90	--
	Oscillation	6.0	5	12	--

2.1.4.5 Crab Angles of the 6000-Mile Orbit Configuration

The ATS MAGGE vehicle is designed to fly at zero attitude error for the nominal half angle between the X rods of 19 degrees. Part of the gravity gradient experimental flight, however, consists of determining the performance at different X rod half angles. Changing this angle will rotate the axes of principal moments of inertia and cause the satellite to fly at an angle out of the orbit plane (i. e., a yaw rotation about the local vertical), or to "crab". The angle of the crab is a function of the rod half angle.

The configuration in this program is assumed to have all the rods radiating from the axis of the cylinder. Recent changes to the proposed configuration have, however, shifted the position of the rods so that they do not pass through the center. This will cause a small change in the computed crab angle. The new crab angles will be evaluated after the actual rod position is finalized.

The nominal half angle between the X-rods for the 6000-mile orbit configuration is 19 degrees. This half angle has been selected to provide a zero attitude error while the vehicle is in orbit. However, the value of the half angle was determined from a simplified analytical model of the gravity gradient configuration, and the presence of the satellite body and the outboard position of the damping boom cause a slight shift in the location of the principal axes of inertia. The attached figure shows the crab angles as determined from the GAPS III computer program, and indicates that the attitude error at 19 degrees is not zero but -0.5 degrees. (The rod half angle to give zero crab angle is approximately 18.8 degrees.) A negative angle means that the "plane" of the X rods is closer to the orbit plane than it is when the X rod half angle is 19 degrees. Hence, the angle between the velocity vector and the X rod plane (measured around the local vertical) is now 20 degrees rather than 20.5 degrees. Similarly a positive sign means that the X rod plane is farther away from the orbit plane than in its nominal position. In the limit, if the X rods were coincident, and there were no difference between the pitch and roll moments of inertia, the satellite would have a 42 degree error, and the damping boom would lie along the velocity vector. The crab angle for other values of rod half angle over the region to be used in orbit are given in Figure 2.1-39.

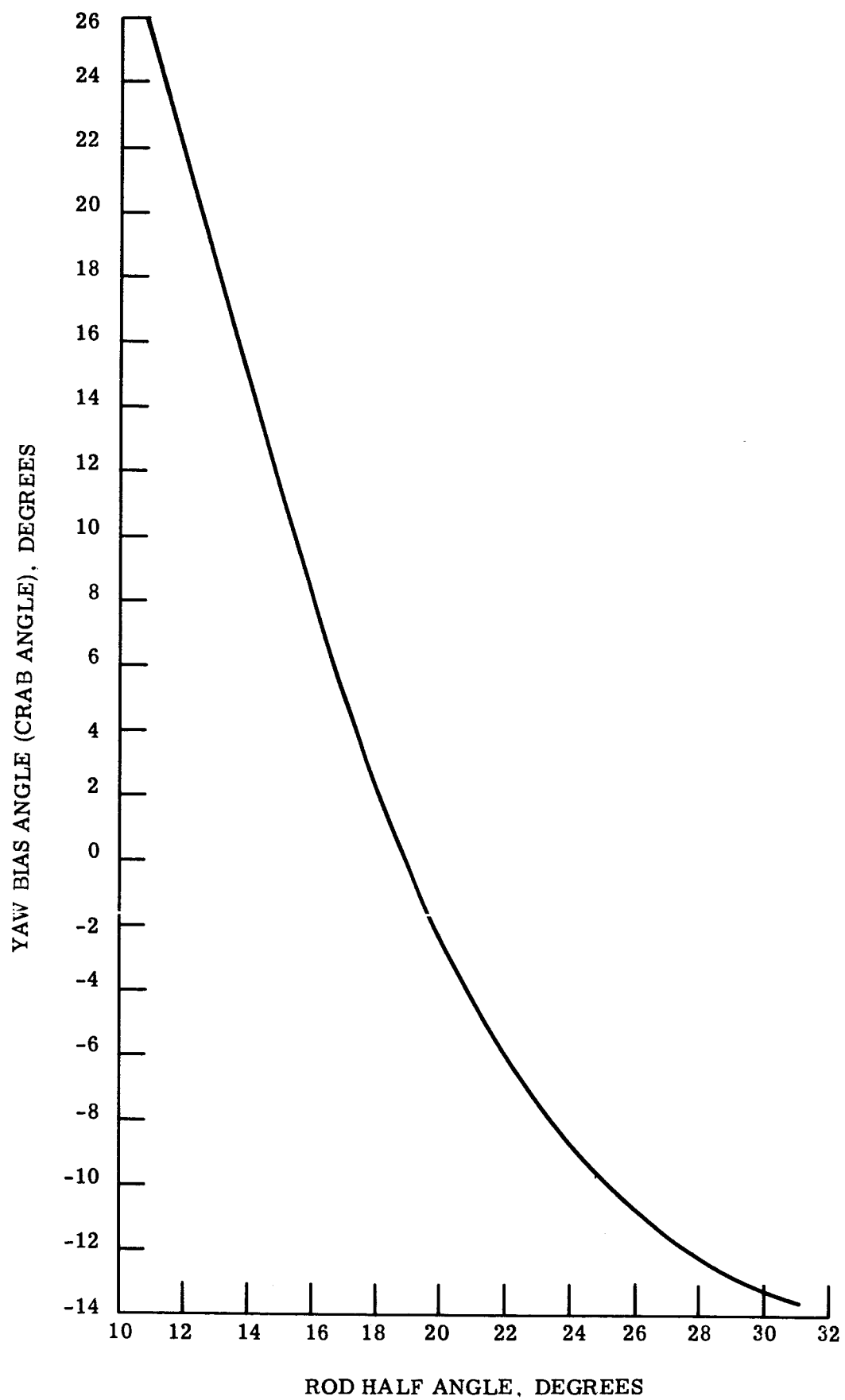


Figure 2. 1-39. Effect of Rod Half Angle on Yaw Bias Angle (Crab Angle)

2.1.4.6 Bottoming of the Damper Due to Thermal Bending

The purpose of this study was to determine if the magnetic damper will bottom, when the Advanced Technological Satellite is leaving shadow and entering sunlight, due to thermal expansion of the rods.

A second order differential equation has been derived to express the relationship between the absolute magnetic damper clearance as an analytical function of thermal expansion of the rods.

Given delta temperature of the rods as a function of time, $\Delta t = f(t)$, radius of curvature can be expressed as a function of time, $R = f(t)$, see Equation (1).

$$R = \frac{2r}{\mu(\Delta t)} \quad (1)$$

Where: $r = .5 \text{ inch}$
 $\mu = 9.9 \times 10^{-6} \text{ } ^\circ\text{F}$
 $\Delta t = 8 \text{ } ^\circ\text{F}$

Knowing: $R = f(t)$, X_2 can be expressed as a function of time.
 See Equation (2)

$$X_2 = R(1 - \cos \theta) \quad (2)$$

Where: $S = 45 \text{ feet}$ (See Figure 2.1-40)
 $\theta = S/R$

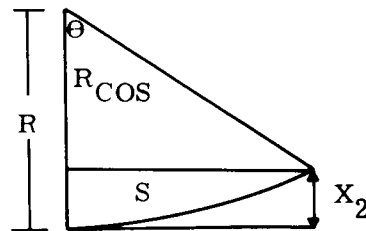


Figure 2.1-40. X_2 as a Function of Time

X_2 vs t is plotted in Figure 2.1-41.

Knowing: $X_2 = f(t)$ an analytical function for X_2 can be derived by using three exponentials:

$$X_2 = K_0 - K_1 e^{-d_1 t} - K_2 e^{-d_2 t} - K_3 e^{-d_3 t} \quad (3)$$

Where $d_2 = 2d_1$
 $d_3 = 3d_1$
 $y = e^{-d_1 \Delta t}$
 $K_0 = K_1 + K_2 + K_3$

This analytical function fits the coordinates in Figure 2.1-42.

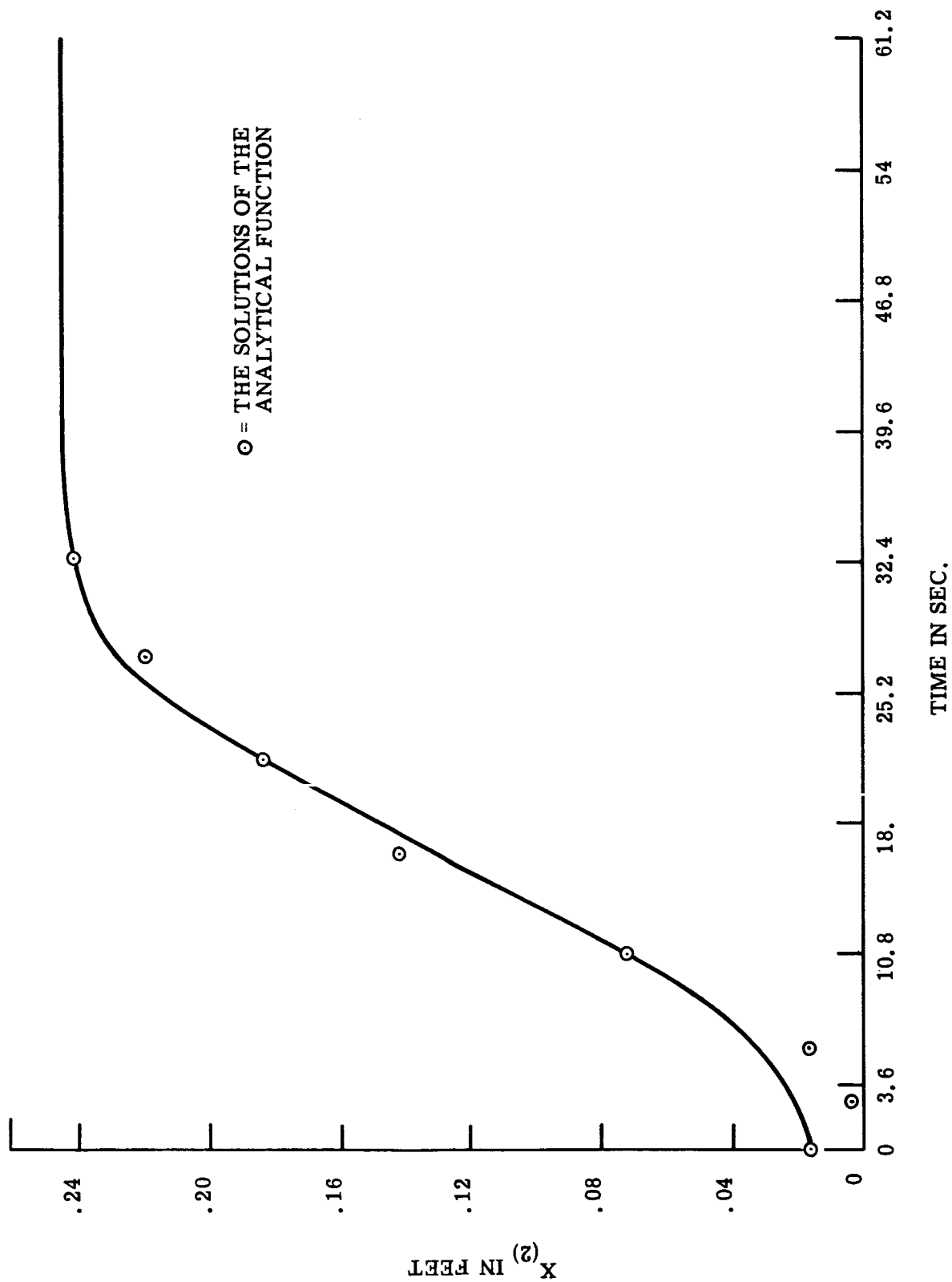


Figure 2.1-41. X_2 Versus t

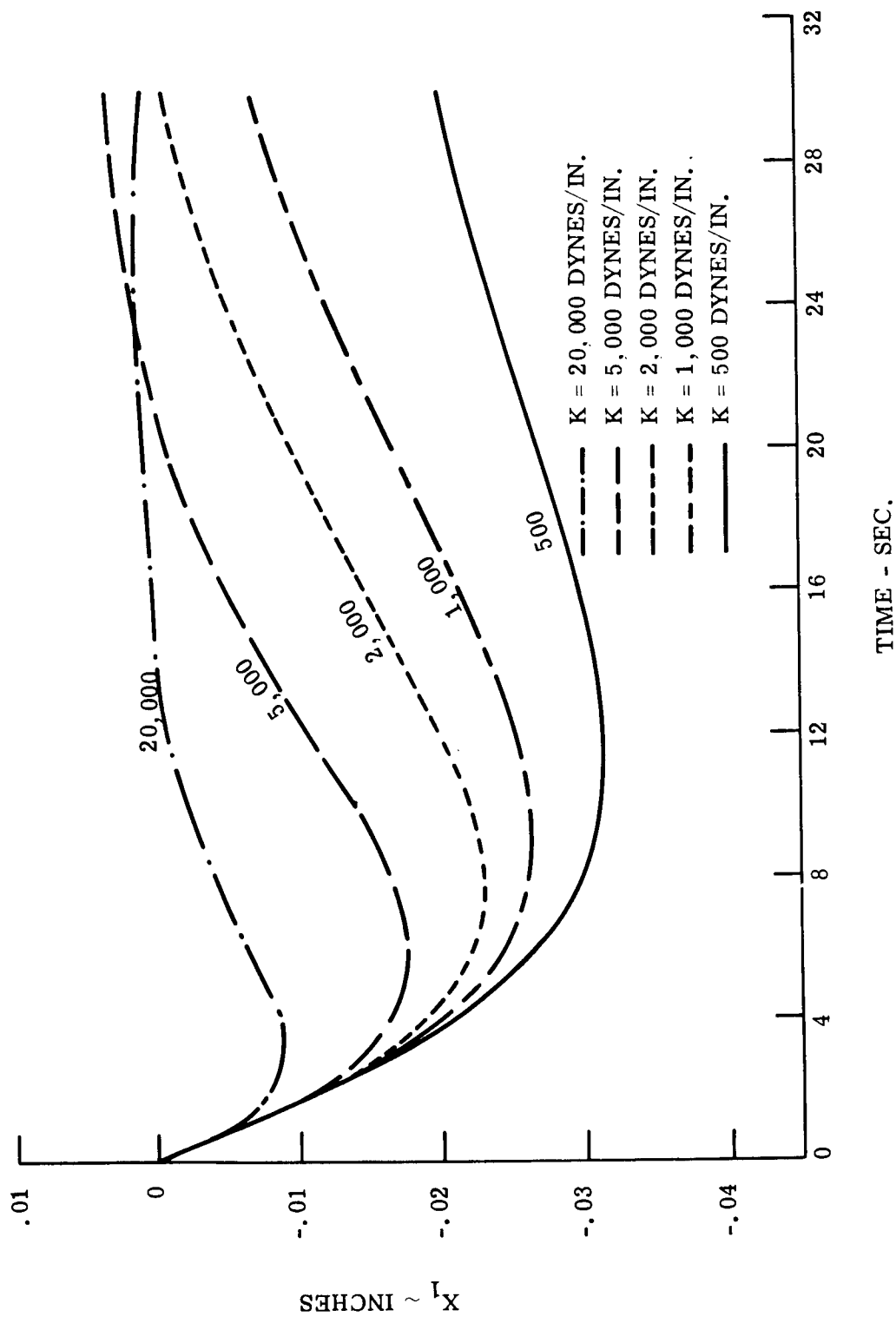


Figure 2.1-42. X_1 Versus t

The solution to, Equation (4), the second order differential equation can now be solved by using a La Place Transformation.

$$\ddot{X}_1 + \frac{b}{m_1 + m_2} \dot{X}_1 + \frac{k}{m_1 + m_2} X_1 = \frac{-m_2}{m_1 + m_2} \ddot{X}_2 \quad (4)$$

Where $b = 15000$ dynes/cm/sec
 $k = 3000$ dynes/inch and 15000 dynes/inch
 $m_1 = 3/32.2$ lbs.
 $m_2 = 3.8/32.2$ lbs.

In the La Place Transformation the solution becomes

$$\ddot{X}_1 + B\dot{X}_1 + CX_1 = K_0^1 + K_1^1 e^{-d_1 t} + K_2^1 e^{-d_2 t} + K_3^1 e^{-d_3 t} \quad (5)$$

Figure 2.1-43 represents two graphs of $X_1 = f(t)$ for two spring constants of 5000 dynes/inch and 15000 dynes/inch, respectively.

The magnetic damper has a clearance of approximately 5/100 inch, and from Figure 2.1-43, the damper will not bottom. The maximum values of X_1 for spring constants of 5000 dynes/inch and 20000 dynes/inch are .0175 inch and .0088 inch, respectively.

2.1.5 ATS Mathematical Model Coordinate Frames

The various coordinate frames that will be needed for the digital computer simulation of the attitude dynamic of the Advanced Technology Satellite are described here, insofar as is possible at present. The nomenclature of offsets and angular rotations is also assigned. The configuration used is sufficiently general to cover all design alternatives presently foreseen.

Additional coordinate frames needed for dynamical, thermal and structural analyses must be related to the systems described herein when the results of the analyses are incorporated into the simulation.

Each reference frame is described by a right-handed system of unit vectors. The positive direction of each axis, and the location of the origin of each reference frame are stated.

Each frame is derived from the previous one by a translation of the origin, if applicable, followed by one or more angular rotations. The order of these rotations is specified, and the elements of the rotational transformation matrix are given.

All angular coordinates will be expressed as Greek letters with subscripts. Greek letters will not otherwise be used.

2.1.5.1 Inertial Reference Frame

The inertial reference frame is described by the triad $X_I Y_I Z_I$, with the origin at the geocenter. This frame is illustrated in Figure 2.1-44.

The positive X_I axis is along the mean vernal equinox of date, and points toward the first point of Aries. The positive Z_I axis points to the north geographic pole. The positive Y_I axis forms a right-handed system.

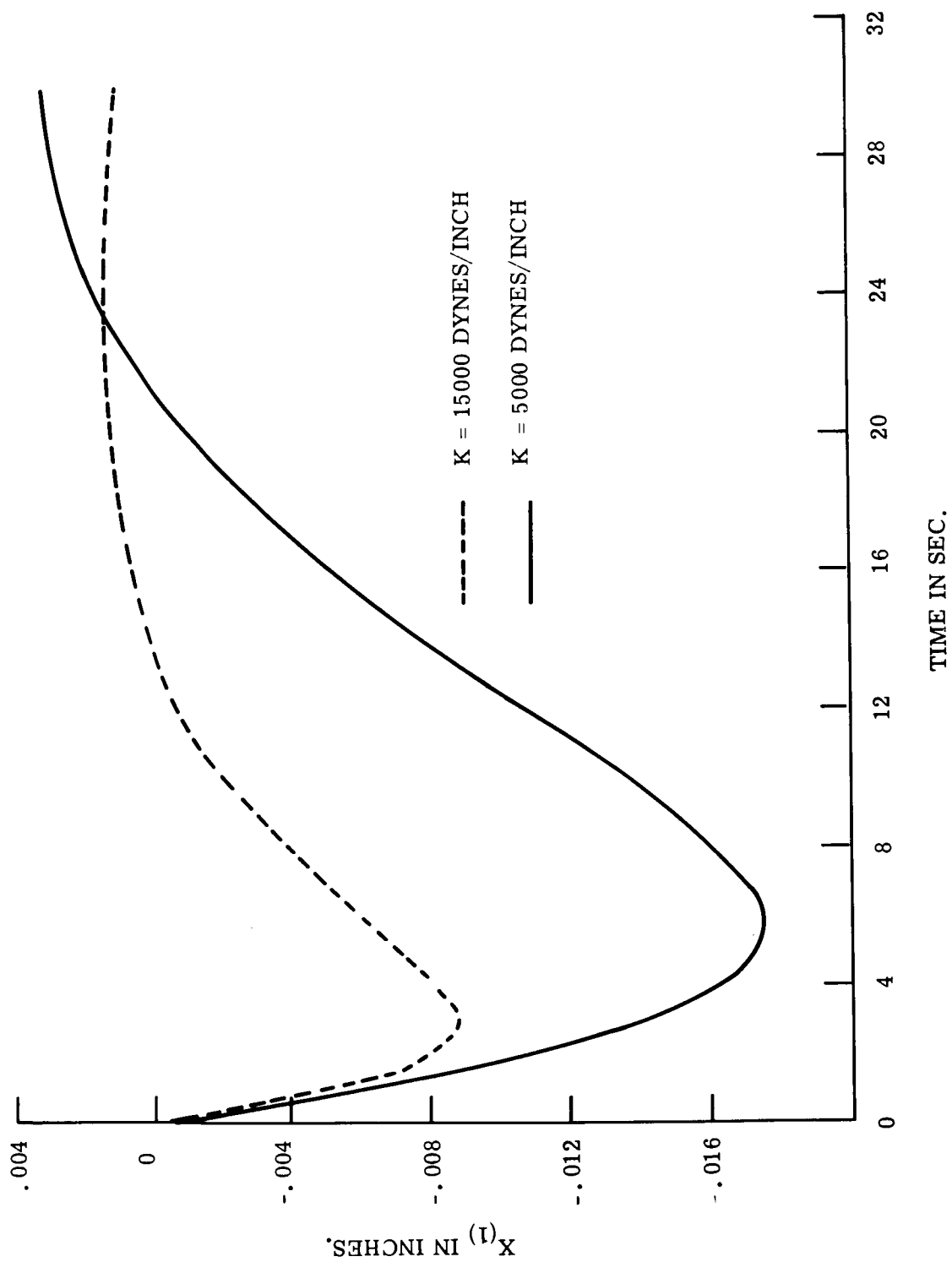


Figure 2.1-43. X_1 Versus t

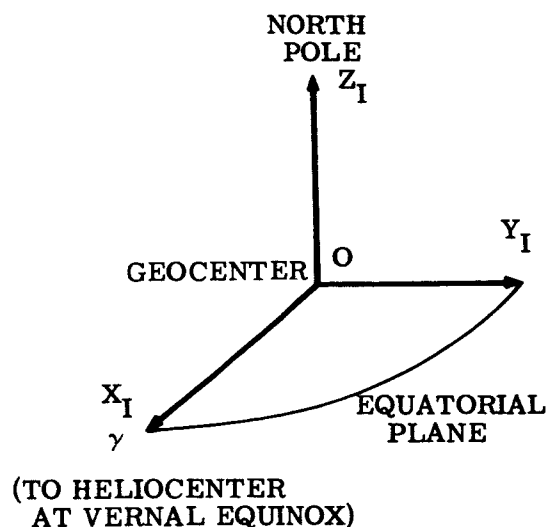


Figure 2.1-44. Inertial Reference Frame

It is convenient to specify a unit vector, S , directed from the heliocenter to the geocenter. S is expressed in terms of its components (direction cosines) in the inertial frame,

$$S = X_I \cos \mu_E + Y_I \sin \mu_E \cos I_E + Z_I \sin \mu_E \sin I_E,$$

where I_E is 23.45 degrees, the angle between the ecliptic and equatorial planes, and μ_E is the instantaneous celestial longitude of the earth. μ_E is calculated from the following equations.

Given the time, t , in mean solar seconds from 0^h U. T. of the day of interest (calendar day n), find the time, t' , in mean solar days and fractions thereof, measured from 0^h U. T. of January 0 of the year of interest,

$$t' = n + \frac{t}{86,400}.$$

The celestial longitude of the earth on January 0 is an input constant determined from

$$\mu_{E0} = \mu_{S0} - 180^\circ,$$

where μ_{S0} is the celestial longitude of the sun on January 0, as found in the nautical ephemeris. The eccentric anomaly, E_{E0} , of the earth on January 0 is found from

$$\tan \left(\frac{E_{E0}}{2} \right) = \sqrt{\frac{1-e_E}{1+e_E}} \tan \left(\frac{\mu_{E0} - \mu_{EP}}{2} \right),$$

where

$$e_E = 0.01672 (1965)$$

is the eccentricity of the earth's orbit, and

$$\mu_{EP} = 102.335^\circ (1965)$$

is the celestial longitude of the earth at its perihelion position. The eccentric anomaly, E_E , of the earth at time, t' , is found from

$$E_E - e_E \sin E_E = \omega_E t' + E_{E0} - e_E \sin E_{E0} ,$$

where the angles are in radians, and $\omega_E = 0.0172028$ radians per mean solar day.

The celestial longitude of the earth, μ_E , is computed from

$$\tan \left(\frac{\mu_E - \mu_{EP}}{2} \right) = \sqrt{\frac{1 + e_E}{1 - e_E}} \tan \left(\frac{E_E}{2} \right) .$$

2.1.5.2 Geographic Reference Frame

The geographic reference frame is described by the triad $X_G Y_G Z_G$, with the origin at the geocenter. This frame is illustrated in Figure 2.1-45.

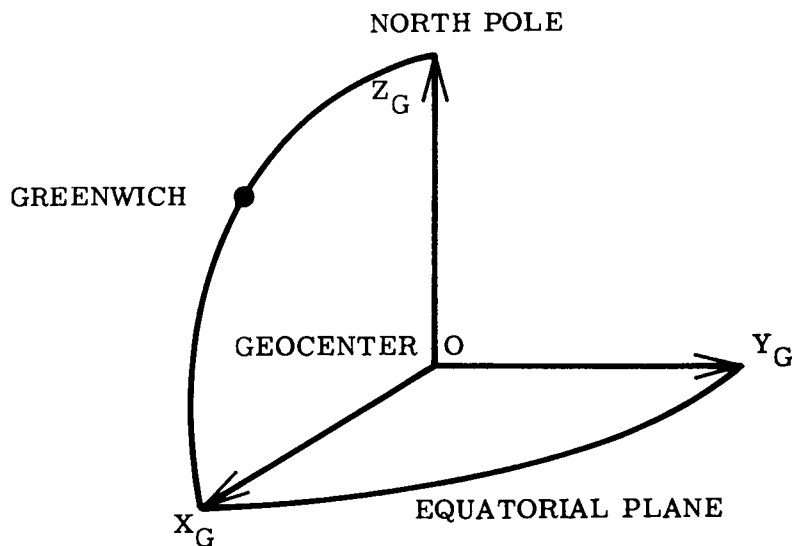


Figure 2.1-45. Geographic Reference Frame

The positive X_G axis lies in the intersection of the Greenwich meridian and the equatorial plane. The positive Z_G axis points to the north geographic pole, and the Y_G axis forms a right-handed system.

The angular coordinates of a vector in this system are longitude, λ , measured positive eastward from Greenwich, and geocentric latitude, ϕ' .

The geocentric latitude is related to the geodetic latitude, ϕ , by the relation,

$$\tan \phi' = (1 - e^2) \tan \phi ,$$

where

$$e^2 = 0.006723 ,$$

and e is the eccentricity of the ellipsoidal earth.

The Greenwich hour angle is designated as G_{HA} . The American Ephemeris lists G_{HA} for 0 hours Universal Time for every day of the year. To avoid a table look-up, G_{HA} is computed as follows. Let G_{HA0} denote G_{HA} at 0^h U. T. on January 0 of the year of

interest. G_{HA0} is obtained from the ephemeris and expressed in sidereal hours and decimal fractions thereof. Then G_{HA} in degrees is computed from

$$G_{HA} = 15 G_{HA0} + 0.98565 n + 0.0041781 t,$$

where n is the calendar day of interest, and t is the time in mean solar seconds since 0^h U. T. of day n .

The geographic reference frame is obtained from the inertial reference frame by a rotation through the angle G_{HA} about the Z_I axis. When G_{HA} is zero, X_G points along X_I , etc.

The matrix of the transformation from the inertial frame to the geographic frame is $[B_1]$,

$$\begin{bmatrix} X_G \\ Y_G \\ Z_G \end{bmatrix} = [B_1] \begin{bmatrix} X_I \\ Y_I \\ Z_I \end{bmatrix}.$$

The elements of the $[B_1]$ matrix are

$$\begin{aligned} B_{111} &= \cos G_{HA}, \\ B_{112} &= \sin G_{HA}, \\ B_{121} &= -\sin G_{HA}, \\ B_{122} &= \cos G_{HA}, \\ B_{133} &= 1, \\ B_{113} &= B_{123} = B_{131} = B_{132} = 0. \end{aligned}$$

2.1.5.3 Orbital Reference Frame

The orbital reference frame is described by the triad RPQ , with the origin at the geocenter. This frame is illustrated in Figure 2.1-46.

The positive R axis points to the satellite, and is therefore along the local vertical at the satellite. The positive Q axis points along the orbital angular velocity vector. The positive P axis makes a right-handed system. If the orbit is circular, the positive P axis is along the satellite velocity vector.

The right ascension of the ascending node is Ω , the orbital inclination is i , and the orbital angular position relative to the ascending node is Y . When all of these angles are zero, R lies along X_I , P lies along Y_I , and Q lies along Z_I . The orbital frame is obtained from the inertial frame by a rotation Ω about Z_I , followed by a rotation i about the line of nodes, followed by a rotation Y about W .

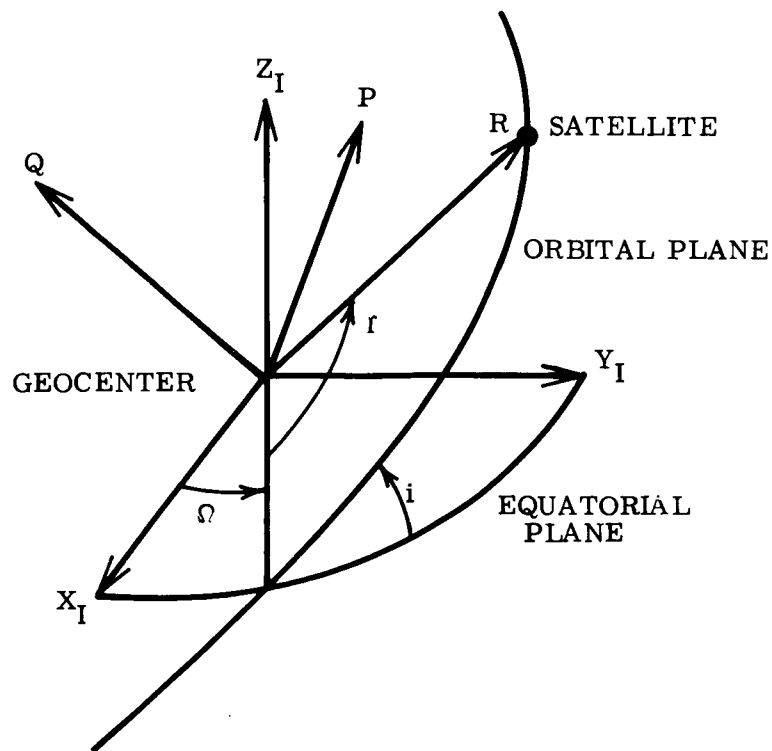


Figure 2.1-46. Orbital Reference Frame

The matrix of the transformation from the inertial frame to the orbital frame is B_2 ,

$$\begin{bmatrix} R \\ P \\ Q \end{bmatrix} = [B_2] \begin{bmatrix} X_I \\ Y_I \\ Z_I \end{bmatrix} .$$

The elements of the $[B_2]$ matrix are

$$B_{211} = \cos \Omega \cos Y - \sin \Omega \cos i \sin Y ,$$

$$B_{212} = \sin \Omega \cos Y + \cos \Omega \cos i \sin Y ,$$

$$B_{213} = \sin i \sin Y ,$$

$$B_{221} = -\cos \Omega \sin Y - \sin \Omega \cos i \cos Y ,$$

$$B_{222} = -\sin \Omega \sin Y + \cos \Omega \cos i \cos Y ,$$

$$B_{223} = \sin i \cos Y ,$$

$$B_{231} = \sin \Omega \sin i ,$$

$$B_{232} = -\cos \Omega \sin i ,$$

$$B_{233} = \cos i .$$

2.1.5.4 Satellite Body Reference Frame

The satellite body reference frame is described by the triad $X_1 Y_1 Z_1$, with the origin at a prescribed point, 0. This point is on the axis of the cylindrical body, at the nominal

center of mass, or in the plane of the interface with the booster, or other convenient point to be specified later. This frame is illustrated in Figure 2.1-47. The coordinates of the center of mass of the main body, in this frame, are X_{MM} , Y_{MM} , and Z_{MM} , as shown in Figure 2.1-48.

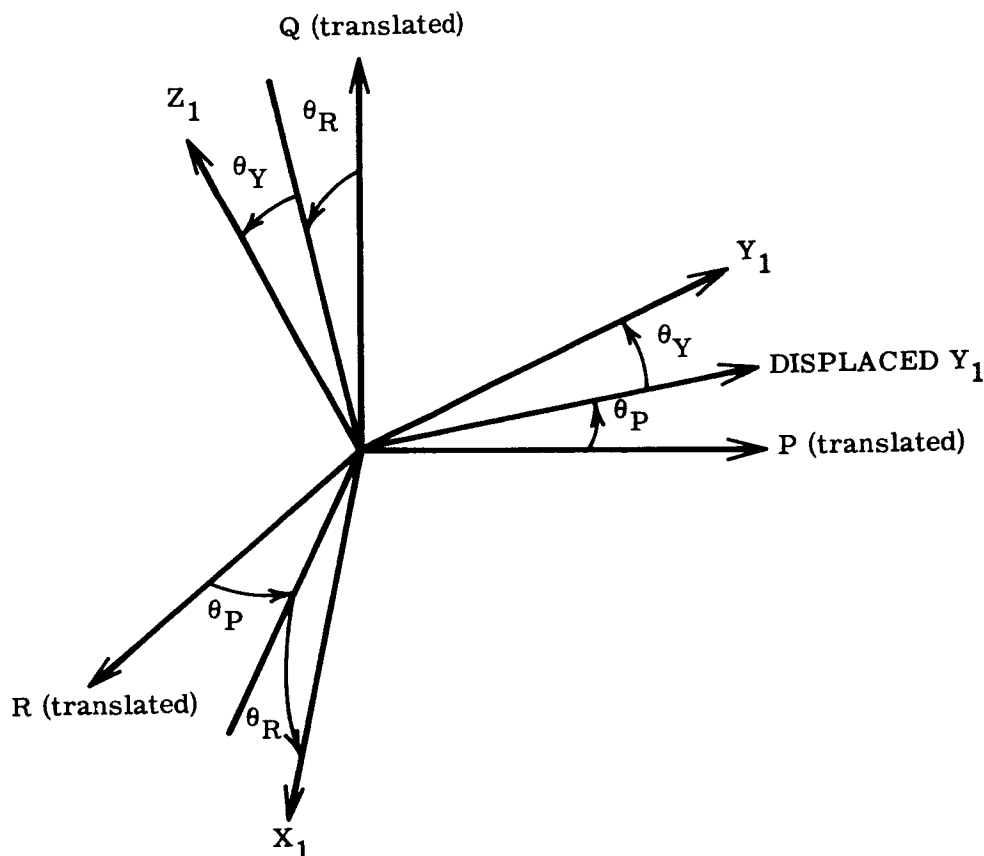


Figure 2.1-47. Satellite Body Reference Frame

The X_1 axis is along the nominal local vertical, and is positive upward. The Z_1 axis is the axis of the cylindrical body, and is positive in the direction away from the end where the solar panels are located. The positive Y_1 axis forms a right-handed system.

For zero attitude errors and zero yaw bias, X_1 is parallel to R , Y_1 is parallel to P , and Z_1 is parallel to Q . The satellite frame is obtained from the orbital frame by a translation without rotation from the geocenter to the satellite frame origin, followed by three rotations. The first is a rotation θ_P about the translated Q axis, the second is a rotation θ_R about the displaced Y_1 axis, and the third is a rotation θ_Y about the X_1 axis.

The matrix of the rotational transformation from the orbital frame to the satellite body frame is $[E_1]$,

$$\begin{bmatrix} X_1 \\ Y_1 \\ Z_1 \end{bmatrix} = [E_1] \begin{bmatrix} R \\ P \\ Q \end{bmatrix}.$$

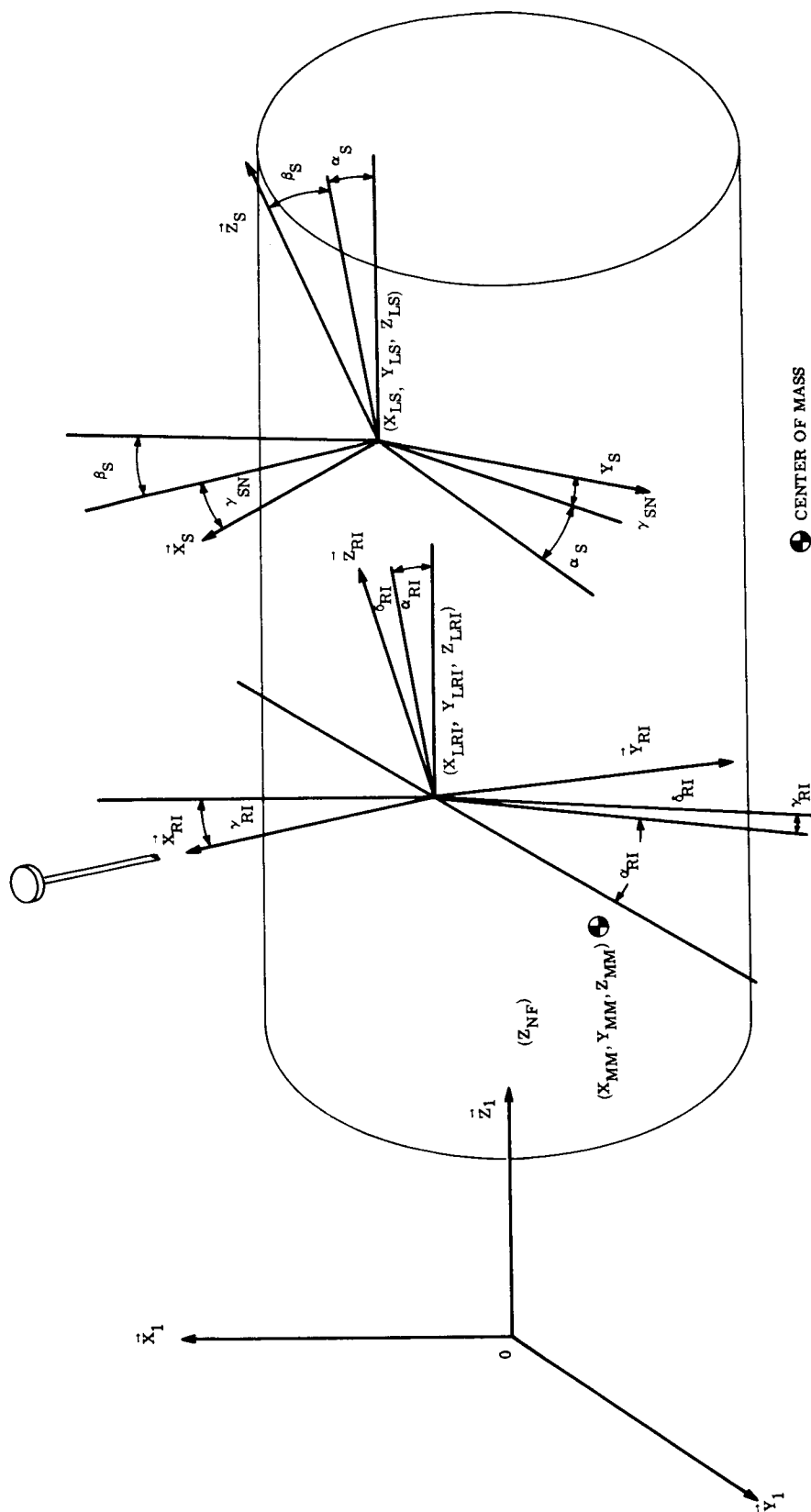


Figure 2.1-48. Satellite Main Body, Rod and Secondary Boom Reference Frames

The elements of the $[E_1]$ matrix are

$$\begin{aligned}
 E_{111} &= \cos \theta_P \cos \theta_R, \\
 E_{112} &= \sin \theta_P \cos \theta_R, \\
 E_{113} &= -\sin \theta_R, \\
 E_{121} &= \cos \theta_P \sin \theta_R \sin \theta_Y - \sin \theta_P \cos \theta_Y, \\
 E_{122} &= \sin \theta_P \sin \theta_R \sin \theta_Y + \cos \theta_P \cos \theta_Y, \\
 E_{123} &= \cos \theta_R \sin \theta_Y, \\
 E_{131} &= \cos \theta_P \sin \theta_R \cos \theta_Y + \sin \theta_P \sin \theta_Y, \\
 E_{132} &= \sin \theta_P \sin \theta_R \cos \theta_Y - \cos \theta_P \sin \theta_Y, \\
 E_{133} &= \cos \theta_R \cos \theta_Y.
 \end{aligned}$$

2.1.5.5 Secondary Boom Reference Frame

The secondary boom reference frame is described by the triad $X_S Y_S Z_S$, and illustrated in Figure 2.1-48. The origin of this frame is at the center of the hinge axis, and has the coordinates X_{LS} , Y_{LS} , and Z_{LS} , relative to 0.

The rotations α_S and β_S align the hinge axis, Z_S , as desired. The rotation γ_{SN} about the hinge axis aligns the secondary body in the position in which the restoring torque of the suspension is zero. The transverse axes X_S and Y_S form a right-handed system with Z_S . When all three Euler angles are zero, X_S is parallel to X_1 , etc.

The secondary boom frame is obtained from the satellite body frame by a translation without rotation from 0 to the center of the hinge axis, followed by three rotations. The first is a rotation α_S about the translated X_1 axis, the second is a rotation β_S about the displaced Y_S axis, and the third is a rotation γ_{SN} about the hinge axis, Z_S .

The matrix of the rotational transformation from the satellite body frame to the secondary boom frame is $[E_2]$,

$$\begin{bmatrix} X_S \\ Y_S \\ Z_S \end{bmatrix} = [E_2] \begin{bmatrix} X_1 \\ Y_1 \\ Z_1 \end{bmatrix}.$$

The elements of the $[E_2]$ matrix are

$$\begin{aligned}
 E_{211} &= \cos \beta_S \cos \gamma_{SN}, \\
 E_{212} &= \sin \alpha_S \sin \beta_S \cos \gamma_{SN} + \cos \alpha_S \sin \gamma_{SN}, \\
 E_{213} &= -\cos \alpha_S \sin \beta_S \cos \gamma_{SN} + \sin \alpha_S \sin \gamma_{SN}, \\
 E_{221} &= -\cos \beta_S \sin \gamma_{SN}, \\
 E_{222} &= -\sin \alpha_S \sin \beta_S \sin \gamma_{SN} + \cos \alpha_S \cos \gamma_{SN},
 \end{aligned}$$

$$E_{223} = \cos \alpha_S \sin \beta_S \sin \gamma_{SN} + \sin \alpha_S \cos \gamma_{SN},$$

$$E_{231} = \sin \beta_S,$$

$$E_{232} = -\sin \alpha_S \cos \beta_S,$$

$$E_{233} = \cos \alpha_S \cos \beta_S.$$

The matrix of the rotational transformation from the orbital frame to the secondary boom frame is $[E_3]$,

$$\begin{bmatrix} X_S \\ Y_S \\ Z_S \end{bmatrix} = [E_3] \begin{bmatrix} R \\ P \\ Q \end{bmatrix}.$$

The elements of the $[E_3]$ matrix are found from the matrix equation,

$$[E_3] = [E_2] [E_1].$$

The coordinates of the center of mass of the secondary boom assembly are X_{SM} , Y_{SM} , and Z_{SM} , in the secondary boom frame, as shown in Figure 2.1-49.

2.1.5.6 Gravity Gradient Rod Reference Frames (Rods Attached to Main Body)

The reference frame of the i th rod attached to the satellite body is described by the triad X_{RI} Y_{RI} Z_{RI} , and is illustrated in Figure 2.1-48. The origin of this frame is at the center of the base of the rod, and has the coordinates X_{LRI} , Y_{LRI} , and Z_{LRI} , relative to 0.

The X_{RI} axis lies along the rod axis (when it is straight), and is positive outward from the satellite body. The positive Y_{RI} axis is directed from the center of the rod radially outward along the bisector of the overlap (in the transverse plane at the base of the rod). The positive Z_{RI} axis forms a right-handed system.

The rotations α_{RI} and γ_{RI} align the (straight) rod axis, X_{RI} , as desired. The rotation δ_{RI} aligns the Y_{RI} axis along the overlap bisector. When all three Euler angles are zero, X_{RI} is parallel to X_1 , etc.

The i th rod frame is obtained from the satellite body frame by a translation without rotation from 0 to the center of the base of the rod, followed by three rotations. The first is a rotation α_{RI} about the translated X_1 axis, the second is a rotation γ_{RI} about the displaced Z_{RI} axis, and the third is a rotation δ_{RI} about the X_{RI} axis.

The matrix of the rotational transformation from the satellite body frame to the i th rod frame is $[R_I]$,

$$\begin{bmatrix} X_{RI} \\ Y_{RI} \\ Z_{RI} \end{bmatrix} = [R_I] \begin{bmatrix} X_1 \\ Y_1 \\ Z_1 \end{bmatrix}.$$

The elements of the $[R_I]$ matrix are

$$R_{I11} = \cos \gamma_{RI}$$

$$R_{I12} = \cos \alpha_{RI} \sin \gamma_{RI}$$

$$R_{I13} = \sin \alpha_{RI} \sin \gamma_{RI}$$

$$R_{I21} = -\sin \gamma_{RI} \cos \delta_{RI}$$

$$R_{I22} = \cos \alpha_{RI} \cos \gamma_{RI} \cos \delta_{RI} - \sin \alpha_{RI} \sin \delta_{RI}$$

$$R_{I23} = \sin \alpha_{RI} \cos \gamma_{RI} \cos \delta_{RI} + \cos \alpha_{RI} \sin \delta_{RI}$$

$$R_{I31} = \sin \gamma_{RI} \sin \delta_{RI}$$

$$R_{I32} = -\cos \alpha_{RI} \cos \gamma_{RI} \sin \delta_{RI} - \sin \alpha_{RI} \cos \delta_{RI}$$

$$R_{I33} = -\sin \alpha_{RI} \cos \gamma_{RI} \sin \delta_{RI} + \cos \alpha_{RI} \cos \delta_{RI}$$

The reference frames, translations, angles, and matrix elements for all four rods are similar. The equations are obtained by letting I take the values 1, 2, 3, and 4.

2.1.5.7 Gravity Gradient Rod Reference Frames (Rods Attached to Secondary Body)

The reference frame of the Jth rod attached to the secondary body is described by the triad X_{SRJ} Y_{SRJ} Z_{SRJ} , and is illustrated in Figure 2.1-49. The origin of this frame is at the center of the base of the rod, and has the coordinates X_{LSRJ} , Y_{LSRJ} , and Z_{LSRJ} in the secondary boom frame and relative to the origin of that frame.

The X_{SRJ} axis lies along the rod axis (when it is straight), and is positive outward from the secondary boom mounting. The positive Y_{SRJ} axis is directed from the center of the rod radially outward along the bisector of the overlap (in the transverse plane at the base of the rod). The positive Z_{SRJ} axis forms a right-handed system.

The rotations α_{SRJ} and γ_{SRJ} align the straight rod axis, X_{SRJ} , as desired. The rotation δ_{SRJ} aligns the Y_{SRJ} axis along the overlap bisector. When all three Euler angles are zero, X_{SRJ} is parallel to X_S , etc.

The Jth rod frame is obtained from the secondary boom frame by a translation without rotation from the origin of the secondary boom frame to the center of the base of the rod, followed by three rotations. The first is a rotation α_{SRJ} about the translated X_S axis, the second is a rotation γ_{SRJ} about the displaced Z_{SRJ} axis, and the third is a rotation δ_{SRJ} about the X_{SRJ} axis.

The matrix of the rotational transformation from the secondary boom frame to the Jth rod frame is $[S_J]$,

$$\begin{bmatrix} X_{SRJ} \\ Y_{SRJ} \\ Z_{SRJ} \end{bmatrix} = [S_J] \begin{bmatrix} X_S \\ Y_S \\ Z_S \end{bmatrix}.$$

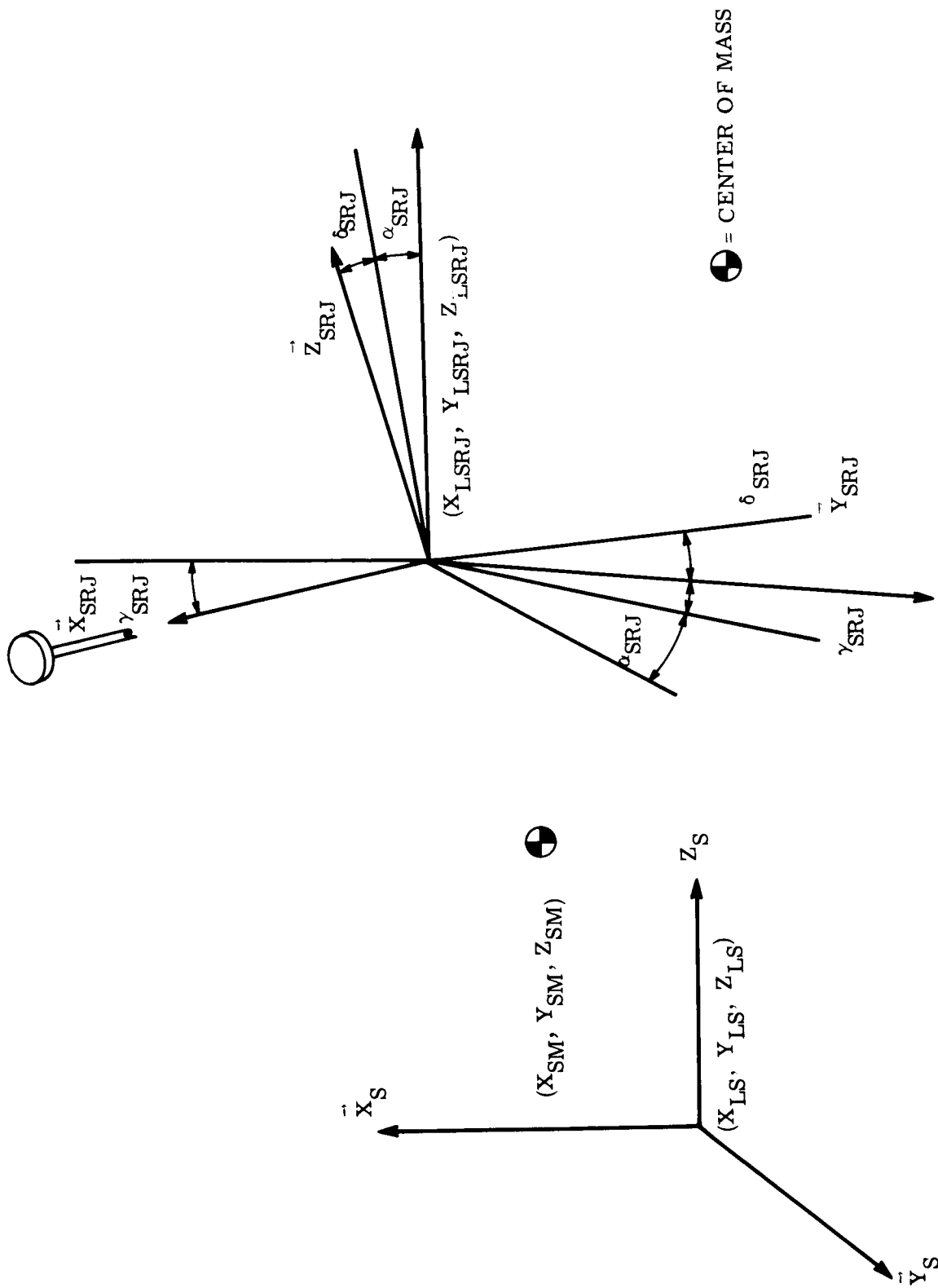


Figure 2.1-49. Rod Reference Frame (Secondary Body)

The elements of the $[S_J]$ matrix are

$$\begin{aligned}
 S_{J11} &= \cos \gamma_{SRJ}, \\
 S_{J12} &= \cos \alpha_{SRJ} \sin \gamma_{SRJ}, \\
 S_{J13} &= \sin \alpha_{SRJ} \sin \gamma_{SRJ}, \\
 S_{J21} &= -\sin \gamma_{SRJ} \cos \delta_{SRJ}, \\
 S_{J22} &= \cos \alpha_{SRJ} \cos \gamma_{SRJ} \cos \delta_{SRJ} - \sin \alpha_{SRJ} \sin \delta_{SRJ}, \\
 S_{J23} &= \sin \alpha_{SRJ} \cos \gamma_{SRJ} \cos \delta_{SRJ} + \cos \alpha_{SRJ} \sin \delta_{SRJ}, \\
 S_{J31} &= \sin \gamma_{SRJ} \sin \delta_{SRJ}, \\
 S_{J32} &= -\cos \alpha_{SRJ} \cos \gamma_{SRJ} \sin \delta_{SRJ} - \sin \alpha_{SRJ} \cos \delta_{SRJ}, \\
 S_{J33} &= -\sin \alpha_{SRJ} \cos \gamma_{SRJ} \sin \delta_{SRJ} + \cos \alpha_{SRJ} \cos \delta_{SRJ}.
 \end{aligned}$$

The reference frames, translations, angles, and matrix elements for both rods are similar. The equations are obtained by letting J take the values 1 and 2.

2.1.6 Boom Studies

2.1.6.1 Gravity Bending

The gravity bending of a rod attached to an orbiting spacecraft is analyzed. The attitude of the spacecraft and rod are assumed not to vary relative to the orbital frame (steady-state case); and there is a weight at the outer end of the rod. The end attached to the satellite is assumed, for simplicity, to coincide with the satellite center of mass. This point is assumed to follow a circular or elliptical point about the geocenter. The earth's gravitational field is assumed to follow an inverse square law, and have perfect spherical symmetry.

It is shown that, with the MAGGE configuration and altitude, the tip deflection is negligible if the orbit is circular. The general equation is given for the elliptical orbit, but no numerical results were obtained. It is believed that the results would not differ from those of the circular case for an orbit of small eccentricity.

Since the rod will be shown to be nearly straight, the gravity gradient effect is practically that due to the variation of the field along a straight line in space. The attitude of this line is expressed in the orbital reference frame, PQR, discussed in Section 2.1.3. X and Y axes are sufficient, as illustrated in Figure 2.1-50. The XY plane makes an angle ϕ with the RP plane, and the X axis makes an angle θ with the R axis. The unit vectors X and Y are

$$X = R \cos \theta + P \cos \phi \sin \theta + Q \sin \phi \sin \theta, \quad (1)$$

$$Y = -R \sin \theta + P \cos \phi \cos \theta + Q \sin \phi \cos \theta. \quad (2)$$

The velocities and accelerations of the unit vectors in the orbital frame are

$$\dot{R} = \omega_0 Q X R = P \omega_0, \quad (3)$$

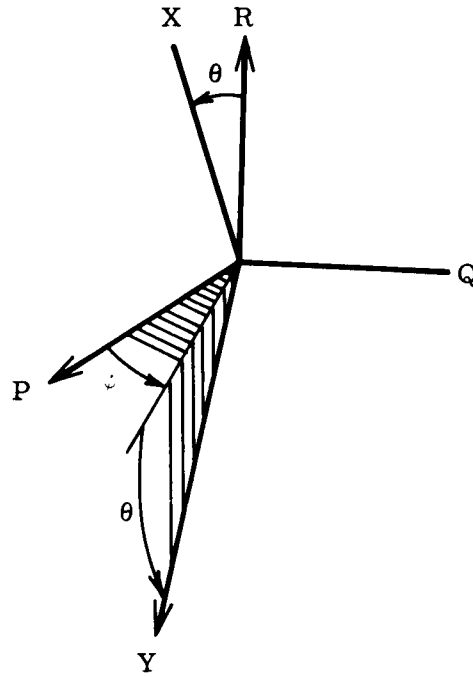


Figure 2.1-50. Reference Frames

$$\dot{P} = \omega_o Q \times P = -R \omega_o, \quad (4)$$

$$\dot{Q} = 0, \quad (5)$$

$$\begin{aligned} \ddot{R} &= \dot{P} \omega_o + P \dot{\omega}_o \\ &= -R \omega_o^2 + P \dot{\omega}_o, \end{aligned} \quad (6)$$

$$\begin{aligned} \ddot{P} &= -\dot{R} \omega_o - R \dot{\omega}_o \\ &= -P \omega_o^2 - R \dot{\omega}_o, \end{aligned} \quad (7)$$

$$\ddot{Q} = 0, \quad (8)$$

where ω_o is the orbital angular velocity and $\dot{\omega}_o$ is the orbital angular acceleration.

The effect of the earth's gravity is illustrated in Figure 2.1-51. The orbital radius is R_A , and RR_A is the vector from the geocenter to the center of mass of the satellite. A rod element has a mass

$$dm = \rho_m dl, \quad (9)$$

where ρ_m is the lineal mass density, and l is the distance from the satellite center of mass to the rod element. The vector distance is XL . The distance to the tip mass is L , the length of the rod, and this vector distance is XL .

The vector from the geocenter to the rod element is, as shown in Figure 2.1-51,

$$\begin{aligned} R_i &= RR_A + XL \\ &= R(R_A + l \cos \theta) + P l \cos \phi \sin \theta + Q l \sin \phi \sin \theta. \end{aligned} \quad (10)$$

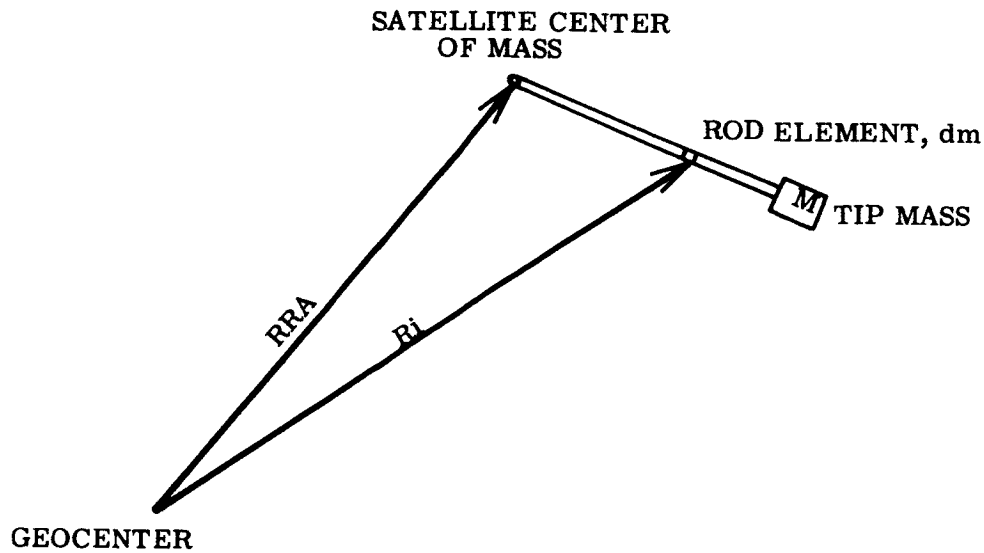


Figure 2.1-51. Gravity Acting on a Straight Rod With a Tip Weight

The vector from the geocenter to the tip weight is the same, with l replaced by L .

The velocity of the rod element is

$$\begin{aligned}\dot{\mathbf{R}}_i &= \dot{\mathbf{R}} (R_A + l \cos \theta) + R \dot{\mathbf{R}}_A + \dot{\mathbf{P}} l \cos \phi \sin \theta \\ &= R \dot{\mathbf{R}}_A + \omega_o \left[-R l \cos \phi \sin \theta + P (R_A + l \cos \theta) \right].\end{aligned}\quad (11)$$

The acceleration of the rod element is

$$\begin{aligned}\ddot{\mathbf{R}}_i &= \dot{\mathbf{R}} \dot{\mathbf{R}}_A + R \ddot{\mathbf{R}}_A + \dot{\omega}_o \left[-R l \cos \phi \sin \theta + P (R_A + l \cos \theta) \right] \\ &\quad + \omega_o \left[-\dot{\mathbf{R}} l \cos \phi \sin \theta + \dot{\mathbf{P}} (R_A + l \cos \theta) + P \dot{\mathbf{R}}_A \right] \\ &= 2 P \omega_o \dot{\mathbf{R}}_A + R \ddot{\mathbf{R}}_A + \dot{\omega}_o \left[-R l \cos \phi \sin \theta + P (R_A + l \cos \theta) \right] \\ &\quad + \omega_o^2 \left[-R (R_A + l \cos \theta) - P l \cos \phi \sin \theta \right].\end{aligned}\quad (12)$$

The velocity and acceleration of the tip mass are the same, except that l is replaced by L .

The gravity force on the rod element is

$$d F_i = - \frac{K d_m}{|R_i|^3} R_i = -R_i \frac{K \rho_m dl}{|R_i|^3}, \quad (13)$$

where K is the universal gravity constant multiplied by the mass of the earth.

The denominator in equation (13) may be approximated by the following procedure. From equation (10),

$$\begin{aligned}
 |R_i|^2 &= (R_A + l \cos \theta)^2 + l^2 \cos^2 \phi \sin^2 \theta \\
 &\quad + l^2 \sin^2 \phi \sin^2 \theta \\
 &= R_A^2 + 2l R_A \cos \theta + l^2 \\
 &= R_A^2 \left(1 + \frac{2l}{R_A} \cos \theta + \frac{l^2}{R_A^2} \right).
 \end{aligned} \tag{14}$$

From the relation,

$$(1+X)^{-3/2} = 1 - \frac{3}{2} X + \frac{15}{8} X^2 + \dots, \tag{15}$$

can be derived,

$$\frac{1}{|R_i|^3} = \frac{1}{R_A^3} \left(1 - \frac{3l}{R_A} \cos \theta + \text{higher-order terms} \right). \tag{16}$$

The higher-order terms in the ratio of l to R_A may be neglected because this ratio is small.

The gravity force on the rod element is then

$$\begin{aligned}
 dF_i &= -\omega_o^2 \rho_m dl \left(1 - \frac{3l}{R_A} \cos \theta \right) \left[R(R_A + l \cos \theta) \right. \\
 &\quad \left. + P l \cos \phi \sin \theta + Q l \sin \phi \sin \theta \right],
 \end{aligned} \tag{17}$$

since

$$\frac{K}{R_A^3} = \omega_o^2. \tag{18}$$

The net load on the rod element is the gravity force minus the product of its mass and acceleration,

$$\begin{aligned}
 dF &= \rho_m dl \left[R \left(3\omega_o^2 l \cos \theta - \ddot{R}_A + \dot{\omega}_o l \cos \phi \sin \theta \right) \right. \\
 &\quad + P \left(-2\omega_o \dot{R}_A - \dot{\omega}_o R_A + 3\omega_o^2 \frac{l^2}{R_A} \cos \phi \sin \theta \right) \\
 &\quad \left. - Q \omega_o^2 l \sin \phi \sin \theta \right].
 \end{aligned} \tag{19}$$

The equation for the gravity force on the tip mass is similar to equation (17),

$$\begin{aligned}
 F_m &= -\omega_o^2 M \left(1 - \frac{3L}{R_A} \cos \theta \right) \left[R(R_A + L \cos \theta) \right. \\
 &\quad \left. + P L \cos \phi \sin \theta + Q L \sin \phi \sin \theta \right].
 \end{aligned} \tag{20}$$

The net force is the gravity force minus the product of mass and acceleration,

$$F_N = M \left[R \left(3 \omega_o^2 L \cos \theta - \ddot{R}_A + \dot{\omega}_o L \cos \phi \sin \theta \right) + P \left(-2 \omega_o \dot{R}_A - \dot{\omega}_o R_A + 3 \omega_o^2 \frac{L^2}{R_A} \cos \phi \sin \theta \right) - Q \omega_o^2 L \sin \phi \sin \theta \right]. \quad (21)$$

In equations (19) and (21), higher-order terms in the ratio of l to R_A or of L to R_A have again been neglected. These equations are for the distributed and concentrated forces which load the rod. The transverse (Y) components load the rod as a cantil  ver beam. The axial (X) components would load it as a column, but since these are tensile forces, their effect on the deflection is neglected.

The transverse component of the distributed load is

$$d F_Y = \rho_m dl \left[-\omega_o^2 l \sin \theta \cos \theta (3 + \sin^2 \phi) + \ddot{R}_A \sin \theta - 2 \omega_o \dot{R}_A \cos \phi \cos \theta - \dot{\omega}_o R_A \cos \phi \cos \theta \right]. \quad (22)$$

The transverse component of the concentrated load is

$$F_{NY} = M \left[-\omega_o^2 L \sin \theta \cos \theta (3 + \sin^2 \phi) + \ddot{R}_A \sin \theta - 2 \omega_o \dot{R}_A \cos \phi \cos \theta - \dot{\omega}_o R_A \cos \phi \cos \theta \right]. \quad (23)$$

The distributed load is integrated with respect to length, with the boundary condition that the shear is $-F_{NY}$ at $l = L$,

$$F_Y = \rho_m \left[\frac{1}{2} \omega_o^2 \sin \theta \cos \theta (L^2 - l^2) (3 + \sin^2 \phi) + (L-l) \left(\dot{\omega}_o R_A \cos \phi \cos \theta + 2 \omega_o \dot{R}_A \cos \phi \cos \theta - \ddot{R}_A \sin \theta \right) \right] + M \left[\omega_o^2 L \sin \theta \cos \theta (3 + \sin^2 \phi) + \dot{\omega}_o R_A \cos \phi \cos \theta + 2 \omega_o \dot{R}_A \cos \phi \cos \theta - \ddot{R}_A \sin \theta \right]. \quad (24)$$

This transverse force is the derivative of the bending moment,

$$\frac{d M_B}{dl} = F_Y. \quad (25)$$

The bending moment at $l = L$ is that necessary to angularly accelerate the tip mass. The angular acceleration of this mass is

$$\ddot{\theta}_M = \dot{\omega}_o \sin \phi \cos \theta. \quad (26)$$

If its moment of inertia is I_M , then

$$M_B \Big|_{l=L} = -I_M \dot{\omega}_O \sin \phi \cos \theta. \quad (27)$$

The reason for the minus sign is that M_B is the reaction on the rod.

Integration of equation (25), using equation (27) as a boundary condition, yields the bending moment as a function of l :

$$\begin{aligned} M_B(l) = & \rho_m \left[\frac{1}{2} \omega_O^2 \sin \theta \cos \theta (3 + \sin^2 \phi) \left(L^2 l - \frac{1}{3} l^3 - \frac{2}{3} L^3 \right) \right. \\ & + \left(L l - \frac{1}{2} l^2 - \frac{1}{2} L^2 \right) \left(\dot{\omega}_O R_A \cos \phi \cos \theta + 2 \omega_O \dot{R}_A \cos \phi \cos \theta \right. \\ & \quad \left. \left. - \ddot{R}_A \sin \theta \right) \right] \\ & + M(1-L) \left[\omega_O^2 L \sin \theta \cos \theta (3 + \sin^2 \phi) \right. \\ & + \dot{\omega}_O R_A \cos \phi \cos \theta + 2 \omega_O \dot{R}_A \cos \phi \cos \theta - \ddot{R}_A \sin \theta \left. \right] \\ & - I_M \dot{\omega}_O \sin \phi \cos \theta. \end{aligned} \quad (28)$$

The second derivative of the deflection is the bending moment divided by the flexural rigidity, EI ,

$$\frac{d^2 y}{dl^2} = \frac{M_B l}{EI}. \quad (29)$$

The first derivative is obtained by integrating equation (28), and using the boundary condition that the slope is zero at the end where l is zero,

$$\begin{aligned} \frac{dy}{dl} = & \frac{1}{EI} \left\{ \rho_m \left[\frac{1}{2} \omega_O^2 \sin \theta \cos \theta (3 + \sin^2 \phi) \left(\frac{1}{2} L^2 l^2 - \frac{1}{12} l^4 - \frac{2}{3} L^3 l \right) \right. \right. \\ & + \left(\frac{1}{2} L l^2 - \frac{1}{6} l^3 - \frac{1}{2} L^2 l \right) \left(\dot{\omega}_O R_A \cos \phi \cos \theta \right. \\ & \quad \left. + 2 \omega_O \dot{R}_A \cos \phi \cos \theta - \ddot{R}_A \sin \theta \right) \left. \right] \\ & + M \left(\frac{1}{2} l^2 - L l \right) \left[\omega_O^2 L \sin \theta \cos \theta (3 + \sin^2 \phi) \right. \\ & \quad + \dot{\omega}_O R_A \left(\cos \phi \cos \theta + 2 \omega_O \dot{R}_A \cos \phi \cos \theta - \ddot{R}_A \sin \theta \right) \\ & \quad \left. \left. - I_M \dot{\omega}_O l \sin \phi \cos \theta \right] \right\}. \end{aligned} \quad (30)$$

The deflection is obtained by integrating equation (30), and using the boundary condition that the deflection is zero at the end where l is zero,

$$\begin{aligned}
 y(l) = \frac{1}{EI} \left\{ \rho_m \left[\frac{1}{2} \omega_o^2 \sin \theta \cos \theta (3 + \sin^2 \phi) \left(\frac{1}{6} L^2 l^3 - \frac{1}{60} l^5 - \frac{1}{3} L^3 l^2 \right) \right. \right. \\
 + \left(\frac{1}{6} L l^3 - \frac{1}{24} l^4 - \frac{1}{4} L^2 l^2 \right) \left(\dot{\omega}_o R_A \cos \phi \cos \theta \right. \\
 \left. \left. + 2 \omega_o \dot{R}_A \cos \phi \cos \theta - \ddot{R}_A \sin \theta \right) \right] \\
 + M \left(\frac{1}{6} l^3 - \frac{1}{2} L l^2 \right) \left[\omega_o^2 L \sin \theta \cos \theta (3 + \sin^2 \phi) \right. \\
 \left. + \dot{\omega}_o R_A \cos \phi \cos \theta + 2 \omega_o \dot{R}_A \cos \phi \cos \theta - \ddot{R}_A \sin \theta \right] \\
 \left. - \frac{1}{2} I_M \dot{\omega}_o l^2 \sin \phi \cos \theta \right\}. \quad (31)
 \end{aligned}$$

The maximum deflection, for any set of satellite and orbital parameters and attitude errors can be found from this equation. In particular, the tip deflection, if the satellite is in a circular orbit, is

$$y(L) = - \frac{\omega_o^2 L^4}{EI} \sin \theta \cos \theta \left(1 + \frac{1}{3} \sin^2 \phi \right) \left(M + \frac{11}{40} \rho_m L \right). \quad (32)$$

For a 6,000 nautical-mile orbit, ω_o is .000,273 radians per second. For a rod 100 feet long, the rod mass, $\rho_m L$, is 0.0465 slugs. The flexural rigidity, EI , is 13.0 pound-feet². With a two-pound tip mass, M is 0.062 slugs. If ϕ is 90 degrees and θ is 45 degrees, the tip deflection is 0.0285 feet (upward).

2.1.6.2 Thermal Bending

The initial work for the ATS program on Gravity Gradient Boom thermal bending has essentially consisted of coordination of results of a program being presently conducted for the NASA Ames Research Center under Contract No. NAS 2-1946. The program is now in its final stages and consists of three principal phases:

1. Thermal Analysis
2. Deflection Analysis
3. Experimental Verification

2.1.6.2.1 Thermal Analysis

Thermal analysis of the gravity gradient rod consists of a nodal point-to-point determination of temperature around the periphery of the rod and along its length. Figure 2.1-52 illustrates the nodes. The work effort considers only steady state temperatures and takes form in a digital computer program. Use of the digital program technique of analysis is most suitable to the configuration details of the rod and affords the means of attaining greatest analytical accuracy in the determination of temperature gradients.

With this method temperature profiles can be obtained for various overlap and twist rate configurations taking into consideration conduction and/or radiation heat exchange at the overlap areas.

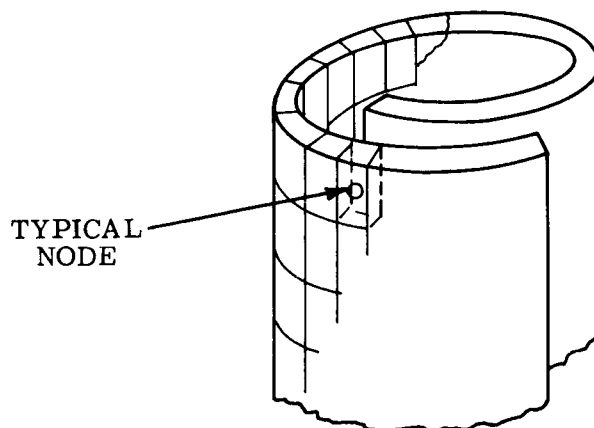


Figure 2.1-52. Nodes of Gravity Gradient Rod

The major portion of the program consists of a steady-state analysis taking a fixed orientation of the rod and a fixed angle of solar incidence with respect to the rod centerline. This work is performed with several given fixed sun angles with respect to the overlapped portion of the rod. An evaluation is performed to determine the effect of variance of the solar angle of incidence with respect to rod centerline on the bending of the gravity gradient rod. It is anticipated that the "changing angle" effect (as the rod bends away from the sun) will be insignificant with gravity gradient rods of practical length.

Preparation for the proposed analyses involves prior assessment of the inter-radiation effect at the internal surfaces of the rod. Accordingly, analyses are performed to evaluate the effect of internal radiation within the rod. Another preliminary task involves the determination of optimum node sizes to be used in the analyses. This is a straightforward task which essentially compares the effects of several node sizes. The selection of an optimum node size provides maximum accuracy for the planned analysis commensurate with efficient use of the computer program. Using the largest node size which still preserves accuracy reduces required levels of effort for the preparation of computer programs. The objective in optimizing node size is to permit the calculation of a smooth temperature profile over the surface of the rod.

A digital computer program is used for the thermal analysis because of its wide applicability, computational accuracy and inherent suitability to the rod structure. The nodal technique permits accurate determinations of temperature profiles by computing a thermal balance for each volumetric element (node) comprising the total rod structure. Presently, the Spacecraft Department of General Electric has a computer program which is capable of handling up to 1000 such nodal elements. The program has provisions for computing node to node conduction of heat as well as inter-radiation among the nodes. It also provides for the inclusion of absorbed surface heat flux, heat storage, inter-nodal surface conductance and internal heat generation (if applicable) in the thermal balance

calculations for each node. Radiation to space and to any fixed or varying temperature boundary is further provided. This digital program is capable of computing transient as well as steady state temperature distributions. In its existing form, the proposed computer program makes use of the linearized approach in computing radiation heat exchange.

The results of this phase of the program will be a set of steady-state temperatures for all the nodes of the given rod configurations and sets of external conditions. These temperature profiles will be used to determine mechanical behavior as discussed in paragraph 2.1.6.2.2.

Although it is recognized that the proposed approach does not yield the desired closed form solution, it is felt that it is the most realistic approach to the problem since a closed form solution could not be undertaken without making certain vital assumptions which might not have been strictly correct. By solving a set of problems which encompass the full range of significant variables, it is felt that we will be able to develop curves which describe the dependence of the thermal bending on these variables. It is also possible that curve fitting techniques might yield "closed form type" expressions for temperature profile. It is also possible that in future attempts at a closed form solution we might be able to mold our assumptions according to what will have been determined to be correct by the node-to-node solution.

2.1.6.2.2 Deflection Analysis

It is anticipated that the thermal profiles resulting from the effort described in paragraph 2.1.6.2.1 will demonstrate little if any symmetry and will vary along the length of the rod as the overlap "seam" rotates with respect to the sun vector. The mechanical picture is further complicated by the fact that the overlap creates the probability that two elements at different temperatures will exist at the same location on the circumference (peripheral angle with respect to sun vector).

It is evident that with temperature profiles as described above, the net result will be bending about two mutually perpendicular axes (the magnitude of this bending will vary over the length of the rod due to the helical overlap) and distortion of the individual nodal sections and the buildup of internal stresses where bending deformation cannot completely accommodate the thermally induced strains.

The program for solving the thermal deformation/stress problem is as follows:

1. Initial Evaluation - The temperature inputs will be used to plot a temperature profile around the periphery of each differential increment of tube length. These temperature profiles will be used to develop a description of the strain states by multiplying by the pertinent α T's. By integrating deformation over the length of the rod, the deflected shape can be defined. It should be noted that this approach does not account for the internal stress created by the probable non-uniform variation of temperature. We must, therefore, carefully assume some idealized temperature distribution (approximating the actual temperature distribution) which would be likely to create a stress-free state of the rod. This would leave small unaccounted for deviations from the actual temperature distributions. These deviations would be representative of the residual stresses

that would exist in the rod after thermal bending. If the effective temperature profiles had been judiciously assumed, these stress patterns would result in zero equivalent external loads and would not significantly alter the direction and magnitude of the thermal deflection.

2. Detail Evaluation - If the actual temperature profiles vary drastically from those which create a stress-free state of the rod, a more rigorous analysis will have to be performed. In this approach, each individual temperature node will be considered as being held at its boundaries by stresses (magnitude $E\alpha T$) which constrains its shape to remain constant. The beam stiffness equations for the rod will be written and solved simultaneously with node boundary stress equations (above) for the condition of zero external loads. This solution will yield thermal deflection and residual stresses.

The results of the above studies will be presented in parametric form together with recommendations of techniques which will eliminate or minimize out-of-plane deflection.

2.1.6.2.3 Experimental Verification

In this phase of the proposed program, beryllium-copper rods, approximately eight feet long, will be tested in a smaller chamber.

These rod specimens will be tested with the sun vector at various angles around the circumference of the rod. In this way the effect of the sun's angular traverse with respect to the overlap edge may be evaluated. An advantage to the use of the straight overlap is that the effect of a particular overlap/sun angle is amplified by allowing the resulting deflection to act over the entire length of the specimen. In this manner we can establish the accuracy with which the analysis can predict the deflection mode of the rod for all possible overlap/sun angles. Integration of the effect of changing overlap/sun angle over the length of the rod (as is caused by twisting) will be a fairly simple analytical task.

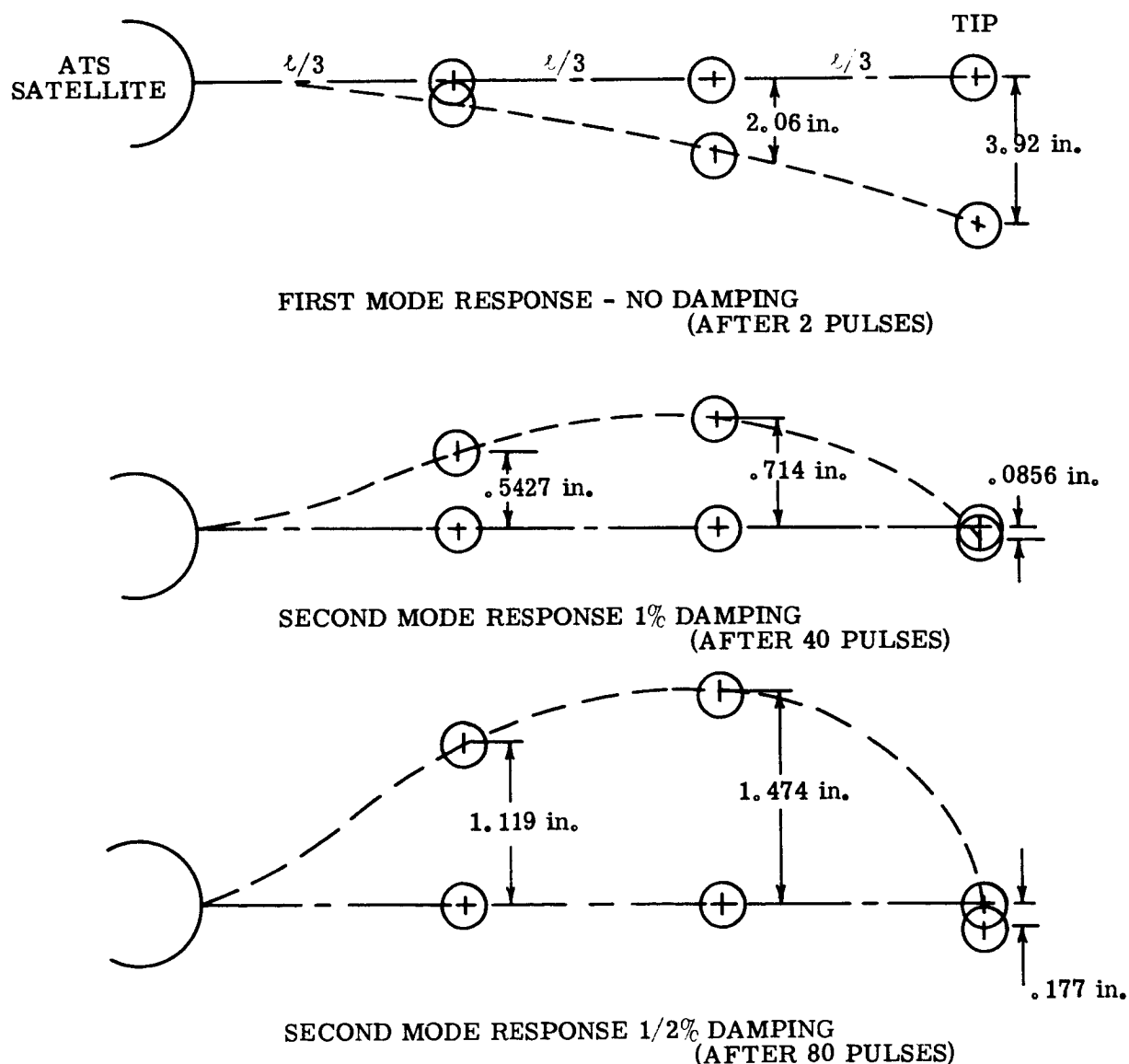
2.1.6.3 Boom Dynamic Response

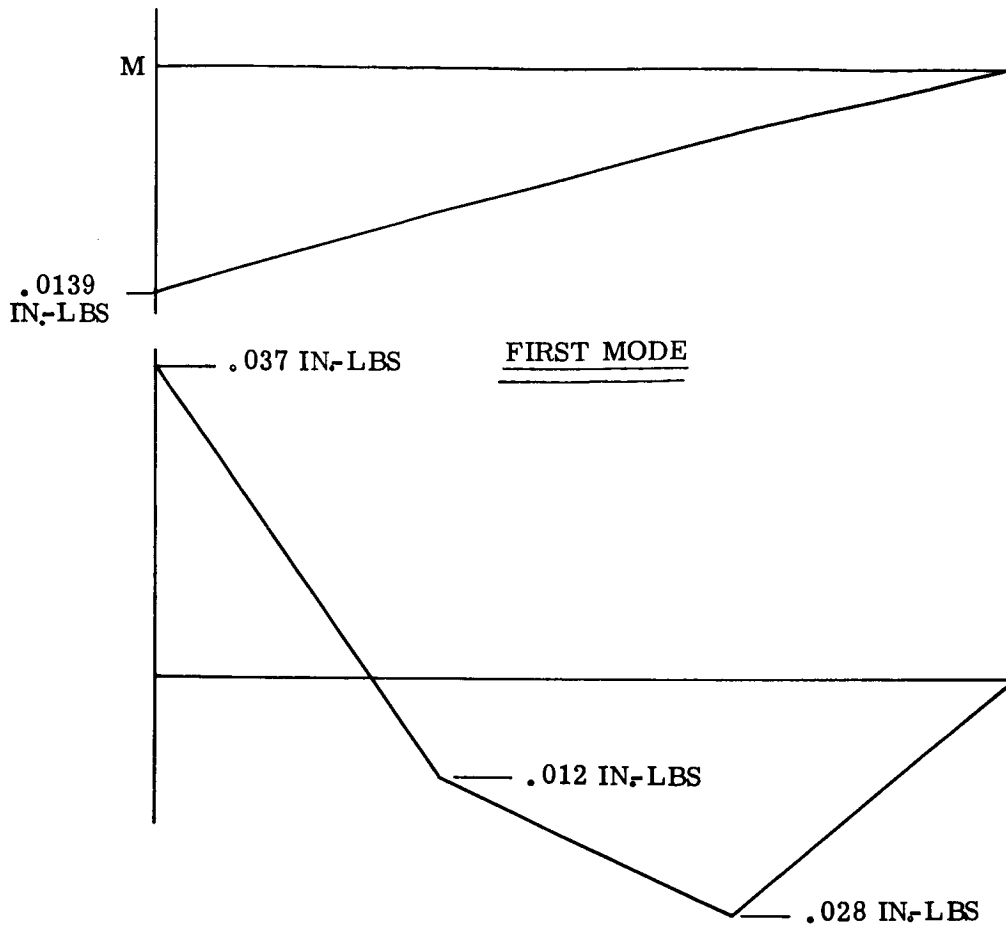
An investigation was performed to evaluate the effects on the rods of the impulse associated with the orbit eccentricity maneuver. The analysis is based on a simplified four-degree of freedom model consisting of the satellite and a 3-mass representation of the rod. The rods are assumed to be straight and only transverse vibratory modes are considered. The method of analysis consisted of developing the equations of vibration in normal coordinates and studying the response of each mode as a single degree of freedom system subjected to a series of pulses.

When no damping is considered, it was found that response of the second mode is high. The inclusion of a small amount of viscous damping, however, greatly reduces the expected response and two values are chosen to determine the excursions of this mode. It is also assumed that the periods of vibration approach the closest multiple or sub-multiple of the pulse period of 80 seconds and the pulse is assumed to be an average of

Mode	T Calculated (milliseconds)	T Assumed (milliseconds)
1	292	320
2	23.7	26.6

Preliminary investigations of rods with initial curvature indicate that the stiffness of the rod in the longitudinal direction is strongly dependent on the amount of initial tip





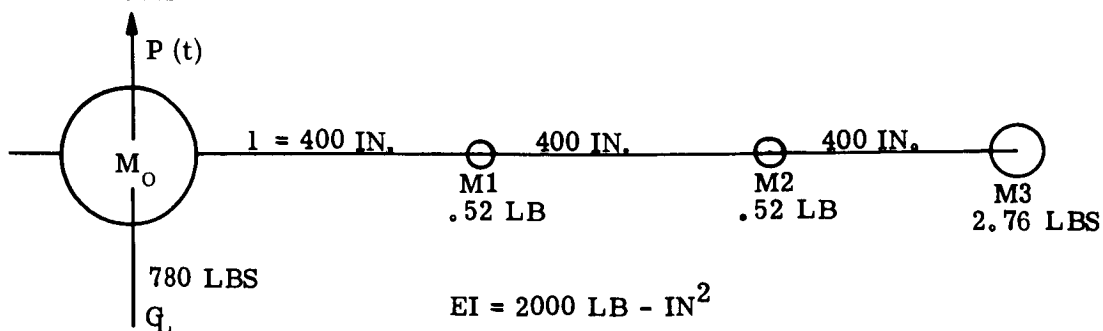
$$f_{\max} \approx \frac{M}{\pi R^2 t} = \frac{.037}{\pi (1/4)^2 (.002)} = 94 \text{ psi}$$

Figure 2.1-54. Bending Moment Diagrams

mass eccentricity. The longitudinal stiffness drops very rapidly for comparatively small tip eccentricities, from its initial value of a perfectly straight rod. The longitudinal stiffness appears to vary inversely as the square of the tip eccentricity and the coupling terms between the longitudinal and transverse stiffness factors vary inversely as the tip eccentricity and become quite significant for tip eccentricities of over five feet.

It is planned to study the problem of coupled transverse and longitudinal response of the booms using the non linearity effects discussed.

Analytical Model (Sym about centerline)



$$(1) \quad |K - \rho^2 M| X| = 0$$

Stiffness Matrix

$$K = \begin{vmatrix} 7.75 & -11.5 & 4.5 & -.75 \\ -11.5 & 20 & -11.5 & 3 \\ 4.5 & -11.5 & 11 & -4 \\ -.75 & 3 & -4 & 1.75 \end{vmatrix} \quad \frac{3 EI}{l^3 (3.25)}$$

Mass Matrix

$$M = \begin{vmatrix} 780 & & & \\ & .52 & & \\ & & .52 & \\ & & & 2.76 \end{vmatrix} \quad \frac{1}{386}$$

Solving (1) by Matrix Iteration:

$$p^2 = \begin{vmatrix} 0 & & & \\ & 4.6 \times 10^{-4} & & \\ & & 7 \times 10^{-2} & \\ & & & .600 \end{vmatrix} \quad \text{rad}^2/\text{sec}^2$$

Eigenvectors are

$$X = \begin{vmatrix} 1 & -.0265 & -.00619 & -.00887 \\ 1 & 1.000 & 6.30 & 25.5 \\ 1 & 3.47 & 8.30 & -17.5 \\ 1 & 6.66 & -1 & 1 \end{vmatrix}$$

Periods of Vibration

$$T_0 = \infty$$

$$T_1 = 292 \text{ sec.}$$

$$T_2 = 23.7 \text{ sec.}$$

$$T_3 = 8.1 \text{ sec.}$$

Normalized Eigenvectors ($X^T M X = 1$)

$$N = \begin{vmatrix} .702 & -.0457 & .01578 & -.0078 \\ .702 & 1.7235 & -16.065 & 22.47 \\ .702 & 5.986 & -21.165 & -15.4 \\ .702 & 11.49 & 2.55 & .881 \end{vmatrix}$$

Equations of Forced Vibration in Normal Coordinates

$$\ddot{\xi} + P^2 \xi = N^T P$$

$$P = \begin{matrix} F(t) \\ 0 \\ 0 \\ 0 \end{matrix}$$

$$\ddot{\xi}_0 = .702 P(t) \quad (\text{Rigid Body Mode})$$

$$(2) \quad \begin{aligned} \ddot{\xi}_1 + P_1^2 \xi_1 &= -.0457 P(t) \\ \ddot{\xi}_2 + P_2^2 \xi_2 &= .01578 P(t) \\ \ddot{\xi}_3 + P_3^2 \xi_3 &= -.0078 P(t) \end{aligned}$$

Equations (2) can be treated as a series single degree of freedom systems. The resultant motion will be the sum of the four, and can be transformed back to the "X" coordinate system by the following transformation

$$|X| = |N| |\xi|$$

The expression for the response of an undamped single degree of freedom system due to a series of impulsive loads can be expressed as: (Reference 2)

$$(3) \quad q(t_1) = \frac{2F}{p^2} \sin p \frac{\Delta}{2} \left[\sin p \left(t_1 - \frac{\Delta}{2}\right) + \sin p \left(t_1 - \tau - \frac{\Delta}{2}\right) + \sin \left(t_1 - 2\tau - \frac{\Delta}{2}\right) + \dots \right]$$

where

$$\begin{aligned} F &= \text{force/mass} \\ p &= \text{circular frequency} \\ \Delta &= \text{pulse width} \\ \tau &= \text{pulse separation} \end{aligned}$$

Since ΔP and Δ will be small equation (3) reduces to

$$(4) \quad q(t_1) = \frac{F}{P} \Delta \left[\sin p t_1 + \sin p (t_1 - \tau) + \sin p (t_1 - 2\tau) + \dots \right]$$

If viscous damping is included the following equation will govern for a single pulse: (Reference 2)

$$(5) \quad q(t_1) = \frac{1}{P} \int_0^{t_1} F e^{-\eta(t_1-t)} \sin p(t_1-t) dt$$

$$\eta = \eta p$$

where η is critical viscous damping ratio

$F = \text{constant for } 0 < t < \Delta$

Substituting in (5) and integrating

$$(6) \quad q(t_1) = F e^{-n(t_1 - \Delta)} \left[2 \sin p \frac{\Delta}{2} \frac{\left\{ \eta \cos p \left(t_1 + \frac{\Delta}{2}\right) + p \sin \left(t_1 - \frac{\Delta}{2}\right) \right\}}{\eta^2 + p^2} \right]$$

For a series of pulses spaced at τ seconds and Δ and P small, equation (6) reduces to:

$$(7) \quad \boxed{q(t_1) = \sum_k e^{-n[t_1 - (k-1)\tau]} \left[\frac{F}{P} \Delta \right] \left[\sin p \left(t_1 - (k-1)\tau\right) \right]}$$

$k = \text{number of pulses}$

Response of First Mode (Equation 4)

$$F = .0457 \quad \Delta = .32$$

$$P = \frac{2\pi}{320} \quad \eta = 0$$

$$\frac{F\Delta}{P} = .75$$

$$\xi_1 = .75 \left[\sin \frac{2\pi}{320} t_1 + \sin \left(\frac{2\pi}{320} t_1 - \frac{\pi}{2} \right) + \sin \left(\frac{2\pi}{320} t_1 - \frac{3\pi}{2} \right) \right. \\ \left. + \sin \left(\frac{2\pi}{320} t_1 - 2\pi \right) \right]$$

$$240 < t_1 < 320$$

It can be seen that ξ_1 is periodic with $T = 320$ seconds. The maximum value of the sine series will be equal to the $\sqrt{2}$ when $t_1 = 160$ seconds. Therefore,

$$\xi_1 = (.75)\sqrt{2} = 1.06$$

$$X = N \xi_1 \sin 19^\circ = \begin{vmatrix} -.015 \\ .59 \\ 2.06 \\ 3.92 \end{vmatrix}$$

Response of Second Mode (Equation 7)

- a) 1% viscous damping
- b) 1/2% viscous damping

$$F = .01578 \quad P = \frac{2\pi}{66.6} = \frac{6\pi}{80} \quad \Delta = .32$$

$$n = \eta (.235)$$

$$\frac{F\Delta}{P} = .0214$$

$$\xi_2 = \sum_k (.0214) \left(e^{-.235 \eta [t_1 - (k-1)80]} \right) \left[\sin \frac{6\pi}{80} t_1 - (k-1) 6\pi \right]$$

$$\xi_2 = .0214 \sum_k \left(e^{-.235 \eta [t_1 - (k-1)80]} \right) \left[\sin \frac{6\pi}{80} - (k-1) 6 \pi \right]$$

a) For $\eta = 1\%$

$$\xi_2 \rightarrow .105 \quad \text{After 40 pulses}$$

b) For $\eta = 1/2\%$

$$\xi_2 \rightarrow .214 \quad \text{After 80 pulses}$$

$$X = N \xi_2 \sin 19^\circ$$

$$X = \begin{bmatrix} .00485 \\ -.5427 \\ -.714 \\ .0856 \end{bmatrix} \quad \text{for } \eta = 1\% \quad \& \quad = \begin{bmatrix} .001 \\ -1.119 \\ -1.474 \\ .177 \end{bmatrix} \quad \text{for } \eta = \frac{1}{2} \%$$

A computer study of the response of the gravity gradient rod to orbit eccentricity pulses has also been made.

The rod has been represented as a beam having an EI of 1800 lb-in.² with a mass of 2.5 pounds and 2.34 lb-in.² of rotational inertia at one end. The weight of the rod was taken as 1/4 ounce per foot. The rods were considered fixed to the vehicle body (i. e. no flexibility in mounting was considered), coordinates at the vehicle body are common with the end coordinates of the rod. The vehicle is considered rigid.

The analysis performed to date ignores axial loads in the rods and lack of initial straightness. Bending is considered in a single plane so that torsional effects are ignored. Only translational coordinates have been included for the body.

The rods were divided into six segments and a stiffness matrix written for each element. A consistent mass matrix (a full four-by-four matrix) was constructed. The six individual elements were assembled into a 13-degree of freedom system (a translation and rotation between each pair of elements and at the end mass, and a translation of the center body). The first six mode shapes and frequencies are shown in Table 2.1-5.

These mode shapes are normalized to a generalized mass of 1. The corresponding generalized stiffnesses are:

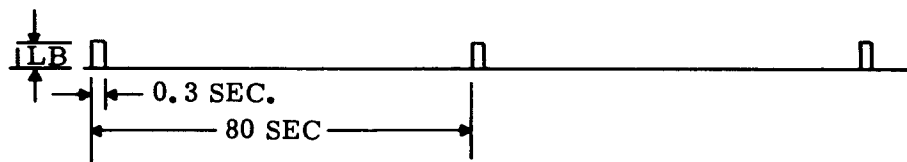
<u>Frequency, CPS</u>	<u>Generalized Stiffness</u>
0	0
.00324	.000428
.0407	.0655
.129	.658
.269	2.85
.462	8.45

TABLE 2.1-5. MODE SHAPES

Frequency, CPS		0	.00329	.0407	.129	.269	.462
Deflection } STA 1200	(end mass)	1.469	11.5	- 3.05	1.74	1.13	-.26
Rotation } 0		0	.0145	- .080	.014	.020	-.26
Deflection } STA 1000		1.469	8.63	12.05	-19.93	-22.17	18.26
Rotation } 0		0	.0141	- .066	.055	.020	.15
Deflection } STA 800		1.469	5.91	21.66	-15.85	5.50	-22.06
Rotation } 0		0	.0130	- .027	- .091	- 1.85	.068
Deflection } STA 600		1.469	3.49	22.54	8.61	20.72	8.60
Rotation } 0		0	.0110	.0180	- .125	.072	- .234
Deflection } STA 400		1.469	1.56	15.46	23.68	-11.61	11.34
Rotation } 0		0	.0082	.049	- .010	.171	.221
Deflection } STA 200		1.469	.267	5.30	13.40	-20.71	-24.45
Rotation } 0		0	.0045	.046	.093	- .091	- .013
Deflection } STA 0	(Vehicle Body)	1.469	- .201	- .070	- .039	.027	- .021
Rotation } 0		0	0	0	0	0	0

The response to orbit eccentricity pulse was calculated by obtaining the LaPlace transform of the pulse in modal coordinates and solving each modal response equation. The inverse transformation yields the modal response which is transformed once more to the physical coordinate set. One percent of critical viscous damping was assumed in all modes.

The excitation applied was a pulse of one-pound for 0.3 sec parallel with the vehicle axis. The pulse was repeated at 80-second intervals.



Computations were carried out for 31 pulses.

Maximum excursion of the end mass occurred just after the second pulse. Figure 2.1-55 shows the motion of the end mass, relative to the vehicle body, through three pulses.

The simplified analyses performed to date are useful to give a general indication of the magnitude of the problem of tuning; however, with regard to actual design process gives a trivial result. Representation of the rods disregarding the deviation from straightness, the actual behavior of the rod (assumed as a tube with shear continuity) and especially

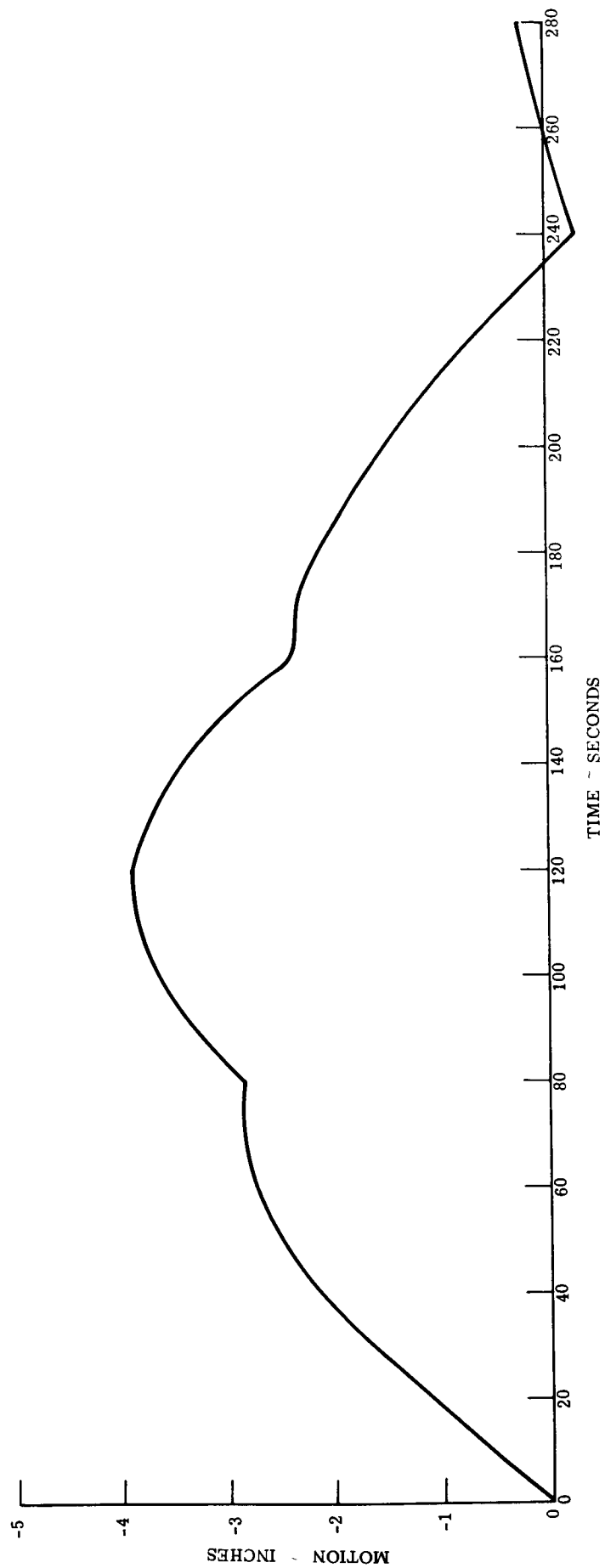


Figure 2.1-55. Motion of Tip Mass Relative to Vehicle Body

the axial load (the major component of the applied force is along the axis of the rod rather than transverse) has ignored the areas of primary significance in actual design of the rod and in determination of its behavior. Primary effort is presently devoted to the development of an improved representation of the behavior of the actual rod under flexural load and to incorporate the (beam column) effects of axial load in the response determination.

2.1.7 Mass Properties Data

The following tables represent the Mass Properties of the Medium Altitude Gravity Gradient Experiment as of October 12, 1964. The dimensions given in Table 2.1-6 represent the smallest rectangular shape that can enclose the packaging excluding connectors and mounting provisions. The weight given for each package includes the bracketry necessary to mount the package in the vehicles. At this time the package center of gravity is assumed to be coincident with the volume centroid. The tentative item list (Table 2.1-7) represents packages which are not in the original work scope but could possibly be added as a future requirement.

Tables 2.1-8A and 2.1-8B represent the sequenced mass moments of inertia of the Damper and Damper Booms Package and the X-Boom Packages respectively. It must be noted that the inertias in Table 2.1-8A represent the inertias of the Damper and Damper Booms only and Table 2.1-8B the inertias of the X-Boom Packages only. The contribution of the vehicle body is not included in these tables.

TABLE 2.1-6. MEDIUM ALTITUDE GRAVITY GRADIENT
EXPERIMENT WEIGHTS AND VOLUMES

PACKAGE	WEIGHT (LBS)	DIMENSIONS (IN.)
No. 1 X-Boom Package	28.1	8.0 x 9.8 x 20.6
No. 2 X-Boom Package	28.1	8.0 x 9.8 x 20.6
Damper and Damper Boom	23.1	10.1 x 10.1 x 16.2
R. F. Attitude Sensor	10.4	6.0 x 6.0 x 6.0
No. 1 Earth Sensor	5.5	5.4 x 5.4 x 6.0
No. 2 Earth Sensor	5.5	5.4 x 5.4 x 6.0
Sun Sensors (5)	1.3	0.9 x 3.1 x 2.8 (Each)
Sun Sensor Electronics	4.0	3.8 x 4.5 x 7.8
No. 1 T.V. Camera	5.0	2.5 x 2.5 x 11.0
No. 2 T.V. Camera	5.0	2.5 x 2.5 x 11.0
No. 1 T.V. Electronics	7.0	3.8 x 5.0 x 7.0
No. 2 T.V. Electronics	7.0	3.8 x 5.0 x 7.0
Power Control Unit	20.0	5.0 x 10.0 x 10.0
Diagnostic Sensors	5.0	—
Harness	6.0	—
TOTAL CURRENT WEIGHT	161.0 LBS	

TABLE 2.1-7. MEDIUM ALTITUDE GRAVITY GRADIENT
EXPERIMENT TENTATIVE ITEMS WEIGHT SUMMARY

PACKAGE	WEIGHT (LBS)	DIMENSIONS (IN.)
Magnetometer Sensor	1.0	2.8 x 3.1 x 4.7
Magnetometer Electronics	2.3	3.0 x 5.5 x 6.5
Center of Pressure Relocation Boom	3.5	4.0 x 4.0 x 8.0
Magnetic Torquing Coil No. 1	0.3	1.2 x 1.2 x 2.1
Magnetic Torquing Coil No. 2	0.3	1.2 x 1.2 x 2.1
Magnetic Torquing Coil No. 3	0.3	1.2 x 1.2 x 2.1
Magnetic Torquing Control	0.3	1.2 x 1.2 x 2.1
TOTAL TENTATIVE PACKAGES	8.0 LBS	

TABLES 2.1-8A&B. SEQUENCED MASS PROPERTY DATA

Sequence Number	Description	Weight (lbs.)	Center of Gravity (In. From Ref. Datum)			Mass Moments of Inertia (Slug-Ft. 2)		
			X*	L*	Y*	I _L **	I _L **	I _Y **
	TABLE 2.1-8A. DAMPER AND DAMPER BOOM PACKAGES.							
1	Booms Stowed	23.1	0	6.8	-22.4	3.8	2.6	1.2
2	Booms Deployed in L-Y Plane	23.1	0	6.8	-22.4	279.2	154.1	125.2
3	Booms Deployed @ 45° to L-Y Plane	23.1	0	6.8	-22.4	141.6	155.8	141.0

	TABLE 2.1-8B. X-BOOM PACKAGES (NO. 1 + NO. 2).							
1	Booms Stowed	56.2	0	22.5	0	5.7	6.0	0.5
2	Booms Deployed @ 19°	56.2	0	22.5	0	457	3822	3469
3	@ 31°	56.2	0	22.5	0	1084	3774	2936
4	@ 25°	56.2	0	22.5	0	718	3801	3226
5	@ 15°	56.2	0	22.5	0	294	3831	3599
6	@ 11°	56.2	0	22.5	0	168	3836	3702

*Denotes Vehicle Axes, L is in Vehicle Station with L = 0 at Spacecraft Separation Plane

**Taken about set of axes passing through vehicle center of gravity and parallel to vehicle axes (Vehicle Center of Gravity of L = 22.5, X = 0, Y = 0).

2.2 Boom Subsystem:

The boom subsystem of the ATS Spacecraft consists of the four primary gravity-gradient booms, the mechanism required for extension and scissoring of the primary booms, and the two damper booms including the canister for storage and ejection of the damper booms.

2.2.1 Design and Analysis

2.2.1.1 Design Concept Selection

The basic requirements for the boom subsystem are as follows:

1. Provide a set of four erectable booms which can be stowed within the confines of the ATS Spacecraft during launch, and then deployed to a length of 100 feet each in an "X" configuration about the Spacecraft, carrying weights at the boom tips in order to achieve a prescribed set of inertias about the three principal axes of the Spacecraft.
2. Provide a means of retracting these rods on command to desired lengths less than 100 feet each.
3. Provide a means of changing the angles included between the booms in a manner that maintains a symmetrical configuration about the satellite yaw axis. This action, which is limited to a total of 20 degrees on each boom, is generally referred to as scissoring.
4. Provide a set of two damper borne booms which will each extend to a length of 45 feet along the same straight line in opposite directions. These booms are to carry tip masses to their ends which will provide the proper inertia for the operation of the damper. After initial deployment, no mechanical connection or wiring is to extend from the damper boom platform to the spacecraft body. The damper booms are not required to retract.
5. Accomplish the above within the tolerance/disturbance constraints of the gravity-gradient stabilization system performance requirements.

The basic extendible boom selected for this mission is the Storable Tubular Extendible Member (STEM) developed by the DeHavilland Aircraft of Canada, Limited. This technique involves the formation of a tubular section from a flat metal strip which is formed and heat-tested in the tubular form then flattened under stress and wound onto a storage drum. Subsequent erection in orbit is accomplished by paying out the stowed strip through a set of guides which allow the boom to form into its natural tubular shape. The edges of the metal strip overlap each other to render stiffness to the operating section. Storage/erection units for the STEM tubing are of both motorized and self-erecting type. The motorized type employs a motor to drive the storage drum and thereby provide a means of retracting the extended booms. The self-erecting type units use the strain energy in the stowed metal strip to rotate the storage drum and erect the boom.

Motorized units were selected for the primary booms due to the requirement to retract. Self-erecting units were selected for the secondary (damper) booms.

Initial considerations for the scissoring mechanism included several which provided mechanical coordination of the motion of all four primary booms. Design studies included versions using bull gears, pulley systems, bellcrank linkages, and jackscrews. However, the constraints imposed by spacecraft size and other equipment in the boom mounting area proved the mechanical connection of all booms to be impractical. An

evaluation of the coordination required between booms for both extension and scissoring showed that a system which depended on electrical synchronization was not impractical. Accordingly, the following system was devised:

1. The four boom units are divided into two pairs.
2. The two units making-up each pair are mounted as close as possible to one another and are coupled by a bell-crank linkage to transmit scissoring motion and a gear train to coordinate extension drum drive.
3. Each pair of units is provided with one motor for extension and one motor for scissoring. The motors are encased in a hermetically sealed container to preserve their useful life in space, torque being delivered through a flexible membrain.
4. The two units of each pair, their drive train, motor, and scissoring linkage are all mounted with a single framework. Extension units are pivoted to this framework.
5. Motion between the two pairs of units is coordinated electrically.

Initially if the units were paired such that a pair of units would be at each end of the satellite yaw axes since this appeared to yield the most compact packages. See Figure 2.2-1, View A.

However, it was learned that the space at the earth-pointed end of the yaw axes was at a premium for all earth pointing experiments. Accordingly, a side mounted pairing of the units was devised to remove the boom packages from the area prescribed for earth pointing experiments. See Figure 2.2-1, View B.

It is this latter arrangement which has been the basis of the further design and development reported on the paragraphs that follow.

2.2.1.2 Major Subcontract:

Since the basic component of this subsystem (erectable STEM type booms) was previously solely manufactured by the Special Products Division of the DeHavilland Aircraft of Canada Limited, it was decided to let a subcontractor to DeHavilland to provide the development, manufacture and qualification of the boom system components. This was done with the approval of NASA-Goddard Space Flight Center.

The current status of this subcontract is as follows:

1. Negotiations have been conducted with DeHavilland and a price has been quoted for the basic boom subsystem subcontractor tasks as outlined in the Work Statement delineated in General Electric Document No. N-20273-A dated August 21, 1964.
2. Additional quotations have been received from DeHavilland covering added scope items associated with subcontractor effort on the boom subsystem as delineated in "Package A" to the N-20273-A document, as well as other added scope efforts as they come to light.
3. The subcontractor has been incrementally funded on a level of effort basis from June 29, 1964 until October 31, 1964. In addition, the subcontractor has requested materials procurement funds commencing with the month of October in order to initiate procurement of long-lead items in time to meet the present schedule. This request is currently being reviewed by GE.
4. The subcontract has not as yet been consummated. A finalized subcontract work statement and boom subsystem specification are now in preparation in anticipation of imminent consummating of the subject subcontract.

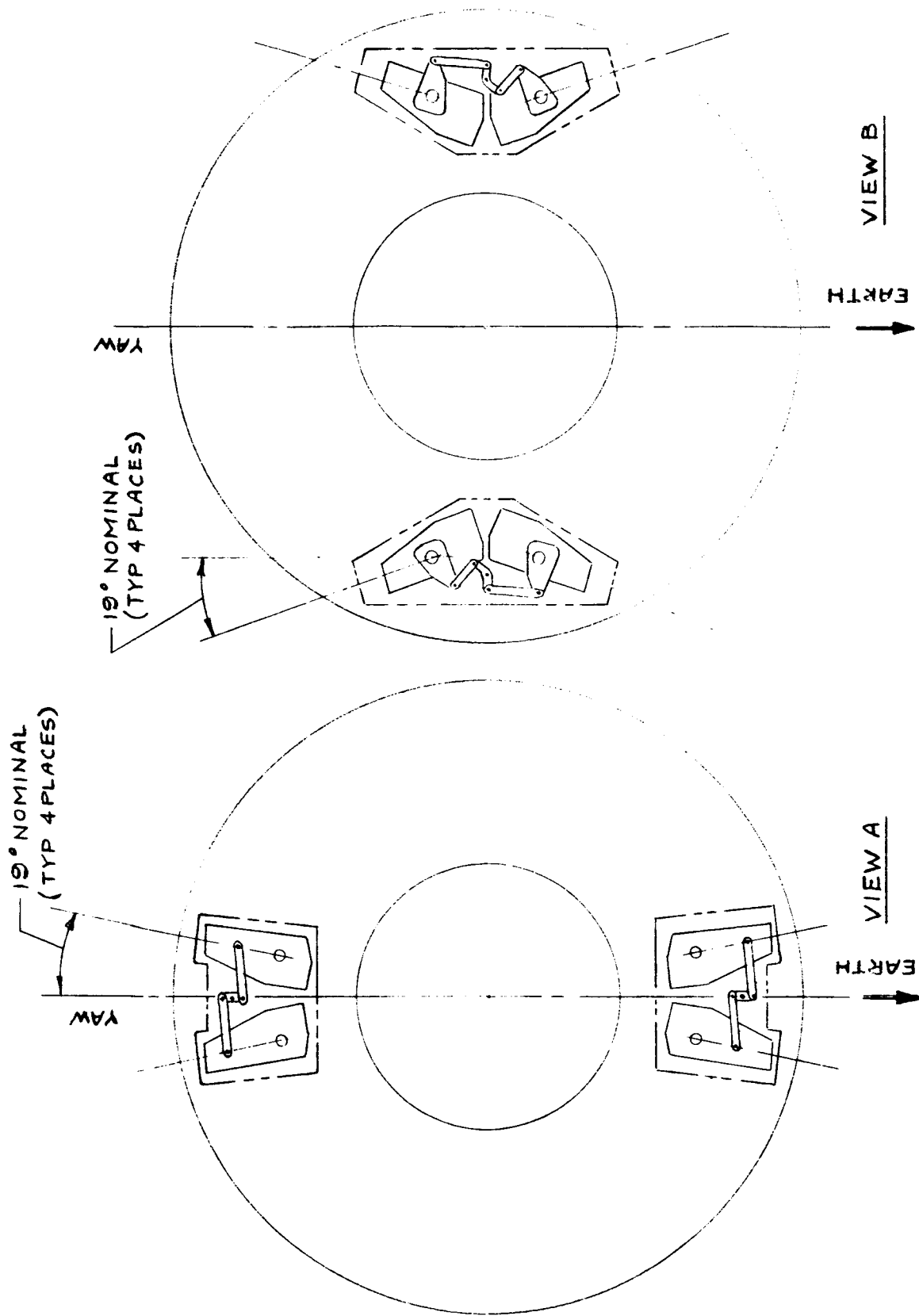


Figure 2.2-1. Extendable Boom Storage Methods: (a) End Storage, (b) Side Storage

5. When the subcontract is consummated, it will reflect the scope of work prescribed by the finally negotiated prime contract (as pertains to the boom subsystem) and will take into account all incremental funding payments made up to that time.

2.2.1.3 Boom Subsystem Specification

General Electric Specification SVS7316 has been prepared for the boom subsystem. It is currently being revised to reflect the latest requirements to be included as an exhibit to the subcontract.

2.2.1.4 Delineation of Design Details

2.2.1.4.1 Erectable Booms

The basic erectable boom is a flat beryllium copper element two inches wide, 0.002 inch thick, and of a length equal to the desired boom length. The element is rolled about its longitudinal axis into an overlapped, right, circular cylinder of one half inch diameter. The tape is heat treated in this form such that its natural stress free condition is the overlap tube. Storage of the boom is effected by elastically flattening the tape and coiling it about a storage spool as shown in Figure 2.2.1-2. Subsequent erection is accomplished by rotation of the storage spool in the direction which drives the stowed tape through the guidance until it reforms into the tubular shape.

Sections A-A and B-B of Figure 2.2-2 show typical sections of the guidance used for erection of the booms.

Beryllium-copper booms are silver plated on their outside diameters to minimize thermal bending.

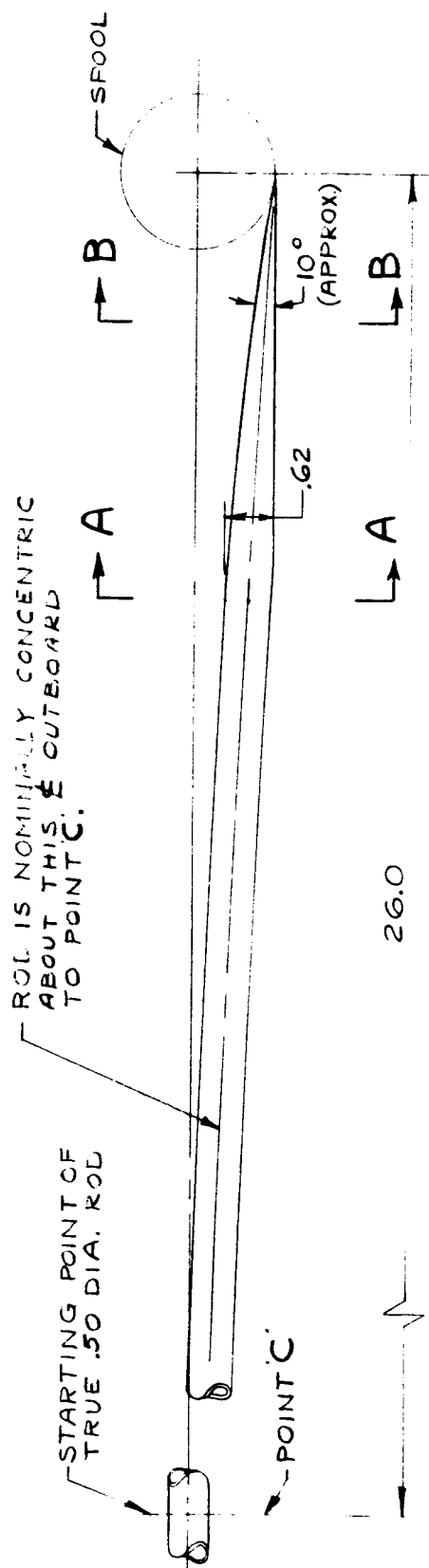
2.2.1.4.2 Erection Units

The erection units for the primary booms house the storage spool and guidance and are driven externally by means of a gear train. They take the form of a roughly rectangular prism 8.25 inches long, 4.5 inches high, and 3.0 inches wide (as shown in Figure 2.2-3).

The erection units also secure the inboard ends of the tip weight assemblies at the point defined by the 3 1/2 degree and 0.22 inch dimensions in Figure 2.2-3. (Additional lateral support during launch is rendered the tip weight by the overall assembly housing at a point near the cg of the tip weight.)

The attachment of the tip weight to the erection unit is so fashioned as to release the tip weight upon initial motion of the boom tape at erection.

Figure 2.2-4 shows a schematic of the functional parts internal to the erection unit. In the stowed condition, the boom tape is wound on the storage spool and fed through the guidance up to the point where it passes just outside of the erection unit and fastens to the tip weight assembly. Torque applied to the spool in the direction shown will drive the stowed tape through the guidance and free the tip weight from its attachment to the erection unit. Continued application of torque will erect the boom to its full length in the tubular configuration, at which time the full extension microswitch will engage a hole in the storage spool and cut-off motor power, as well as provide a telemetry event monitor.



NOTE:
MEASUREMENTS MADE AT
DEHAVILLAND AIRCRAFT LTD.
14 SEPT 1964.

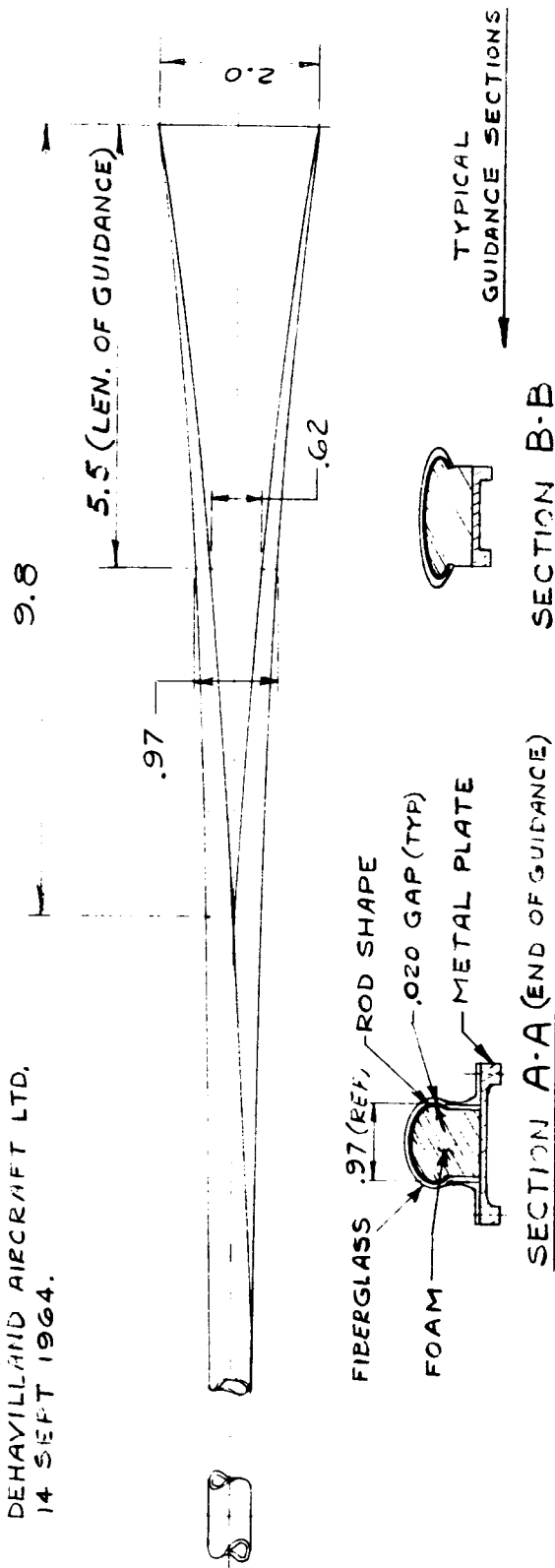
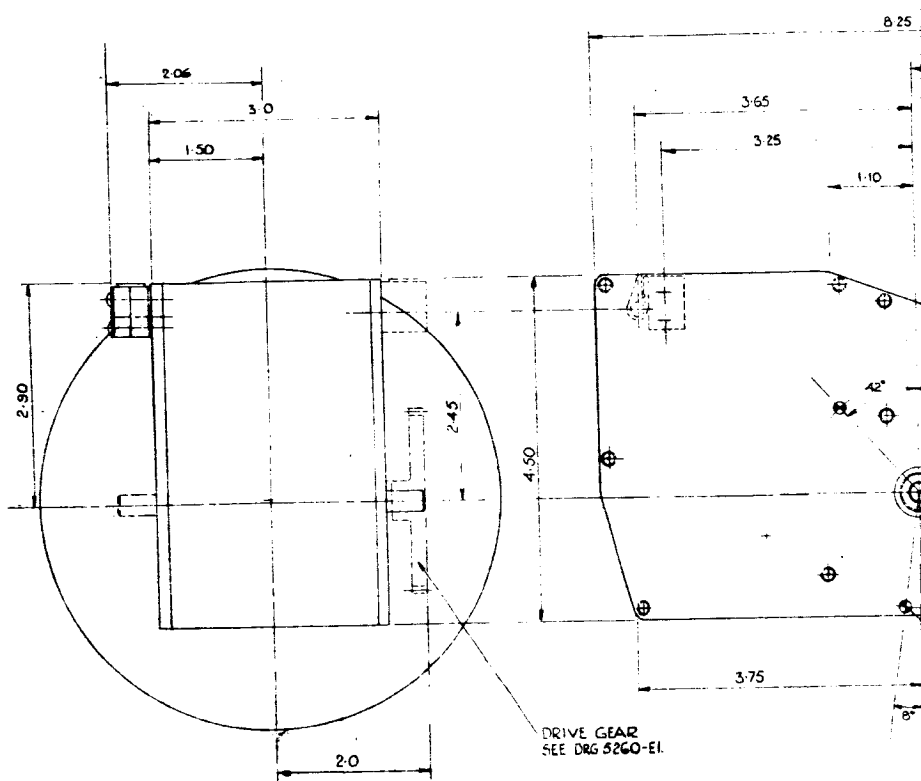


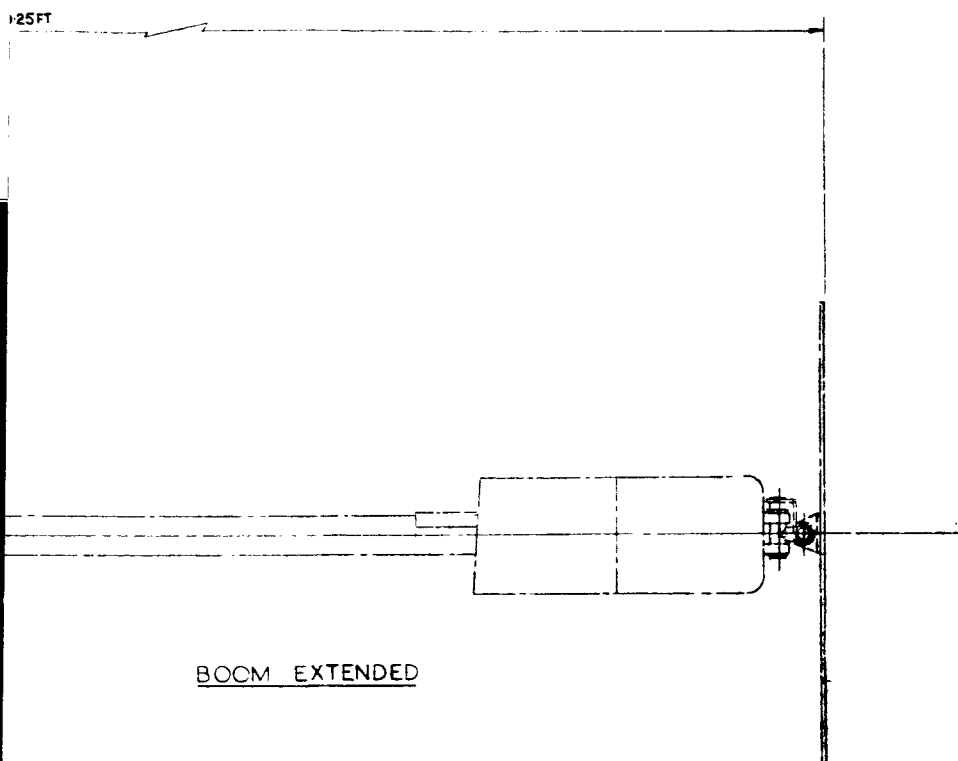
Figure 2.2-2. ATS Gravity Gradient Rods, Play Shape and Guidance Sections



2-MICRO-SWITCH
MS 27216-2
1-ACTUATOR SWITCH
HONEYWELL JS-35

2-9512-96





NOTES:-

1. UNITS ARE HANDLED BY DRIVE SHAFT AND MICRO-SWITCHES.
2. TOTAL WEIGHT :- 6.56 lbs
3. TIP & TARGET WEIGHT :- 2.50 lbs
4. ELEMENT WEIGHT :- 1.56 lbs
5. UNIT WEIGHT :- 2.50 lbs
6. ELEMENT :- 2.000 ± 0.002 TH Be Cu — SILVER PLATED.
7. EXTENSION RATE :- 2 FT/SEC ± 1 FT

FOR STRUCTURAL ATTACHMENTS SEE FIGURE 2-2-6

Figure 2.2-3. Outline of Primary Boom

3

Reversal of the direction of applied torque will retract the booms. A revolution counter mounted external to the erection unit will provide telemetry input of boom length, thereby providing the capability of stopping the erection or retraction process on command at points other than full extension or full retraction.

As shown in Figure 2.2-4, the storage spool bearings are mounted in arc-shaped slots. This allows the spool centerline to move in the direction necessary to keep the point of tangency to the stowed tape always in line with the entry to the guidance at the tape pay-off point. This motion is necessary since the diameter of the stowed tape will decrease as the boom is extended. The motion is controlled by a roller that rides on the stowed tape just below the tape pay-off point. The drum is spring loaded against this roller by the tension in the spring belt system (see Figure 2.2.1-4) which serves the additional function of keeping the strain flattened tape wound tightly on the storage spool.

Since the storage spool centerline moves relative to the housing, external torque can not be delivered directly to the spool. Therefore, a set of drive gears is provided. This consists of two gears (one at each side of the erection unit) that are pinned to a common shaft which is driven externally. Each of these gears meshes with gear teeth cut in the side cheeks of the storage spool. As seen in Figure 2.2-4, the slot in which the spool bearing ride is an arc-shaped slot centered at the drive gear shaft. Therefore, the storage spool is constrained to move in an arc type motion about the drive gear, always maintaining tooth engagement at the pitch diameter of the drive gear. The double gear (one at each cheek) is provided in order to stabilize the spool and maintain the spool centerline always parallel to the drive gear shaft.

The housing of the erection unit is constructed of chem-milled aluminum side and end plates and of a light aluminum top and bottom covers. Tip weights will be tungsten.

The end of each tip mass assembly will be equipped with an aluminum disk to serve as a TV camera target. The exact coating of this target for optimum TV visibility is yet to be resolved. Each tip target is fully articulated in order to allow it to lie flush against the spacecraft "skin" during launch, and erect itself normal to the boom centerline upon boom erection.

Each ATS boom subsystem requires four such erection units and tip mass assemblies.

2.2.1.4.3 Scissoring Concept

It is a basic requirement of the system that the primary boom be "scissored"; that is the angles, in the plane of the basic "X", between the primary booms must be changed over a prescribed range while in orbit. In order to mechanize this feature, it is necessary to pivot the primary boom erection units. The motion must be coordinated such that all four primary booms move simultaneously in order to maintain a symmetrical configuration about the satellite yaw axes. This is accomplished by pairing the four primary erection units into two sets, as shown in Figure 2.2-5. View A shows the details of the scissoring linkage, which is typical for both boom packages but has been shown only in View A for clarity. The centrally located bellcrank is driven by a shaft which extends from the drive unit. Rotation of this bellcrank is transmitted through the push-pull links to the bellcranks on the erection units. Each erection unit is pivoted with

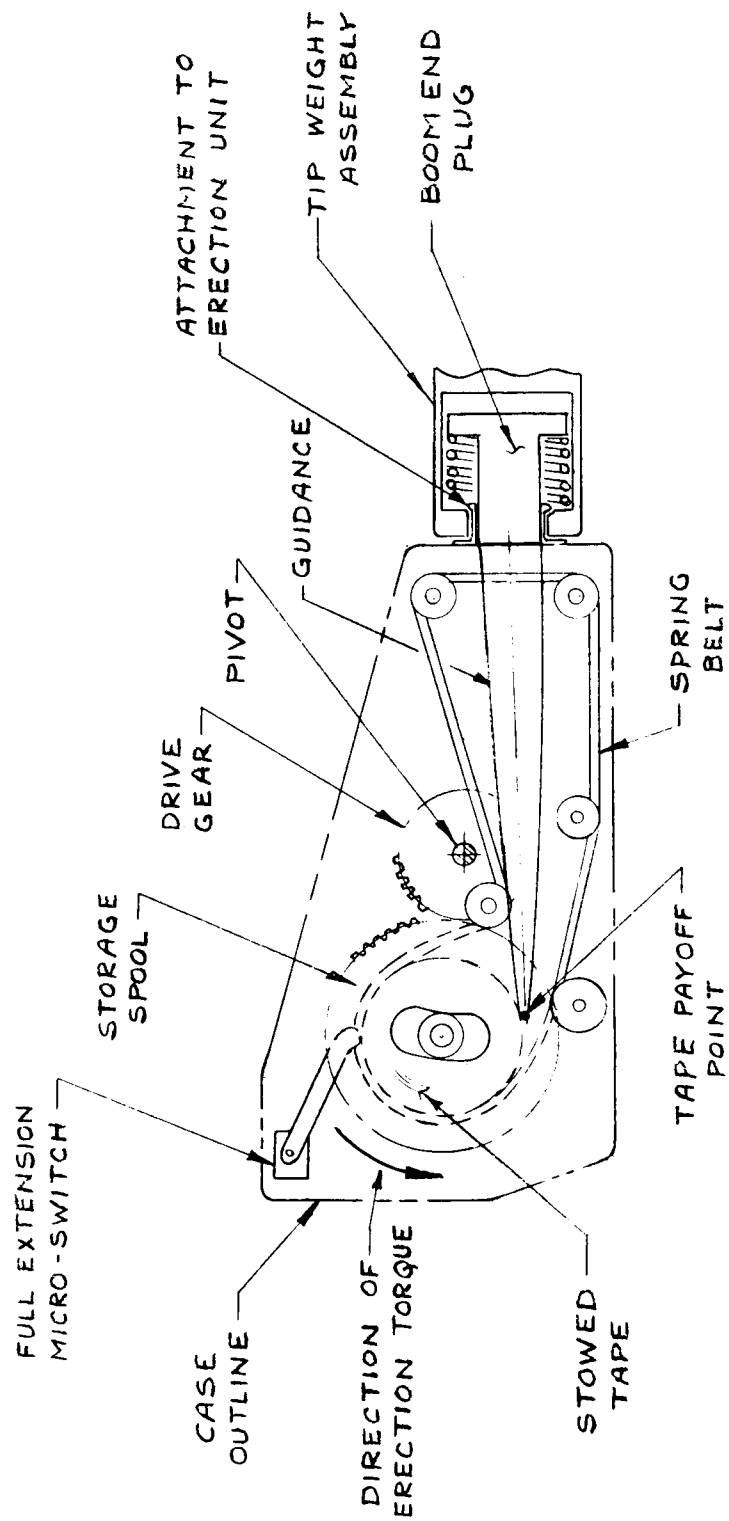


Figure 2.2-4. Primary Erection Unit Schematic

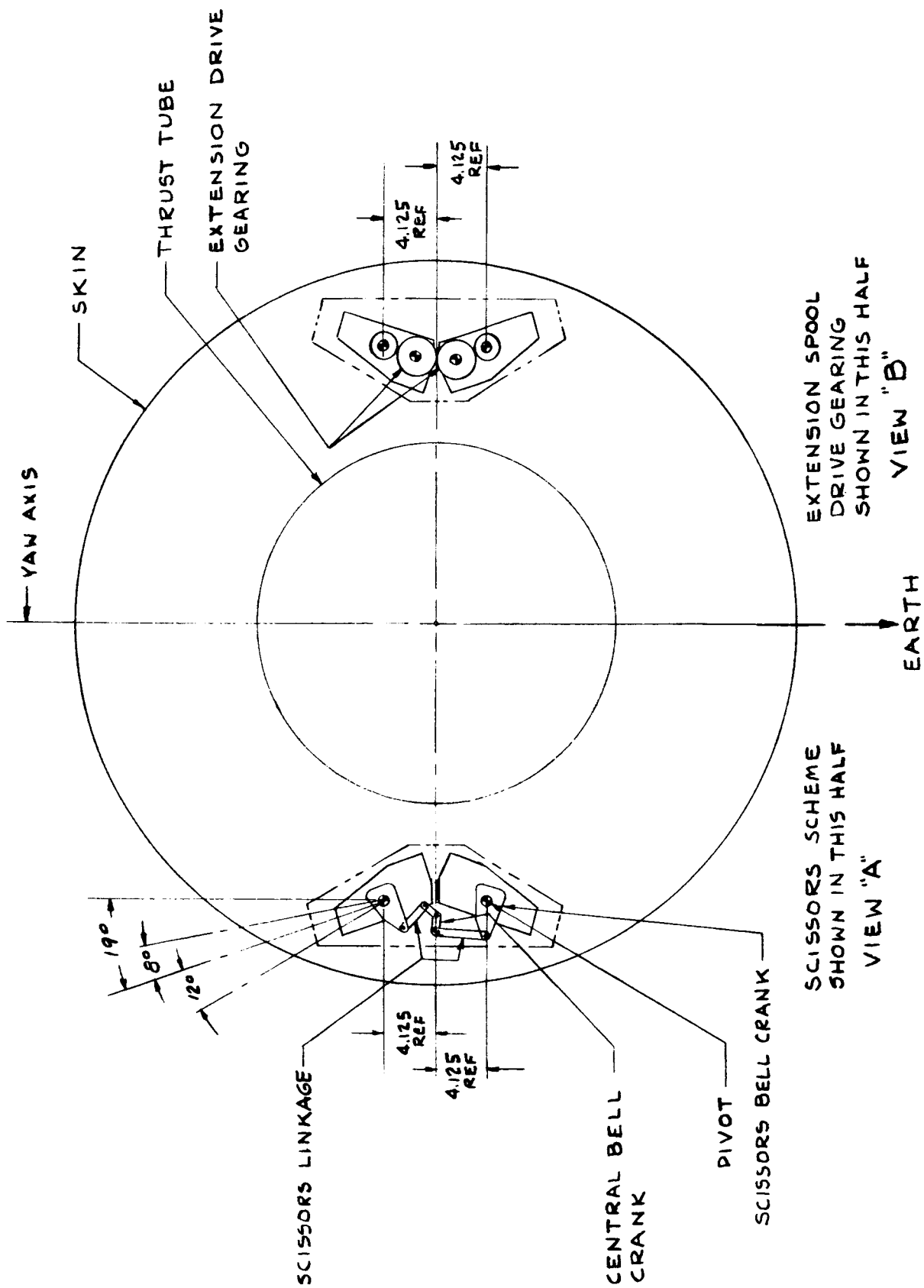


Figure 2.2-5. Scissoring and Drive Train Schematics

respect to the overall package at a point concentric with the drive gears. Therefore, rotation of a single shaft (the central bellcrank drive shafts) manifests itself in equal and opposite rotation on the part of two primary erection units.

The two separate sets of paired erection units are synchronized electrically so that all four booms move in the fashion required for proper scissoring.

At launch each boom unit will be caged at the nominal scissor angle which is 38° included angle between the booms at the top and bottom of the satellite. After initial boom deployment, the booms are free to move on command about their scissor axes. (The method of caging the tip masses also cages the erection units about their scissor axes. Therefore, release of the tip masses by boom erection also releases the scissors cages.) The range of included angles over which the scissor linkage can move the booms is 22° minimum and 62° maximum.

All pivots in the scissor linkage will be of the flex-pivot type in order to minimize the number of bearings to be protected from the space environment.

2.2.1.4.4 Drive Train

2.2.1.4.4.1 Gear Train

The primary boom erection units require externally applied torque at the drive gear shaft, as mentioned above. This is provided by a train of four gears for each pair of primary erection units. This gear train is shown in View B of Figure 2.2-5; it is typical for both pairs of primary boom units.

One of the center gears of the train is driven by the transmission unit. It, in turn, drives one erection unit directly and drives the second erection unit by means of an idler gear. Both erection units are thus driven by a single motor and their spool rotations are mechanically synchronized by the gear train.

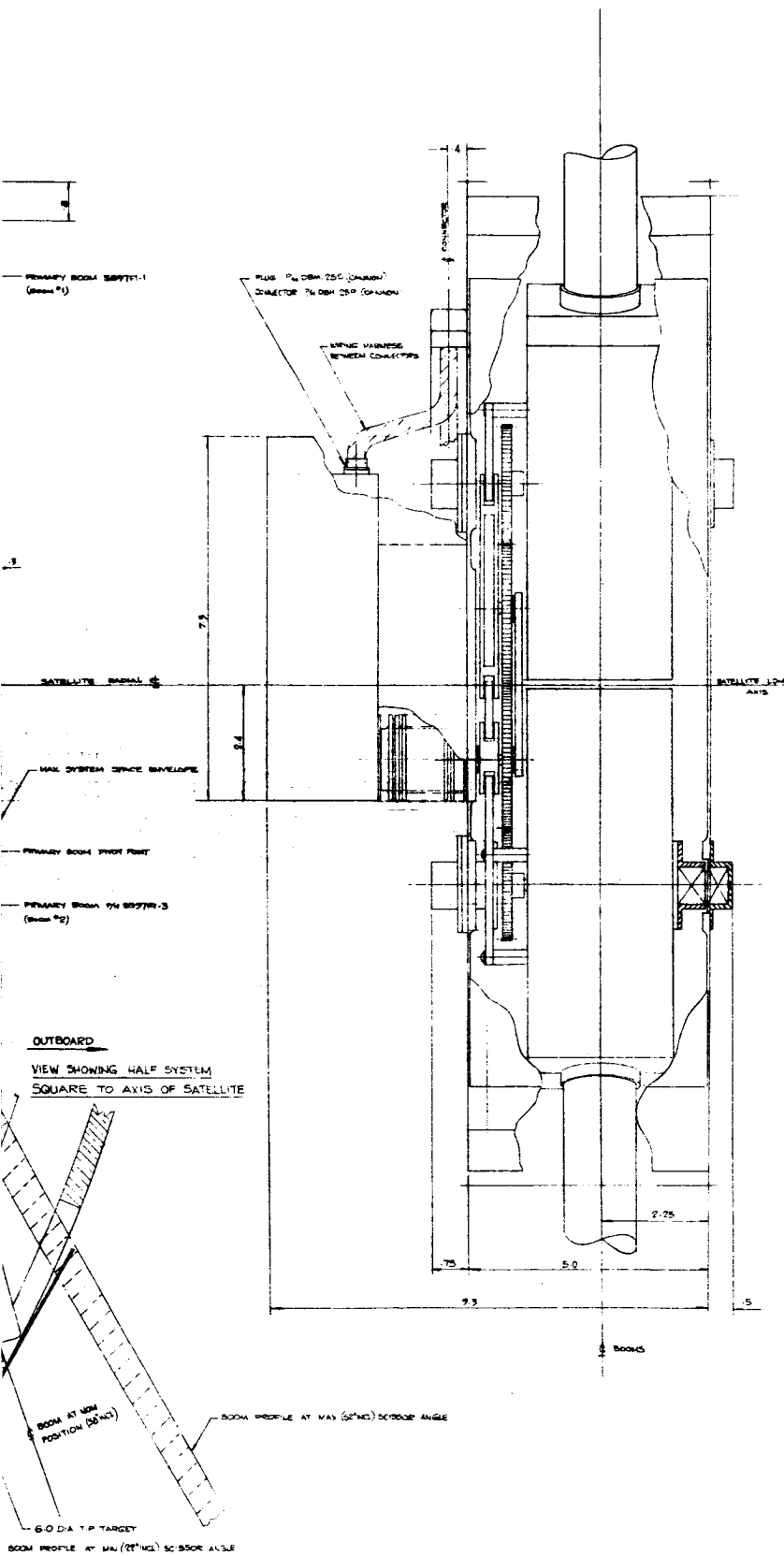
Note that the center of the erection unit drive gear must be concentric with the axes about which the erection unit is pivoted in order to allow the gear train to remain engaged during scissoring motion (see Figures 2.2-5 and 2.2-6).

2.2.1.4.4.2 Drive Unit

Each primary boom unit pair is equipped with one drive unit which provides the torque required by the scissors bellcrank and the gear train. Each drive unit contains two Brush GJY type d-c motors, one for boom extension drive (via gear train) and one for scissors drive (via bellcrank linkage). The scissors drive motor is equipped with an integral gear reducer to reduce speed to that required for scissoring rate.

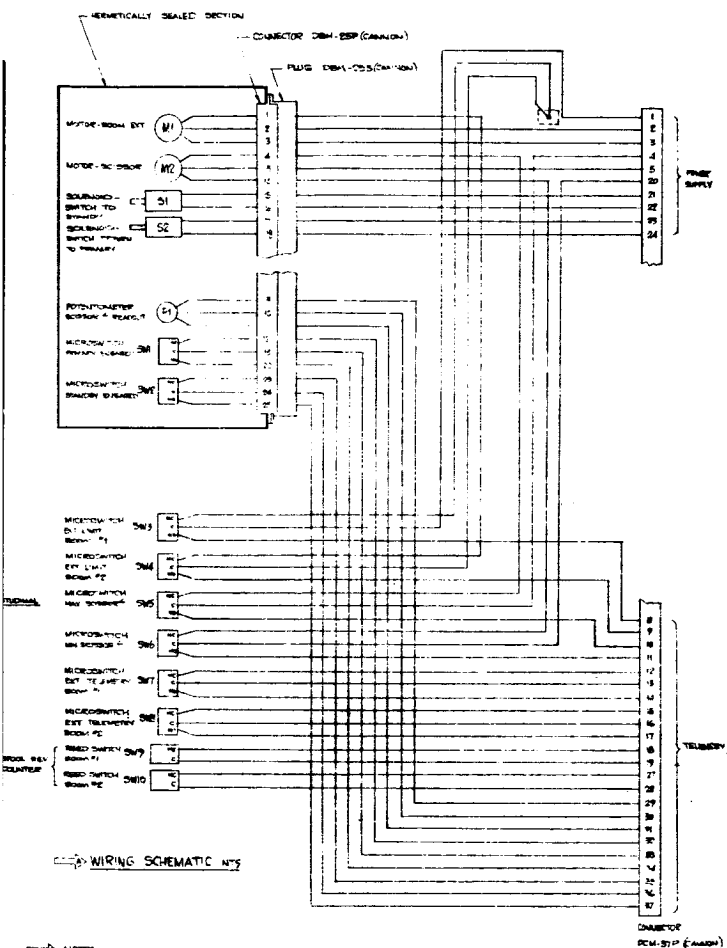
The drive unit also includes an emergency clutch (solenoid operated) which enables each motor to assume the function of its mate in the event of failure of either motor on a given set.

At present two designs are under consideration for enveloping the motors with a vacuum tight shroud to protect them from the space environment. One design uses a Harmonic Drive unit (as manufactured by the United Shoe Machine Company) at each motor and leaves the clutching portion of the drive unit relatively exposed to vacuum. Labrinth type



2-101/2-102

2



- NOTES**
- POWER REQUIREMENTS**
 - ES WIRE NORMAL EXTENSION 11 AMP FOR 50 SEC
 - SCISSORING 0.5 AMP FOR 15 SEC (ESTIMATED)
 - ES WIRE PROXIMITY ONE SYSTEM (2 50% SMALL)
 - EXTENSION 2.5 AMP FOR 30 SEC
 - SCISSORING 1.0 AMP FOR 10 SEC
 - BOOM SPECIFICATIONS**
 - DIMENSION 500 X 100 X 10
 - MATERIAL 2024-T3 ALUMINUM STRIP
 - STRENGTH 2.5 TON COME FOR 10 FT FROM JAW POINT
 - 1.25 DIA CYL FROM 9 TO 100 FT
 - EXTENSION RATE** 0.11 FT/SEC
 - SCISSOR RATE** 0.0015 FT/SEC
 - LENGTH COORDINATION** FIRST BOOM 100 FT 4.115 4.0 SECOND BOOM 100 FT 4.115 4.0
 - WEIGHT (ESTIMATED)** 26 TO 100 LBS (ESTIMATED)
 - ANGLE STABILITY** 0.15 DEG

PRELIMINARY

GENERAL NOTE: ONE HALF SYSTEM ONLY SHOWN
STRUCTURE SHOWN ON SHEET 2

Figure 2.2-6. Primary Boom Subsystem
Outline and Installation

seals and silicone oil reservoirs would provide a partial pressure in the clutch box. The other design encloses the entire motor and clutch assembly in a vacuum tight envelope and uses a bellows type coupling to deliver the torque through the pressure shell. In either case, two drive shafts would protrude from the clutch box: one for the gear train and one for the scissors bellcrank.

The clutch box will also house the solenoids for clutch actuation, the microswitch for solenoid cutoff/telemetry event monitor, and the potentiometer to readout scissors position.

2.2.1.4.5 Gears and Bearings

The design involves certain gears and bearings which will be at least partially exposed to the space vacuum and will be expected to operate after long periods of soak in orbit. Investigations are currently being undertaken to determine the best method for lubricating these items.

Approaches under consideration are:

1. Various types of dry film lubricants and laminar solids
2. Vacuum stable silicone oils and greases in reservoirs and protected by labyrinth or static type seals
3. Filled plastic gears in mesh with metal gears.

2.2.1.4.6 Structural Housing

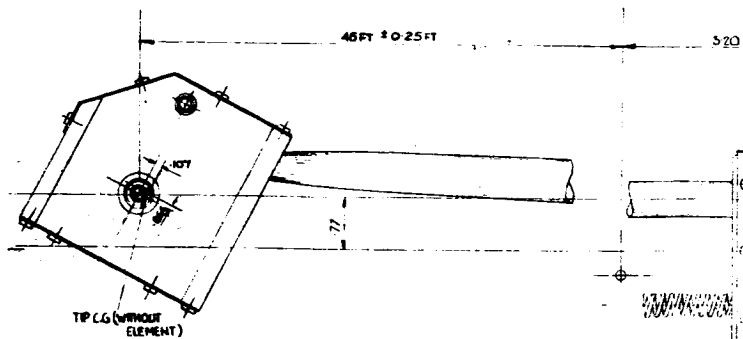
As shown in Figure 2.2-6, each pair of primary boom units, together with the associated drive train and scissor linkage, will be housed by a local structure which coordinates the locations of all pivots and bearing supports, and provides structural support and caging of all components as a single unit. This unit will be mounted to the spacecraft structure, in the appropriate attitude, by means of bracketing. Alignment adjustments of this housing will be made relative to the satellite body axes. This housing will be fabricated from chem-milled aluminum plate and aluminum sheet.

Two such assemblies, shown in Figure 2.2-6, make up one spacecraft set of primary gravity-gradient boom equipment.

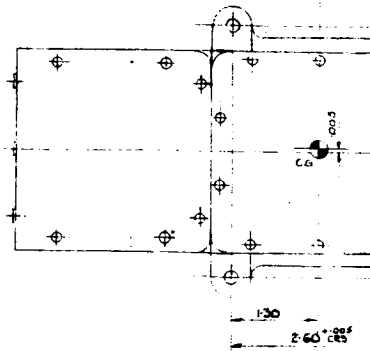
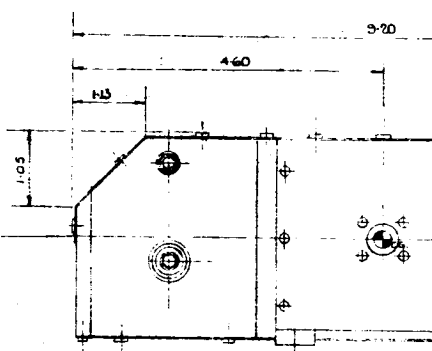
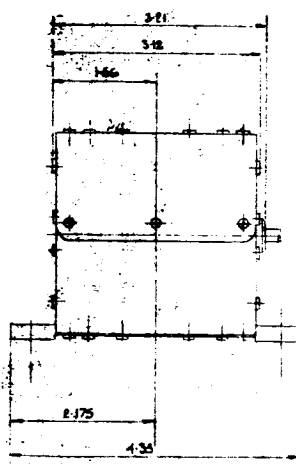
2.2.1.4.7 Damper Boom Units (Secondary Boom Unit)

Each ATS boom subsystem requires one damper boom unit to be mounted on the damper borne platform and to act as a gravity anchor for the damper. The basic erectable boom for this unit is the same as that described above (paragraph 2.2.1.4.1) for the primary booms. The damper boom unit will extend two 45-foot long booms in diametrically opposite directions from the damper axes of rotation and in a plane normal to the same.

The erection technique for this unit is the self erecting scheme. The ends of the booms are fastened to that portion of the unit which remains at the damper axes. The two storage spools, however, are each mounted in a section of the unit which is propelled away from the damper axes as the strain energy in the stowed tape causes the tape to unwind off of the spool. (see Figure 2.2-7).



DAMPER 8

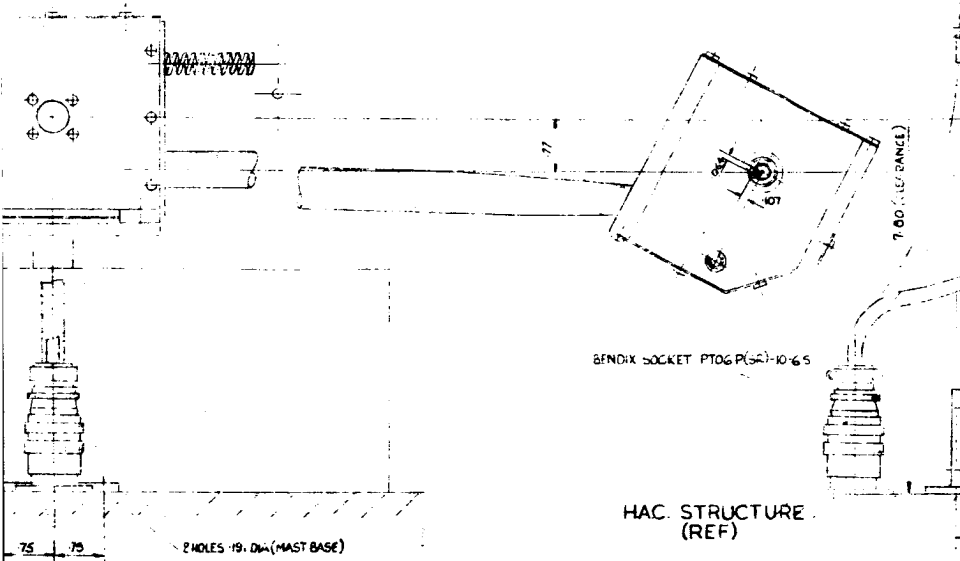


DAMPER

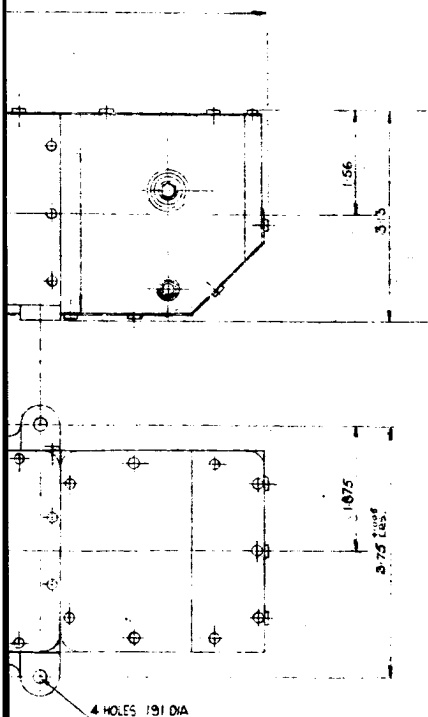
2-105/2106

3 20

45ET 10.25 FT



DOM-EXTENDED



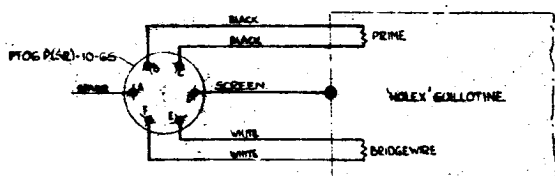
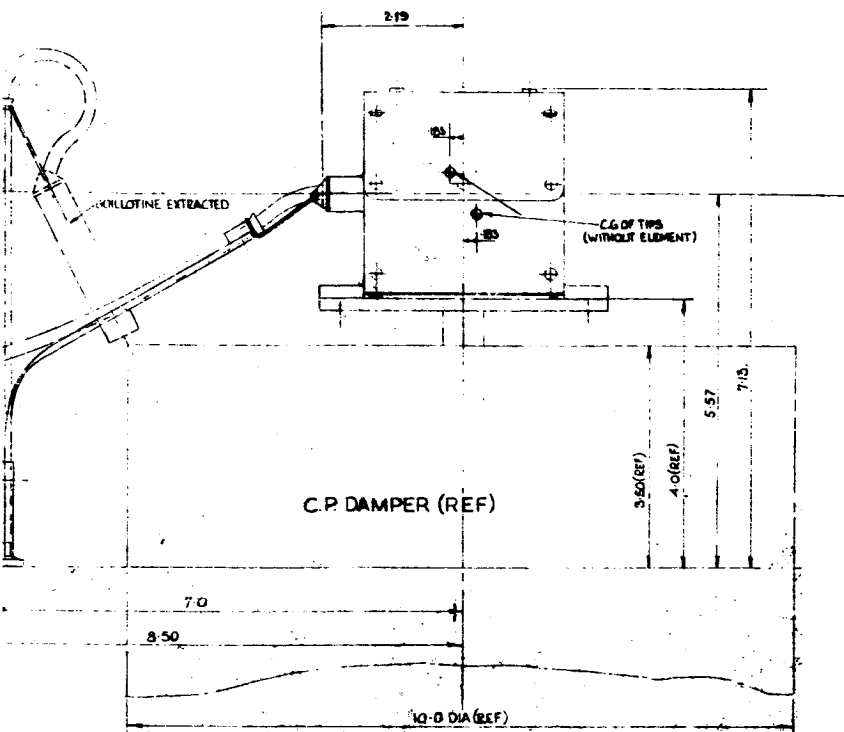
NOTES:-

1. TOTAL WEIGHT 6.25 LBS
2. TIP WEIGHT (EXCLUDING BOOM) 1.90 LBS EACH
3. BOOM WEIGHT 0.80 LBS EACH
4. BODY WEIGHT 0.85 LBS
5. ELEMENT 2-000 2-002TH Bc Co (0.56 DIA) SILVER
6. EXTENSION RATE 4-0 FT/SEC MAX

ER BOOM-RETRACTED

2-105/2-106

✓



FIRING CHARACTERISTICS (EACH BRIDGEWIRE)

NO-FIRE CURRENT 0.5 AMP MAX
 100% FIRE CURRENT 1.50 AMP MIN
 RESISTANCE (THRU LEAD WIRES) 0.66 ± .08 OHM
 LEAD WIRE TO CASE NO-FIRE 1000 V AC RMS MAX
 LEAD WIRE TO CASE RESISTANCE 2 MEGAOHMS MIN AT 300V D.C.
 RECOMMENDED FIRING CURRENT 5 AMPS PER BRIDGE

PRELIMINARY

SCHEMATIC WIRING DIAGRAM

Figure 2.2-7. Outline and Installation-
Data-Damper Boom

3

3. Clearance for boom scissor travel (slots in solar array, etc.)
4. Cushions for tip target or solar array
5. Alignment with spacecraft center of mass, center of pressure and satellite axes (also requiring proper balance of spacecraft CM & CP)

The location within the spacecraft volume (item 1. above), clearance for scissor travel (item 2. above), and alignment with the spacecraft (item 5. above) have been the subject of negotiations between General Electric and Hughes Aircraft Company for the past two months. The following agreements have been reached:

1. The boom packages will be symmetrically located about the overall spacecraft cg (presently located at Station 22.5).
2. The booms will extend in planes parallel to one another.
3. The boom packages will be equidistant from and on opposite sides of a plane passing through the overall spacecraft cg (at Station 22.5) and making an angle of 20.5° with satellite yaw/roll plane. The angular relationship of the boom package to this plane will be such that the center of gravity for each boom assembly will lie in said plane. This angular relationship will be symmetrical.
4. The center of pressure of the spacecraft body (not including booms) will be balanced to be coincident with center of gravity of the spacecraft body.
5. Slots will be provided in the solar array and other spacecraft equipment will be located to accommodate the scissor travel delineated in paragraph 2.2.1.4.3.

Figure 2.2-8 shows the basic alignment and orientation details pertinent to this agreement.

Mounting attachments and tip target cushioning remain to be resolved. These topics will be the subject of meeting with Hughes Aircraft Company personnel scheduled for the immediate future.

The interface drawing has not been signed.

2.2.1.5.2 Sensor Interface

Since the gravity-gradient booms extend as much of 100 feet from the spacecraft they enter the field of view of various sensors located on board. Since the presence of the booms in the field of view of certain of the sensors might have deleterious effects on sensor performance, an investigation was undertaken to determine the extent of the boom transgression of sensor fields of view. In addition it is required that the TV camera be able to "see" the tips of the booms over the full travel of possible boom tip excursion.

Accordingly, the following layouts were prepared:

1. Figure 2.2-9, a layout of TV field of view camera/boom intercepts,
2. Figure 2.2-10, a layout of R-F Attitude Sensor field of view/boom intercepts,
3. Figure 2.2-11, a polar coordinate plot of possible positions of the primary booms within the field of view of the I/R reliable earth sensor.

Figure 2.2-9 was plotted for a primary boom plane located at Station 19.83 and TV camera location also at Station 19.83. Current location of boom plane is Station 22.5 and TV cameras at Station 19.5. This 3-inch displacement between camera lens and boom location will have only a slight effect on the information presently in Figure 2.2-9. It

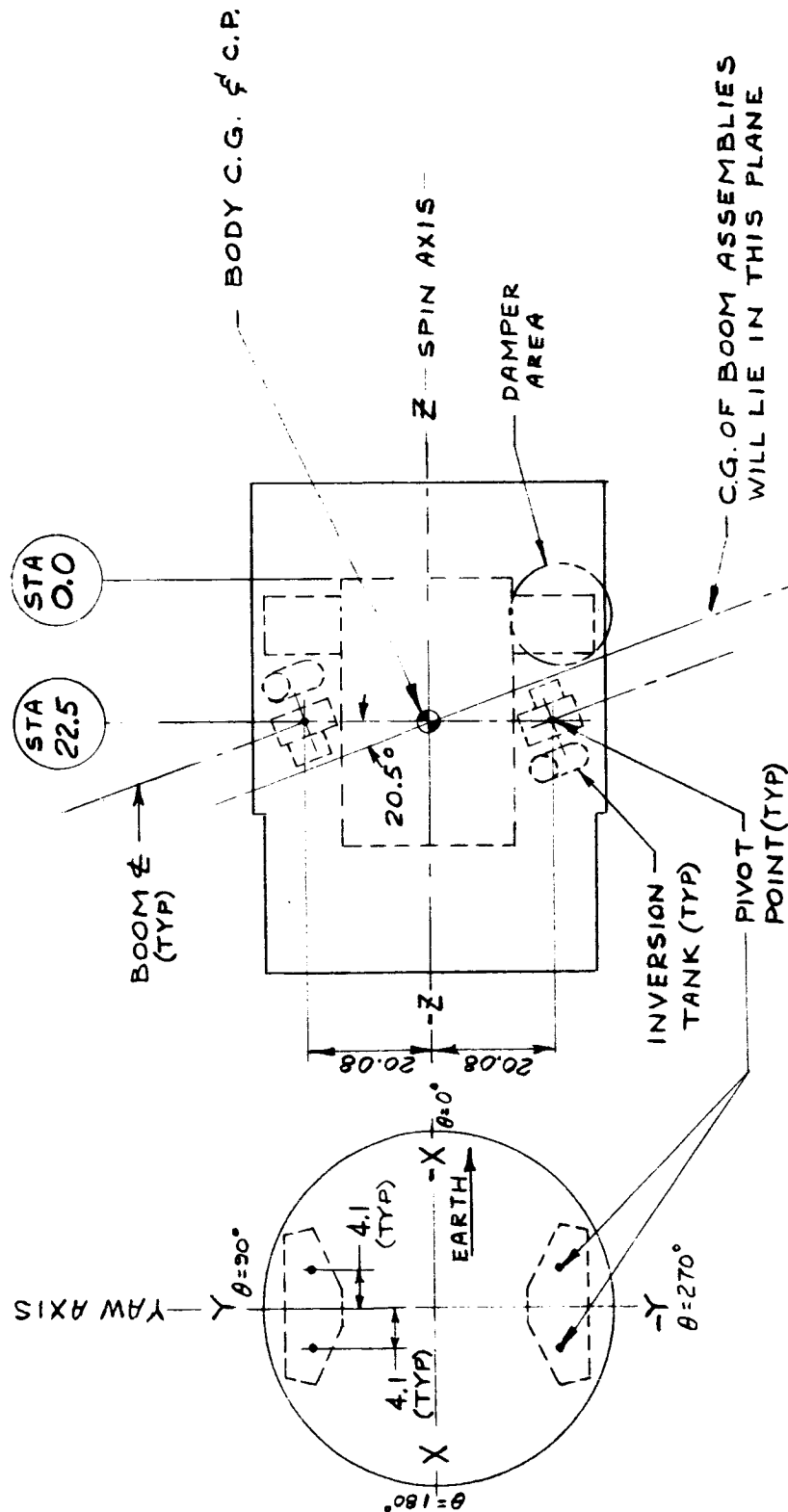
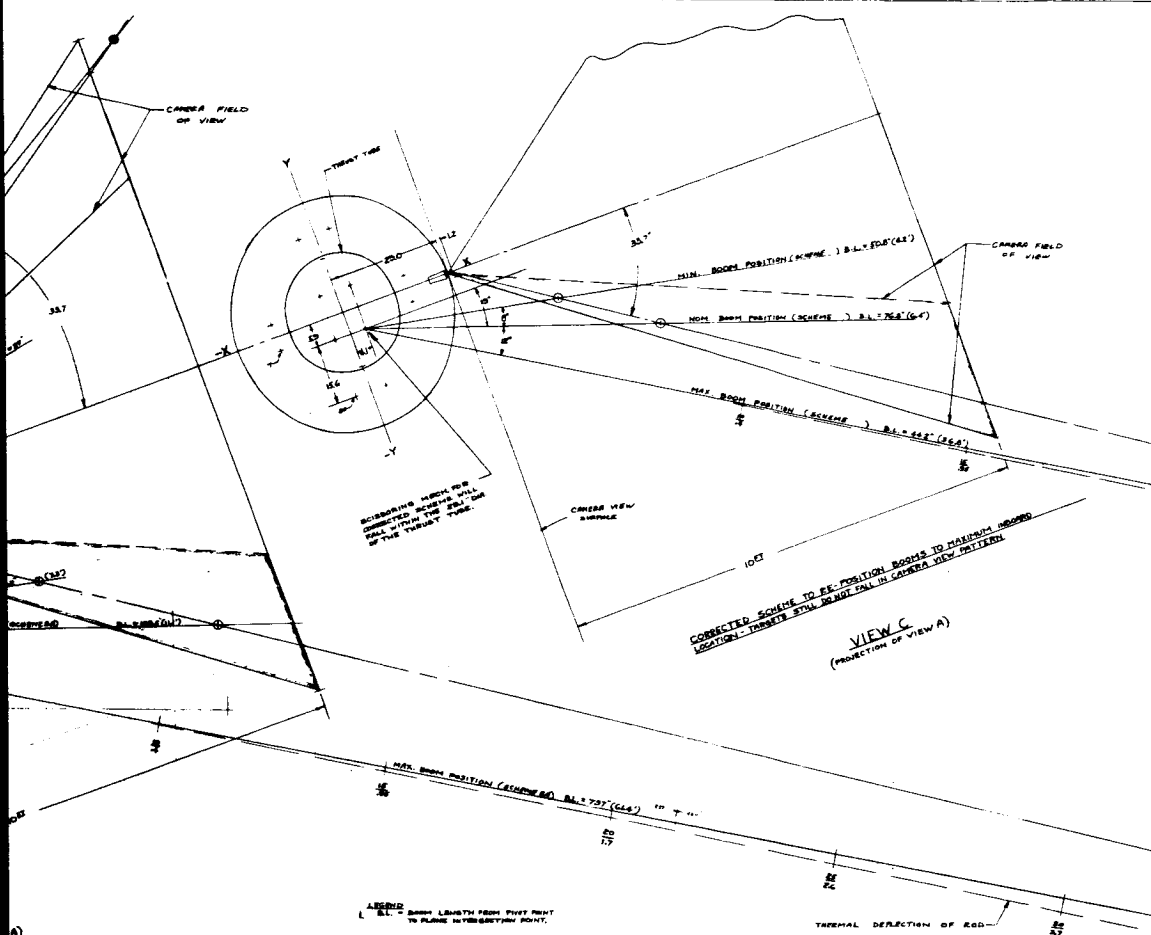


Figure 2.2-8. Pertinent Interface Dimensions Agreed Upon
With Hughes Aircraft Co. 15 October 1964
MAGGE

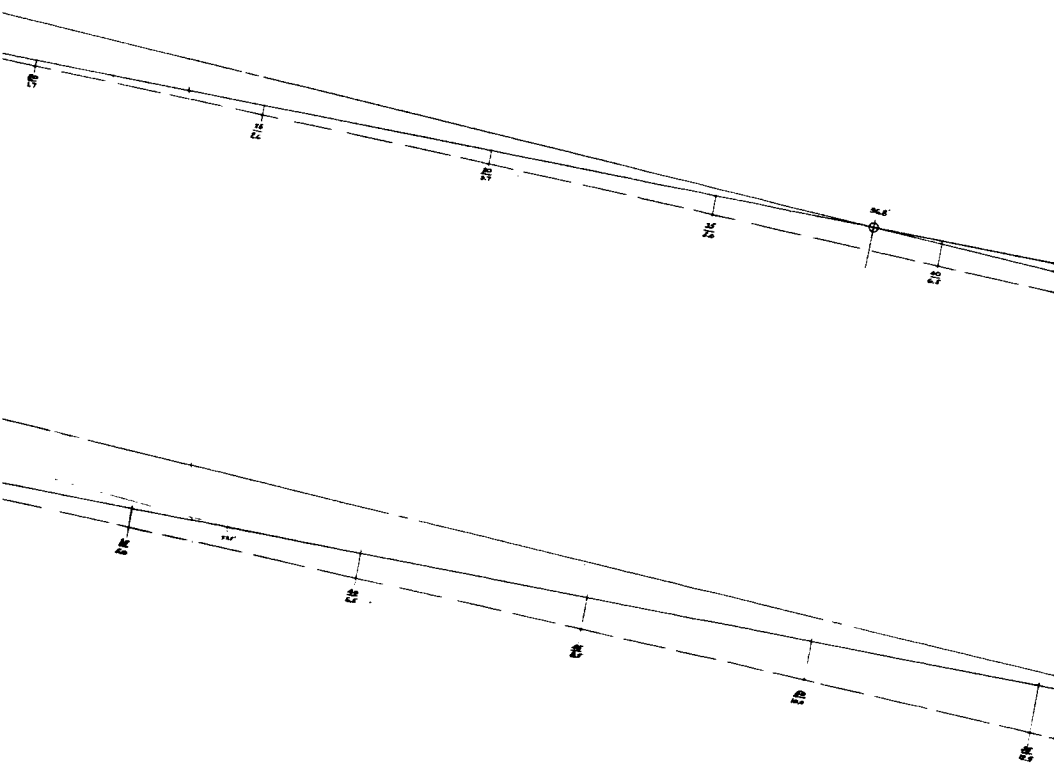


- LEGEND
1. S.L. = BOOM LENGTH FROM FIRST POINT TO PLANE INTERSECTION POINT.
 2. THERMAL DEFLECTION OF RODS
 SEE EXPLANATION DUE TO THERMAL BOWING OF 1/2" DIA ALUMINUM PLATED BOOMS. BOWING DUE TO TEMPERATURE DIFFERENTIAL ACROSS ROD DIAMETER ($\Delta T = 2.67^\circ$)

-BOOM INTERSECTION POINTS WITH TV CAMERA VIEWING PATTERN AND THERMAL DEFLECTION OF RODS

2-111 1/2 - 112

2



2-111/2-112

3

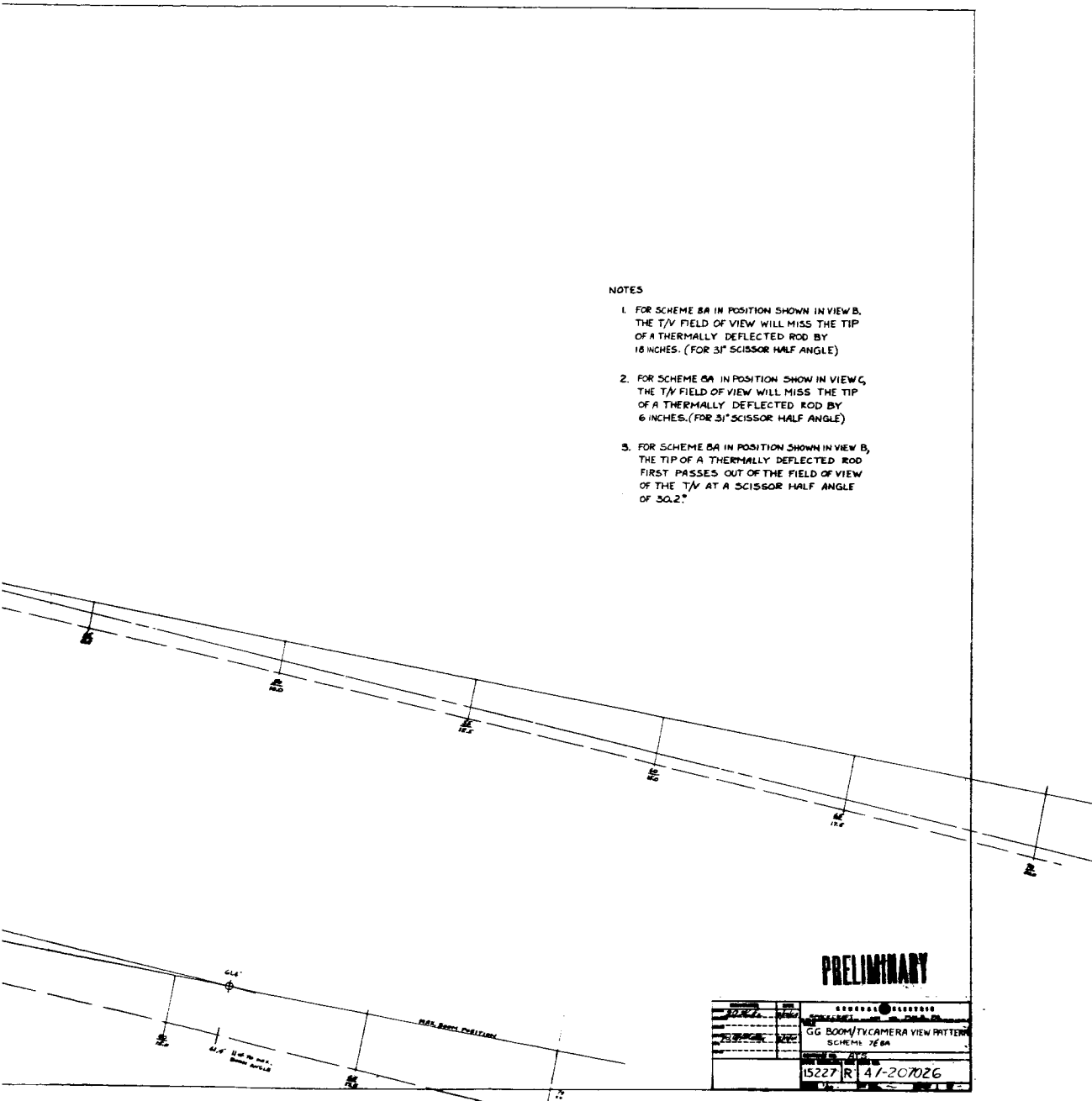


Figure 2.2-9. Gravity Gradient Boom/
TV Camera View Pattern

4

was determined from this plot that for the camera field of view lined with the satellite axes, as shown, there is a slight risk that the tips of the boom will be outside the field of view during the worst case condition of maximum scissor angle and maximum thermal bending. However, a rotation (about the lens centerline) of approximately 12° will enable the camera to "see" the boom tips at all times due to diagonal effect. This amount of rotation is planned for TV camera installation.

The plot in Figure 2.2-10 was based on an R-F sensor location near the forward end of the vehicle. This sensor has been recently relocated and the plot will need up-dating.

Figure 2.2-11 was generated at the specific request and per the instructions of NASA-GSFC. This plot and explanatory notes were delivered to NASA-GSFC as required. This item will be up-dated when boom and sensor positions are firm.

2.2.1.5.3 Power and Telemetry Subsystems Interface

The boom subsystem interfaces directly with the Power Control Unit (also supplied by GE). Power and telemetry requirements have been defined by internal GE documentation. These items will be reflected in the GE-HAC electrical/electronic interface reported in paragraph 2.3.2.

2.2.1.6 Current Weight Status

The currently estimated weight for the total boom system (one satellite set) including the primary boom system and the damper boom package is 58.5 pounds.

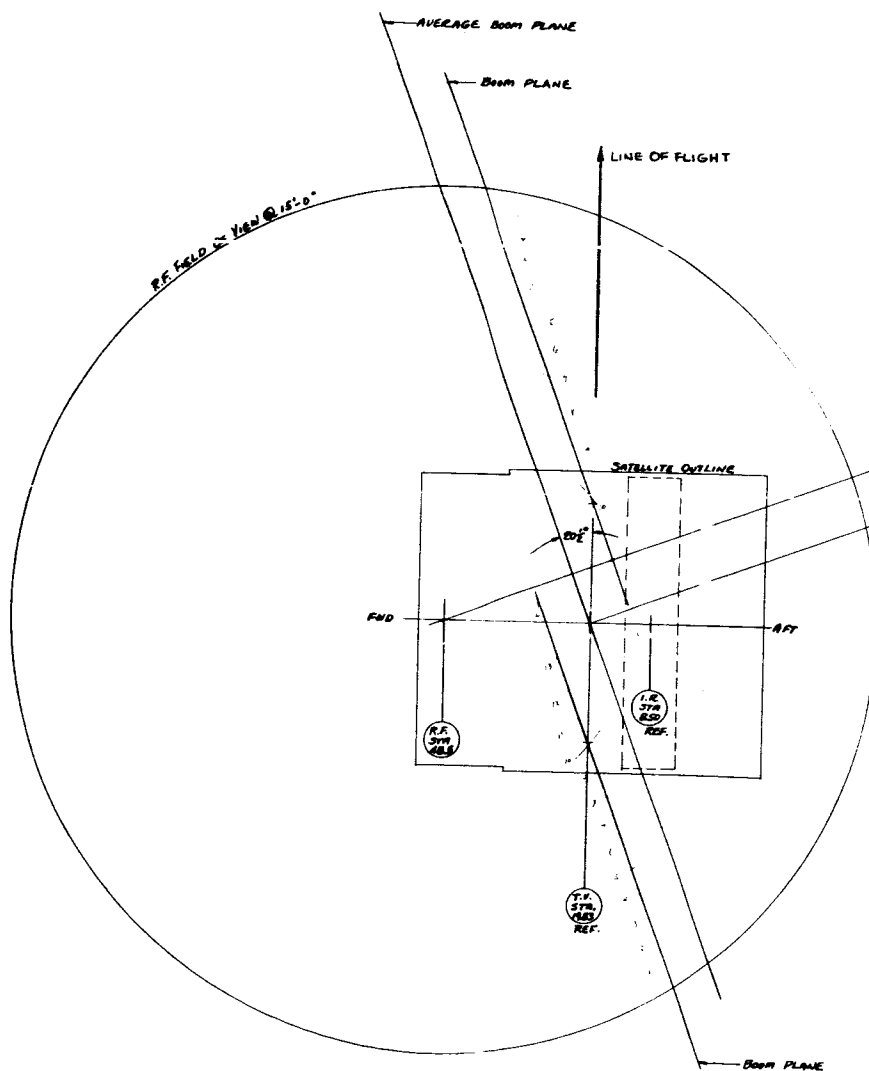
2.2.2 Test (Development)

The only testing underway to date is an evaluation test of bellows coupling being considered for transmitting torque through the pressure shell of the drive unit. The test is being conducted on bellows slightly different in configuration than that envisioned for final design (due to availability of hardware). This test has demonstrated the feasibility of the basic scheme. However, tests on more representative hardware are required.

2.2.3 Expected Activity Next Quarter

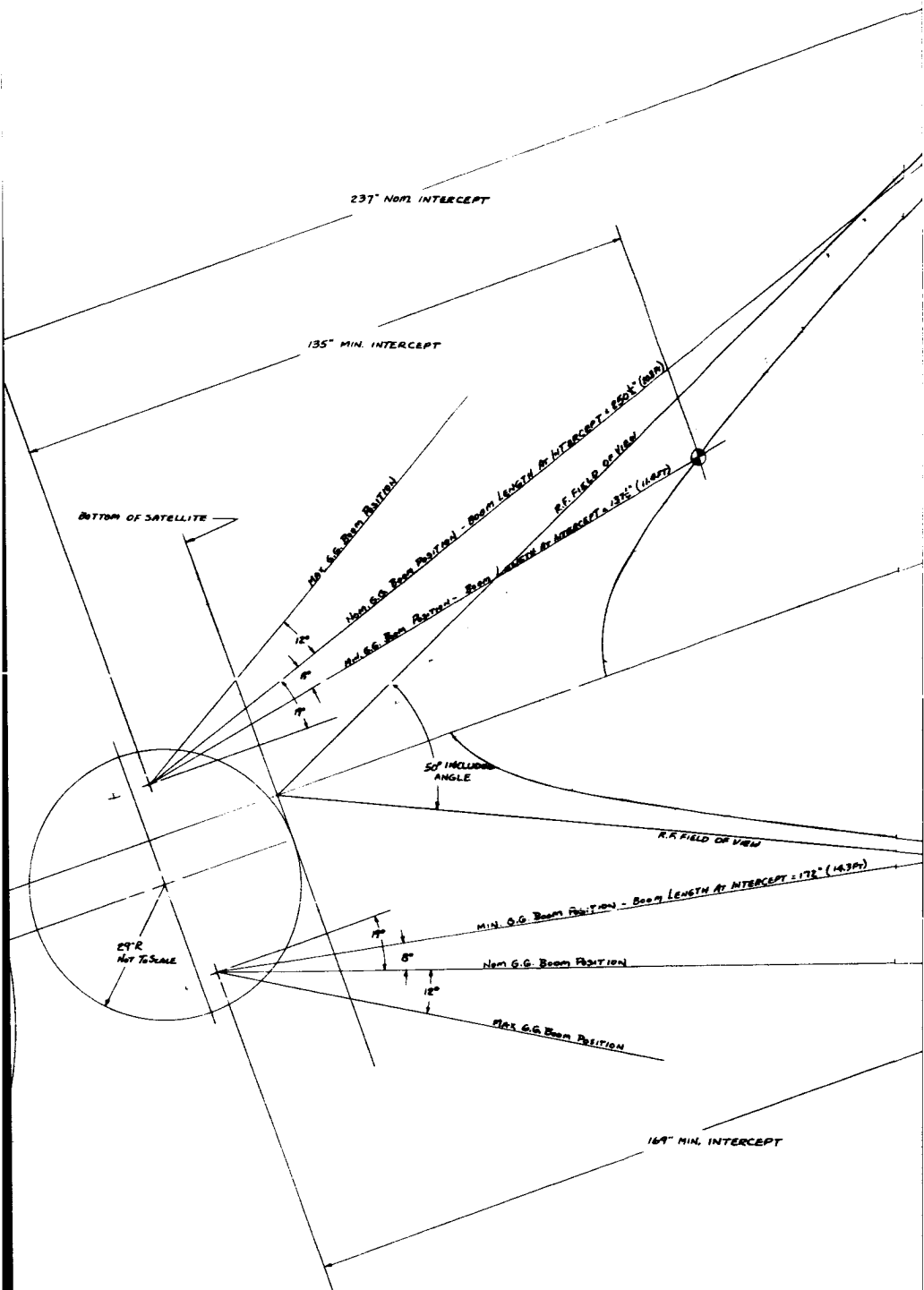
The following activity is planned for next quarter:

1. Issue final copy of specification and subcontractor work statement
2. Consummate subcontract
3. Issue final specification control drawings for all boom system hardware
4. Sign-off on spacecraft interface
5. Sub-component development testing of certain critical parts (gears, bearings, booms, drive bellows, etc.)
6. Detail design and analysis in support of Stage III drawing release
7. Issue Stage III release
8. Procure raw materials and purchased parts for engineering unit fabrication
9. Fabricate test special equipment (test tracks and straightness checker)



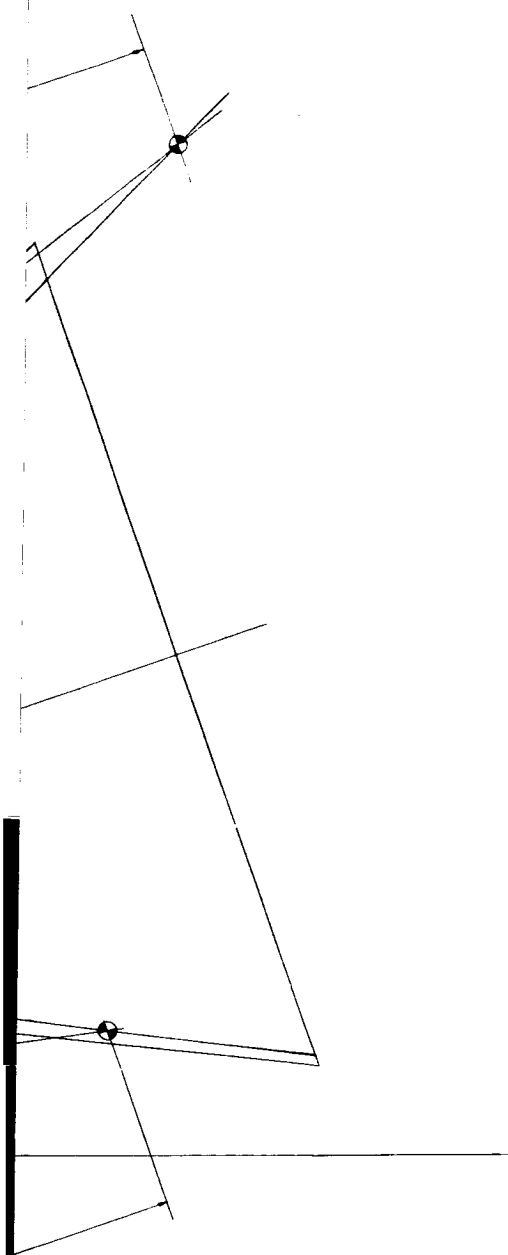
2-115/2-116

1



2

2-115/2-116

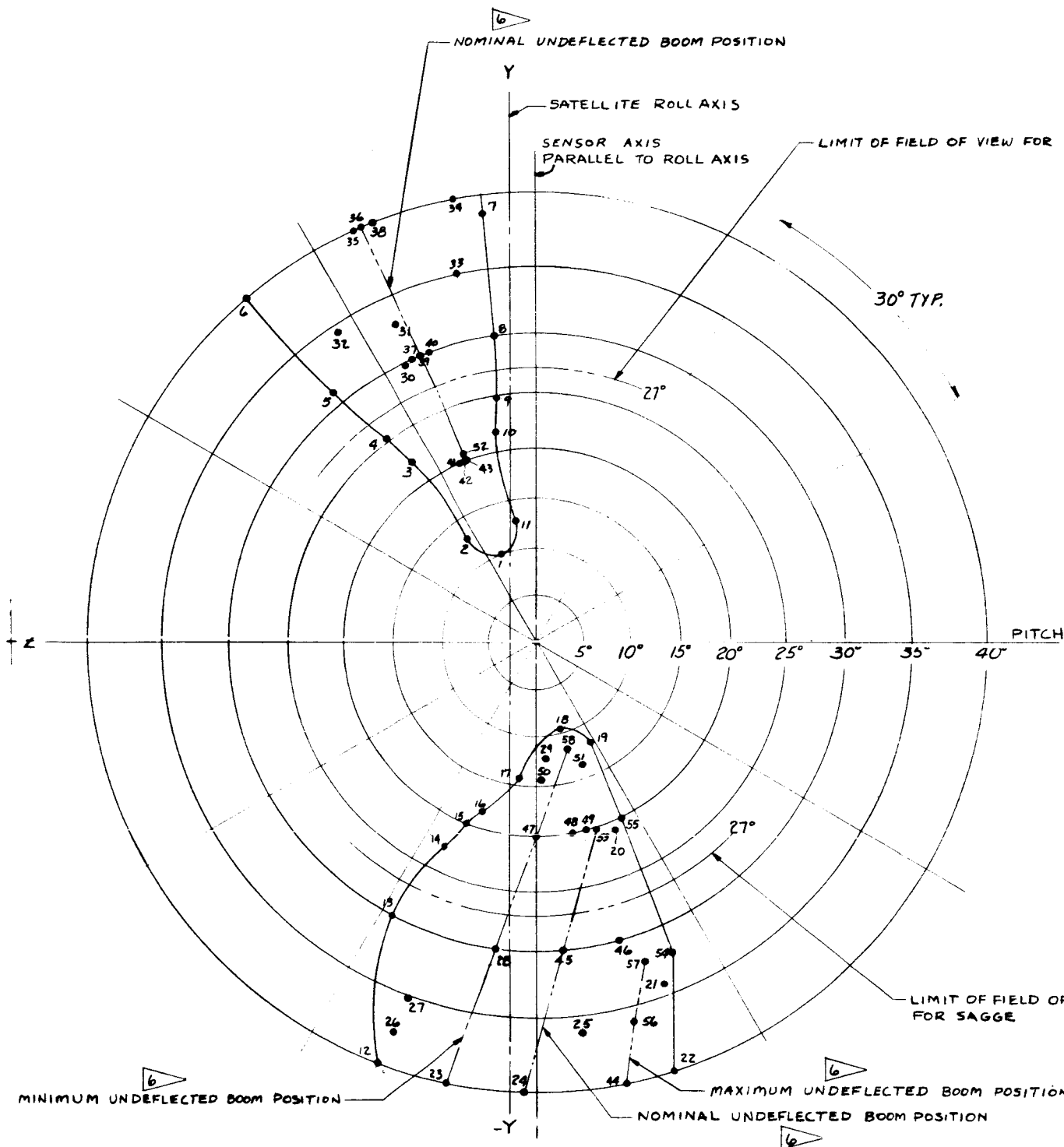


PRELIMINARY

DESIGNATION		DATE	GENERAL ELECTRIC	
G.G. BOOM / R.F. SENSOR FIELD		1/1/68	SOMERSET, MASS. PHILA. L. PA.	
TITLE		G.G. BOOM / R.F. SENSOR FIELD		
		OF VIEW INTERCEPTS		
		SCHEME BA		
DRAWING NO.		15227		
15227		47-207025		
SCALE		1/4" = 1'		

Figure 2.2-10. Gravity Gradient Boom/R-F
Sensor Field of View Intercepts

3



THIS LAYOUT IS FOR I.R. SENSOR LOCATED
 AS SHOWN IN G.E. DRAWING 47-207027.
 AND BOOMS LOCATED IN G.E. DRAWING SK-56130-811
 (REF. I.R. SENSOR AT STA. 8.50 & NOMINAL
 BOOM PLANE AT STA. 19.83) - AXIS DESIGNATIONS
 AS SHOWN ON G.E. DRAWINGS 47-207027 & SK-56130-811

2-117/2118

AGGE



PT. No	AXIAL DISTANCE	BOOM DISTANCE	SCISSORING ANGLE	NOM. OR DEFLECTED POSITION OF ROD
1	97'0"	100'0"	MIN.	DEFLECTED
2	96'0"	100'0"	MIN.	DEFLECTED
3	12'8"	15'0"	MIN.	DEFLECTED
4	9'6"	11'9"	MIN.	DEFLECTED
5	6'7"	8'10"	MIN.	DEFLECTED
6	4'4"	6'6"	MIN.	DEFLECTED
7	4'4"	6'6"	MIN.	DEFLECTED
8	6'7"	8'10"	MIN.	DEFLECTED
9	9'6"	11'9"	MIN.	DEFLECTED
10	12'8"	15'0"	MIN.	DEFLECTED
11	96'2"	100'0"	MIN.	DEFLECTED
12	4'9"	6'10"	MIN.	DEFLECTED
13	2'7"	4'6"	MIN.	DEFLECTED
14	3'10"	5'9"	MIN.	DEFLECTED
15	4'8"	6'11"	MIN.	DEFLECTED
16	5'9"	8'0"	MIN.	DEFLECTED
17	12'2"	14'6"	MIN.	DEFLECTED
18	97'0"	100'0"	MIN.	DEFLECTED
19	96'0"	100'0"	MIN.	DEFLECTED
20	54'9"	60'0"	NOM.	DEFLECTED
21	32'8"	40'0"	MAX.	DEFLECTED
22	12'4"	16'6"	MAX.	DEFLECTED
23	3'8"	5'9"	MIN.	NOM.
24	5'2"	7'6"	NOM.	NOM.
25	3'5"	5'4"	MIN.	DEFLECTED
26	5'4"	6'4"	MIN.	DEFLECTED
27	5'9"	8'0"	MIN.	DEFLECTED
28	5'9"	8'0"	MIN.	NOM.
29	96'2"	100'0"	MIN.	DEFLECTED
30	3'11"	6'11"	MIN.	DEFLECTED
31	5'9"	8'3"	NOM.	DEFLECTED
32	8'4"	11'0"	NOM.	DEFLECTED
33	8'4"	11'0"	NOM.	DEFLECTED
34	5'9"	8'3"	NOM.	DEFLECTED
35	3'11"	6'11"	MIN.	NOM.
36	5'9"	8'3"	NOM.	NOM.
37	6'7"	8'10"	MIN.	NOM.
38	14'3"	19'0"	MAX.	NOM.
39	12'2"	15'1"	NOM.	NOM.
40	54'3"	63'4"	BETWEEN NOM & MAX	NOM.
41	14'7"	17'0"	MIN.	NOM.
42	35'10"	39'4"	BETWEEN MAX & NOM	NOM.
43	58'0"	63'0"	BETWEEN MIN & NOM	NOM.
44	12'8"	16'6"	MAX.	NOM.
45	10'2"	12'10"	NOM.	NOM.
46	32'8"	39'5"	BETWEEN MAX & MAX	NOM.
47	12'2"	14'6"	MIN.	NOM.
48	25'5"	28'6"	BETWEEN MIN & NOM	NOM.
49	41'10"	46'0"	BETWEEN MIN & NOM	NOM.
50	37'2"	40'0"	MIN.	DEFLECTED
51	37'2"	40'0"	MIN.	DEFLECTED
52	92'6"	100'0"	NOM.	NOM.
53	92'6"	100'0"	NOM.	NOM.

Z

VIEW

2

2-117/2118

- 1 DISTANCE FROM I.R. SENSOR LENS ALONG THE AXIS OF THE SENSOR FIELD OF VIEW PARALLEL TO THE SATELLITE YAW AXIS.
 - 2 DISTANCE ALONG BOOM \bar{C} FROM PIVOT POINT ON BOOM MECHANISM TO POINT PLOTTED
 - 3 SEE G.E. DRAWING SK-56130-811 VIEW A-A
 - 4 DEFLECTED POSITIONS INCLUDE THE VARIATION FROM AN IDEALLY STRAIGHT ROD DUE TO INITIAL STRAIGHTNESS TOLERANCE & THERMAL BENDING - NOMINAL POSITIONS ARE THOSE FOR AN IDEALLY STRAIGHT ROD AT THE SCISSORS ANGLE INDICATED.
- 5 - WITH DAMPER BOOMS IN POSITION SHOWN ON G.E. DRAWING SK-56130-806 AND THE I.R. SENSOR LOCATED AS SHOWN ON G.E. DRAWING SK-56130-811, DAMPER BOOMS WILL NOT INTERCEPT THE I.R. SENSOR FIELD OF VIEW (REF 80° INCLUDED CONE) THROUGHOUT THE FULL EXCURSION OF THE BOOMS
- 6 MIN.-NOM.-MAX REFER TO THE SCISSORS ANGLE - (11° MIN, 19° NOM, 31° MAX)

PT NO	AXIAL DISTANCE	BOOM DISTANCE	SCISSORING ANGLE	NOM OR DEFLECTED POSITION OF ROD
54	83'9"	100'0"	MAX	DEFLECTED
55	92'6"	100'0"	NOM	DEFLECTED
56	20'0"	25'8"	MAX	NOM
57	83'9"	100'0"	MAX	NOM
58	96'0"	100'0"	MIN	NOM

3

Figure 2.2-11. Envelope of Boom Positions in R. E. S. Field of View

10. Prepare test plans

11. Begin engineering unit fabrication

2.2.4 Conclusions and Recommendations

The design of the boom system is progressing satisfactorily to date. It is felt that the design as presently conceived can be developed into final hardware that will perform the mission requirements with a high probability of success. The schedule constraints, however, are very tight, and a concerted effort (possibly including overtime) is required to meet the key events. Barring any changes in requirements redirection of the course down which the design is progressing, our objectives should be met within the present schedule and planned funding.

2.3 Combination Passive Damper

2.3.1 Introduction

Two dampers, one a hysteresis damper and the other an eddy-current damper, are combined with a clutching mechanism into a single package referred to as the Combination Passive Damper (CPD). These dampers (coupled to a damping boom) are alternately operated during the Advanced Technology Satellite (ATS) mission to damp the vibrations of those vehicles which utilize gravity gradient stabilization techniques. In addition to providing damping torques, the CPD also must meet a requirement to restore the damper boom to a "null" position with respect to the satellite. This restoring torque is provided by a magnetic torsional restraint device incorporated in the eddy current damper system, and by the torsion wire suspension (tendency to "untwist") in the hysteresis damper system. Basic functions which must be incorporated in the CPD design and the associated hardware to perform these functions are listed below:

<u>Function</u>	<u>Associated Component(s)</u>
Damping	Hysteresis Disc & Magnets Eddy Current Disc & Magnets
Torsional Restraint	Torsion Wire (Hysteresis Damper) Magnetic T. R. (EC Damper)
Suspension	Torsion Wire (Hysteresis Damper) Diamagnetic Cones & Magnets (EC Damper)
Clutching Mechanism	Actuator, bell cranks, aligning cam faces, etc.
Boom Angle Detector	Optical Device
Contact Indicator to indicate bottoming of EC damper	Not established
Temperature Indication	Thermocouples
Mode Indicator	Not established
Caging for launch	Pyrotechnic Device
Stops at $\pm 45^\circ$ rotation extremes	Hard stop - rod bending absorbs energy without failure
Minimum dipole	Outer cover of Mu-Metal or similar material

2.3.2 Design and Analysis

2.3.2.1 General

During the first six weeks of the reporting period (Program Definition Phase), a study (including laboratory tests) was performed to evaluate two possible suspension systems: diamagnetic suspension and torsion wire suspension, which could be utilized with the eddy-current damper. The results of this study were published in GE Document No. 64SD4326, Evaluation of Suspension System for the Eddy-Current Damper, Combination Passive Damper, Advanced Technology Satellite, dated 5 August 1964.

Prior to receiving a firm decision on 11 September 1964 from the NASA to utilize diamagnetic suspension for the eddy current damper, the conceptual design effort was split by the necessity to consider both types of suspension, diamagnetic suspension versus torsion wire suspension, in each concept studied. Other problem areas which have resulted in design iterations include:

1. In-orbit Thruster Effects on Damper Suspension

Efforts to provide sufficient "stiffness" in either damper suspension to prevent bottoming under thruster loads proved impractical. Current design philosophy is to allow the damper to bottom during this maneuver.

2. Interface with Hughes Aircraft Co.

The CPD envelope and location on the vehicle structure has not been finalized. The original envelope was 10 inches in diameter and 14 inches long. Latest (September 22, 1964) HAC recommendation reduced the length of the envelope and drastically reduced utilization of "corner" areas as shown in Figure 2.3-1. Current concepts are in process of being revised in an attempt to meet HAC envelope recommendations.

3. Systems Requirements

CPD loads criteria and damping requirements have not been firmly established. Preliminary conservative load requirements (as shown in Figure 2.3.-2) were established 17 September 1964 to allow detail design to proceed for Stage III drawing release.

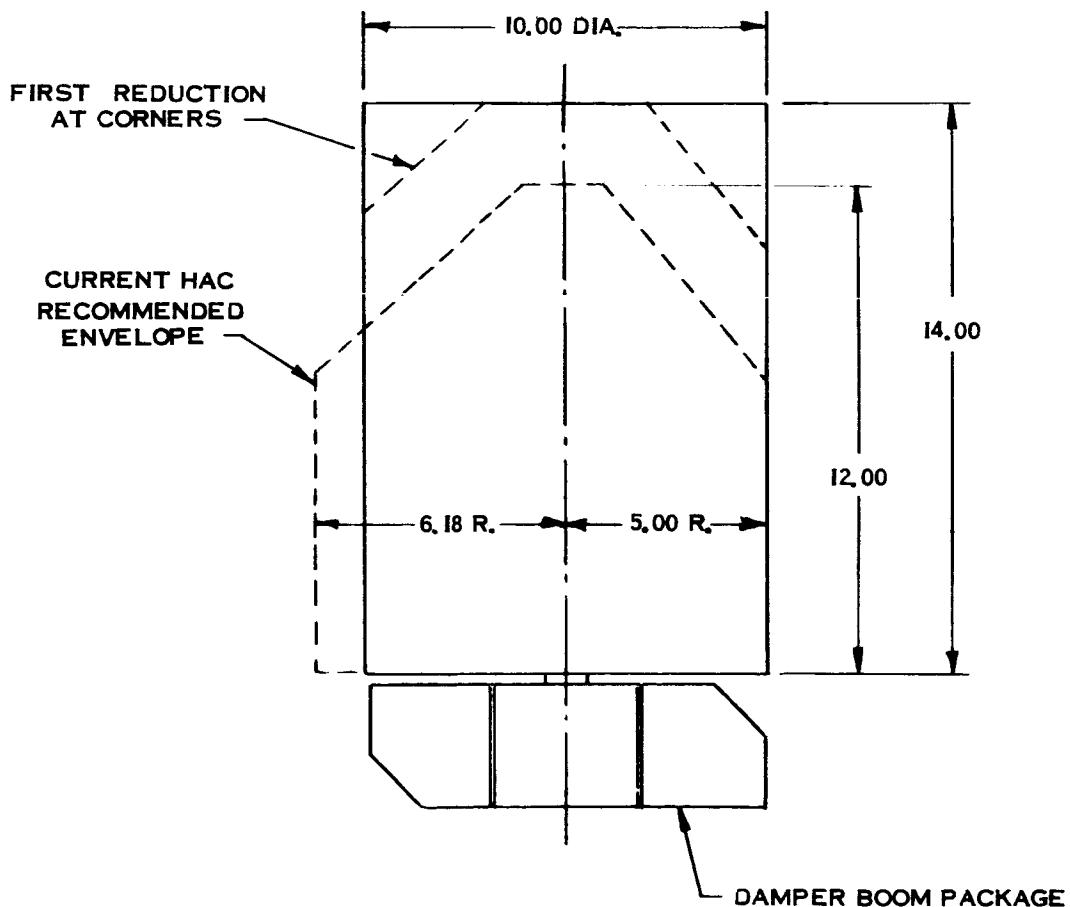


Figure 2.3-1. Combination Passive Damper Envelope History

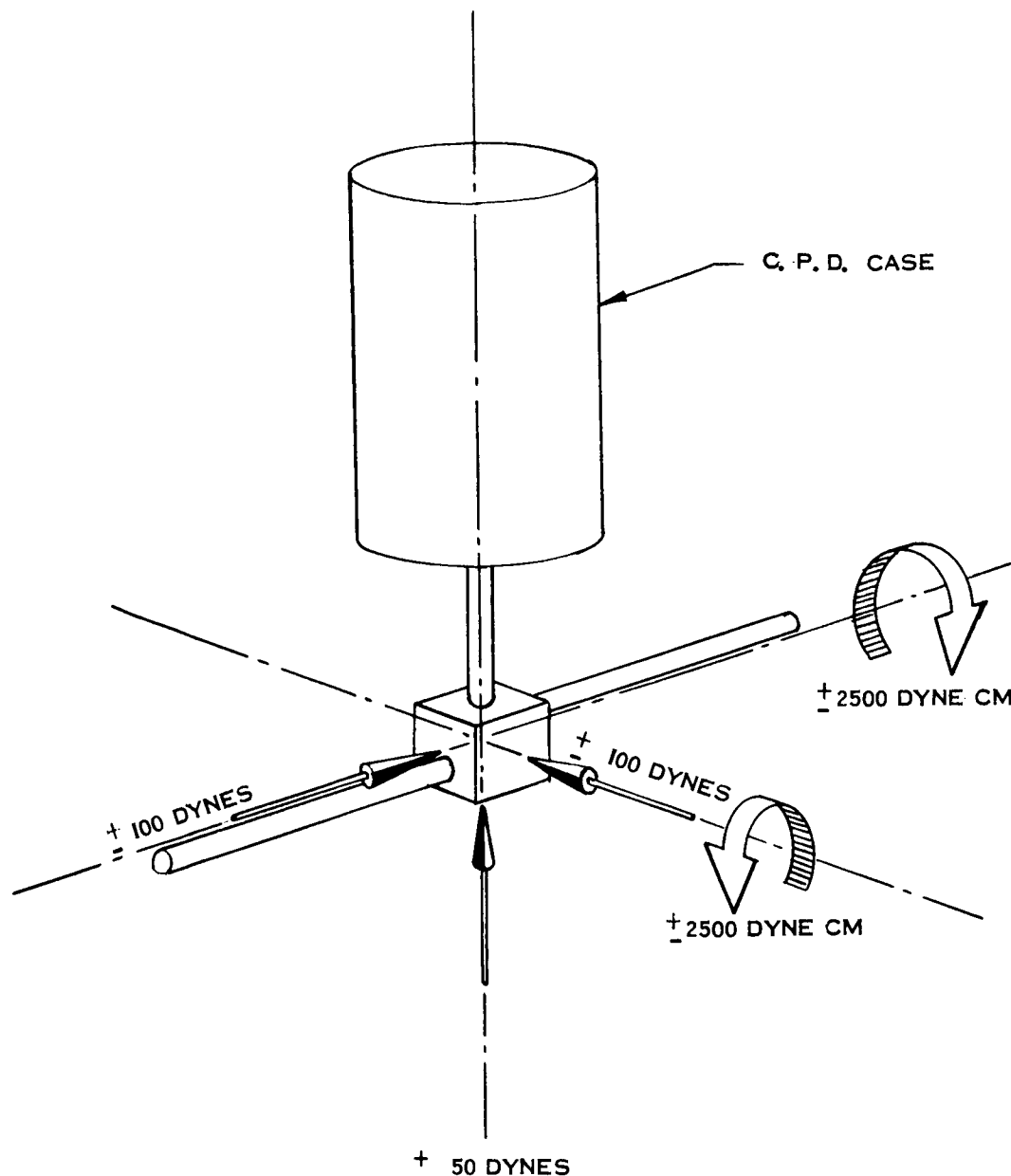


Figure 2.3-2. Preliminary Design Load Requirements

4. Visit to Bell Telephone Labs

This visit was delayed until 25 September by NASA request. Very useful information relative to the hysteresis damper design and test program was obtained during the visit.

2.3.2.1.1 Conceptual Design Progress

Twelve basically different concepts have been carried through layout stage to date with several intermediate variations. Four of these concepts were included in GE Document No. 64SD4326 which was published at the end of the six weeks Program Definition phase. On 12 August, a design meeting was held at GE, and two concepts were selected for further study. Refinement of these two concepts (considering both possible suspensions for the eddy current damper) continued until the decision was reached on 11 September

to use diamagnetic suspension. At approximately the same time, one of the two original concepts utilizing a magnetic clutching principle was discontinued because of magnetic interaction and the difficulties encountered when an attempt was made to replace the magnetic clutch principle with mechanical latches. The remaining original concept has been refined into the current proposed design (Figure 2.3-3) after several iterations.

Another concept (Figure 2.3-4) was developed in the interim, but because of its complexity and questionable reliability in a space environment, it is now considered as a back-up version. The configuration shown is not up to date due to an increase in the number of magnets required in the diamagnetic suspension system and a required redesign in the boom shaft area to accommodate the additional magnets would enlarge the envelope considerably. Work has been discontinued on this concept and all effort is being applied to the concept shown in Figure 2.3-3.

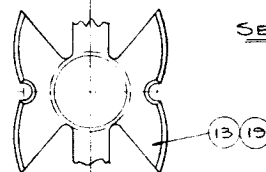
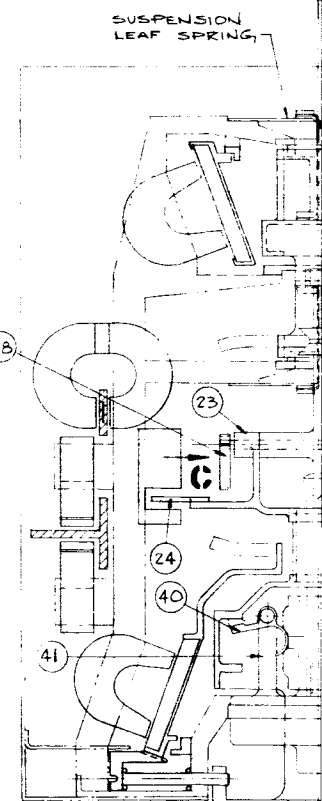
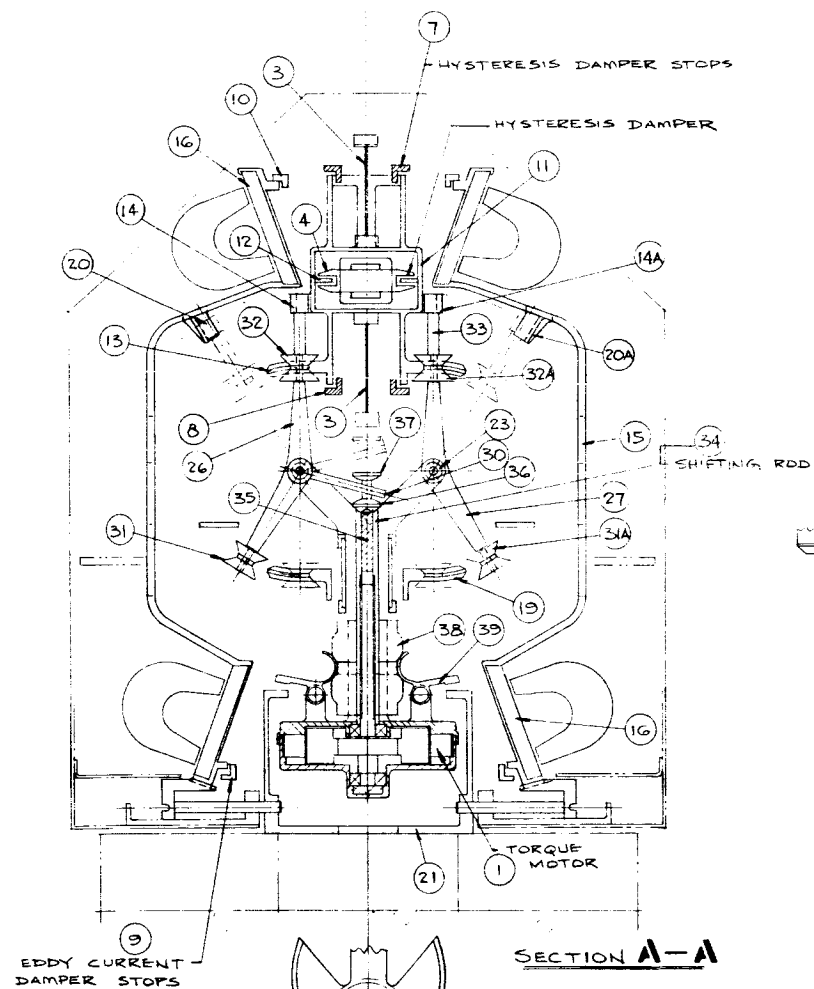
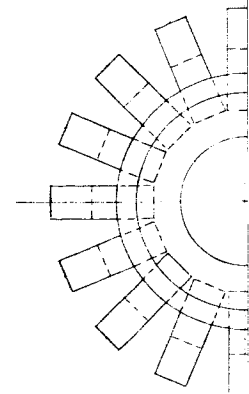
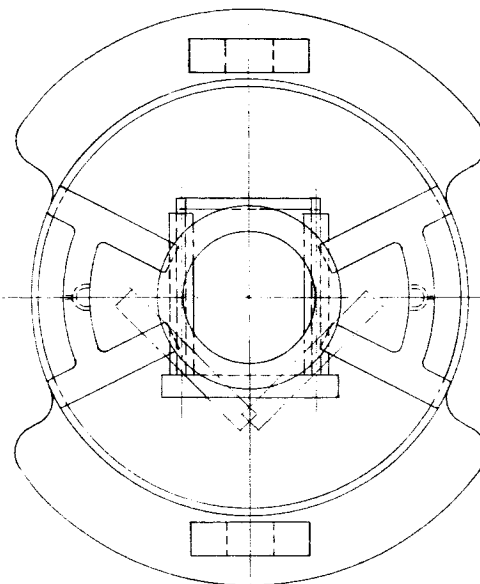
The major problem in all concepts has been the clutching mechanism, which, to fulfill the following requirements, becomes quite complex:

<u>Requirement</u>	<u>Component</u>
Actuating device	Motor
Device to connect boom to the desired damper and provide force and moment reactions	Rotating member (bellcrank, lever, etc.)
Device to align damper index points with boom position at time of clutching	Aligning cam faces on each damper
Free $\pm 45^\circ$ boom rotation when damper engaged	No part can induce friction
Clutching capability at any point within $\pm 45^\circ$ boom rotation range	Strike, clutch, release action mandatory

2.3.2.1.2 Boom Angle Detector

The boom angle detector has presented a major problem as indicated by the fact that only three out of twenty-three potential vendors responded to the preliminary RFQ. The difficulty is the excursion of the boom in three planes, i. e., the boom shaft "floats" and is neither concentric nor fixed during operation with a damper. This makes it extremely difficult for an indicating device to differentiate pure rotation from the translatory movements. The requirements for no friction (thus no direct attachment can be used) and no magnetic devices further complicate the design. A specification (SVS 7315) and a work statement (No. 9744-WS-005) were released on 26 September to three potential vendors for a final bid on the boom angle detector.

The general requirement for the angle detector is that it shall provide a continuous signal that is proportional to the angular displacement of the boom with respect to the CPD package within an accuracy of ± 1 degree for a boom rotation of ± 10 degrees about null, and ± 10 percent in the range of ± 10 degrees to ± 40 degrees about null. Originally, it



PLAN VIEW OF CAN

2.125/2-126

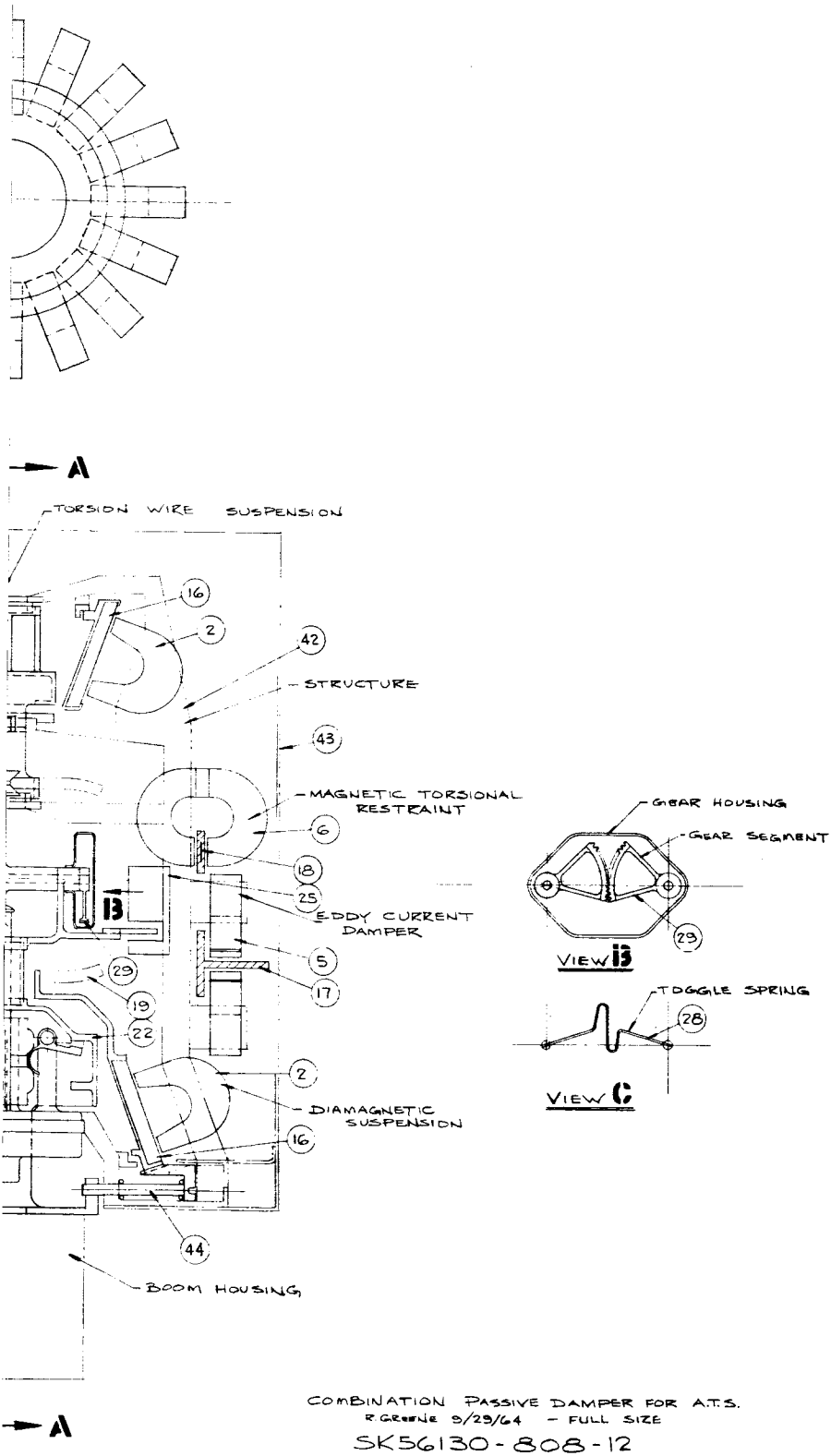


Figure 2.3-3. Combination Passive Damper for ATS

2

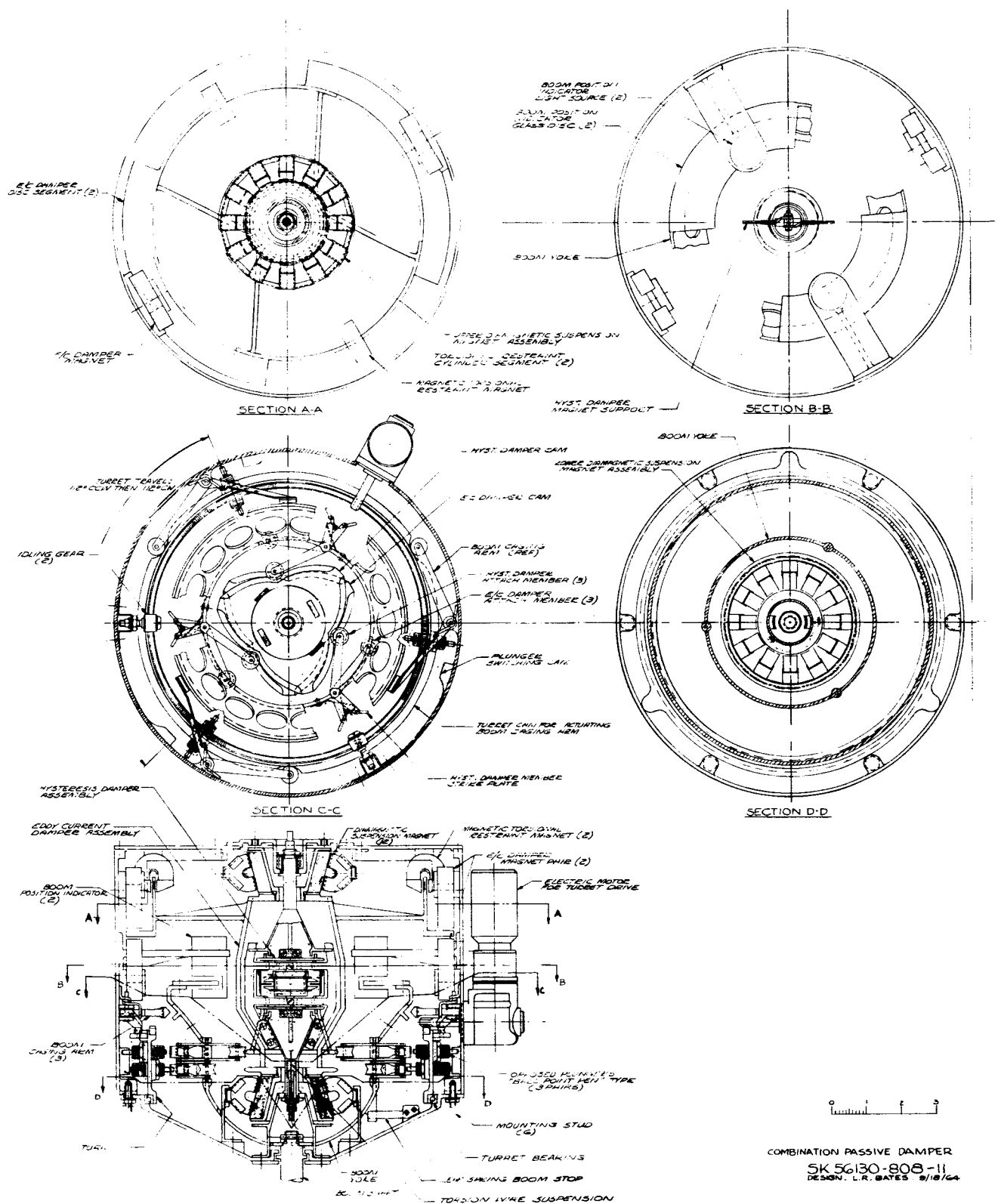


Figure 2.3-4. Combination Passive Damper Details

was thought that an off-the-shelf item with the trade name "Optisyn" could be modified to meet CPD requirements; however, investigation revealed that the "Optisyn" as currently available is not frictionless, and will not allow axial, radial, and cocking motions of the magnitude encountered in the CPD. Therefore, extensive development work would be required, and the "Optisyn" manufacturer is quoting on a system which, in their opinion, is more suitable and less expensive for the CPD application.

2.3.2.1.3 CPD Description and Operation

Figure 2.3-3 represents the current configuration of the Combination Passive Damper (CPD) with numbered component parts as an aid to the description presented below. This configuration is in the preliminary design stage and may change considerably in detail, but it shows the basic concept. Components of the CPD which are attached to basic structure (42) include the torque motor (1), the magnets of the diamagnetic suspension system (2), the supporting leaf springs of the hysteresis damper suspension/torsion wires (3), the magnet assembly of the hysteresis damper (4), the eddy current damper magnets (5), the eddy-current damper torsional restraint magnets (6), the hysteresis damper stop rings (7) and (8), the eddy-current damper stop rings (9) and (10), and the boom angle detector heads (25).

The freely rotating and suspended portions of the hysteresis damper consist of the damper body (11) containing the ferromagnetic damping disc (12), the aligning cam (13), and secondary support cam (14) and (14A).

The rotating and suspended parts of the eddy-current damper consist of the damper frame (15) to which is attached the diamagnetic cones (16), damper disc (17), torsional restraint cylindrical segment (18), the aligning cam (19), and the secondary support cam (20) and (20A).

The boom shaft and switching assembly consists of the boom attach plate (21), boom in-orbit lock housing (22), switching shaft pedestal (23) which includes the boom angle detector disc (24), switching levers (26) and (27), overcenter spring (28), synchronizing gear segments (29) and switching lever (30). The switching levers are composed of rollers (31) and (32), and extensions (33). A shifting rod (34) is engaged to screw jack or other device to convert rotary motion to longitudinal motion (35). The end of the shifting rod (34) is spool shaped with button ends (36) and (37) which actuate the switching lever (30) during switching. Attached to the lower portion of the switching rod and moving with it is a cammed cylinder (38) which operates in-orbit boom lock levers (39) and (40); these are pivoted on the fixed structure motor mount (41).

Assuming the boom is initially attached to the hysteresis damper, a description of the switching operation follows:

Torque motor (1) is actuated which, acting through jack screw (35), actuates the shifting rod (34) upward. Cammed cylinder (38) immediately rotates boom lock levers (39) and (40) to clamp the flange of the boom longitudinally and rotationally. Further longitudinal movement of the shifting rod causes the switching lever (30) to contact button (36)

which rotates switching lever (26) counterclockwise. The geared connection (29) causes switching lever (27) to rotate clockwise simultaneously. At a point in this rotation, the toggle spring (28) goes over center imparting a counterclockwise force to lever (26) whose roller (31) has, by this time, contacted the eddy current damper aligning cam (19) and started aligning the damper to the arbitrary boom position (anywhere within the $\pm 45^\circ$ rotation range). Roller (32) that has left the hysteresis damper aligning cam (13) and extension (33) is approaching the (eddy current) secondary support cam (20). Lever (27) is performing the same motions during this time in an opposite hand manner. As the rollers (31) and (31A) seek the center of cam (19), the shift rod (34) continues its upward motion until switching lever (30) floats freely between the button ends (36) and (37) and cam (38) has released boom locking levers (39) and (40) from the boom housing (22). Switching is thus completed; the boom is attached at four points (31), (31A), (14), and (14A) to, and is restrained rotationally by, the eddy current damper. The hysteresis damper returns to its "null" position through the action of the torsion wire. To switch back to the hysteresis damper, the motor (1) reverses and moves the shifting rod (34) downward.

A preliminary boom and eddy-current damper caging device is indicated (44) and a magnetic shield (43) envelope is also shown in Figure 2.3-3. However, further design effort is necessary to define these areas.

Because of the back-up nature of the concept shown in Figure 2.3-4, a complete description is considered superfluous for this report. However, the basic operating cycle consists of a counterclockwise rotation of the turret through approximately 110 degrees (refer to View C-C in Figure 2.3-4). At this point, both dampers are engaged. The turret is then reversed (clockwise rotation) back to its starting position. The damper levers are actuated during the cycle by "ball point pen" type plungers mounted on the turret. At the end of the counterclockwise rotation, these plungers are reversed by contact with a cam mounted on the structure. Thus the plungers alternately contact and/or clear their respective damper levers during each half cycle. A feature of this design is that it provides in-orbit caging of the boom and both dampers at the end of the counterclockwise rotation by simply stopping the motor at this point.

2.3.2.1.4 Design Analysis of Diamagnetic Suspension of the Eddy-Current Damper

2.3.2.1.4.1 Basis for Utilizing Diamagnetic Suspension

To support the eddy-current damper, it has been decided to use a truly frictionless suspension system - diamagnetic suspension. It has been shown by Maxwell, Jeans, and Tonks, based on the work of Samuel Earnshaw, that a stable suspension system which uses only passive magnetic elements (such as permanent magnets) can be obtained only if the elements being acted upon by the magnets have a permeability of less than unity (i.e., negative susceptibility). Some types of active control (with sensors, feedback, etc.) must be used if a stable suspension is to be obtained with elements having a permeability of greater than unity (i.e., paramagnetic or ferromagnetic materials which have positive susceptibility).

2.3.2.1.4.2 Selection of Materials

The force acting on a body placed in a magnetic field is discussed in paragraph 2.3.2.1.4.5 (Analytical Approach). In these equations, it is shown that the force is directly proportional to the susceptibility of the material which is being acted upon. Diamagnetic materials with their negative susceptibility are repelled by a magnetic field. Many materials are slightly diamagnetic, but those having the largest negative susceptibilities (and thus capable of the largest repulsion forces) are bismuth and pyrolytic graphite. The volume susceptibility of bismuth is -13×10^{-6} and that of pyrolytic graphite perpendicular to the deposition plane is approximately -47×10^{-6} . Thus, the actual susceptibility realizable for support forces depends upon the configuration of the magnetic field and its relationship to the graphite in the field.

Bismuth was used by General Electric in early experiments on diamagnetics and was subsequently used in the construction of the PODS damper because of ready availability and ease of manufacture. Since that time, pyrolytic graphite has become more generally available and its various physical properties more accurately defined. Graphite has the advantage of a density which is only 22.5% of that for bismuth. Therefore, in the interest of obtaining maximum suspension capability with minimum weight, pyrolytic graphite will be used in the suspension of the eddy current damper.

2.3.2.1.4.3 Suspension Loads

As indicated above in paragraph 2.3.2, preliminary external load requirements have been established for the design of the CPD. These loads are exerted by the damper boom on the damper rotor and are caused by external forces such as inertial effects and solar pressure. Both the diamagnetic suspension for the eddy current damper and the wire suspension for the hysteresis damper must be able to withstand these forces. However, the diamagnetic suspension must be capable of supporting not only these external loads, but also an internal load - the "lateral force" from the magnetic torsional restraint. This lateral force of attraction varies with displacement from null, and has been measured to be about 10,000 dynes per inch, or ± 600 dynes for ± 0.060 inch displacement. These loads on the diamagnetic suspension are summarized below:

<u>Symbol</u>	<u>Load</u>	<u>Magnitude</u>
P_r	External Radial Force	± 100 dynes
P_a	External Axial Force	± 50 dynes
Q	External Cocking Torque	± 2500 dynes-cm
W	Internal Radial Lateral Force	± 600 dynes

Any combination of these loads can be supported by two radial diamagnetic reaction forces of 500 dynes, separated by 8 inches - such as is planned for the conceptual design of the CPD.

2.3.2.1.4.4 Diamagnetic Forces

In order to determine the optimum suspension design, considering the type and quantity

of magnets, material of diamagnetic rotor, cone angle and thickness of diamagnetic rotor, and air gap spacing, it is necessary to know the repulsion force versus air gap characteristic for a single magnet in combination with the diamagnetic material. These characteristics have been obtained for a variety of magnets in combination with both bismuth and pyrolytic graphite in a variety of thicknesses. These results have been obtained experimentally by direct measurement of forces, and also analytically, based on measurement of the magnetic field pattern for a given magnet.

2.3.2.1.4.5 Analytical Approach

The force exerted on a diamagnetic specimen (see Figure 2.3.1-5) in a non-uniform field may be expressed as follows:

$$dF = \frac{1}{2} K \frac{dH^2}{ds} dv \quad (1)$$

where

F = force, dynes

K = volumetric susceptibility of the specimen, cgs units/cu cm

H = field strength, oersteds

v = volume of specimen, cu cm

s = distance from pole face, cm.

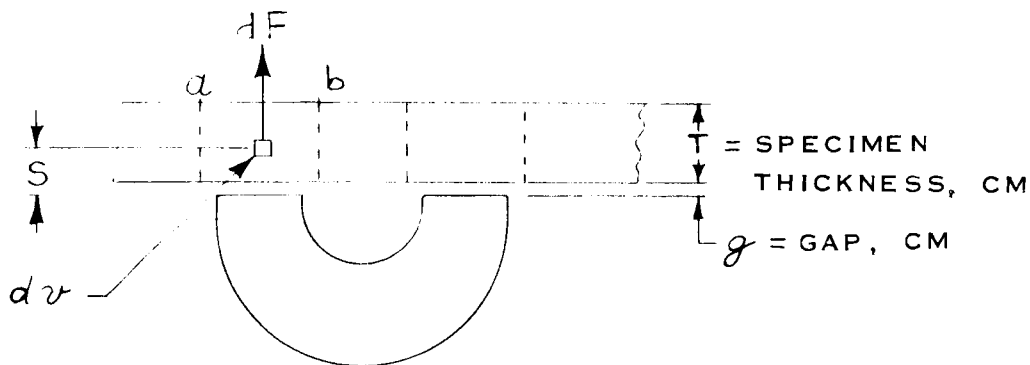


Figure 2.3-5. Force on Diamagnetic Specimen in Non-Uniform Field

The field strength was measured as a function of distance from the pole face for several magnets. When values for H^2 were plotted against s , it was found that a decaying exponential curve gave a very close approximation of the measured data.

$$H^2 = H_0^2 e^{-ms}$$

$$\frac{dH^2}{ds} = -H_0^2 m e^{-ms} \quad (2)$$

where

H_0 = field strength at $s = 0$

$-H_0^2 m$ = initial slope, oersted²/cm

m = decay rate, cm⁻¹

A simplifying approximation was made by assuming that the same value of dH^2/ds exists for a given value of s , at points between a and b , which define the effective pole face area. It was further assumed (based on analysis of extensive test data) that the effective pole face area equals 1.8 times the actual pole face area. The differential volume for both poles, dv , may then be expressed as follows:

$$dv = 2 \times 1.8 A ds \quad (3)$$

where A = actual pole face area, sq cm

The total force on specimen, from both magnet poles, is obtained by combining Equations 1 and 3:

$$dF = \frac{1}{2} K (-H_0)^2 m e^{-ms} (2 \times 1.8 A ds)$$

By integration,

$$\begin{aligned} F &= \int dF = -\frac{1}{2} K H_0^2 m (2) (1.8) A \int_g^{g+T} e^{-ms} ds \\ &= -1.8 AK H_0^2 m \left[\frac{e^{-ms}}{m} \right]_g^{g+T} \\ &= -1.8 AK H_0^2 \left[e^{-m(g+T)} - e^{-mg} \right] \\ &= -1.8 AK H_0^2 \left[e^{-mT} - 1 \right] e^{-mg} \\ F &= 1.8 AK H_0^2 (1 - e^{-mT}) e^{-mg} \quad (4) \\ F &= F_0 e^{-mg} \end{aligned}$$

Equation 4 expresses the force between one magnet and a specimen in a non-uniform field. If the specimen is diamagnetic, the susceptibility, K , is negative, and the force is repulsive. The factor $(1 - e^{-mT})$ shows the dependence of force on the thickness, T , of the specimen. The force is seen to decay exponentially with air gap, g .

2.3.2.1.4.6 Experimental Approach

For the many measurements which have been made of force versus air gap, it has been found possible to fit a decaying exponential characteristic to the measured data. This characteristic to the measured data. This characteristic is of the following form:

$$F = a + F_0 e^{-mg} \quad (5)$$

This form differs from the analytical result only by the constant term, a .

2.3.2.1.4.7 Diamagnetic Suspension Design Equations

The diamagnetic suspension consists of a conical diamagnetic element located at each end of the rotor, and a ring of n magnets fixed to the stator, equally spaced around the diamagnetic cone, as shown schematically in Figure 2.3-6.

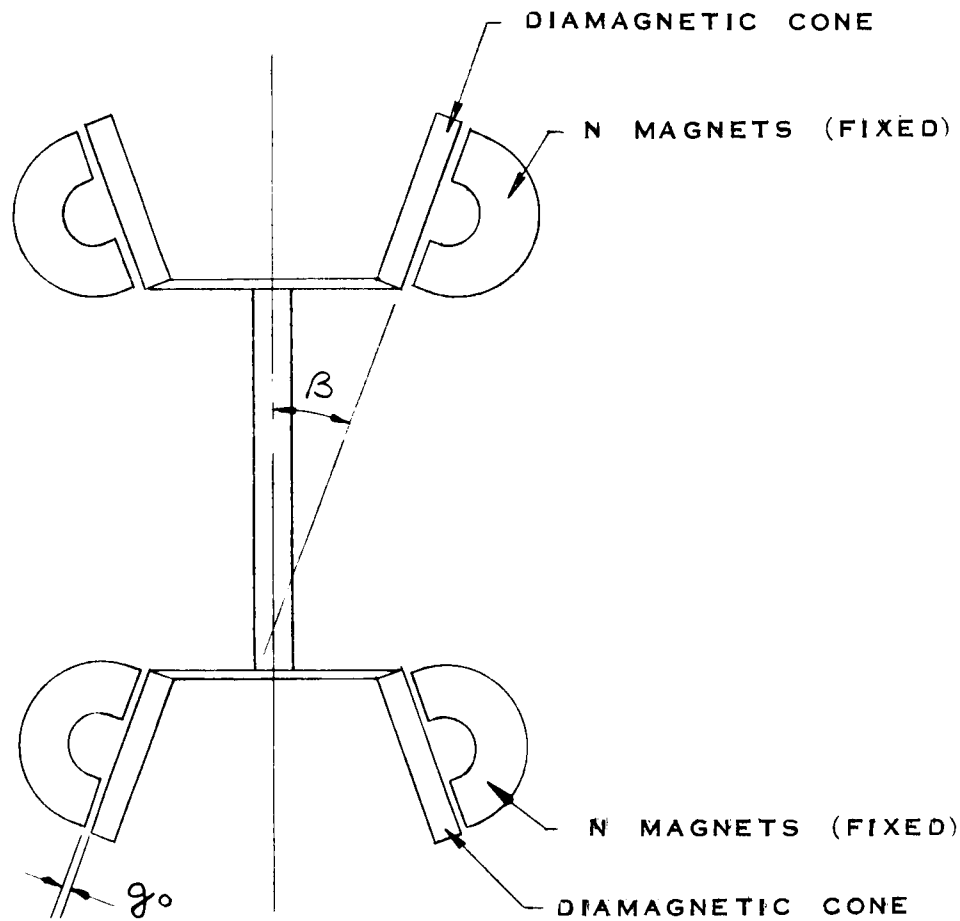


Figure 2.3-6. Diamagnetic Suspension Schematic

The diamagnetic forces tend to keep the rotor centered in the null position. The general shape of the force versus displacement characteristic of a diamagnetic suspension has been shown both analytically and experimentally to have the non-linear form of Figure 2.3-7.

For component design purposes, a linear approximation may be used, as follows:

$$F = -Kx$$

where

F = restoring force

x = displacement from null

K = slope of the actual characteristic at null point.

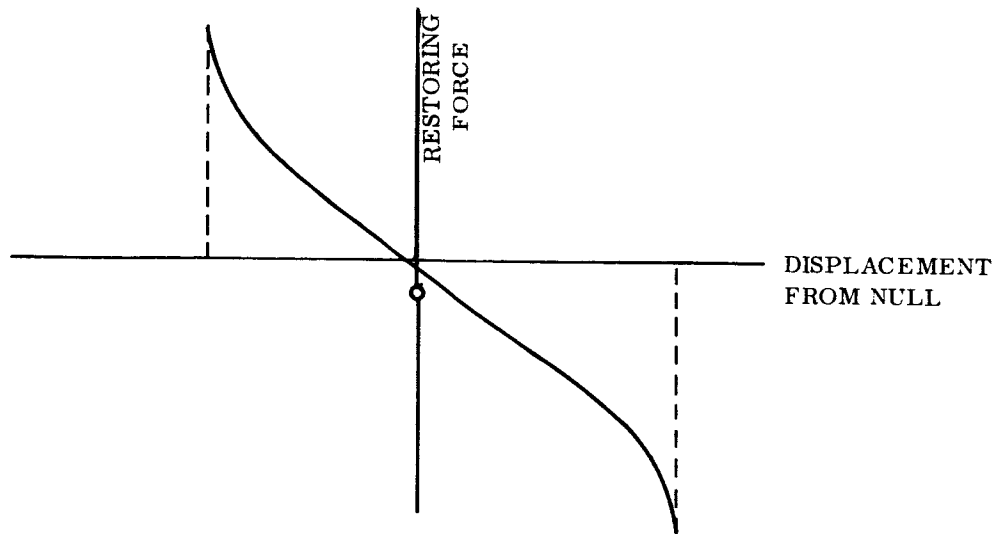


Figure 2.3-7. Diamagnetic Suspension Characteristic

The value of K represents the force gradient, or stiffness, of the suspension at the null position. Since the stiffness actually increases with displacement, use of the linear approximation yields a properly conservative design.

The radial force gradient at the null point of a diamagnetic suspension has been found to be as follows:

$$K_r = \left. \frac{dPr}{dr} \right]_{r=0} = F_o m e^{-mg_o} \frac{n}{2} \cos^2 \beta \quad (6)$$

where $F_o e^{-mg}$ can be determined from the equation $F = a + F_o e^{-mg}$ which expresses the single magnet force versus gap characteristic, and the symbols are as previously defined. This expression represents the stiffness due to one diamagnetic cone and n magnets. The total force capacity at that end of the rotor is found by multiplying K_r by the radial displacement at that end.

Similarly, the axial force gradient at the null point of a diamagnetic suspension has been found to be as follows:

$$K_z = \left. \frac{dP_z}{dz} \right]_{z=0} = F_o m e^{-mg_o} n \sin^2 \rho \quad (7)$$

This expression represents the axial stiffness at each end of the suspension. The total axial force gradient due to both ends of the suspension is $2K_z$. The total axial force capacity is found by multiplying $2K_z$ by the axial displacement of the rotor.

2.3.2.1.4.8 Sample Calculation

Determine the suspension characteristics for a design which uses 12 magnets (Type CU-506) at each end, and a pyrolytic graphite cone ($\beta = 20^\circ$) which is 0.25 inch thick. The initial air gap, g_o , is set at 0.060 inch = 0.15 centimeter. The single-magnet force

characteristics for a CU-506 magnet in combination with 0.25 inch pyrolytic graphite was found experimentally to be as follows:

$$F = 15 + 335 e^{-4.4g}$$

where

F = force, dynes

g = gap, centimeters

and

$$a = 15 \text{ dynes}$$

$$F_0 = 335 \text{ dynes}$$

$$m = 4.4 \text{ cm}^{-1}$$

These values are substituted into Equation (6) to determine the radial stiffness at each end of the rotor:

$$K_r = (335) (4.4) e^{-4.4(0.15)} \frac{12}{2} \cos^2 20^\circ$$

$$K_r = 4040 \text{ dynes/cm.}$$

If the load on the suspension at each end is 500 dynes, then the radial displacement at each end will be

$$r = \frac{Pr}{Kr}$$

$$r = \frac{500}{4040} = 0.124 \text{ cm}$$

or 0.049 inches.

This is well within the 0.060-inch initial air gap, indicating that this particular design will support the specified load of 500 dynes at each end of the suspension. As a check for axial support, the axial displacement will be calculated for the specified 50 dyne load. From Equation (7), the axial stiffness at each end is as follows:

$$K_z = (335) (4.4) e^{-4.4(0.15)} (12) \sin^2 20^\circ$$

$$K_z = 1070 \text{ dynes/cm each end}$$

$$\begin{aligned} \text{The total axial stiffness} &= 2K_z \\ &= 2140 \text{ dynes/cm.} \end{aligned}$$

Under the specified axial load of 50 dynes, the rotor will displace $\frac{50}{2140} = 0.0234 \text{ cm}$
or 0.009 inch.

Thus, the given design will support all combinations of the originally specified loads; i. e. ± 100 dynes external radial force, ± 50 dynes external axial force, ± 2500 dyne-cm external cocking torque, and ± 600 dynes internal radial lateral force from the magnetic torsional restraint.

It is also important that the total radial force gradient from both ends be greater than the radial force gradient of the magnetic torsional restraint, which is given as 10,000 dynes per inch, or 3930 dynes per centimeter. This criterion is more than satisfied, as the total radial stiffness of this design is $2(4040) = 8080$ dynes per centimeter.

2.3.2.2 Development Testing

2.3.2.2.1 Torsional Restraint

During the first six weeks of this quarterly report period, a major portion of the development engineering effort on the Combination Passive Damper was spent in establishing the feasibility and practicability of the magnetic torsional restraint element for the eddy-current damper. The results of this work are reported in General Electric Document No. 64SD4326, which has previously been submitted to the Goddard Space Flight Center but is summarized here for convenience.

In these tests, the desired torsional restraint (i. e., the apparent spring constant) obtained from the ferromagnetic torquing member as well as the accompanying (but undesired) lateral force were determined. These characteristics were measured as a function of:

1. Presence or absence of pole pieces
2. Gap length
3. Flux density
4. Misalignment (tilting) of torsional restraint element

It was concluded from the results of these tests that:

1. Torsional and lateral forces are approximately proportional to flux density
2. The ratio of the lateral force to torsional force is independent of flux density
3. Pole pieces reduce the ratio of lateral force to torsional force
4. Larger air gaps produce less lateral force and a smaller ratio of lateral force to torsional force.
5. Tilting the torsional member with respect to the imposed magnetic field had little effect on the torsional force.

It was also found in these tests that it is practical, within the expected physical limitations of the CPD package, to provide a ferromagnetic torsional restraint element which will have the required effective spring constant that is linear over the required $\pm 45^\circ$ travel of the damper. The element is a relatively simple geometric shape (crescent or

variation thereof) which should cause no fabrication problems. The development effort established that Type 302 stainless steel, which had been suitably cold worked, was the optimum material to use for the torsional element.

Therefore, it was concluded that a torsional restraint member could be designed that would supply the proper spring constant and could be supported by the diamagnetic suspension system planned for the eddy-current damper.

2.3.2.2.2 Mechanical Hysteresis Loss of Torsion Wire Suspension

In considering the techniques which might be utilized to support the eddy-current damper, a torsion wire suspension is an obvious candidate. However, the inherent hysteresis loss present in a torsion wire suspension could mask the damping effects obtainable from the eddy-current damper if this loss were large enough. During the first six weeks effort, the relative magnitude of this loss was evaluated and the results also reported in General Electric Document No. 64SD4326. It was concluded in the report that with the torsion wires required for the eddy-current damper in this application, the mechanical hysteresis loss would be less than 1% of the required eddy-current damping. Although such a suspension would be practical, it has been decided because of other considerations to utilize a diamagnetic suspension for the eddy-current damper.

2.3.2.2.3 Hysteresis Damper

Tests to permit evaluation of some of the operating characteristics of the hysteresis damper were initiated during the reporting period. In these tests, a simplified arrangement (shown in Figure 2.3.1-8) of a hysteresis damper utilizing an annular disc of cold rolled steel attached to a weighted plastic disc was suspended above a rate table by a long torsion wire. The torsion wire and rate table were so located that their respective axes were collinear. A total of three discs were tested with thicknesses of .0001, .002, and .004 inch. A magnet was attached to the rotating table top and placed so that the damping disc was between the North and South pole of the combined magnet arrangement.

When the table was driven at very low speeds, it was observed that, as soon as the magnet started rotating, the disc became "locked" on to it. This observation was

somewhat different from the results reported by the Bell Telephone Laboratories (BTL) where a lag of about 8 degrees was noted before "lock-on" occurred. Subsequent discussions with BTL revealed that the apparent contradiction existed because of a difference in flux paths in the two arrangements. In GE's test set up, the path of the flux is through the disc and at a right angle to the disc. Because of a different magnet arrangement, BTL caused the flux to enter at one point on the magnetic disc, pass longitudinally around its periphery for 180° and then emerge to the other pole of the magnet. Thus, in the BTL design, approximately 8 degrees was required to cause the induced poles in the magnetic disc to switch and develop full damping torque.

Because of the flux path in the GE tests, pole switching occurred immediately and no $\Delta \theta$ was observed.

However, in the GE test set up it was noted that the damping disc would smoothly follow the magnet for about 20° - 30°, at which point the coupling torque would drop markedly and the rotor "slip" back some 20°. While the subsequent discussions with BTL did not

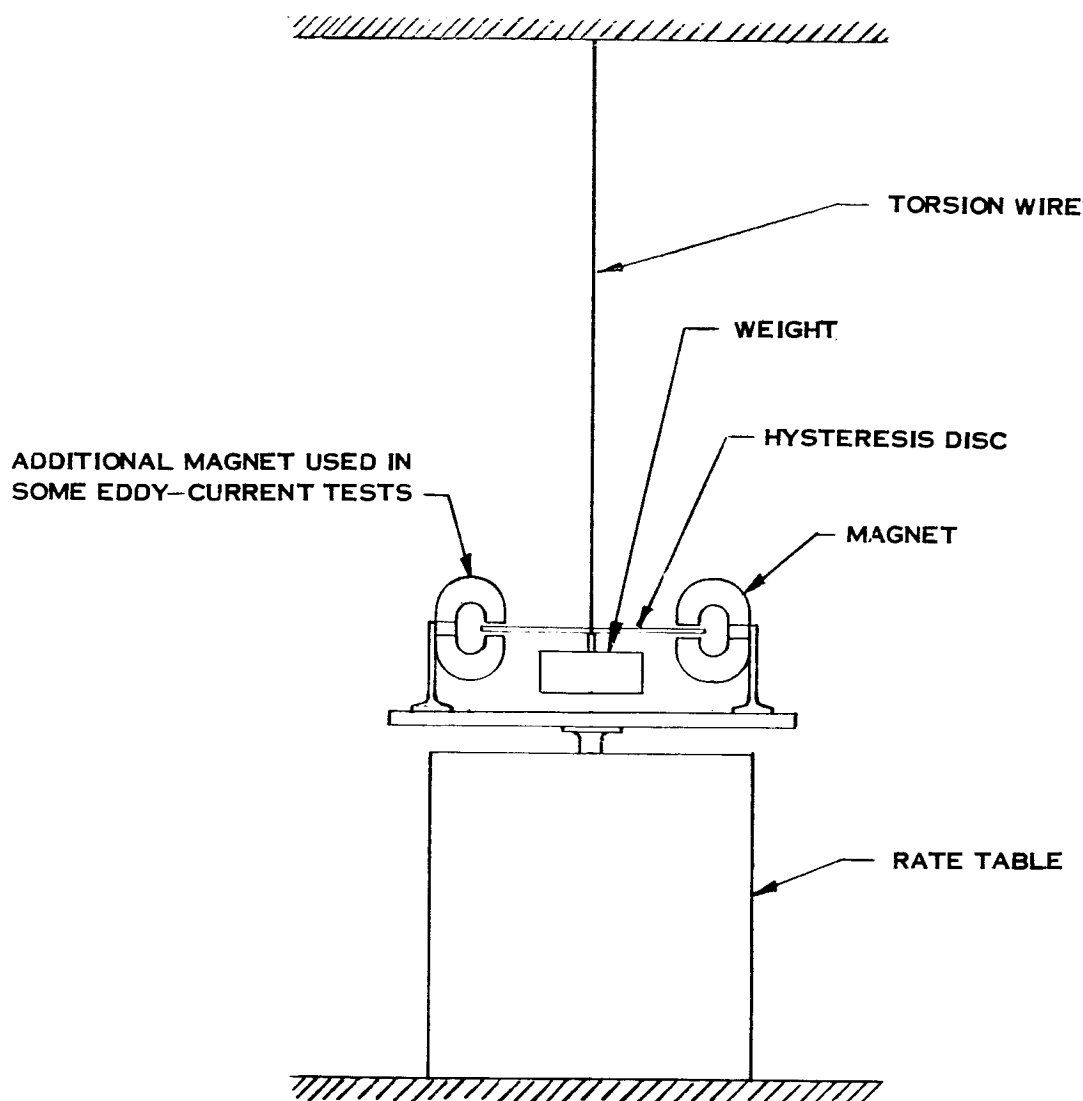


Figure 2.3-8. Simplified Hysteresis Damper

result in any clear-cut, definitive decision as to the cause of this "cogging" effect, it was concluded that the flux path of GE test set-up made the damping torque more sensitive to minute, localized variations in the magnetic properties of the damping disc. BTL has noted similar effects in some of their early testing but not to the large degree observed by GE.

It should be pointed out that one of the more valuable elements of the work on the hysteresis damper performed during this period was the visit and discussion with the engineers at the Bell Telephone Laboratories. They were extremely helpful in discussing with GE engineers their problems and the solutions they had achieved during their development activity on the hysteresis damper. It is felt that this contact will result in a much more efficient development program for the hysteresis damper.

To continue the development effort on the hysteresis damper, two pieces of test equipment were designed during the period of this report and are now being fabricated by the Manufacturing Operation. One piece of equipment has been designed to permit a

hysteresis damper (which is essentially identical to the damping elements of the BTL unit) to be placed on a rate table and its damping characteristics evaluated. This unit can then be utilized to evaluate the magnet and disc configuration required to meet the damping requirements of ATS (which are of much less magnitude than those for which the original BTL damper was designed). The second piece of engineering test equipment is to permit exploratory tests on means of attachment to the torsion wire suspension. It will also be used to:

1. Measure fatigue life of various attachment means and of several configurations of torsion wire
2. Measure the spring rates obtained from various torsion wires
3. The effect of wire tension on torsion rates.

2.3.2.2.4 Eddy Current Damper

The damping coefficient of an eddy-current damper may be expressed as follows:

$$B^2 = K \gamma B^2 D^2 \eta$$

where b = damping coefficient (torque/angular velocity)

K = proportionality constant

γ = electrical conductivity of damper disc material

B = flux density through disc

D = distance of magnet from axis of rotation

η = number of magnets

From this equation the fruitful areas for application of development engineering effort can be identified. Each factor will be discussed in turn to illustrate its effect on the damper design. As in all equations of this type, the proportionality constant assures dimensional compatability, is independent of these factors, and is fixed. The diameter of the circle at which the magnets are placed is limited by the physical demensions allowed for the package. In the physical design of the CPD, the eddy-current magnets are placed at the maximum radius possible which is outside of all other functional elements of the package. It is planned to use only two pairs of magnets for this damper because of physical constraints on the mechanical design of the CPD.

The electrical conductivity of the disc is affected by the:

1. Material used in its construction
2. Thickness of the disc
3. Configuration of the return path for the eddy-current generated in the disc.

As will be discussed later, the present design can utilize an aluminum disc and still provide adequate damping torque. Increasing the thickness of the disc increases its conductivity but also reduces the flux density obtainable from a given magnet. Since thickness directly affects conductivity, and damping is proportional to the square of flux density, a tradeoff evaluation is necessary before the thickness can be chosen for the

final design. It has been found that if the magnets are placed too close to the edge of the damper disc, the conductivity of the return path for the eddy-current in the disc is too low. Therefore, care will be taken to assure adequate clearance from the magnet to the edge of the disc.

The remaining factor, flux density, has been the object of considerable engineering effort during the report period. Measurements have been made of the total flux and the flux density as a function of air gap. These measurements were made using a CU-507 magnet, the same magnet that was used in the damper built for the Passive Orientation and Damping System (PODS) by General Electric in 1963. Tests were made to be certain that the method used in charging the magnets resulted in maximum stored energy being imparted to the magnet for every measurement point. The results of these flux tests are shown in Figure 2.3-9 and 2.3-10 where flux density is plotted as a function of air gap and for various magnetic circuit configurations. Since flux density is a parameter which is difficult to measure accurately, the data plotted in Figure 2.3-9 was taken to establish the general validity of the data, at least on a comparative basis. Flux density was determined for this plot both by measuring the total flux in the air gap and by using a different instrument which actually indicates flux density. It can be seen that although the curves are not coincidental they have the same general shape. It was found that the flux density increased inversely as the square root of the gap length. Measurements were also made of the effect of various types of pole pieces as shown in Figure 2.3-10. The flux density followed the same shape shown in Figure 2.3-9 and it was found that there is some increase in flux density due to tapered pole pieces.

The real measure of the value of various configurations is the change in damping torques obtained. A test set up similar to that shown in Figure 2.3-8 (modified as indicated) was used to evaluate the effects of various configurations with a copper disc approximately 6 inches in diameter substituted for the plastic disc of the hysteresis test. The results of these tests are tabulated in Table 2.3-1. A comparison of the tests: 1 and 2, 1 and 4, 5 and 6, and 5 and 7 is inconclusive as to the merit of pole pieces. Additional tests are planned to determine why such tests do not demonstrate the advantage of pole pieces that theoretically should be present. Figure 2.3-11 depicts the arrangement of magnets used for the single penetrations and double penetration referred to in Table 2.3-1. A comparison of Tests 5 and 10 indicates the twofold increase obtained with the double penetration configuration. Tests 10 and 13 indicate the gain achievable by reducing the air gap.

The system requirement for damping torque from the eddy-current damper is approximately 1,560,000 dyne-cm-seconds. To achieve this value, various techniques must be utilized to increase the torque obtained in Test 13. The basic equation given above for eddy-current damping will be examined to determine the feasibility of reaching the design value.

In comparing the damping torque of the test damper (b_t) to that of the actual design (b_d), a slight modification of the basic damping equation is used:

$$b_d = b_t \left(\frac{D_d}{D_t} \right)^2 \left(\frac{B_d}{B_t} \right)^2 \left(\frac{\rho_t}{\rho_d} \right) \left(\frac{\eta_d}{\eta_t} \right) \left(\frac{t_d}{t_t} \right)$$

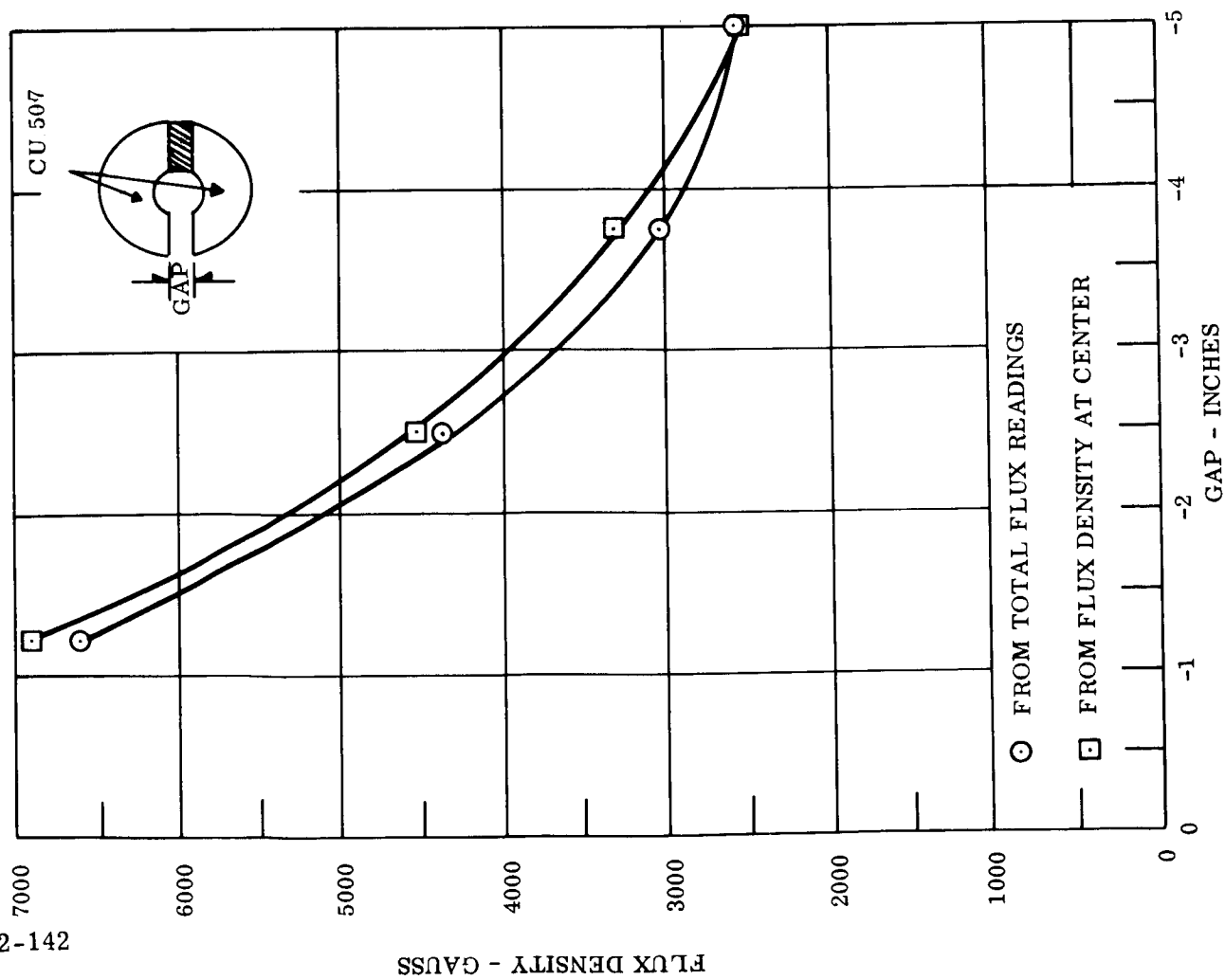


Figure 2.3-9. Flux Density Measurements

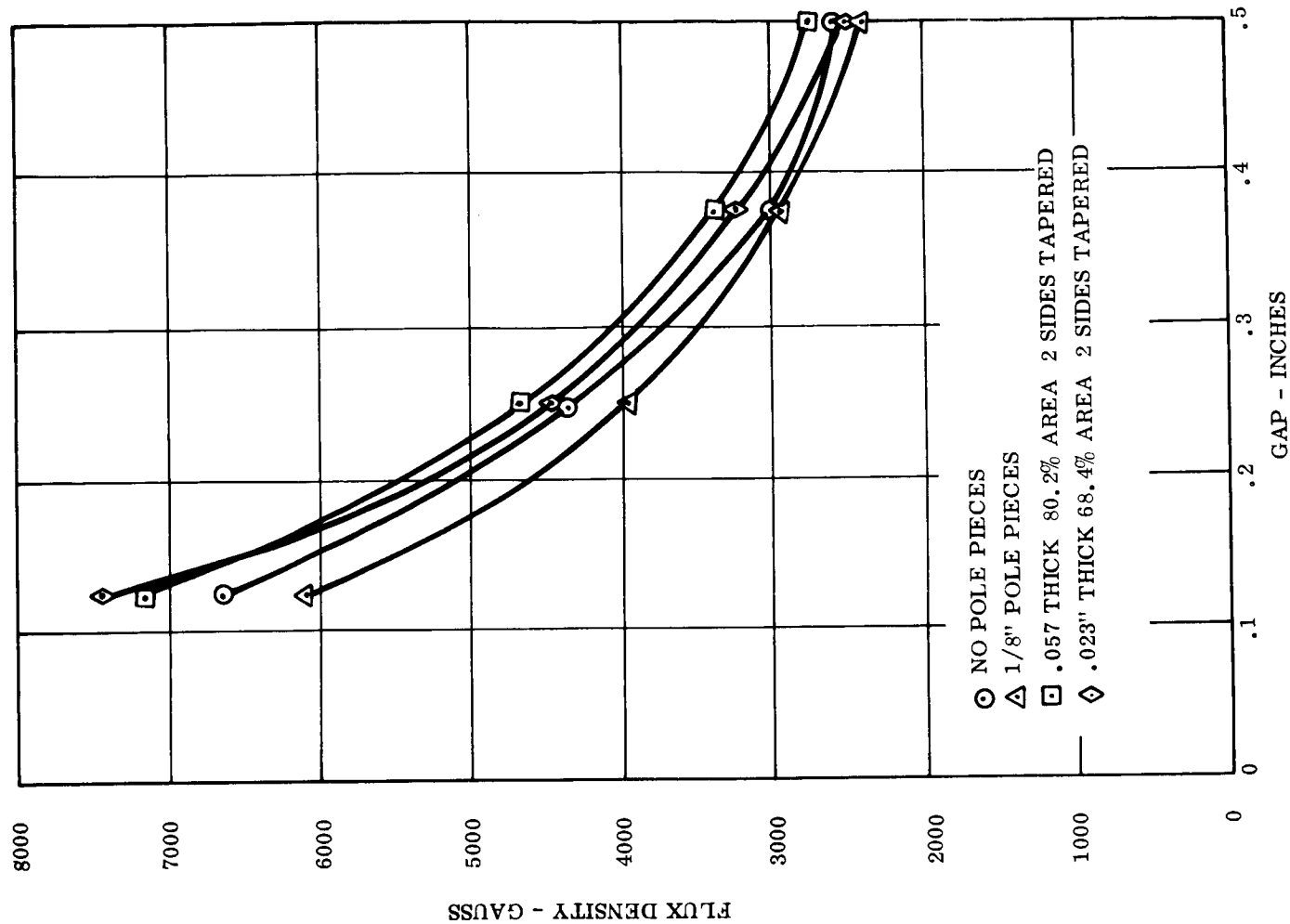
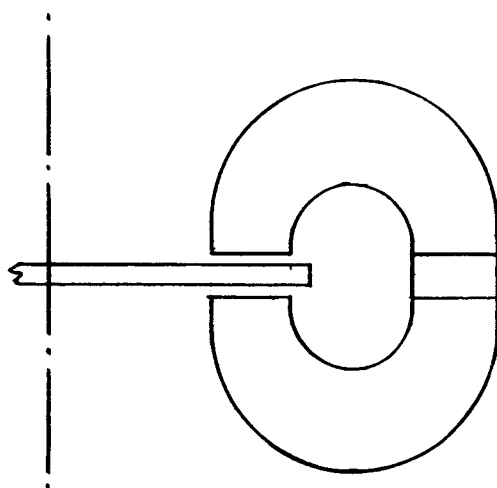
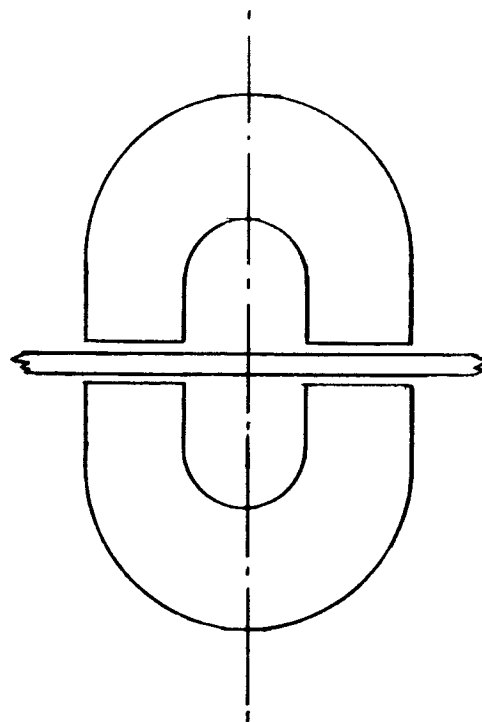


Figure 2.3-10. Flux Density Measurements Effect of Pole Pieces



SINGLE PENETRATION



DOUBLE PENETRATION

Figure 2.3-11. Magnetic Arrangement for Single and Double Penetration

where: subscript "d" refers to design values, subscript "t" refers to test values

ρ = resistivity of damper disc

t = thickness of damper disc

and other symbols are as used previously.

TABLE 2.3-1 DAMPING TORQUE OF EDDY CURRENT DAMPER

TEST CONSTANTS: 1. All Magnets CU 507

2. .125 in. Copper Disc, 5.85 in. dia.

Test No.	Magnet Arrangement	Air Gap (in.)	Pole Pieces	Radius (in.)	Damping Constant Dyne-cm- sec
1	2 single penetrations	.25	None	2.06	218,000
2	2 single penetrations	.25	1 Mag only 80% *	2.06	222,000

* Percentage indicates ratio of area of pole piece face as compared to magnet face area

TABLE 2.3-1. DAMPING TORQUE OF EDDY CURRENT DAMPER
(Continued)

Test No	Magnet Arrangement	Air Gap (in.)	Pole Pieces	Radius (in.)	Damping Constant Dyne-cm- sec
4	2 single penetrations	.25	2 Mags each 50%	2.06	209,000
5	1 single penetration	.25	None	2.06	105,400
6	1 single penetration	.25	Yes-56% area	2.06	98,000
7	1 single penetration	.25	Yes-80% area	2.06	110,000
8	1 single penetration	.25	Yes-80% area	2.31	111,000
9	1 single penetration	.25	Yes-80% area	2.56	89,500
10	1 double penetration	.25	None	2.00	228,000
11	1 single penetration	.195	None	2.31	171,000
12	1 single penetration	.195	None	2.31	142,000
13	1 double penetration	.195	None	2.31	336,000

Then the following factors may be used to determine how the required damping may be achieved in the design of the CPD:

$$\frac{D_d}{D_t} = \frac{4}{2} = 2 \quad (\text{measurement of parts})$$

$$\frac{B_d}{B_t} = \frac{5000}{4500} = 1.11 \quad (\text{flux measurement indicates some improvement in design})$$

$$\frac{\rho_t}{\rho_d} = .6 \quad (\text{ratio of resistivity of copper to aluminum})$$

$$\frac{\eta_d}{\eta_t} = \frac{4}{2} = 2 \quad (\text{design})$$

$$\frac{td}{t_t} = \frac{.100}{.125} = .8 \quad (\text{measurement of discs used or to be used})$$

$$\therefore b_d = 336,000 \times 2^2 \times 1.11^2 \times .6 \times 2.0 \times .8$$

$$= 1,600,000 \text{ dyne-cm-seconds}$$

Thus it can be seen that the calculated damping is only slightly higher than the actual damping required. However, there are still several changes available which can provide a greater margin, if it is found to be necessary: (1) the design diameter may be made as much as 25% larger; (2) pole pieces may prove to provide somewhat more flux density;

- (3) the disc could be made of copper and accept the penalty of slightly higher weight;
- (4) a more optimum disc thickness may be found considering the thickness effect on flux density and resistance of the disc. Therefore, it is concluded that the required eddy-current damping is feasible within the presently defined envelope.

2.3.2.2.5 Diamagnetic Suspension

As indicated in paragraph 2.3.2.1.4.2 (Selection of Materials), the actual susceptibility of graphite is difficult to define accurately and, more pointedly, it is not possible to determine the suspension capabilities of the graphite-magnet system from pure theoretical analysis. Therefore, a number of samples of graphite have been obtained from various vendors and measurements of force available have been made during this reporting period. Since the force available from an assembled bismuth suspension system is known from the PODS damper, measurements were made on bismuth samples to provide a basis of reference for the tests performed. Two pieces of equipment have been used to make these measurements. In the method shown in Figure 2.3-12, the diamagnetic material was mounted on a disc that was suspended from a torsion wire; a test magnet was secured to a rotating table placed under the disc so that its rotation was coaxial to the torsion wire. A light beam reflected from the disc onto a scale which could be seen behind the disc arrangement. This reflection was used as a measure of the rotation of the disc which, in turn, was a measure of the force being exerted upon the diamagnetic material by the magnet.

The other equipment utilized is the Low Order Force Fixture (LOFF) developed by the General Electric Company. The LOFF is shown set up for measuring the diamagnetic

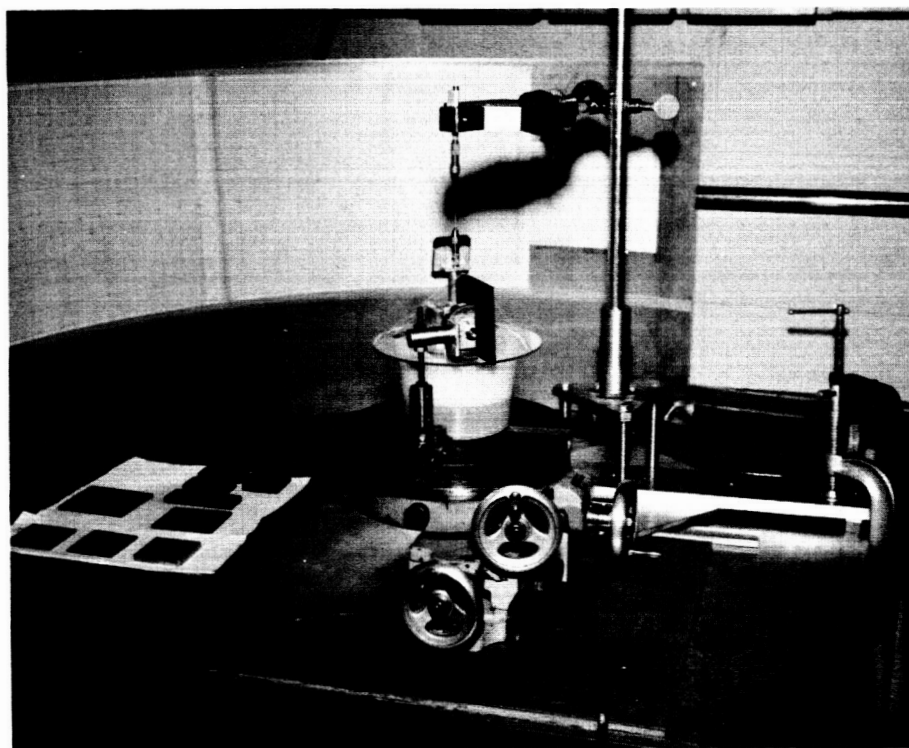


Figure 2.3-12. Diamagnetic Suspension Test Set-Up Using Bismuth Samples

force of the pyrolytic graphite system in Figure 2.3-13. Figure 2.3-14 shows an overall view of the LOFF as set up for a test run in 1963 on the PODE damper. This picture shows the general arrangement more clearly while Figure 2.3-13 shows the equipment as set up for the force versus displacement measurements for diamagnetic material. The LOFF utilizes a spherical gas bearing for supporting the weight of the element being tested. The structure to which the air bearing is attached is mounted on a leveled eight-inch thick stone plate which is supported by an angle-iron framework. The gas bearing is rigidly attached to a horizontal arm and the test sample is attached to the end of the arms. Beneath the arm, and concentric with the vertical axis of the gas bearing, is fastened a calibrated torsion wire. A precision dividing head, mounted below the torsion wire and under the stone slab, is attached to the wire which is passed through a hole drilled in the slab. The dividing head imparts the required twist or torque to the wire. Departures of 0.001 inch of the arm from its horizontal null position can be detected by the theodolite, which is positioned to observe lateral movements at the end of the arm.

In operation, the null position is established with the theodolite. A change of force is applied to the end of the arm (in this case, by moving the magnet closer to the diamagnetic material). The torsion wire is then twisted back so that end of the arm is again at null. The amount of twist required can be translated into a change of torque. Knowing the length of the torque arm at which the force is applied (i. e., the distance of the magnet from the vertical torsion wire) permits the calculation of the change of force applied to the test sample. Test results achieved during the past two years of operation show that the data is repeatably accurate to at least 0.25 dyne. The LOFF has been used to supplement the simple torque wire mechanism because of its greater accuracy and to serve as a check on the data taken. In practice, the simpler test device which was the torsion wire support requires considerably less time for set up and data recording.

As indicated previously, several samples of pyrolytic graphite were tested for force characteristics. The results of typical data have been plotted on Figure 2.3-15. On this curve, it can be seen that there was a considerable increase in force available from the graphite, although it was not nearly as large as would have been expected based on a comparison of susceptibilities. For the 0.125-inch thick samples, there was only a change of 2:1 increase in force from the bismuth. The results of another test with a different magnet (Figure 2.3-16) indicates an improvement of about 2.5:1 for the graphite. However, for both magnets, an increase of about 4.5 to 1 is possible by increasing the thickness of the graphite by a rate of about 3.1 to 1 so that a substantial increase in force is available with graphite which because of its much lower density, would represent a gain in force per unit weight.

The disparity between the theoretical and experimentally determined ratios of forces available from graphite as compared to bismuth must be due to differences in susceptibilities of the materials actually tested. Only one reference (Fishback) has given a value for the susceptibility of pyrolytic graphite and discussions with vendors indicate that there is a wide variation in some of the physical properties between samples. During the next period, it is planned to check representative samples of the graphite to determine that the susceptibility available is adequate for the needs of the design. As indicated

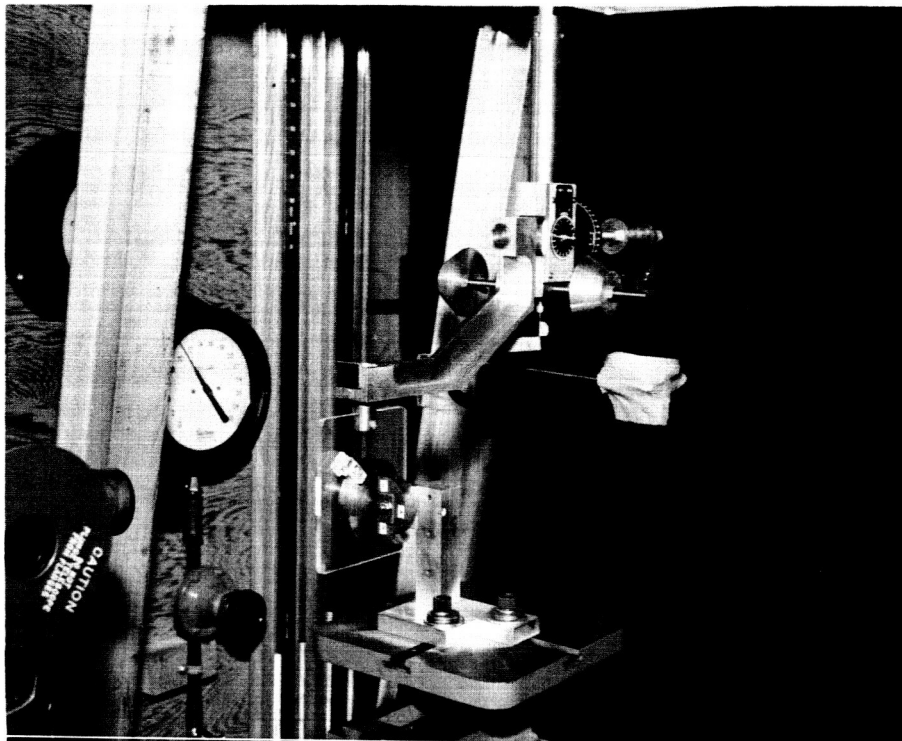


Figure 2.3-13. Low Order Force Fixture for Evaluating Pyrolytic Graphite

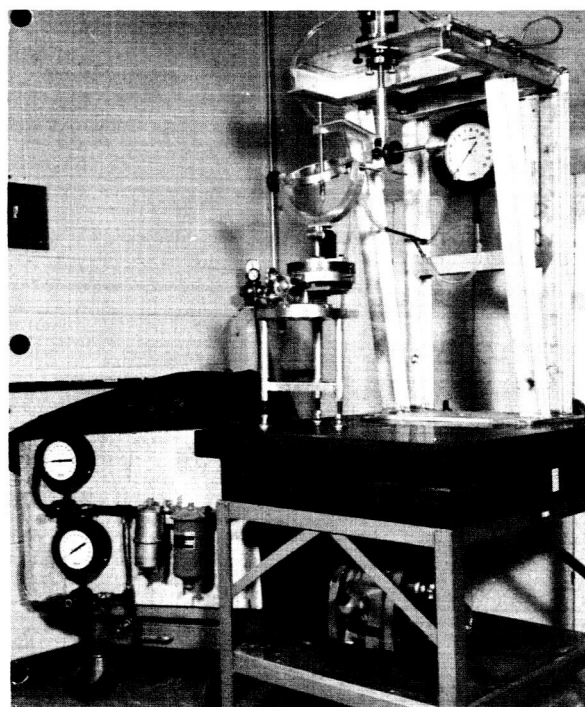


Figure 2.3-14. Overall View of Low Order Force Fixture Test Set-Up

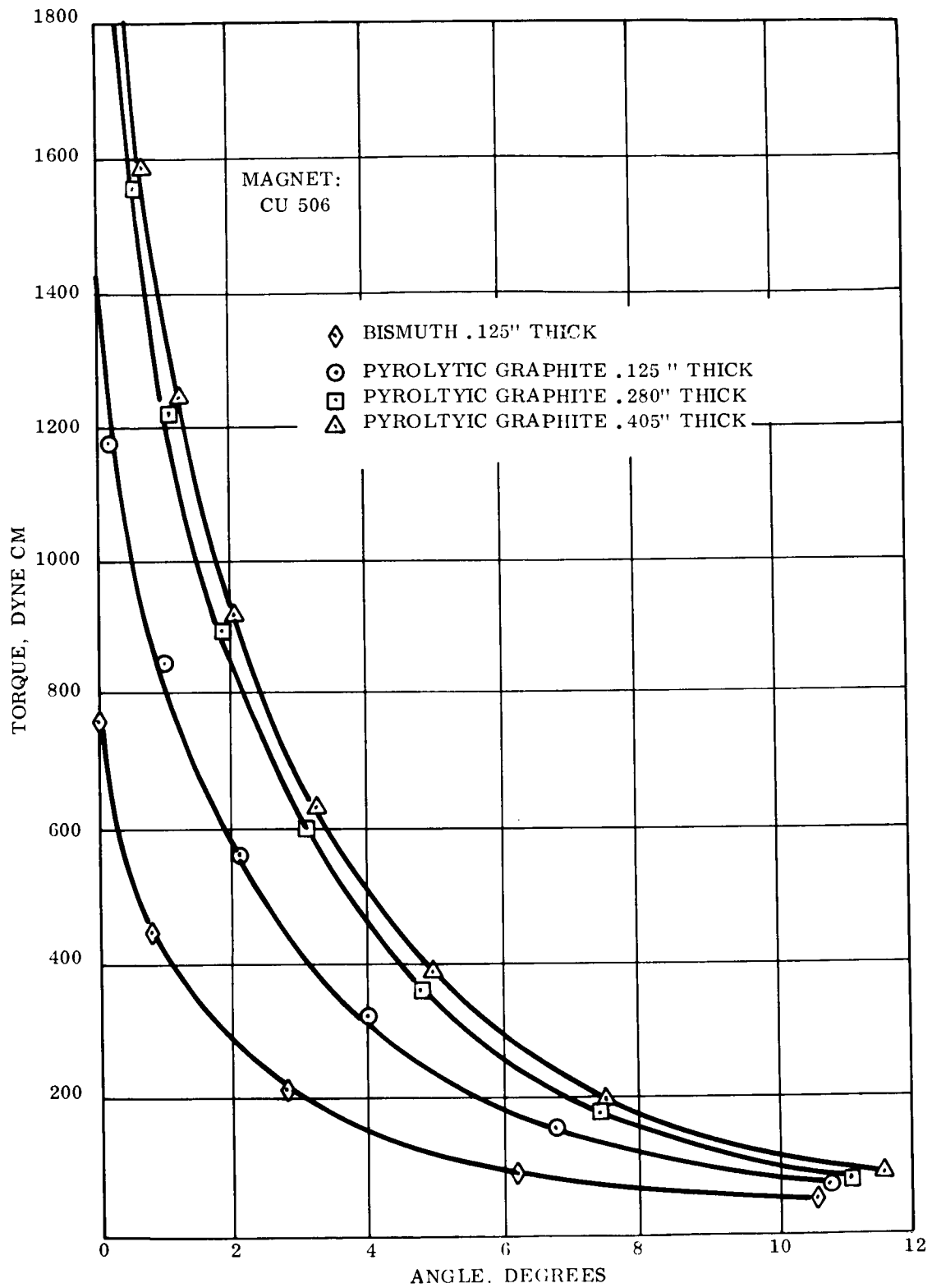


Figure 2.3-15. Torque Angle Characteristics Bismuth and Various Thicknesses of Pyrolytic Graphite

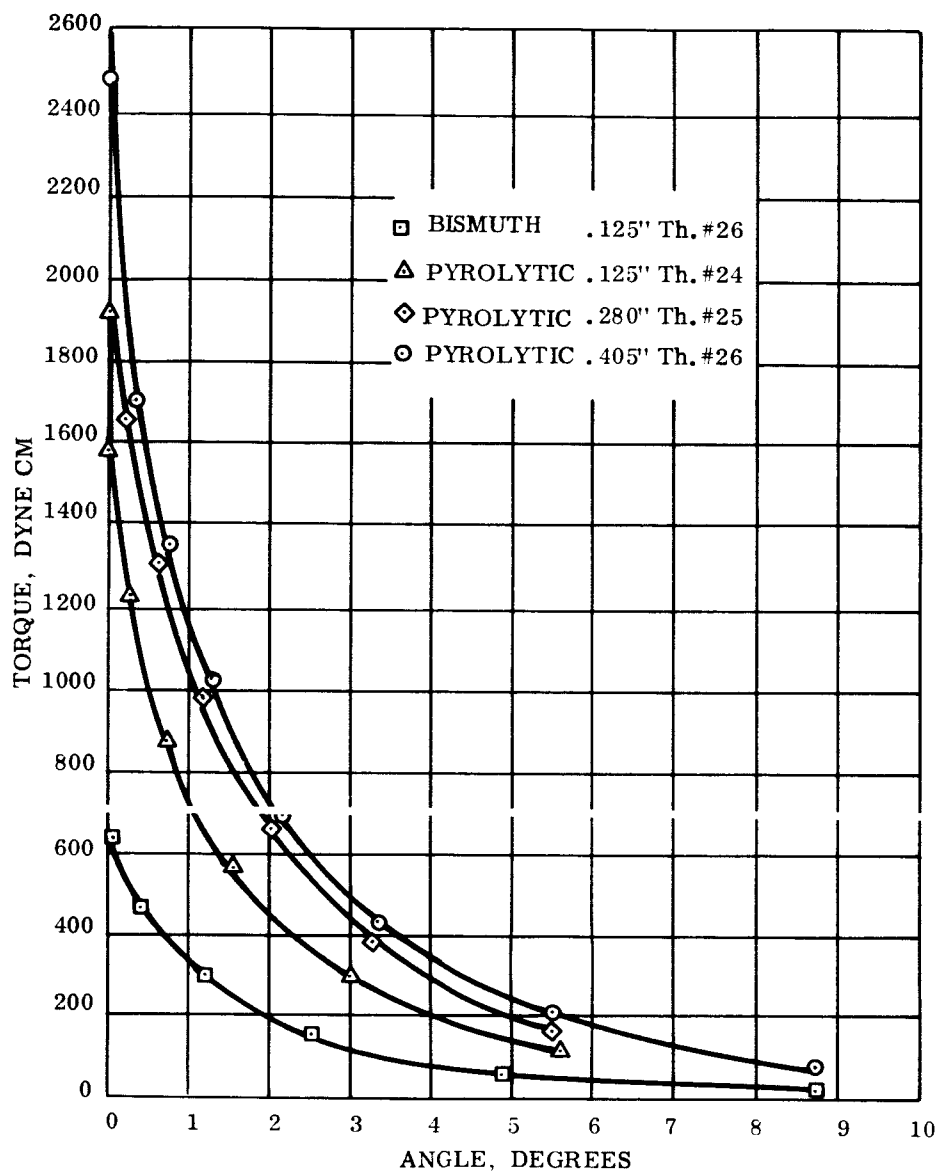


Figure 2.3-16. Torque Angle Characteristics Bismuth and Various Thickness of Pyrolytic Graphite

below, the design requirements of the CPD for ATS can be met within the required envelope utilizing materials having susceptibilities similar to that now available from vendors.

2.3.2.3 Expected Activity Next Quarter

1. Finalization of a preliminary design layout.
2. Fabrication of a working model of the clutching mechanism to check operation.
3. Laboratory tests to be performed:
 - a. Torsion wire selection tests
 - b. Eddy-current damping tests
 - c. Hysteresis damping tests
 - d. Magnetic torsional restraint tests
 - e. Magnet variables (gaps, strength, etc.)

4. Detail design and structural analysis in support of Stage III drawing release.
5. Detail drawings of the engineering unit of the CPD will be prepared and released (Stage III Release) for Manufacturing.
6. Raw materials and purchased parts will be procured.
7. Test procedures will be prepared.

2.3.3 Conclusions and Recommendations - CPD

Preliminary design and test efforts on the CPD are progressing satisfactorily. Early integration and design problems on the CPD have been more numerous and more difficult to resolve than had been foreseen; however, it is believed the CPD concept now proposed can be developed to meet requirements within schedule.

2.4 Attitude Sensor Subsystem

2.4.1 Subsystem Description

The Attitude Sensor Subsystem of the Gravity Gradient Stabilization System for the Advanced Technological Satellite is described in detail in the Program Plan (Reference 1). The plan was compiled during the first six weeks of the contractual effort. A brief description is presented here, however, with particular emphasis on those details which have been re-defined.

The Attitude Sensor Subsystem consists of four attitude sensors built or procured by the General Electrical Company, one or two sensors supplied by the National Aeronautics and Space Agency on the 6000-mile orbit and 24 hour orbit flights, respectively, and the power, command, control, and telemetry circuits associated with the entire Gravity Gradient Stabilization System. The components to be supplied for the 6000 mile orbit satellite are listed below:

Two	TV Cameras Subsystems
One	Solar Aspect Sensor Subsystem
One	Radio Frequency Attitude Sensor
One	Power Control Unit
	Temperature Detectors (Quarterly not yet defined)

In addition, the Goddard Space Flight Center of the National Aeronautics and Space Administration will furnish to the General Electric Company, two Infrared Earth Sensors which will then become incorporated into the Attitude Sensor Subsystem. On the 24 hour orbit flights, only one TV Camera Subsystems will be flown and a Star Field Reader is to be supplied to GE by NASA. Additional equipments proposed by the General Electric Company for use on the 6000 mile orbit flight include,

One	Three-Axis Magnetometer
One	Three-Axis Magnetic Torquing Coil
One	Center of Pressure Displacement Boom

Although the boom is not part of the Attitude Sensor Subsystem, it is mentioned here because the power, command, control and telemetry circuits associated with the Center Displacement Boom are included of the Power Control Unit.

2.4.2 Power Control and Distribution

The functions of the previously defined Attitude Sensor Power Control Unit, Gravity Gradient Booms Power Control Unit, and Interface Electronics have now been combined into one package (Power Control Unit or PCU) for simplicity of design and to reduce the weight taken by three separate chassis.

The Power Control Unit contains the command reception and driver circuits to operate the boom motors, boom solenoids, damper squibs, damper motor, instrumentation and attitude sensors. The five motors, four solenoids, and three squibs will operate from individual power inputs off the spacecraft battery bus; whereas, the sensors and instrumentation will operate from a single spacecraft quadrant power regulator.

Two types of command circuits will be used: discrete and proportional. Discrete commands will turn the attitude sensors either ON or OFF, operate the damper motor, fire the squibs, operate the solenoids, and will be driven by a single command execute tone pulse of somewhat arbitrary length.

Proportional commands will be used to extend and retract, expand and contract the gravity gradient stabilization booms. In this type of control, power will be applied to the motors only for the duration of the command execute tone, which may be preprogrammed at the ground station in increments of 5 milliseconds and may be set to start at any given GMT to within 10 seconds.

Both extension motors may be extended or retracted by a single command, and each motor may be operated individually to compensate for any possible differences in the drive rates of the two motors. The two scissor motors may be controlled in the same manner. The PCU will provide current sensors for all four primary boom motors.

The PCU will also receive a periodic synchronizing pulse from either of the two telemetry encoders (but not both simultaneously), will buffer and retransmit these pulses to both the Solar Aspect Sensor and the RF Attitude Sensor to initiate their "Read" cycles. Seven milliseconds after receipt of this "Read" signal, the SAS will present new attitude data at its output terminals. Similarly the RFAS will present new data, approximately 0.1 milliseconds after receipt of the "Read" signal.

Other circuits in the PCU will monitor the battery voltage, the regulated voltage, will switch between the video outputs of the two TV Camera Subsystems, and will supply a reduced operating voltage for the temperature sensors. Circuits are incorporated to control or degauss the proposed Three-Axis Magnetic Torquing Coil.

A breadboard of the PCU is presently being constructed utilizing squib drive circuits, and command decoder interface circuits suggested by the Hughes Aircraft Company. The discrete command circuits will operate latching relays of a type which has been qualified for satellite applications by the General Electric Company. To date no breadboard testing has been performed.

Since the command and control circuits for the second TV Camera Subsystem will not be required for the 24-hour orbit vehicle, these circuits will be used to operate the Star Field Reader. The video switch used to alternately transmit data from the TV cameras on the 6000-mile orbit flight will function between the single TV Camera and the Star Field Reader on the 24-hour orbit flight.

2.4.3 Solar Aspect Sensor

A preliminary specification was prepared for a Solar Aspect Sensor Subsystem and quotations were requested from several potential suppliers. The only vendor to respond positively was the Adcole Corporation, and therefore, they were requested to review their quotation with respect to the requirement to use Hughes Aircraft Corporation (HAC) approved parts and a revised component design specification, which included an operational transfer

function relating an assigned maximum error to an external alignment surface. Calibration of the sensor is thus referenced to a surface and marks which also will be used for alignment in the final configuration on the vehicle. A preliminary copy of the detector alignment drawing is shown in Figure 2.4-1.

Expressions for the values of the plane angles of measurement of the Solar Aspect Sensor in terms of actual displacements on the measurements patterns were derived and are presented in Appendix A. However, recent discussions with representatives of the Adocle Corporation have revealed that cross coupling occurs between the two detector eyes in the measurement of compound angles. The Solar Aspect Sensor with the one-half degree digital increments is capable of measuring the angle to the sun with an accuracy of $\pm 1/2$ degree only when the sun angle is in a plane normal to one of the detector axes. When compound angles are measured, both of the orthogonally mounted detector eyes respond and the total error compounds to a value larger than $\pm 1/2$ degree. The total error is thus a function of the sun angle.

A preliminary thermal analysis was conducted, resulting in a specification on the operating temperature limits for the Solar Aspect Sensor detectors, which are on the outside of the spacecraft, of -70°C to $+90^{\circ}\text{C}$. The range of the resistance thermometers to be attached to these five components was specified accordingly. A minimum response level was specified for the Solar Aspect Sensor to avoid triggering a false signals. Further details are included in the revised General Electric Component Specification, SVS-7306, dated 25 September 1964.

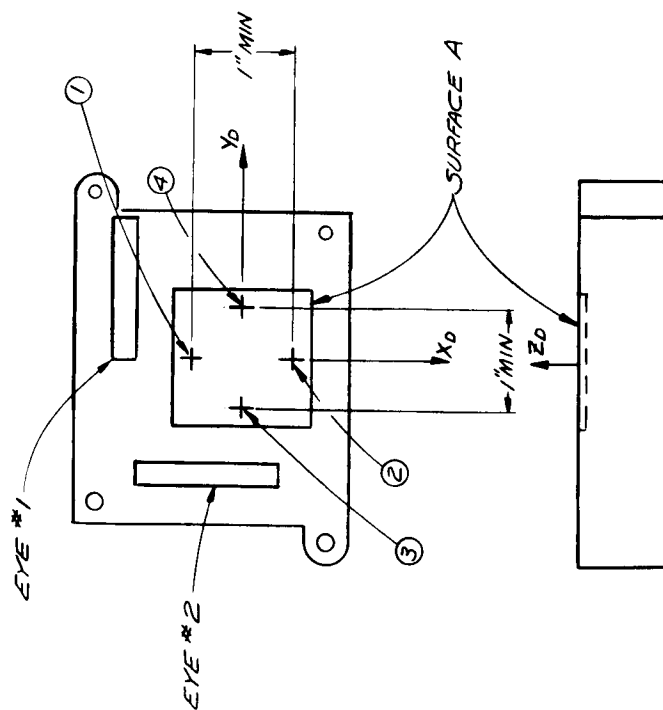
2.4.4 RF Attitude Sensor

2.4.4.1 Subsystem Requirements

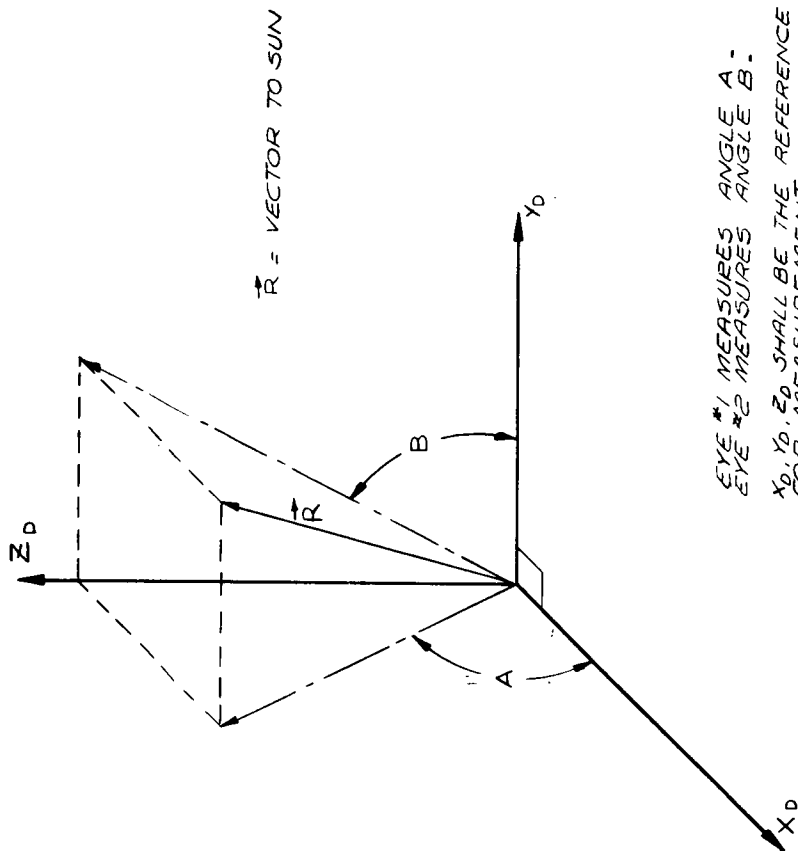
The function of the RF Attitude Sensor is to measure the angle of arrival of an electromagnetic wave transmitted from the ground with respect to the boresight of the sensor. The angle of arrival is determined by measuring this angle with respect to each of two orthogonal axes which are perpendicular to the boresight; these axes are termed the "pitch" and "roll" axes. Telemetry signals that are functionally related to the angles are then transmitted to the ground, where computations are performed to determine the attitude of the vehicle with respect to its local vertical. To perform these computations, information from the various attitude sensors is required, as well as a knowledge of ground station locations and vehicle position in orbit.

A preliminary design study has been conducted to establish the parameters and performance of the RF Attitude Sensor; the detailed results of this study are embodied in a previously-issued report.⁽¹⁾ In that report, a particular method of implementing the RF Attitude Sensor was chosen to serve as a reference system. On the basis of this reference system, specifications were established and a standard of comparison was set up against which responses to the request for proposal could be measured.

1. See the Bibliography, Section 4.



SURFACE A SHALL BE OPTICALLY FLAT. IT MAY BE EXTERNALLY ATTACHED TO THE COMPONENT, BUT SHALL NOT BE ADJUSTABLE.



EYE #1 MEASURES ANGLE A.
EYE #2 MEASURES ANGLE B.

X_D, Y_D, Z_D SHALL BE THE REFERENCE COORDINATE SYSTEM FOR MEASUREMENT.

MARKS ① & ② SHALL DEFINE THE X_D-AXIS.

MARKS ③ & ④ SHALL DEFINE THE Y_D-AXIS.

THE Z_D-AXIS SHALL BE DEFINED BY THE NORMAL TO SURFACE A.

Figure 2.4-1. Solar Aspect Sensor Detector Alignment

The RF Attitude Sensor will sense angles of arrival up to 25 degree off boresight. Over this angular range, the angular measurement accuracy will be 1 degree rms. This includes the effect of varying or random component parameters, up-link signal-to-noise ratio, and telemetry quantization. The contribution of these factors to angular measurement accuracy has been determined by analysis for the reference system; the results in Table 2.4-1 indicate that the accuracy objective of 1 degree can be met.

TABLE 2.4-1. ESTIMATED RMS ACCURACY

Telemetry (0.2 quantization error only)	0.08° at boresight
Noise	<< 0.2°
Equipment error	0.5° at boresight 1° near $\theta = 15^\circ$ < 1° at $\theta = 25^\circ$

The RF Attitude Sensor will operate in the 6 Gc/s band, and the sensor antennas will be circularly polarized. A common design of the sensor will be employed for satellites in either medium altitude or synchronous orbits.

Component design has been studied, and it has been established that a feasible design can be achieved employing printed Archimedean spiral antennas, stripline microwave circuits, and solid-state electronics. Under these conditions, the dimensions of the RF Attitude Sensor will be approximately 6 by 6 by 6 inches, the weight will be 8.5 pounds or less, and the power consumption will be 5 watts or less.

Interface requirements with vehicle subsystems and with the ground stations have also been considered. It has been determined that the signal transmitted by the ground stations will be CW. The signal frequency at the satellite will be within ± 150 kc of the nominal transmitted frequency in the 6 Gc/s band, including the effects of ground transmitter stability and doppler shift. The power density at the satellite will lie in the range of 10^{-7} to 10^{-5} watts per square meter. The RF Attitude Sensor will be able to handle either linear or right-hand circular polarization of the transmitted signal.

The RF Attitude Sensor will provide conditioned signals to the vehicle PCM telemetry system. Provision for turning the RF Attitude Sensor on and off will be incorporated in the power subsystem.

A detailed description of the specifications and conditions placed on the RF Attitude Sensor is contained in the General Electric Subsystem Design Specification (SVS-7305), and the Work Statement (9750-002 WS) both dated 1 October 1964.

2.4.4.1.1 Proposal Evaluation

Proposals covering the design and fabrication of the RF Attitude Sensor were submitted by the following suppliers:

1. Radio Guidance Operation, General Electric Co., Utica, N.Y.
2. Re-entry Systems Dept., General Electric Co., Valley Forge, Pa.
3. Cubic Corp., San Diego, Calif.
4. Advanced Development Lab., Nashua, New Hampshire
5. Hughes Aircraft Co., El Segundo, Calif.

All proposals were evaluated technically by three independent teams of evaluators, the Advanced Technological Laboratory and Electronics Laboratory of the General Electric Company. Each proposal was evaluated on the basis of the following technical criteria:

1. Responsiveness to Work Statement
2. Design Concept
3. Analysis
4. Components
5. Test Program

2.4.4.1.2 Background and Experience

For every criterion, a numerical rating was assigned by each evaluator, according to the following rating scale:

- 5 — Exceeds requirements
- 4 — Meets requirements
- 3 — Very nearly meets requirements
- 2 — Partially meets requirements
- 1 — Fails to meet requirements
- 0 — No reply

A written discussion was required of each evaluator to support the numerical rating chosen.

Since not all criteria were judged to be of equal importance, weighting factors were applied to the numerical ratings. The analysis and test program discussions, in particular, were regarded as important but somewhat less critical criteria than the other four.

Following this independent assessment of capability, the evaluators met to arrive at a consensus on the relative technical ranking of the proposals. The Radio Guidance Operation (RGO) was ranked first among the suppliers on the basis of a technical approach that avoided the critical sources of phase error that degrade accuracy, the completeness of performance and reliability analysis, the use of state-of-the-art components, and the completeness of the reliability program. In addition, RGO has extensive experience in phase-measuring systems through the Mistrum Program. Visits to inspect the engineering and manufacturing facilities supported the choice of RGO as the supplier for the RF Attitude Sensor. Design activity by RGO has just commenced. A functional description of the RGO technical approach is given below in paragraph 2.4.4.3.

2.4.4.1.3 Technical Approach

The RF Attitude Sensor measures the angle of arrival at the satellite of an electromagnetic

wave transmitted from the ground. An antenna array senses the phase of the arriving wave at each of three elements in the array, where the elements are arranged in an L-shaped configuration. Pitch angle is to be derived from the phase difference between the central element and the second element, while roll angle is to be derived from the phase difference between the central element and the third element.

The three signals are initially processed in separate channels. A pilot tone is combined with each signal in the microwave circuit preceding the RF mixer. The purpose of the pilot tone is to compensate for phase differences in the three channels. The pilot is offset from the incoming signal by a fixed audio frequency. The pilot tone is generated by phase-locking a voltage-controlled oscillator (VCO) to the incoming signal, and by multiplying the VCO frequency to the proper microwave band. A local oscillator signal is also generated by multiplication of the VCO output.

In each of the three channels, the pilot tone and signal are translated to IF frequencies, amplified, and detected in an envelope detector. The audio-frequency signal at the detector output contains the phase angle sensed by the antenna element, but the phase shift through the first mixer and IF amplifier is eliminated in the envelope detection process.

The audio signals in the central channel and in the pitch channel then gate a fixed frequency oscillator into a counter so that the count is proportional to the phase difference between the central and the pitch antenna elements. The audio signals in the central and roll channels are similarly processed. These binary counts are stored, and are read out to the telemetry system upon receipt of read signals. This information is then telemetered to the ground. Using this data, together with a knowledge of ground-station location, vehicle location in orbit, and vehicle attitude information obtained from other sensors, the attitude of the vehicle with respect to its local vertical can be computed.

The format of the signal transmitted from a ground station to the RF Attitude Sensor is CW, at a frequency of 6.212094 Gc/s. The frequency as measured at the satellite will be within ± 150 kc of this nominal ground-transmitted frequency, as a result of doppler shift and oscillator instability. The power density at the satellite will be 10^{-7} to 10^{-5} watts per square meter, and the polarization is linear.

The electrical axes of the RF Attitude Sensor will be defined with respect to optical alignment axes, in roll, pitch, and yaw. The optical alignment will be accomplished by means of a mirror containing suitable index marks, mounted on the surface containing the antennas, as an integral part of the RF Attitude Sensor.

The requirements of Military Specification MIL-I-26600 will be used as a guide in determining acceptable levels of interference and susceptibility. To prevent mutual interference between the RF Attitude Sensor and the 6.212 Gc/s communication transponder, the transponder will be turned off when the RF Attitude Sensor is turned on, and vice versa. In addition, the RF Attitude Sensor will incorporate filtering at the input to protect against any degradation in performance as a result of 4 Gc/s transmission from the 6.301 Gc/s transponder. The

signal and power leads of the RF Attitude Sensor shall be filtered to protect against any degradation in performance of the RF Attitude Sensor or of other components in the satellite.

2.4.4.2 Vehicle Attitude Determination

Formulations have been made of the equations required for computation of attitude angles from on-board sensor measurements, with the following possible schemes:

1. Line-of-sight signal from one radio station, and on-board IR earth-sensor
2. Line-of-sight signal from one radio station, and on-board sun sensor
3. Line-of-sight signals received nearly simultaneously from two radio stations
4. Line-of-sight signals received from two radio stations and sun-sensor.

Systems 1 and 4 are completely deterministic; the other systems require resolution of ambiguities by other means.

Complete formulations were made of error partials for insertion in error programs to evaluate the accuracies of the various systems, for an equatorial-synchronous orbit and for an inclined orbit. An expected range of attitude angles has been specified; maximum probable measurement errors are also specified.

Thus far, the error program for System 1 has been programmed, with the angular position of the satellite and of the radio station taken as independent parameters. Exclusion zones based on non-sighting of the satellite from the station have been ascertained; field-of-view limitations of the RF Attitude Sensor are incorporated in the error program. Computer runs will next be made to evaluate the accuracy of vehicle attitude determination.

2.4.4.3 Development Tests

2.4.4.3.1 Stripline Components

As part of the preliminary design study on the RF Attitude Sensor, a number of tests were conducted on microwave stripline components.¹ Temperature tests were made on a 6 Gc/s rat-race (hybrid) to determine the differential phase shift between the two signal paths in the rat-race. Over a range of -10°C to 60°C, no detectable change occurred within the precision of the measurement, which was 0.72 degree at 6 Gc/s.

The power split and isolation of the rat-race was also measured at 6 Gc/s. The power split for any of the possible modes of connection was -3.0 ± 0.1 db, and the minimum isolation of the decoupled arms was -26 db.

2.4.4.3.2 Boom Interference Effects

2.4.4.3.2.1 Preliminary Model with Flat Ground Plane

To investigate the interference effects from the gravity gradient stabilization booms, measurements were made on a preliminary model as shown in Figure 2.4-2. The model consisted of two spiral antennas mounted on a flat ground plane. The booms were 1/2 inch

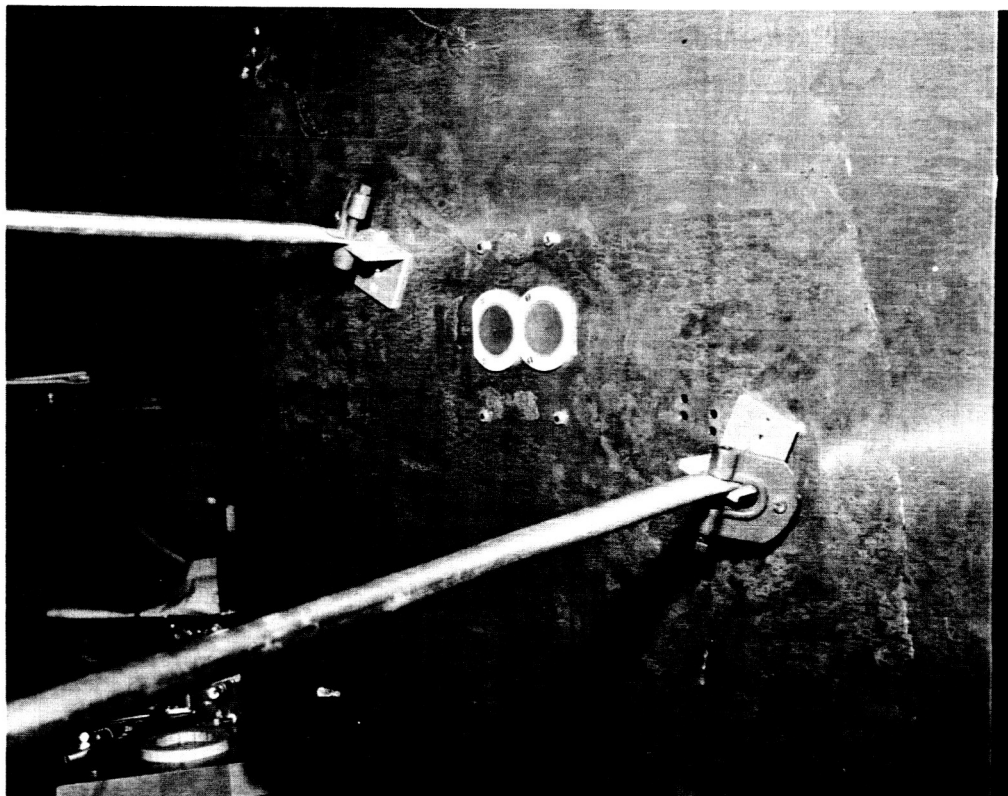
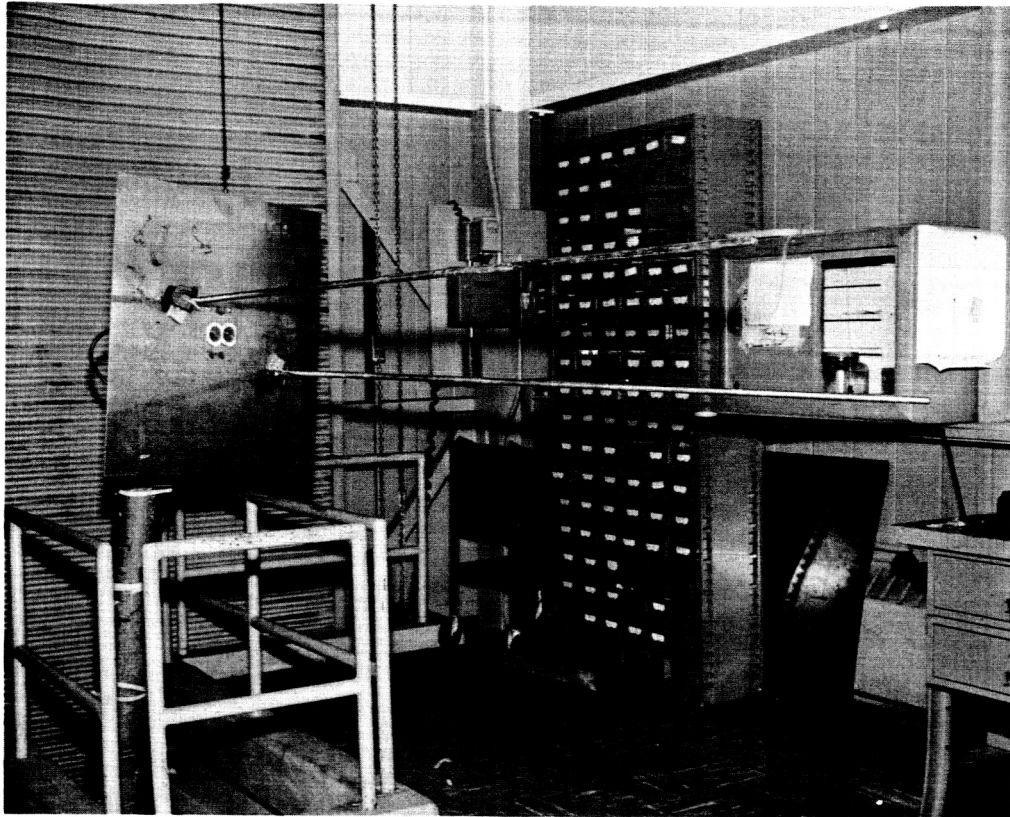


Figure 2.4-2. Ground Plane Antenna Model for Boom Interference Evaluation

diameter aluminum tubes; both 3-foot and 6-foot boom lengths were used. The spacing between the exit points from the ground plane was variable, as was the angle of the booms with regard to the boresight axis. First, reference sum and difference patterns were taken without booms. It was found that the spirals excited currents in the ground plane with the result that both sum and difference patterns showed an interference ripple near the boresight axis. Attempts were made to eliminate this disturbing effect by shielding the spirals from the ground plane and by using absorbing material on the outer portions of the ground plane failed. Since the prime objective of this test was to determine the boom interference effects this approach was abandoned. While it is felt that this ground-plane problem can be overcome in the actual system by proper design of the antennas and their own reflecting plane, the result does point up the need for careful integration of the RF Attitude Sensor into the vehicle structure.

2.4.4.3.2.2 Preliminary Model Without Ground Plane

In view of the above difficulties with the flat ground plane it was decided to eliminate the ground plane altogether and support the booms from a wooden beam. The configuration is shown in Figure 2.4-3. Since boom effects were known to be present, a larger spacing between the boom attaching points was selected (24 inches). Again reference patterns without booms were measured, this time with good success as shown in Figures 2.4-4 thru 2.4-5. Then patterns with the 6-foot long booms were measured, with the boom angle varying from 0° to 90° . All patterns were measured in a plane containing the two booms. Patterns were measured with both horizontal (parallel to booms) and vertical (orthogonal-to-booms) polarization. The boom interference is more pronounced for horizontal polarization. Typical patterns are shown in Figures 2.4-6 thru 2.4-11. As expected, the interference is larger for small boom angles.

There was no marked difference in results between booms of 3-foot and 6-foot lengths. An accurate extrapolation from booms of these short lengths to full-length booms is, of course, not possible.

The effect of this boom interference on the angular measurement accuracy of the RF Attitude Sensor will depend on the type of phase-measuring method as well as upon the proximity of the sensor to the booms. This effect remains to be evaluated.

2.4.5 TV Camera Subsystem

The Television Camera Subsystem will consist of a small transistorized vidicon camera with a wide-angle lens on an interconnected electronics package. The video output will have a baseband of 0 to 8 mc and will modulate a voltage controlled oscillator in one of the De Havilland Aircraft Corporation communication transponders. The camera will view a target at the end of each of the earth directed gravity gradient booms. With the targets approximately 100 feet from the camera, the earth also falls within the 48° by 64° field of view under normally stabilized orbital conditions. On the 6000-mile orbit flight, a second TV camera will view the two gravity gradient booms normally pointing away from the earth. After the spacecraft is inverted, the earth will be visible through this additional camera.

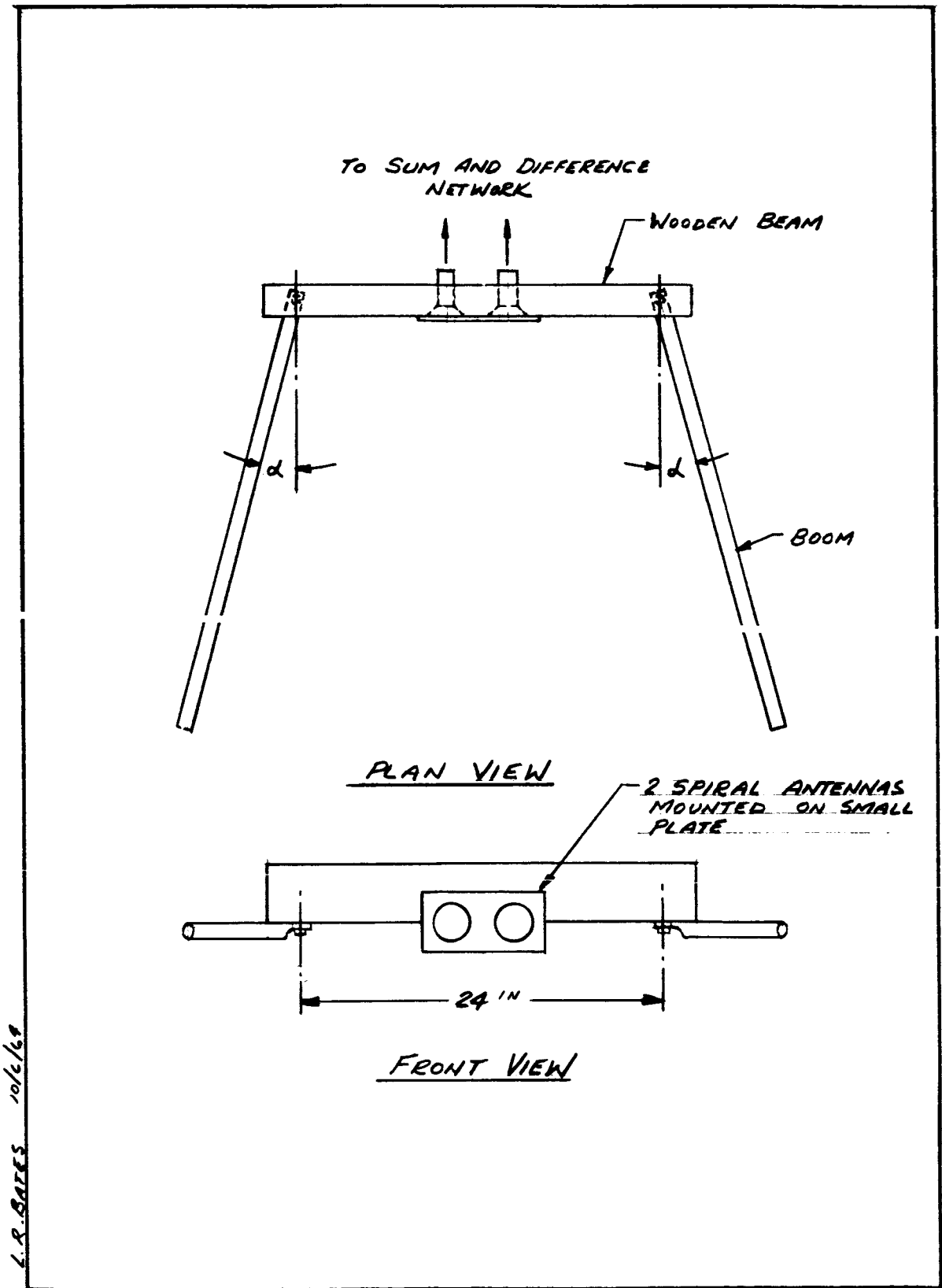
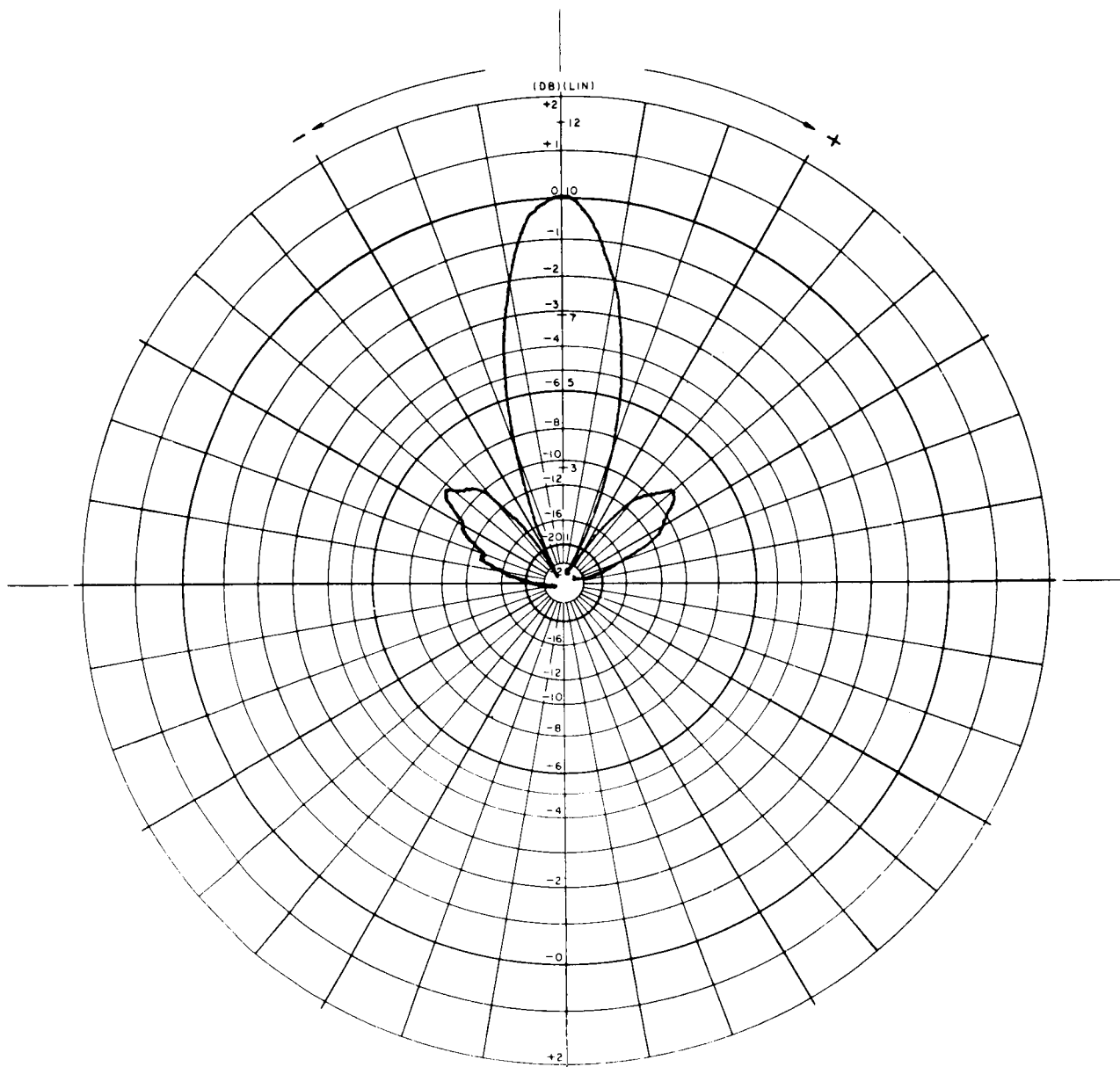


Figure 2.4-3. Antenna Model Without Ground Plane

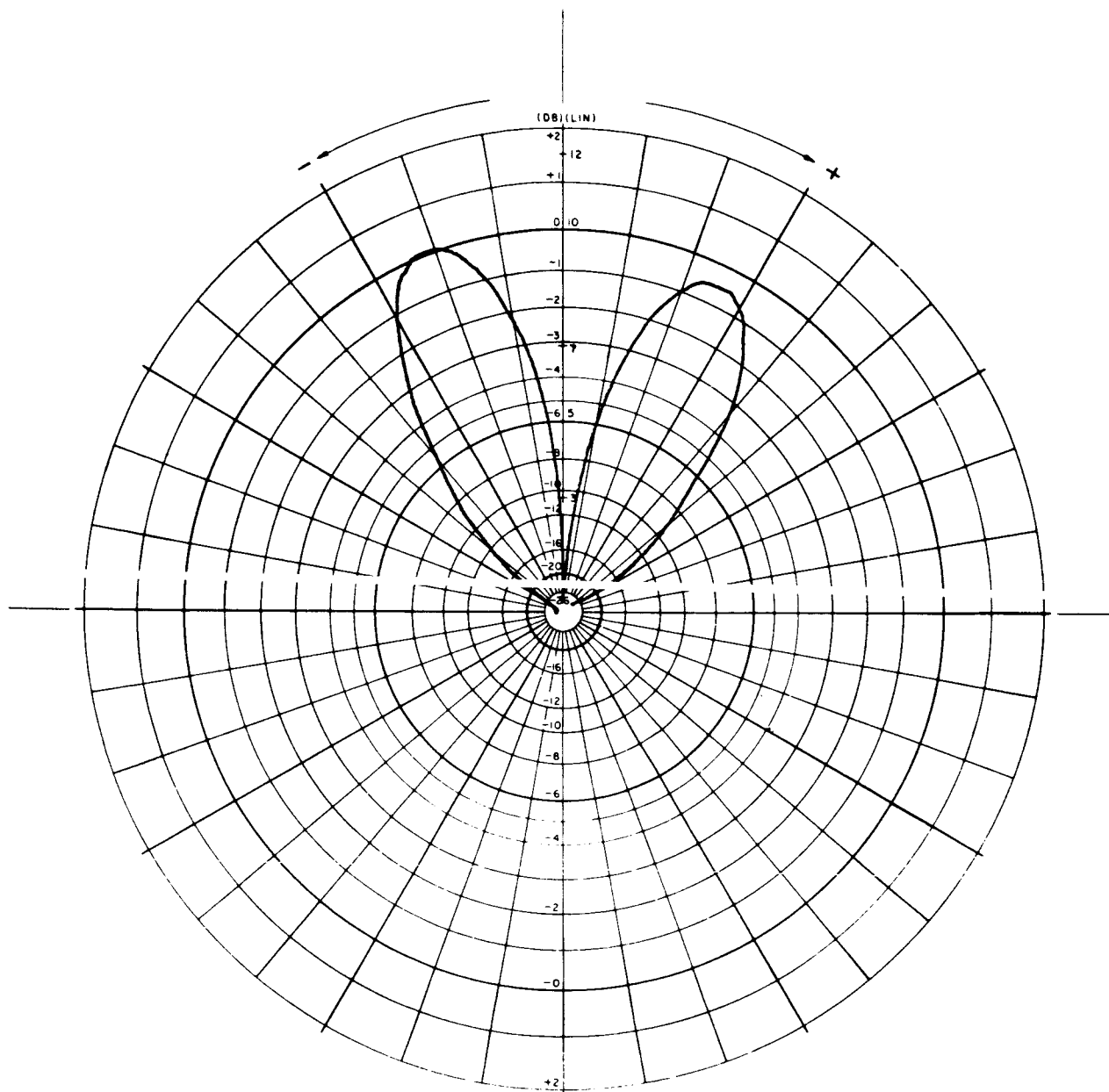


REFERENCE SUN PATTERN WITHOUT BOOMS

FREQ. : - 6GC

POL. : - HORIZONTAL

Figure 2.4-4. RF Attitude Sensor Antenna Pattern No. 1



REFERENCE DIFF. PATTERN WITHOUT BOOMS

FREQ. : - 6GC

POL. : - HORIZONTAL

Figure 2.4-5. RF Attitude Sensor Antenna Pattern No. 2

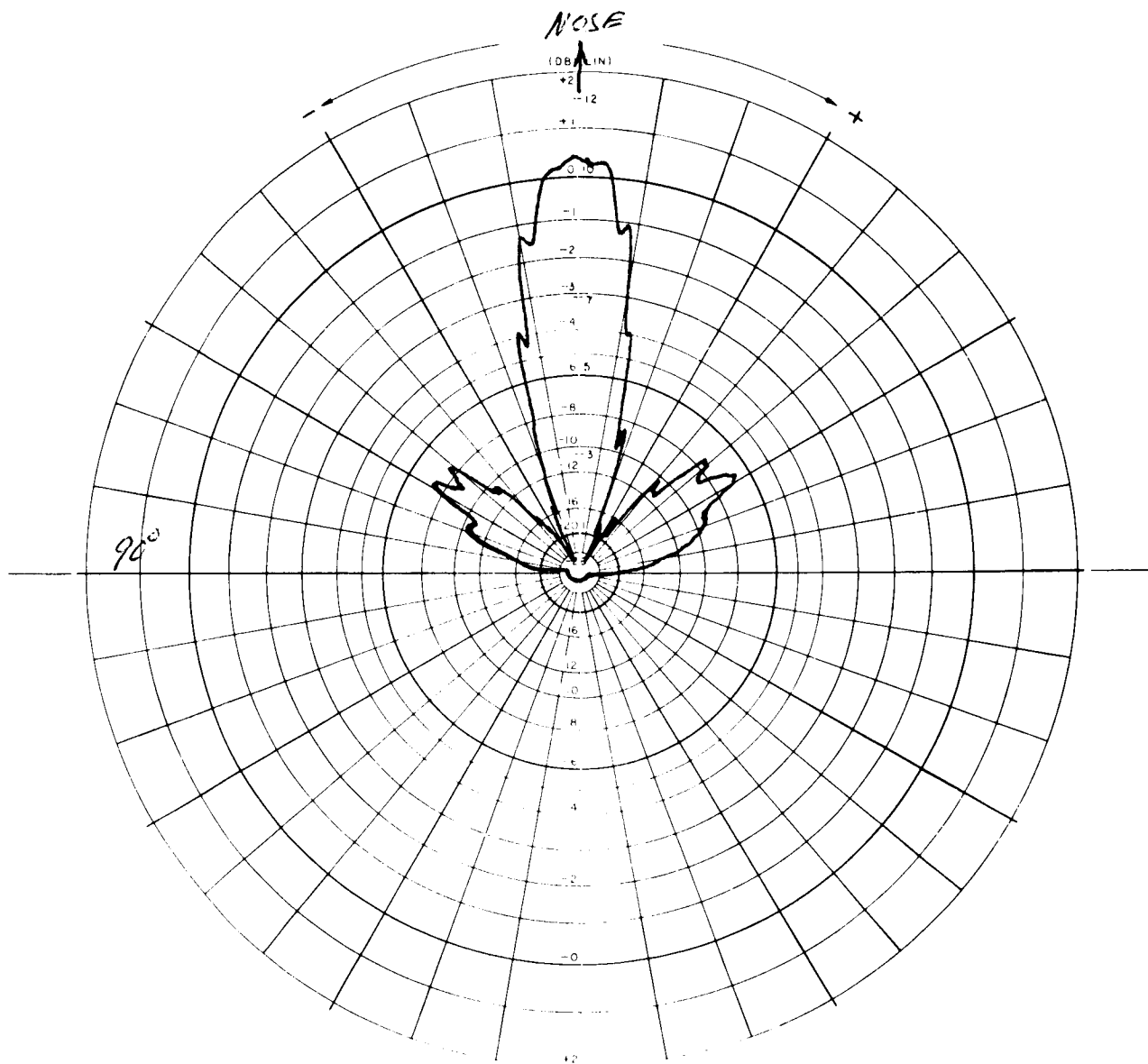


Figure 2.4-6. RF Attitude Sensor Antenna Pattern No. 3

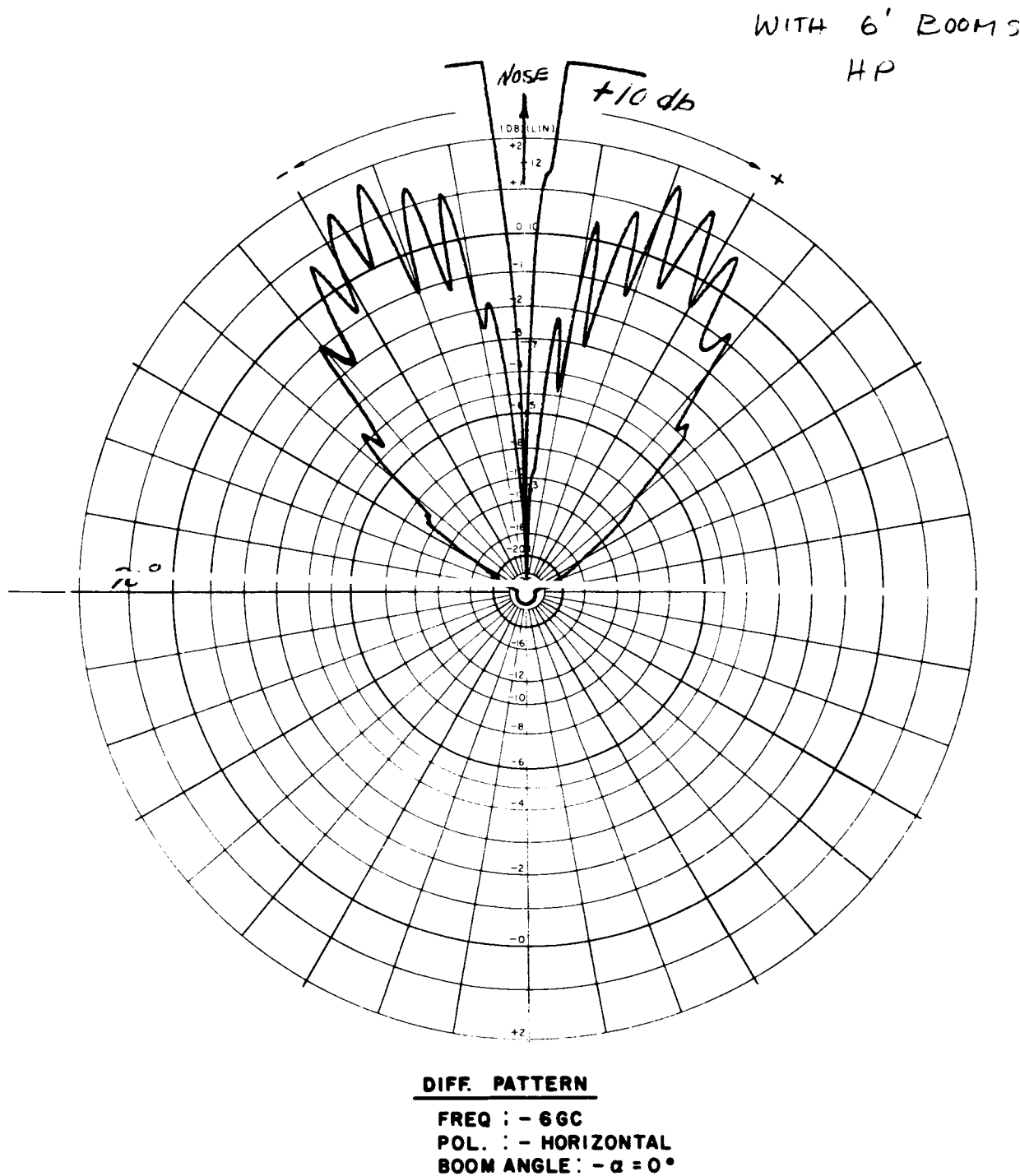
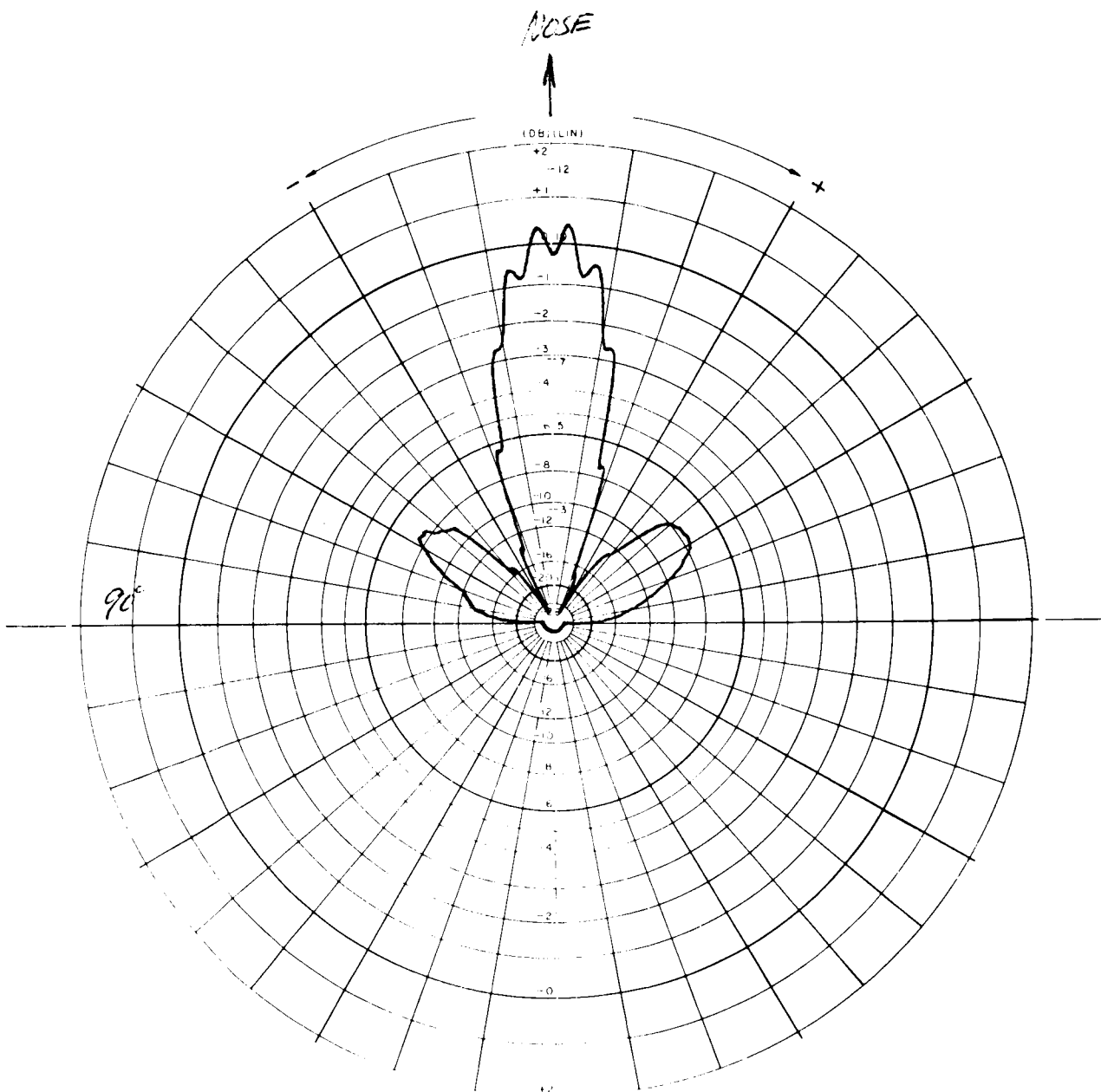


Figure 2.4-7. RF Attitude Sensor Antenna Pattern No. 4



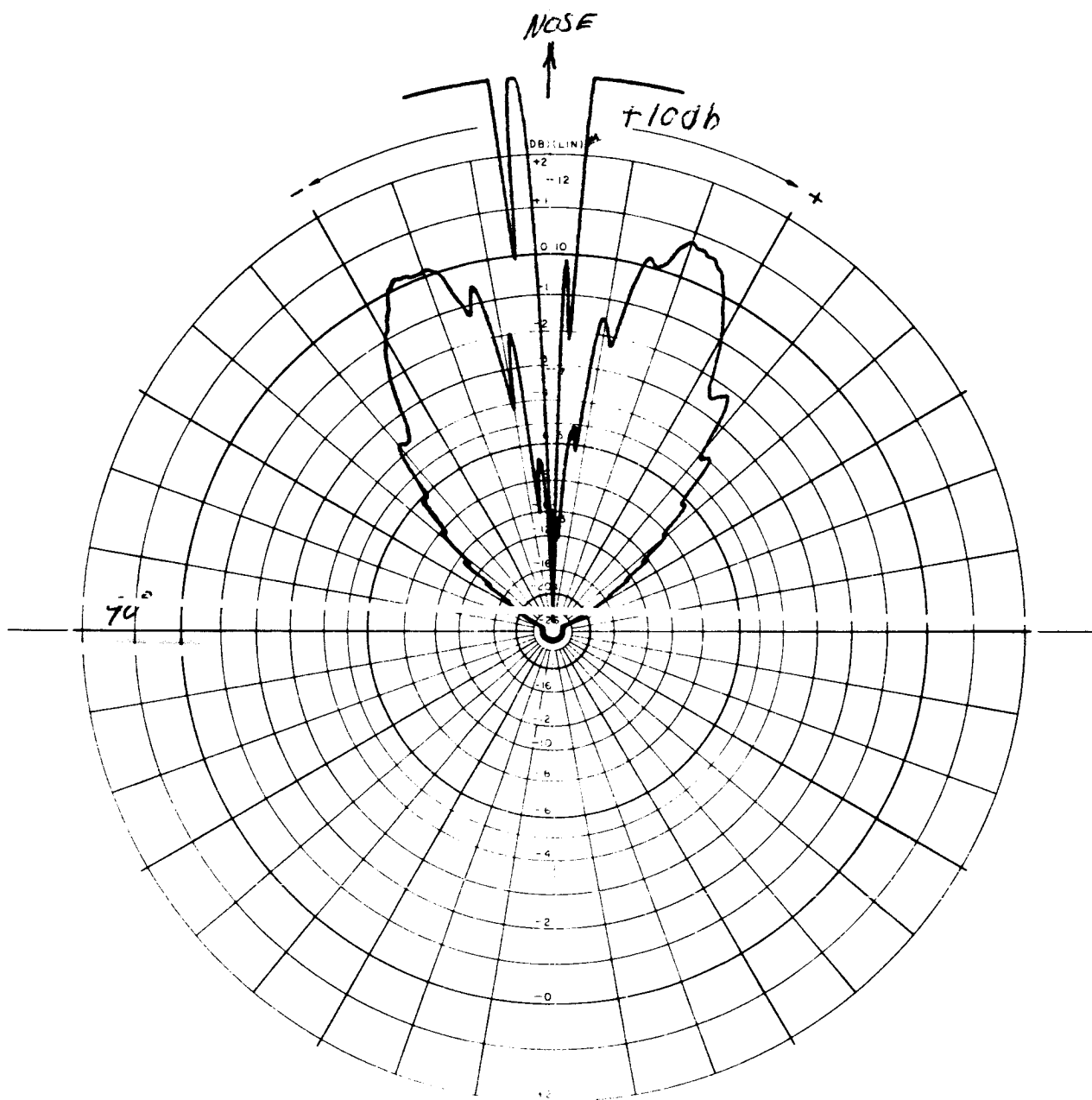
SUN PATTERN

FREQ. : - 6 GC

POL. : - HORIZONTAL

BOOM ANGLE : - $\alpha = 20^\circ$

Figure 2.4-8. RF Attitude Sensor Antenna Pattern No. 5



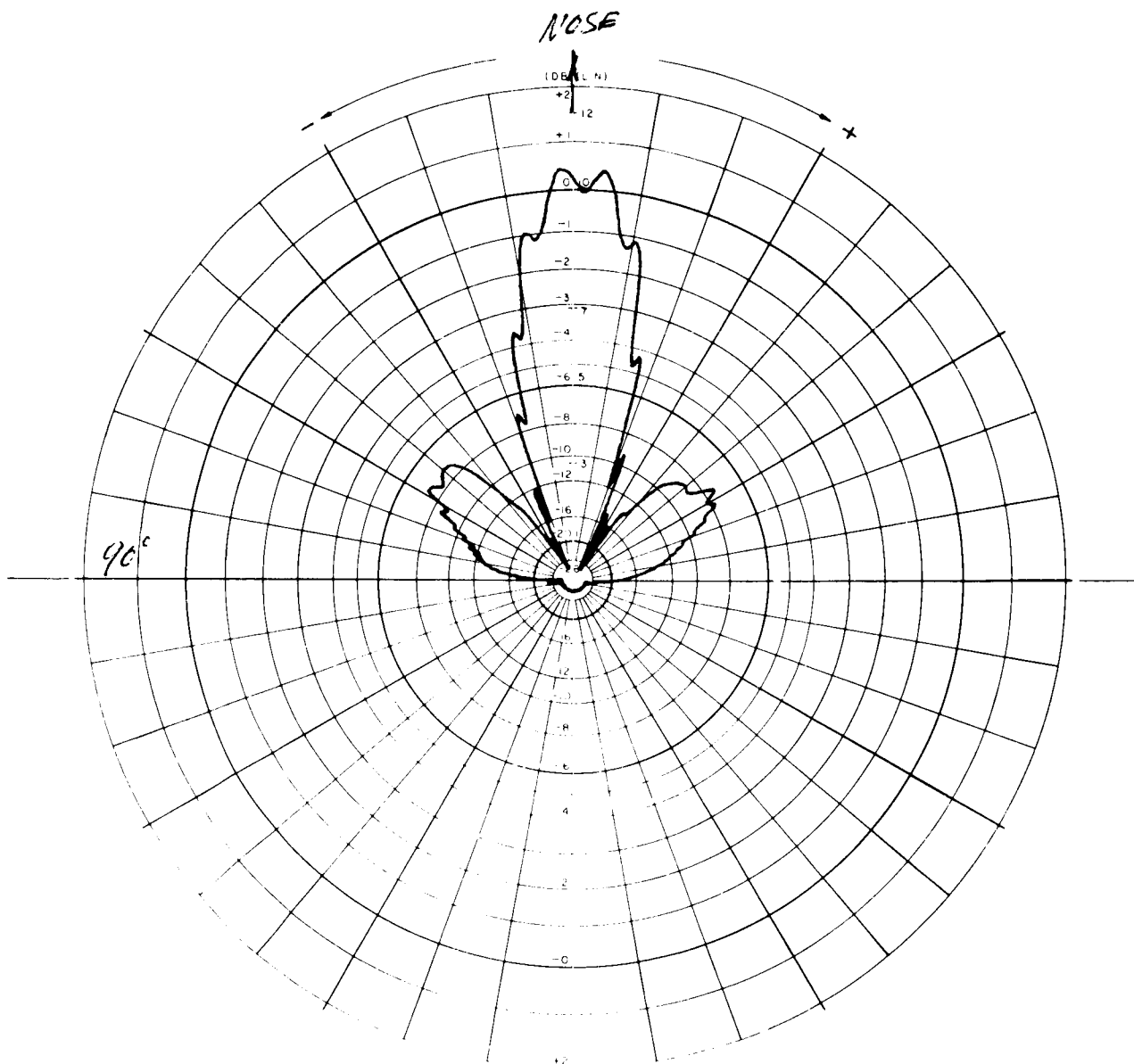
DIFF. PATTERN

FREQ.: - 6GC

POL.: - HORIZONTAL

BOOM ANGLE: - $\alpha = 20^\circ$

Figure 2.4-9. RF Attitude Sensor Antenna Pattern No. 6



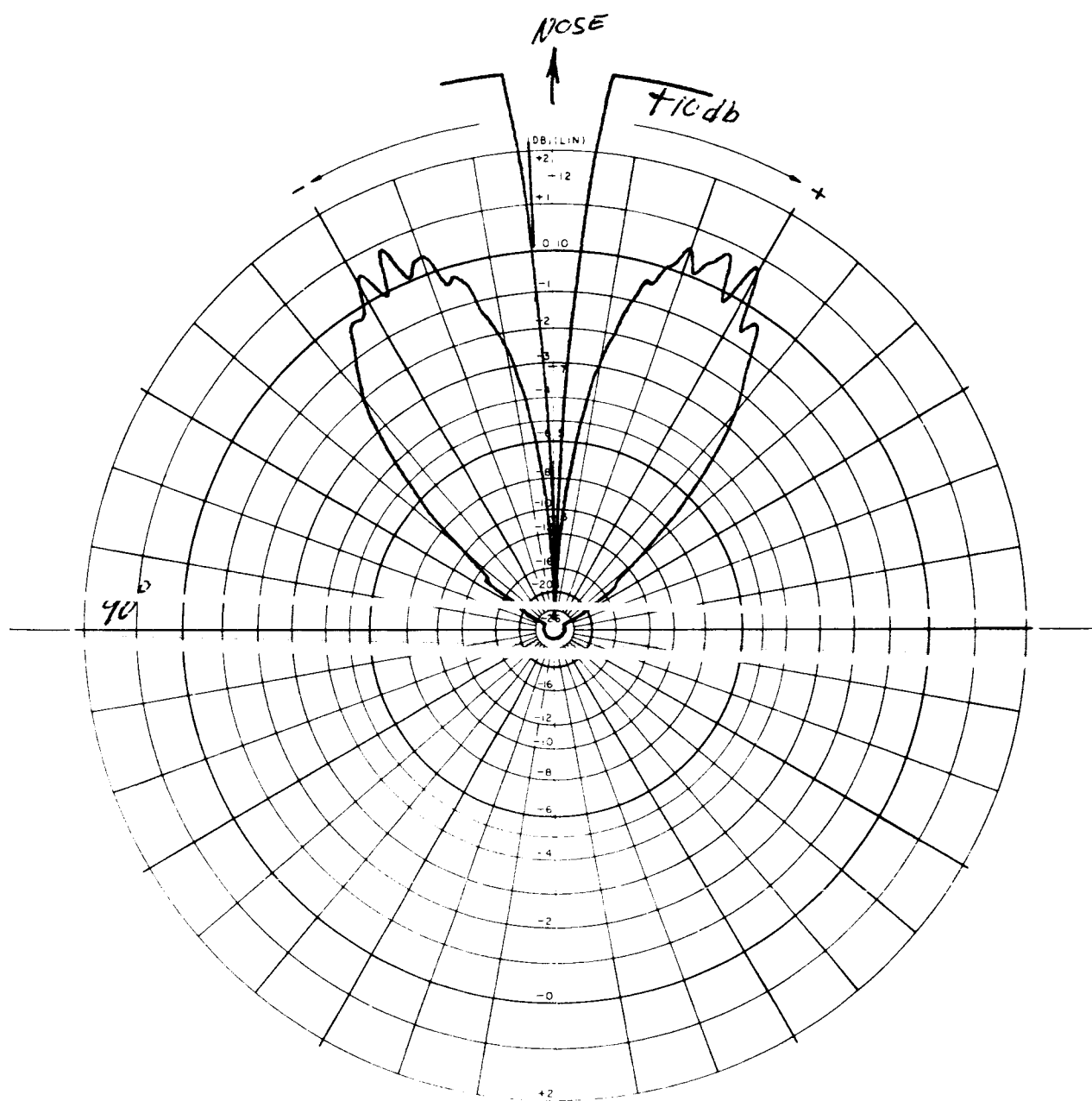
SUN PATTERN

FREQ. : - 6GC

POL. : - HORIZONTAL

BOOM ANGLE : - $\alpha = 40^\circ$

Figure 2.4-10. RF Attitude Sensor Antenna Pattern No. 7



DIFF. PATTERN

FREQ. : - 6GC

POL. : - HORIZONTAL

BOOM ANGLE : - $\alpha = 40^\circ$

Figure 2.4-11. RF Attitude Sensor Antenna Pattern No. 8

2.4.5.1 Design and Analysis

An analysis was made of the temperature extremes expected for the TV Camera Subsystem (TVCS) during a mission. Three locations were considered, namely: the TVCS Electronic Control Unit; the TVCS Camera Unit case and the TVCS Camera Unit Optics. The most extreme temperatures will be experienced by the TVCS Camera Unit Optics for which temperatures between 0 and 170°F are expected.

An estimate of TVCS life was made based upon data supplied in the vendor's proposal and use of a 20,000 hour heater in the vidicon image tube as the limiting component part. A reliability of 75% for three years with a 16% duty factor was calculated. This duty factor represents approximately 60 minutes of TVCS operation per orbit for the medium altitude flight.

The telemetry channels useful for the TVCS status were defined. The original list of 16 was divided into three groups for priority proposes. The least group of three is considered essential and consists of

1. Vidicon Filament Current
2. Vidicon Faceplate Temperature
3. Vidicon Target Voltage

The stabilization booms have been located on the vehicle in such a way as to require the TVCS to be aligned in a position that is skewed both to the vehicle axes and to the boom axes. This alignment is considered to be optimum and is a compromise between changing the TVCS field of view with degraded accuracy as a penalty and the restricting maximum boom angle with reduced scope of experiments as the penalty.

2.4.5.2 Resolution and Accuracy

At the Co Contractors Interface Meeting at NASA/GSFC on 30 July 1964, the General Electric Spacecraft Department was informed that the video bandwidth of the TV pictures received at the ground station would be limited to 5 mc, and was directed to study the effects of this reduction from 8 to 5 mc on the resolution and accuracy of the TV Camera Subsystem. This study is presented below.

The available resolution and accuracy of the TV Camera Subsystem are calculated on the assumption that optics and scan voltage fluctuations are not the limiting factors but vidicon retina, raster and scan beam are. Of particular interest is the degradation of accuracy by reducing video bandwidth from 8 to 5 mc. It is calculated that the accuracy of horizontal readout is 2.8 and 3.7 inches for 8 and 5 mc bandwidths, respectively.

Limitations on resolution and accuracy are determined in a TV camera by the raster characteristics (number of scan lines, aspect ratio, width of scan lines), by the stability of beam deflection, blur circle of the optics, field of view of the optics, and brightness characteristics of the scene. For this analysis, the optical and deflection circuit deficiencies are assumed to be not limiting and are not specifically considered. The target brightness is

assumed to be controllable to some extent and for this analysis it is assumed that target brightness is adequate and not limiting. This assumption is not necessarily true in practice and affects the target signal according to the following. The target signal shape and amplitude (voltage versus time) might not be consistently related to target position. This condition will occur for a change in lighting level of the target, change in aspect angle of the target as viewed by the camera, change in background scene, and change in reflection properties of the target. These sources of error can be minimized, but not eliminated. Appositively, a greater video bandwidth, by rendering greater detail, overcomes some of this difficulty. For the present analysis it is assumed that target brightness is optimum.

Specifically, then, the resolution and accuracy as limited by the selected raster, available electron beam characteristics, available vidicon retina characteristics and video bandwidth are considered.

2.4.5.2.1 Bandwidth

The video bandwidth is determined from the d-c level up to the maximum frequency required, so that numerically the video bandwidth is equal to the maximum frequency. The maximum frequency is given by Fink² as

$$f_{\max} = \frac{(\frac{w}{h}) m k f n^2}{2} \times \frac{1 + \frac{1}{K_h}}{1 + \frac{1}{K_v}}$$

where

f_{\max}	=	maximum frequency
w/h	=	aspect ratio (4:3)
m	=	ratio of horizontal to vertical resolution
k	=	utilization factor
f	=	frame rate (30 frames/sec)
n	=	total number of lines (525)
K_h	=	horizontal velocity factor
K_v	=	vertical velocity factor

The ratio of horizontal to vertical resolution (m) can be adjusted by changing the video bandwidth on the following basis. The vertical resolution is determined by the number of horizontal lines and how well points can be distinguished between one line and the adjacent lines. In actual systems even a point source always subtends more than one line, so that the maximum vertical resolution approaches line separation, and is something less than this if the two points to be resolved are vertically stacked. On the other hand, the horizontal resolution depends in the extreme on the ability to separate two adjacent points on the same line. Here the signal level must drop between the maxima of two point source signals to some value sufficiently low so as to make the two maxima evident. Hence, the more rapidly this can be done (on a scan line) the better the resolution. Obviously, the smaller the time interval between maxima, the shorter the period of video writing cycle and the higher the upper video frequency required.

The utilization factor (k) is a correction factor based upon the fact that scan lines are discrete and separated. Some signal elements of the image on the camera tube retina will fall between the scan lines so that it can be presumed that some low contrast points will be entirely lost and some high contrast points will be rendered with lower contrast. The effect this phenomenon has upon resolution is accounted for by the utilization factor. Fink indicates utilization factor ranges from 0.6 to 0.95. Since the target is being designed to have good contrast most of the time a high utilization factor is reasonable. It is important to recognize that use of a high utilization factor implies that the target subtends an angle greater than one resolution element and is of high contrast. At this time this is the design intention and requires that the target be six inches in diameter and be two-toned so as to realize high contrast against either sun-illuminated earth or space background.

The velocity factors (K_h and K_v) are the respective ratios of writing velocity to flyback velocity for the horizontal and vertical, respectively. The raster parameters determine the vertical flyback velocity and K_v has a value between 11 and 13. A value of 12 is assumed here -- the actual value is determined in the circuitry by the width of the vertical sync pulse. The horizontal flyback time, determined in the circuitry by the width of the horizontal sync pulse, determines the value of K_h . If 87.5% of the horizontal line period is used for video signals, K_h has a value of 7.

Solving now for f_{\max} , leaving m unspecified it is found that

$$f_{\max} = 5.24 \text{ m (mc)}$$

Thus, if f_{\max} is limited to 5.00 mc, m must have a value of 0.955.

2.4.5.2.2 Resolution

With standard sweep rates each line is scanned in 63.5 microseconds. Assuming 87.5% of the time is utilized and the width of the field is 64 degrees, there are 1.15 degrees scanned per microsecond. A 5 mc frequency has a period of 0.2 microseconds and can thus resolve points that far apart in scan time. Hence, the available horizontal resolution (unlimited by other factors such as optics) is 0.23 degree. At 100 feet, this angle amounts to 4.81 inches.

In the vertical direction the number of used scan lines in the picture height is determined from K_v to be 92.3%. There are 525 total scan line intervals available and thus 485 are used. Each line, if lines are equally spaced, then subtends $48/485$ which is 0.0989 degree. Signals on adjacent lines cannot be resolved, but signals on alternate lines may possibly be resolved. Under such conditions the resolution amounts to 4.14 inches at 100 feet.

2.4.5.2.3 Accuracy

While the resolution of the TVCS is most important when the boom target is viewed against the earth as background, there can be considerable operating time when the boom target is viewed against a space background where the resolution is secondary. In all events, the exact location of the target in the scene is the desired datum and the tolerance associated with the location is determined by the accuracy. It is, therefore, important to assess the effect of bandwidth upon accuracy.

A technique known as aperture correction is available to reduce the effects of beam spot size. By this technique the high frequency response of the video amplifier is boosted without a net change in phase shift. The effect is to electronically compensate for beam spot size by a factor of perhaps two. The net inaccuracy due to beam spot size can thus be reduced by this technique to 0.064 degree. Then with aperture correction, the accuracy becomes 0.179 degree. This amounts to 3.7 inches at 100 feet.

If, on the other hand, bandwidth were maintained at 8 mc instead of 5 mc, position uncertainty would be 0.072 degree and total inaccuracy would be 0.136 degree. This amounts to 2.8 inches at 100 feet.

In the vertical direction the location of a small source can probably be estimated to within one line. That is, it can be determined that the center of an imaged source lies on one line or another. Again this is based upon the image occupying more than one line, viz., three more lines. The source can then be located to within 48 degrees/485 active lines, which is 0.0989 degree. This amounts to approximately 2.1 inches at 100 feet.

2.4.5.3 Limitations of the TVCS Due to Orbital Illumination

The primary function of the TVCS is to relay the boom position to the gravity gradient stabilization system. The conditions that make this a difficult problem are basically geometrical and optical. Referring to Figure 2.4-12, the 6000-mile orbit is represented by the outer circle and the earth by the smaller circle. The rectangles A, B, C, D represent the ATS at four orbital positions. Position C is in earth shadow. If the boom ends are reflecting discs, it should be appreciated that the TV camera, being located at the apex of the booms, will be looking at the sunlit side of both boom ends at and near position A only. At positions B and D the wrong side of one of the booms is illuminated by sunlight.

Upon further analysis of this situation the following conditions are seen to apply for the boom angle at maximum ($\alpha = 62$ degrees).

1. Neither boom end is front illuminated for an orbital angle of 118 degrees centered about position C.
2. Only one boom end is front illuminated for two orbital regions, each of which is 62 degrees of orbit. Total angle of single boom end illumination is 124 degrees.
3. Both boom ends are front illuminated for an orbital angle of 118 degrees centered about position A.

If the boom angle is minimum ($\alpha = 22$ degrees) the three angles are 158, 44 and 158 degrees, respectively.

While the exact times for reading out boom position have not yet been defined, it appears that as originally planned the TVCS would not give the total boom information more than 33% to 44% of each orbit, depending upon boom angle.

This usage level is further reduced if one considers the fact that the boom end target will not be discernable in an edge-on aspect but will disappear from the TVCS at some shallow aspect angle dependent upon the target diameter and reflection properties.

Starting with some assumptions about the target and the camera. It is assumed that:

1. The fiduciary marks on the camera tube retina can be accurately determined with respect to the electronic time base.
2. The electronic time base is perfectly linear and stable.
3. Neglecting all other influences on accuracy not associated with the raster generation and bandwidth.

The accuracy now becomes a matter of how well a target can be measured with respect to the fiduciary marks when the target representation by the video circuits is dependent upon raster and bandwidth. In theory, readout can be accomplished by making measurements on an "A" scope presentation. In this arrangement the horizontal axis represents time from line start, and the vertical axis represents voltage amplitude of the video signal. The signals will have sloping leading and trailing edges as determined principally by the available rise time of the electronics. The rise time of the electronics is directly expressible in terms of bandwidth, once an amplitude characteristic shape is determined. Assuming a simple relationship, the shortest signal pulse would be one that is as long in time as half the period of the maximum frequency.

However, in practice, a bright point source of signal imaged on the vidicon retina spreads out radially over about 5 resolution elements, so that the signal pulse generated electronically is about five times this value. Then,

$$\tau_{\min} = \frac{5}{a f_{\max}}$$

With a 5 mc bandwidth, τ_{\min} is 0.5 microseconds. The accuracy of readout now depends upon how accurately the time interval can be measured from a reference amplitude on the fiduciary signal to a reference amplitude on the target signal. It is now assumed that the fiduciary signal is well enough defined so as to serve its intended purpose. It is estimated that a trained observer could read signal position on the "A" scope to one-fifth of a pulse width. Best accuracy of readout then becomes 0.1 microseconds. Since it has already been determined that the scan rate is 1.15 degrees per microsecond, the accuracy becomes 0.115 degree, if the scan beam has infinitely small diameter.

However, the electron scan beam has a finite diameter that can be readily determined. If a vidicon has a rated resolution of 1000 TV lines per inch (and is so operated), then in scanning the 64-degree width in a one-half inch wide raster on the tube retina, 500 lines can be distinguished. If it is assumed that the lines are equally spaced and that a line width equals a line spacing, then a line has a width of one mil. Consequently, the limiting beam spot size for 1000 TV lines/inch must also be one mil. Since 128 deg/inch are scanned by the beam, a one mil beam diameter means 0.128 degree is the diameter of the scan beam. Hence, the total error contributing to inaccuracy is 0.115 degree pulse position uncertainty plus 0.128 degree beam width uncertainty, which is 0.243 degree. This amounts to 5.1 inches at 100 feet.

A technique known as aperture correction is available to reduce the effects of beam spot size. By this technique the high frequency response of the video amplifier is boosted without a net change in phase shift. The effect is to electronically compensate for beam spot size by a factor of perhaps two. The net inaccuracy due to beam spot size can thus be reduced by this technique to 0.064 degree. Then with aperture correction, the accuracy becomes 0.179 degree. This amounts to 3.7 inches at 100 feet.

If, on the other hand, bandwidth were maintained at 8 mc instead of 5 mc, position uncertainty would be 0.072 degree and total inaccuracy would be 0.136 degree. This amounts to 2.8 inches at 100 feet.

In the vertical direction the location of a small source can probably be estimated to within one line. That is, it can be determined that the center of an imaged source lies on one line or another. Again this is based upon the image occupying more than one line, viz., three more lines. The source can then be located to within 48 degrees/485 active lines, which is 0.0989 degree. This amounts to approximately 2.1 inches at 100 feet.

2.4.5.3 Limitations of the TVCS Due to Orbital Illumination

The primary function of the TVCS is to relay the boom position to the gravity gradient stabilization analysts. The conditions that make this a difficult problem are basically geometrical and optical. Referring to Figure 2.4-12, the 6000-mile orbit is represented by the outer circle and the earth by the smaller circle. The rectangles A, B, C, D represent the ATS at four orbital positions. Position C is in earth shadow. If the boom ends are reflecting discs, it should be appreciated that the TV camera, being located at the apex of the booms, will be looking at the sunlit side of both boom ends at and near position A only. At positions B and D the wrong side of one of the booms is illuminated by sunlight.

Upon further analysis of this situation the following conditions are seen to apply for the boom angle at maximum ($\alpha = 62$ degrees).

1. Neither boom end is front illuminated for an orbital angle of 118 degrees centered about position C.
2. Only one boom end is front illuminated for two orbital regions, each of which is 62 degrees of orbit. Total angle of single boom end illumination is 124 degrees.
3. Both boom ends are front illuminated for an orbital angle of 118 degrees centered about position A.

If the boom angle is minimum ($\alpha = 22$ degrees) the three angles are 158, 44 and 158 degrees, respectively.

While the exact times for reading out boom position have not yet been defined, it appears that as originally planned the TVCS would not give the total boom information more than 33% to 44% of each orbit, depending upon boom angle.

This usage level is further reduced if one considers the fact that the boom end target will not be discernable in an edge-on aspect but will disappear from the TVCS at some shallow aspect angle dependent upon the target diameter and reflection properties.

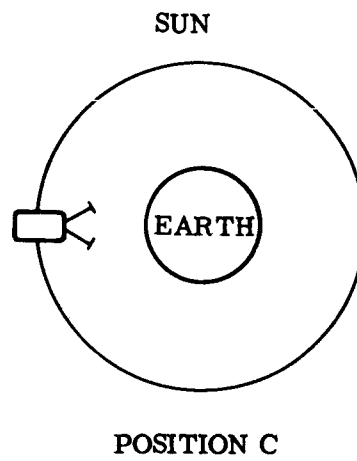
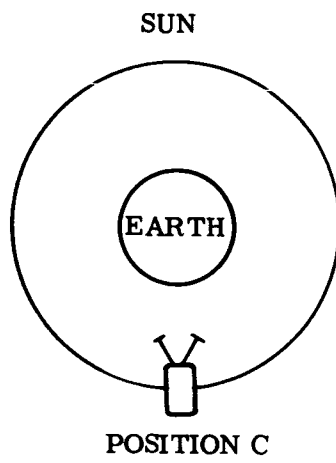
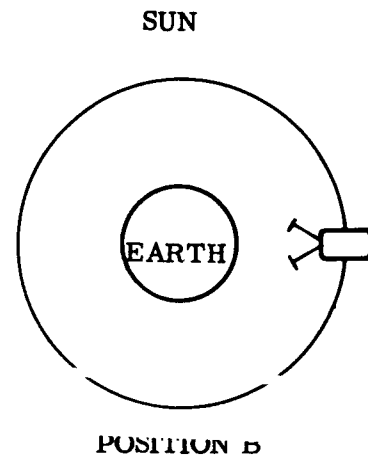
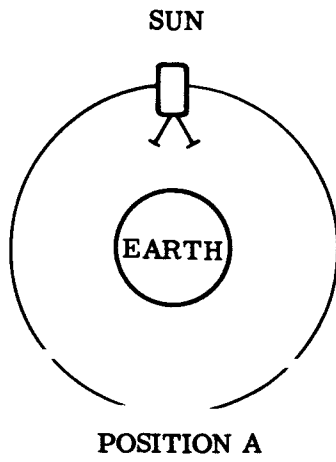
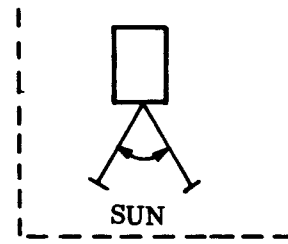


Figure 2.4-12. Target Illumination Effects

Furthermore, neither opaque boom target is illuminated near the orbital region of the earth's shadow -- a region that is well suited to thermal bending studies.

For these reasons a successful design is dependent upon what times with relation to orbital position it is required to read-out the boom end location, and exactly how the boom end target is designed.

There is also a consideration of how well the TVCS can determine boom properties. It has been assumed that the early decision to read boom end position only is still dominant. However, there may be some advantage to being able to see the boom itself and determine its shape and plane of bending. If so, there are considerations of boom illumination that should not be overlooked. Thus, in addition to the orbital restrictions mentioned above, there is also a requirement for high reflection from the boom. Since its diameter is so small, beyond 22 feet from the TV camera its diameter is less than a resolution element.

There are two other factors that bear mention. One is that the camera cannot operate with the sun in the field of view. The other is that there will be times when the earth will occupy the background of the TV scene so that the boom end will appear superimposed on the earth. For the most part, the boom end targets will be illuminated by the sun from behind whenever the sun would appear in the field of view. There will be times, however, when the earth will appear illuminated and the boom end targets will appear within the earth disc, such as position A when the boom angle is less than 40 degrees. Under these conditions, the sunlit boom end must be resolved against the sunlit earth. When this happens, the reflected light from the boom end may be greater, equal to, or less than the reflected light from the earth around it, depending upon sun angles to earth and boom end, and the reflection factors of the earth (cloud, land feature, ocean) and of the boom end. It will be impossible to maintain a fixed contrast between boom end and earth background. Target contrast under these conditions should be optimized. This can best be done after it is known when in orbital time the TVCS is expected to read out boom position. The TVCS cannot discern a very low contrast target.

Up to the present the design options for the boom end targets have been based upon considerations of making the targets visible for a maximum part of the orbit. The options open to the design are limited to the following general approaches in order to maximize the fraction of an orbit during which the TVCS can be used.

2.4.5.3.1 Use of Two-Toned Target

This approach was mentioned in a Hughes Aircraft document. It offers two apparent brightnesses to the boom end in some kind of pattern; for example, a dull outer ring and an inner bright disc. Against a bright (earth) background the target would appear as a black ring; against a black (sky) background it would appear as a bright disc. To function, the target ring diameter would have to be large enough so that the ring could be resolved against a bright earth; and the target disc would have to be bright enough (a function of diameter and reflection factor) to be seen against the sky background. Targets could be seen only when front-illuminated.

2.4.5.3.2 Use of Translucent Target

This approach would have part of the target translucent to light so that it would have some forward brightness when illuminated from both ends. Since the boom end is weighted, it is likely that the center of the target should remain opaque and the outer edge translucent. To be of benefit against the sunlit earth, however, the outer ring should appear dark against the earth background. Now this would require special properties of the target ring, since it must transmit light from the rear and be highly absorptive to light from the front. This may be done, it is thought, provided very high contrast is not a necessity.

2.4.5.3.3 Use of Solid Target

This approach would require the boom end target to be, for example, a spherical cup so that it would present a reasonable cross section to the camera over more than 180 degrees of sun angle. The mechanical considerations before boom deployment may dictate what can be done on this approach, since depth of target is involved.

It should be mentioned that at the start of the program, the target diameter was limited to 6 inches maximum. This establishes the maximum reflective area, so that maintaining sufficient brightness for all sun angles will severely limit dividing the target into regions or patterns of different contrast. This is so since dividing a target into a low and high contrast area against a given background effectively reduces its brightness in proportion to the percent of low contrast area.

2.4.5.3.4 Use of Active Target

One other approach was considered briefly. It was to put a source of illumination in the target so that its contrast could be changed by turning the illumination off or on. This does not appear feasible at this time unless some manner of wiring the boom end can be allowed.

In addition to designing the light contrast for the targets, the problem of camera optical setting must be resolved. It has been determined that in order to enable a maximum accuracy of readout, a reticle will be placed on the vidicon image retina. By this means, a grid overlay is effectively available for reading out boom position from each TV picture. In order to make this reticle appear on each picture, the retina-target voltage of the vidicon must be set for optimum reticle reproduction. By doing this, the brightness level of the scene imaged by the optics is effectively preset and the image brightness must be set by the lens stop. At the present time there is no provision in the design for changing the lens stop as a function of background (earth or sky). It may be found necessary to change lens opening as a function of background and this will be resolved during the planned testing phase with the engineering model of the TV camera.

2.4.5.4 Development Tests

An experimental measure of accuracy and resolution of a nominal 8 mc bandwidth vidicon camera subsystem with aperture correction was made to give experimental support to the resolution and readout accuracy study. Camera used was a GE Model TE-15 having 500

non-interlaced lines, 30 frames per second and using a 7735A vidicon. Tests results referred to the 100-foot boom distance are, in brief: dot resolution 6 inches, bar resolution 1.6 inches, accuracy approximately one inch. (It should be noted that this system has higher performance than the TVCS will have.)

Three simulated targets were made to serve as model targets for evaluating the lighting conditions, target reflectance properties and target patterns for optimum boom perception by the TVCS.

In a second test, a one-inch Shibaden TV Vidicon Camera was set up to look at scale models of boom targets in order to obtain an indication of the kind of video signals to be processed from the TV Camera Subsystem.

The Camera used had a one-inch vidicon Type DY2B and a 15 mm focal length, f/1.9 Cosmicon lens. The camera was set up 20 feet from the model targets. Targets were 1.2-inch diameter aluminum discs, giving a 5 to 1 scale. A 25:1 illumination level was used, making the light level at the target 400 foot candles, as measured by a Weston Light meter Model 756. By means of a resolution chart it was determined that the camera had approximately 350 lines resolution, corresponding to a bandwidth of slightly more than 4 megacycles.

The following significant data was obtained, and is based upon data scaled up to TVCS conditions expected on the satellite:

1. With sunlight normal to boom target and camera line-of-sight normal to boom target, a 7.2-inch diameter spot in a 14.4 inch diameter disc can be resolved. The spot signal level is 30% of the peak signal level. The resolution of the spot and the estimate of the signal level was determined from the top and bottom traces of the photograph in Figure 2.4-13.
2. If the target diameter is reduced to 9.6 inches and the spot to 4.8 inches the modulation is 8%.
3. The relative signal strength for other than normal sunlight and target normal to camera are shown in Figures 2.4-14. It should be recognized that the angle between camera line of sight and target normal will range from 5.5° to 31° as a function of scissor angle. Angle of sun light will change 360° per orbit.
4. For 60° boom angle the greatest allowable sun angle for a 2 to 1 signal-to-noise ratio and a 6-inch plain target is approximately 51° . The plain target has a machined aluminum surface so as to contain many rough reflecting grooves.
5. As a strictly laboratory experiment the target model having the inner darkened disc was sprayed with Krylon No. 1310 dulling spray. With sun and camera normal to target the modulation of the signal due to the dark spot changed from an estimated 1% without dulling material to 10% with it. The bright part of the model target is a smooth machined finish. Adding the dulling material gives it a frosted appearance.
6. The optimum lens opening was determined to be f/2.8.

Further tests are planned to determine the effects of using a Xenon lamp which has a spectral output more like the sun than the 500 watt flood lamp (tungsten) used in these experiments. It is also recognized that the optimum target surface reflection material has not yet been determined.

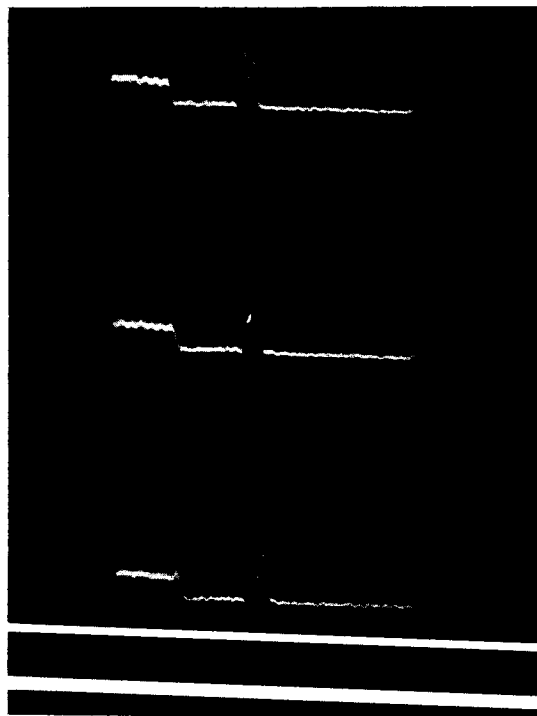


Figure 2.4-13. Resolution of Black Spot in Center of Illuminated Disc by Oscilloscope Trace of the Video Sweep Line

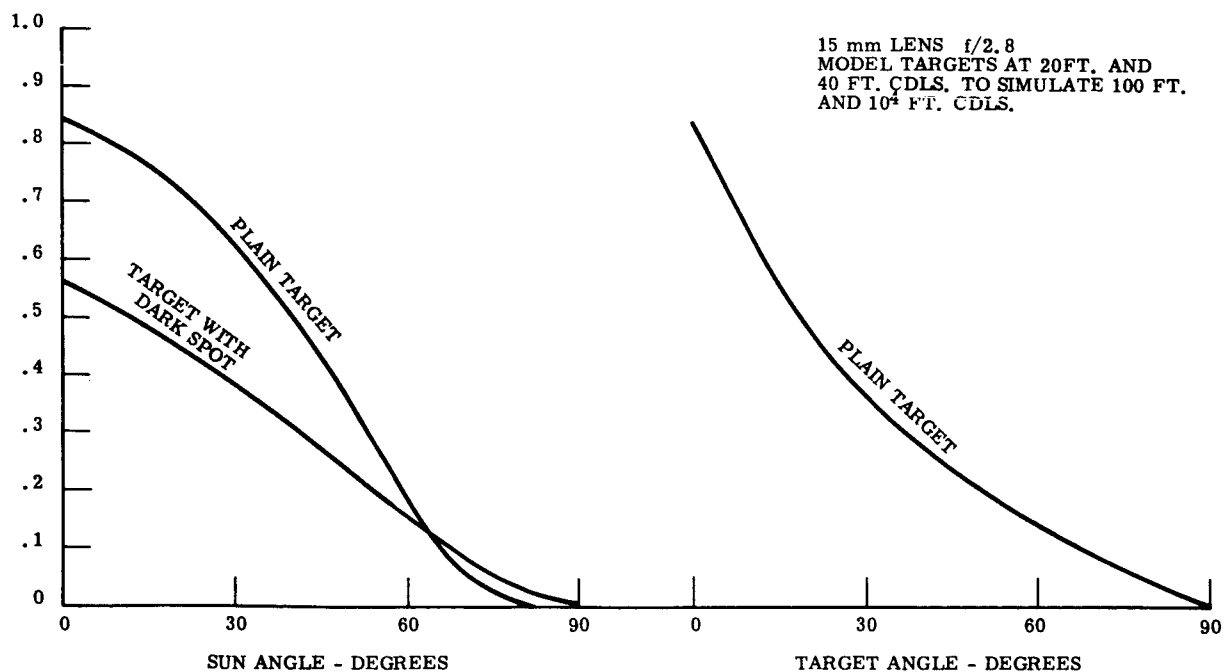


Figure 2.4-14. Relative Signal Strength for Other Than Normal Sunlight and Target

2.5 Reliability

An apportionment of the Advanced Technological Satellite Configuration was made to determine the reliability goals applicable to each of its constituent components. An arbitrary mission lifetime of \geq three years was selected as the reliability goal in order to conform to the performance requirements shown in the Hughes Aircraft Company (HAC) document SSD 4277B, dated June, 1964.

Table 2.5-1 summarizes the apportionment in respect to the duty cycle, reliability design goal and the required Mean Time To Failure (MTTF) for each component.

Based on the product of the component reliability values, $\prod_{i=1}^n R_i$, the Configuration would have an estimated reliability of .55 for the three-year mission. These values have been used as the design goals in each component specification.

2.5.1 Apportionment Factors

Four primary factors influenced the apportionment:

1. Data obtained from subcontractor responses to the RFQ
2. Criticality of each component to the mission objective
3. Short lifetime of the vidicon tube in the TV camera
4. Relative complexity and the design problems of the components.

Secondary factors involved in the reliability computations were:

1. The dampers are essentially redundant in that a failure of either one does not affect the function of the other.
2. All of the five sensor components may not be used in the final configuration. At most, three will be required, probably the solar aspect sensor, RF sensor and the magnetometer. In turn, any two, out of the three, are necessary to establish pointing accuracy.
3. The gravity gradient booms will be deployed and scissored a maximum of ten operations in the mission.
4. Relays and driver circuits for power distribution will see a maximum of 3000 operations in the mission, except the motor controls.
5. The angle detector is not essential to the mission, being used solely for information concerning boom position.
6. All components are functionally independent, except the power control unit.
7. The TV camera will have a maximum duty cycle of .16 of the total mission hours.
8. All sensor components will have a maximum of 3000 on-off cycles and a duty cycle of .5 of the total mission hours.

TABLE 2.5-1. ATS APPORTIONMENT

COMPONENT	DUTY CYCLE	RELIABILITY DESIGN GOAL	6000-MILE ORBIT VEHICLE
TV Camera	.16	.75	15,000 Hrs
Solar Aspect Sensor	.50	.80	55,000 Hrs
RF Sensor	.50	.80	55,000 Hrs
Magnetometer	.50	.80	55,000 Hrs
Power Control Unit	.50	.95	Not Applicable
Gravity Gradient Rods	10 Op/Mission	.95	Not Applicable
C. Passive Damper	1.00	.91 (Redundant) .55	65,000 Hrs Each

2.5.2 Apportionment

2.5.2.1 TV Camera

As previously mentioned, the limiting item toward achieving a high reliability for the Experimental Package is the vidicon tube in the TV camera. Using high reliability parts and a duty cycle of 60 minutes operation per orbit, the estimated reliability is ~ .75 for the three-year mission, if the vidicon tube selected for use in the component has an MTTF of 20,000 hours.

2.5.2.2 Sensor Components

The complexity (number of parts) of the Solar Aspect Sensor and the RF Sensor are approximately the same. Assuming the magnetometer to be of the same complexity gives an equivalence of 1:1 among all three sensor components. Since, under worst case conditions, two out of the three components are required for attitude determination, then the Binomial Expression can be used to compute the survival probability of any two out of three equivalent components:

$$P(s_1 n) = \sum_{x=s}^n \binom{n}{x} P^x (1 - P)^{n-x}$$

where P is the reliability of any one of the three equivalent components.

Assigning a reliability of .80 for each component, results in a probability of survival of .90 for any two out of the three components. This would require an MTTF of approximately 55,000 hours at a 50% duty cycle for each component.

2.5.2.3 Power Distribution

Approximately 25 relays and 50 driver circuits will be used in this component. Most driver circuits and relays will be operated a maximum of 3000 operations at approximately 50 milliseconds per operation, and will remain in a standby mode for the greater share of the mission.

A reliability estimate based on this type of operation shows a reliability of .95 can be expected in the mission.

2.5.2.4 Gravity Gradient Rods

The gravity gradient booms are one of the two components critical to the mission, because the failure of this component will result in improper orientation of the spacecraft.

A reliability estimate was made based on 10 operations of the rods in a deployment, retraction or scissoring operation and the duration of the mission in a standby mode. The estimate shows a probability of operation of .99 for the 10 cycles and a standby reliability of approximately .67 during the three-year mission. It is reasonable to suppose that with the selection of proper materials, processing, and manufacturing techniques, the standby mode of failure (degradation due to environment) of the mechanical and electromechanical parts can be reduced by an order of magnitude. This would result in an estimated reliability of .95 for the booms.

2.5.2.5 Combination Passive Damper

This component, in conjunction with the gravity gradient booms, is most critical to the mission, since it has an operational requirement for the full mission life to control oscillation. Since two units are used, a back-up is provided in case of failure of any one unit, so this component has true redundancy.

Each of the units must have an MTTF approximately 2 1/2 times the mission hours (26,000) to attain a reasonable probability of survival. Therefore, based on each unit having an MTTF of 65,000 hours the units in true redundancy, and neglecting the clutch; a reliability of .91 would be the design goal.

2.5.3 Parts

The "ATS Authorized Parts List" received from HAC does not encompass all part types which may be required in certain equipments. Therefore, a policy has been adopted to use the most reliable part available and suitable for each application.

For overall system consistency, this places priority on:

1. The use of Hughes High Reliability Part Specifications wherever applicable to the engineering requirements
2. The use of GE "space qualified" high reliability parts
3. The use of contractor recommended high reliability parts.

All parts which are selected for use in equipment but which do not appear on the ATS parts list will be qualified by tests consistent with the HAC Specifications.

With the decision to use HAC parts in all GE-SD components, an Approved Parts List, 490L106, was generated using the duplicate parts specified on the "ATS Authorized Parts List" received from HAC. All available HAC part specifications were compiled and distributed to all subcontractors and in-house design personnel for use in their components.

The distribution of applicable part specifications referenced in 490L106 is not complete since all specifications have not been received by GE-SD. The missing specifications were verbally requested from the Technical Officer on September 24, 1964.

HAC is to supply GE-SD with a Qualification Status List for all parts on the authorized list, since all parts with an "X" preceding the drawing number are not yet qualified.

Specification SVS 7325, entitled, "Standard Parts, Materials and Processes, Use of," was issued and defines part usage, intermittent life tests and extended power ageing for the engineering models, prototype and flight unit components.

Parts appearing on the ATS "APL" are being analyzed for their susceptibility to the radiation environments specified for the medium altitude orbit (6000-mile orbit) and the synchronous orbit (24-hour orbit).

2.5.4 Standards

All component specifications and work statements sent to the subcontractors have been reviewed to assure compliance with existing Military, GE-SD, or NASA specifications relating to processing techniques, inspection procedures, etc.

An "Approved Materials and Processes for ATS" (Document 490L107), has been issued and transmitted to all subcontractors for application on all equipment designs.

2.6 Quality Control Activity

Technical support was provided to the design engineering effort to establish the requirements for test equipment and facilities. Support was also furnished in providing the Quality Control requirements for the component work statements and specifications.

2.7 Manufacturing

Close liaison has been established between Design Engineering and Manufacturing Engineering to identify the required manufacturing processes and formalize plans for availability by the time drawings are released.

2.7.1 Process Development

Work was initiated to establish the required cleaning procedures to control against surface magnetic particle contamination of the combination passive damper parts during the manufacturing cycle. The work to date has been in establishing test procedures as recommended by Design Engineering to measure the effectiveness of cleaning methods to be evaluated. Test samples of aluminum will be contaminated with magnetic particles known to exist in the shop area, and tests will be conducted before and after cleaning.

2.7.2 Mechanical Interface

Eighteen mechanical interfaces have been identified, and plans have been formalized to provide appropriate tooling to control each of these interfaces.

2.7.3 Make or Buy Structure

One change has been made in the Make or Buy structure; the RF Attitude Sensor is now a "make" item. The sensor will be produced by the Radio Guidance Operation of the General Electric Company, Utica, New York.

SECTION 3. NEW TECHNOLOGIES

There are no new technologies to be reported this quarter. Efforts to monitor the analytical and developmental areas will continue, and new technologies will be reported as they are developed.

SECTION 4. BIBLIOGRAPHY

1. "Gravity Gradient Stabilization System", Volume I, Program Plan, General Electric Document No. 64SD4324, dated 7 August 1964 (referenced in paragraph 2. 4)
2. Timoshenko, Vibration Problems in Engineering, Third Edition, January 1955 (referenced in paragraph 2. 1. 6. 3)
3. "RF Attitude Sensor - Preliminary Study", General Electric Document No. 64SD982, 19 August 1964.
4. Principles of Television Engineering, Fink D. G., McGraw-Hill

SECTION 5. GLOSSARY

The following is a list of abbreviations and definitions for terms used throughout this report:

CPD	Combination Passive Damper
Crab Angle	Out-of-orbit angle flight caused by changes in X-rod angle
EC	Eddy Current
GE-SD	General Electric Company Spacecraft Department
HAC	Hughes Aircraft Company
LOFF	Low Order Force Fixture
MAGGE	Medium Altitude Gravity Gradient Experiment (6000-mile orbit flight)
MTFF	Mean Time To Failure
RFAS	RF Attitude Sensor
SAGGE	Synchronous Altitude Gravity Gradient Experiment (240 hour orbit flight)
STEM	Storable Tubular Extendable Member
SVA Fixture	Shock and Vibration Attachment Fixture
Thermal Twang	Sudden thermal bending which the booms will experience in passing from a region of total eclipse into a region of continuous sunlight or vice versa
TR	Torssional Restraint
TVCS	TV Camera Subsystem

APPENDIX A

DETERMINATION OF GRAVITY GRADIENT
STABILIZATION ADVANCED TECHNOLOGICAL
SATELLITE PITCH, ROLL AND YAW ANGLES
FROM SOLAR ASPECT INFORMATION

APPENDIX A

1. Summary

The digital output of the ATS Solar Aspect Sensor indicates the illuminated detector number and the inclination of two planes. These planes are each orthogonal to the detector eyes and their intersection determines the vector from the detector to the sun.

This information, two angular values, must first be brought into a form which is easily transformed and then the transformation operation to vehicle coordinates can be performed.

The procedure is detailed in this appendix and an expression for the vehicle coordinates corresponding to a unit vector to the sun is derived in terms of the two angles that are indicated by the instrument. Combination of this information with the known unit vector to the sun in orbital coordinates yields pitch, roll and yaw angles, the expressions for which are also derived.

2. Derivation of Cartesian Coordinate Values in Terms of the Detector Angles

Figure A-1 shows a schematic top view of a solar detector and the placement of the coordinate system of Figure A-2.

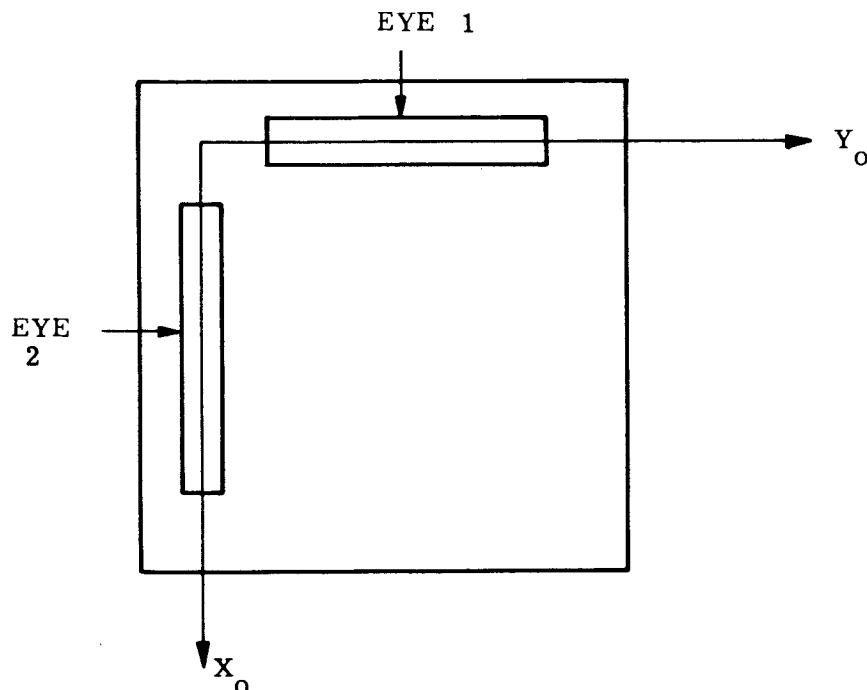


Figure A-1. Schematic Top View of Solar Detector

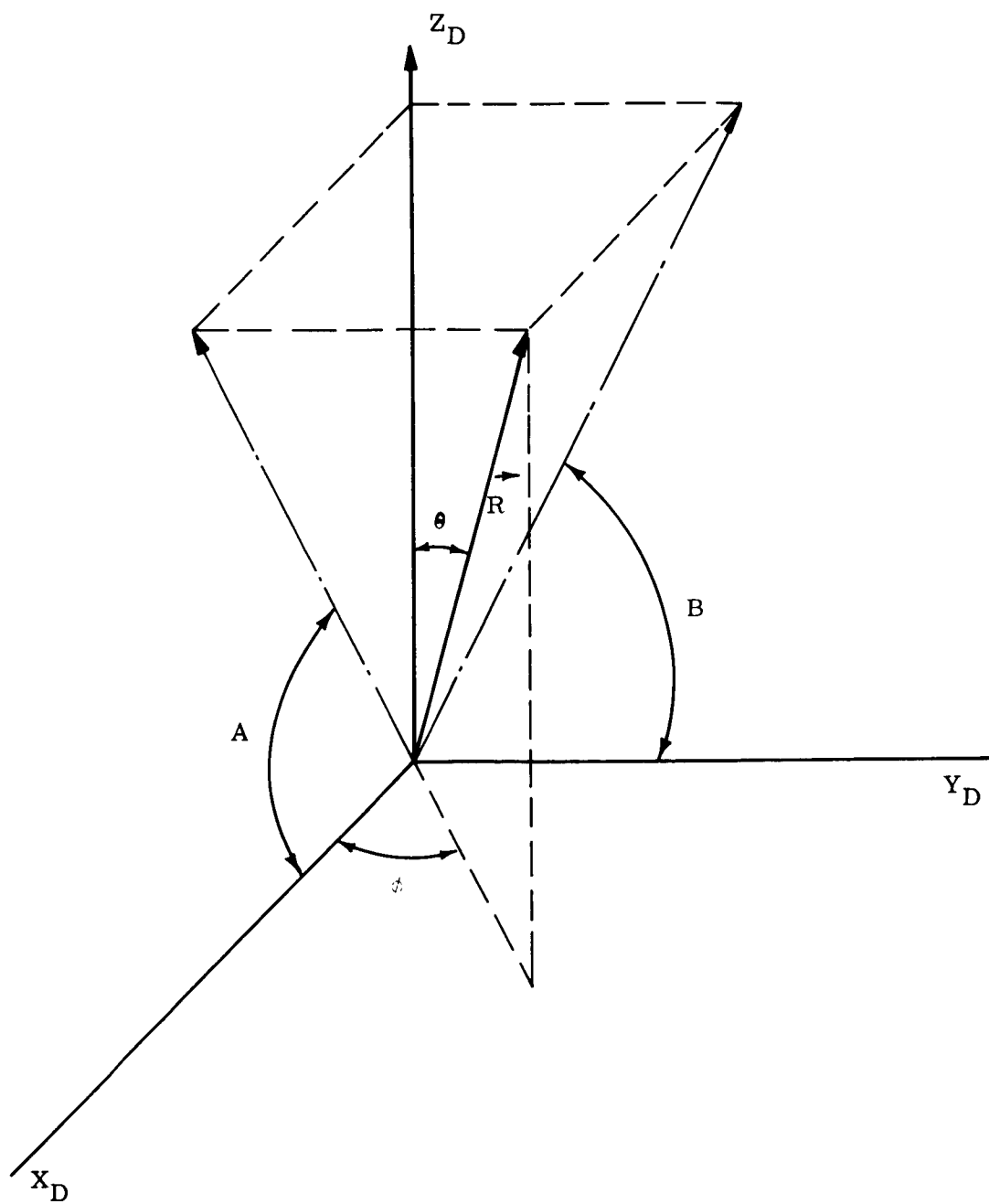


Figure A-2. Unit Vector \vec{R} to the Sun

A unit vector \vec{R} to the sun is shown in Figure A-2 in the coordinate system X_D, Y_D, Z_D and the spherical coordinate system r, θ, ϕ . Eye 1 of the detector measures angle A and Eye 2 measures angle B.

The cartesian coordinates of vector \vec{R} can then be described in two ways:

$$\begin{aligned} X_D &= R_1 \cos A \\ Y_D &= R_2 \cos B \\ Z_D &= R_1 \sin A = R_2 \sin B \end{aligned} \tag{1}$$

$$\begin{aligned} X_D &= \sin \theta \cos \phi \\ Y_D &= \sin \theta \sin \phi \\ Z_D &= \cos \theta \end{aligned} \tag{2}$$

From Equations (1) and (2), R_1 and R_2 can be found in terms of A and B.

$$R_1 = \frac{1}{\sin A \sqrt{1 + \cot^2 A + \cot^2 B}}$$

$$R_2 = \frac{1}{\sin B \sqrt{1 + \cot^2 A + \cot^2 B}}$$

Then the cartesian coordinates of the detector in terms of the detector angles A and B are:

$$\begin{aligned} X_D &= \frac{\cos A \sin B}{\sqrt{\sin^2 B + \sin^2 A \cos^2 B}} \\ Y_D &= \frac{\sin A \cos B}{\sqrt{\sin^2 B + \sin^2 A \cos^2 B}} \\ Z_D &= \frac{\sin A \sin B}{\sqrt{\sin^2 B + \sin^2 A \cos^2 B}} \end{aligned} \tag{3}$$

3. Transformation to Vehicle Coordinates

Positioning of the detectors (D_1 through D_5) with respect to the vehicle axes is shown in Figure A-3. X_1 is the vehicle yaw axis, Y_1 the roll axis, and Z_1 the pitch axis.

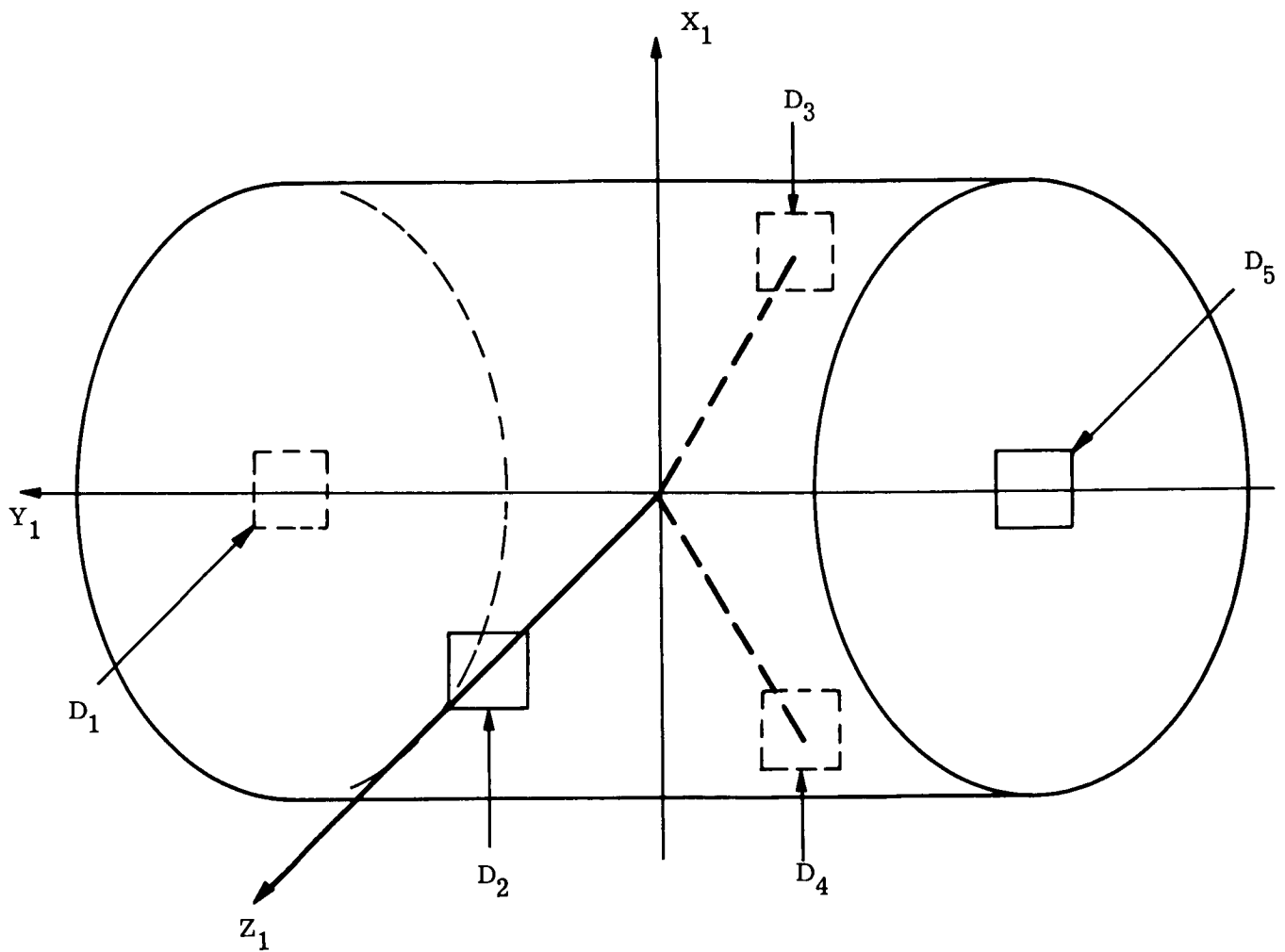


Figure A-3. Position of Detectors D_1 through D_5 with Respect to the Vehicle Axes

Figures A-4 and A-5 indicate the detector axes with respect to the vehicle axes.

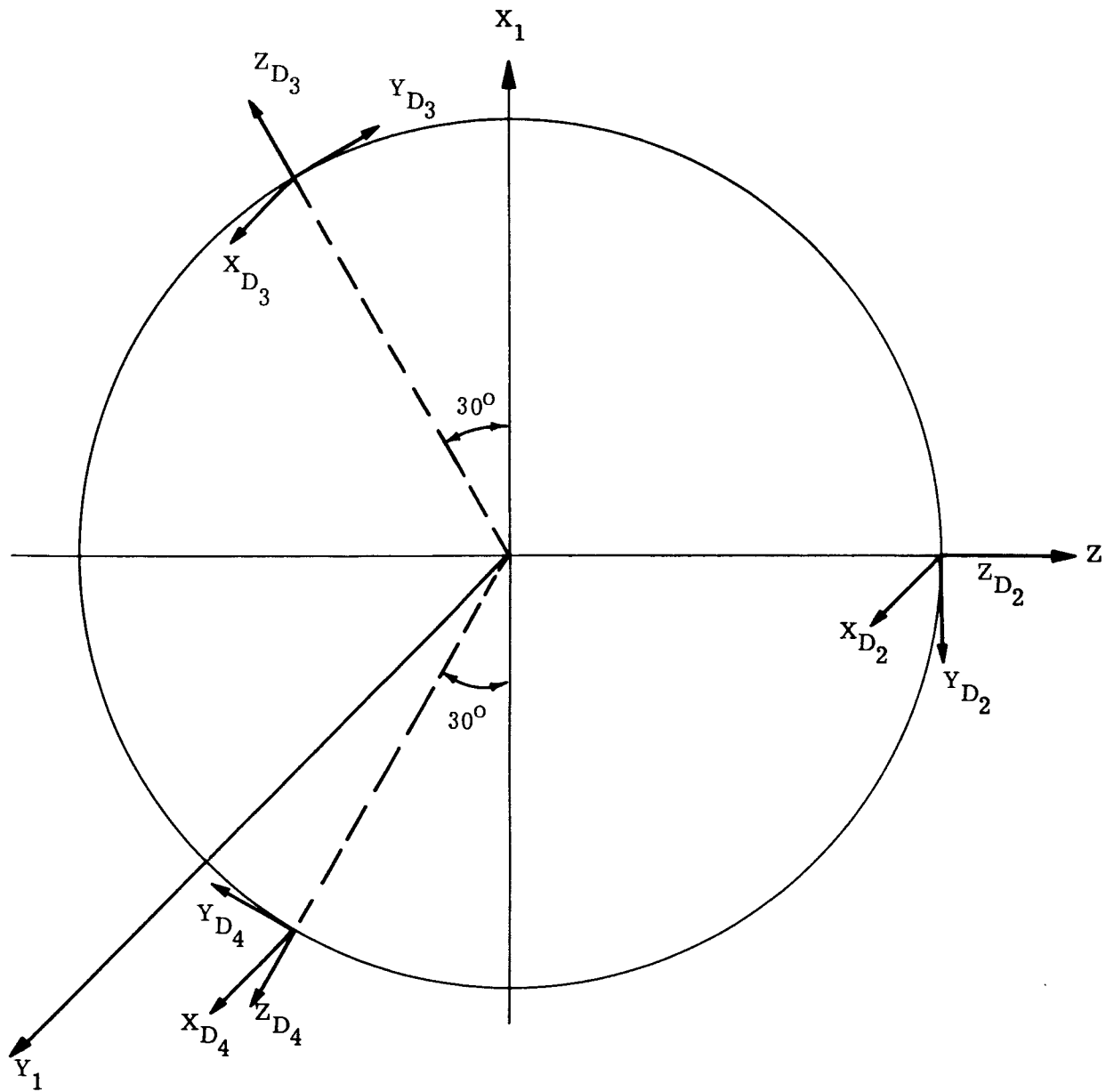


Figure A-4. Detector Axes with Respect to the Vehicle Axes (Top View)

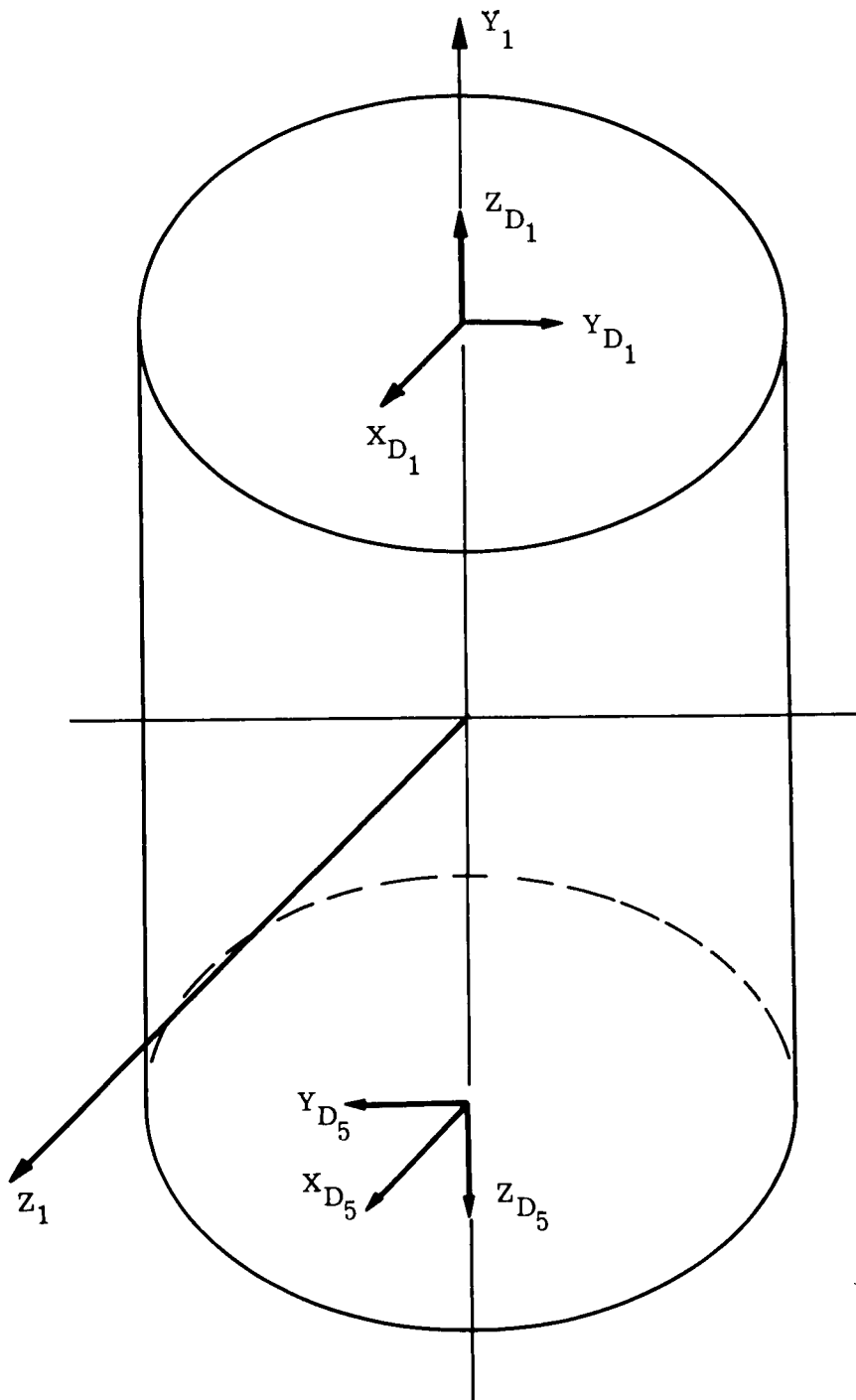


Figure A-5. Detector Axes with Respect to the Vehicle Axes (Side View)

The coordinate transformations are:

$$\begin{aligned}
 \begin{pmatrix} X_1 \\ Y_1 \\ Z_1 \end{pmatrix}_1 &= \begin{pmatrix} 0 & 1 & 0 \\ 0 & 0 & 1 \\ 1 & 0 & 0 \end{pmatrix} \begin{pmatrix} X_{D1} \\ Y_{D1} \\ Z_{D1} \end{pmatrix} \\
 \begin{pmatrix} X_1 \\ Y_1 \\ Z_1 \end{pmatrix}_2 &= \begin{pmatrix} 0 & -1 & 0 \\ 1 & 0 & 0 \\ 0 & 0 & 1 \end{pmatrix} \begin{pmatrix} X_{D2} \\ Y_{D2} \\ Z_{D2} \end{pmatrix} \\
 \begin{pmatrix} X_1 \\ Y_1 \\ Z_1 \end{pmatrix}_3 &= \begin{pmatrix} 0 & \sin 30 & \cos 30 \\ 1 & 0 & 0 \\ 0 & \cos 30 & -\sin 30 \end{pmatrix} \begin{pmatrix} X_{D3} \\ Y_{D3} \\ Z_{D3} \end{pmatrix} \\
 \begin{pmatrix} X_1 \\ Y_1 \\ Z_1 \end{pmatrix}_4 &= \begin{pmatrix} 0 & \sin 30 & -\cos 30 \\ 1 & 0 & 0 \\ 0 & -\cos 30 & -\sin 30 \end{pmatrix} \begin{pmatrix} X_{D4} \\ Y_{D4} \\ Z_{D4} \end{pmatrix} \\
 \begin{pmatrix} X_1 \\ Y_1 \\ Z_1 \end{pmatrix}_5 &= \begin{pmatrix} 0 & -1 & 0 \\ 0 & 0 & -1 \\ 1 & 0 & 0 \end{pmatrix} \begin{pmatrix} X_{D5} \\ Y_{D5} \\ Z_{D5} \end{pmatrix}
 \end{aligned} \tag{4}$$

The subscripts in Equations (4) refer to the detector number which will be indicated by the sensor output.

4. Determination of Vehicle Attitude

It is assumed that the direction to the sun in orbital coordinates is known, e.g., a column matrix $\begin{pmatrix} r \\ p \\ q \end{pmatrix} = S$ whose components are orthonormal is given.

Footnote 1 gives the transformation from orbital coordinates to vehicle coordinates as:

$$\begin{pmatrix} X_1 \\ Y_1 \\ Z_1 \end{pmatrix} = \begin{pmatrix} e_{11} & e_{12} & e_{13} \\ e_{21} & e_{22} & e_{23} \\ e_{31} & e_{32} & e_{33} \end{pmatrix} \begin{pmatrix} r \\ p \\ q \end{pmatrix} \tag{5}$$

1. "Final Report for Feasibility Study of Passively Oriented Lenticular Satellites," General Electric Missile and Space Division, date 21 June 1963 to 30 August 1963.

where

$$\begin{aligned}
 e_{11} &= \cos \theta_p \cos \theta_r \\
 e_{12} &= \sin \theta_p \cos \theta_r \\
 e_{13} &= -\sin \theta_r \\
 e_{21} &= \cos \theta_p \sin \theta_r \sin \theta_y - \sin \theta_p \cos \theta_y \\
 e_{22} &= \cos \theta_p \cos \theta_y + \sin \theta_p \sin \theta_r \sin \theta_y \\
 e_{23} &= \cos \theta_r \sin \theta_y \\
 e_{31} &= \sin \theta_p \sin \theta_y + \cos \theta_p \sin \theta_r \cos \theta_y \\
 e_{32} &= \sin \theta_p \sin \theta_r \cos \theta_y - \cos \theta_p \sin \theta_y \\
 e_{33} &= \cos \theta_r \cos \theta_y
 \end{aligned} \tag{6}$$

and

$$\begin{aligned}
 \theta_r &= \text{roll angle} \\
 \theta_p &= \text{pitch angle} \\
 \theta_y &= \text{yaw angle}
 \end{aligned}$$

Letting $\begin{pmatrix} X_1 \\ Y_1 \\ Z_1 \end{pmatrix} = V$ Equation (5) can be written as

$$V = ES \tag{7}$$

Then $E = VS^+$ (8)

since the components of S are orthonormal.

$$\begin{aligned}
 \begin{pmatrix} e_{11} & e_{12} & e_{13} \\ e_{21} & e_{22} & e_{23} \\ e_{31} & e_{32} & e_{33} \end{pmatrix} &= \begin{pmatrix} X_1 \\ Y_1 \\ Z_1 \end{pmatrix} (r \ p \ q) \\
 \begin{pmatrix} e_{11} & e_{22} & e_{13} \\ e_{21} & e_{22} & e_{23} \\ e_{31} & e_{32} & e_{33} \end{pmatrix} &= \begin{pmatrix} X_1 r & X_1 p & X_1 q \\ Y_1 r & Y_1 p & Y_1 q \\ Z_1 r & Z_1 p & Z_1 q \end{pmatrix}
 \end{aligned} \tag{9}$$

From Equations (6), θ_r , θ_p , θ_y can be found in terms of the elements of E.

$$\begin{aligned}
 \theta_p &= \tan^{-1} \left(\frac{e_{12}}{e_{11}} \right) \\
 \theta_r &= \sin^{-1} (-e_{13}) \\
 \theta_y &= \tan^{-1} \left(\frac{e_{23}}{e_{33}} \right)
 \end{aligned} \tag{10}$$

Equations (10) are double-valued functions, but the assumption of $\cos \theta_r > 0$ removes the ambiguity. The signs of e_{11} , e_{12} , e_{23} and e_{33} in Equation (7) then indicate the signs of $\sin \theta_p$, $\cos \theta_p$, $\sin \theta_y$ and $\cos \theta_y$ and so the angles are uniquely determined. $\cos \theta_r > 0$ places θ_r in the first and fourth quadrant and implies oscillations of less than 90° around zero which is certainly a reasonable assumption.